TESIS DE LA UNIVERSIDAD DE ZARAGOZA

2016

125

Ana María Repollés Rabinad

Quantum computing with molecular magnets

Departamento

Física de la Materia Condensada

Director/es

Luis Vitalla, Fernando María

Sesé Monclús, Javier

ISSN 2254-7606

Prensas de la Universidad Universidad Zaragoza

ISSN 2254-7606

Universidad Zaragoza
1542

Tesis Doctoral

QUANTUM COMPUTING WITH MOLECULAR MAGNETS

Autor

Ana María Repollés Rabinad

Director/es

Luis Vitalla, Fernando María
Sesé Monclús, Javier

UNIVERSIDAD DE ZARAGOZA

Física de la Materia Condensada

2016

Universidad Zaragoza
1542

Tesis Doctoral

Quantum computing with molecular magnets

Autor

Ana María Repollés Rabinad

Directores

Fernando Luis Vitalla
Javier Sesé Monclús

Facultad de Ciencias

2015

Contents

Resumen

En esta tesis se ha pretendido realizar y testar los componentes básicos necesarios de un futuro ordenador cuántico usando para ello moléculas magnéticas sencillas. Con este fin se ha comprobado que estas moléculas cumplen con los tres ingredientes principales que necesita reunir un buen candidato: qubits bien definidos y diferenciables, coherencia cuántica y buen acoplo a dispositivos de sintonización. También se ha estudiado, por tanto, su integración en dispositivos atendiendo a cómo se acoplan a ellos y a si conservan sus propiedades magnéticas, tales como el spín, la anisotropía, la interacción entre distintos iones, etc. El trabajo que aquí se presenta se divide fundamentalmente en tres partes.

Desarrollo, mejora y testado de dispositivos superconductores de interferencia cuántica (SQUID)

En esta parte de la tesis se realiza un análisis detallado de varios modelos de dispositivos pertenecientes a nueva generación de susceptómetros SQUID, especialmente diseñados para medir las propiedades magnéticas de muestras de tamaño micrométrico, hasta 30 μm de diámetro (capítulo 3). En particular, presentamos un estudio del ruido de estos sensores, teniendo en cuenta las distintas contribuciones extrínsecas al SQUID y provenientes de la electrónica. También se estudia la posibilidad de incluir una etapa amplificadora de bajo ruido, que permita reducir esta contribución. Por otro lado, se ha hecho un cuidadoso análisis sobre el origen de la respuesta magnética de los susceptómetros vacíos, con el fin de llegar a un protocolo común de tratamiento de los datos de susceptibilidad ac, obtenidos para distintas muestras.

Por último, y con el objetivo de mejorar la sensibilidad de los sensores en la detección de muestras de tamaño nanométrico, en este trabajo se presenta la realización mediante Focused Ion Beam (FIB) de una nanoespira de unos 500 nm de diámetro, en serie con la bobina detectora del SQUID. Esta nanoespira permite mejorar la sensibilidad del dispositivo en esa zona y, para comprobarlo,

se incluyen varias medidas con muestras cuyo comportamiento magnético es conocido.

Caracterización de cristales de moléculas magnéticas con los que se pueden llevar a cabo puertas lógicas computacionales

La segunda parte incluye un estudio de imanes moleculares, que contienen uno, dos o tres espines magnéticos débilmente acoplados, con el fin de comprobar que pueden utilizarse para llevar a cabo operaciones propias de la computación cuántica. Por un lado se estudian los dímeros constituidos por dos iones Ln^{3+} donde Ln es un lantánido (capítulo 4). Cada uno de los espines que forman el dímero tiene una estructura de niveles tal que los dos niveles de menor energía están fuertemente separados de los niveles superiores, formando, por tanto, sistemas de dos niveles efectivos o qubits. Por otro lado, estos espines están débilmente acoplados entre sí, lo que constituye un sistema de cuatro niveles entrelazados con los que es posible realizar puertas cuánticas de dos qubits, en particular las puertas CNOT y SWAP. En esta tesis se presentan los primeros resultados de realización de estas puertas, en los dímeros de Tb_2 y ErCe.

En cuanto a los trímeros, o imanes moleculares con tres espines magnéticos, en esta tesis se presenta un estudio para el trímero compuesto por dos iones Cu^{2+} y un ion Er^{3+} (capítulo 5). En primer lugar se analiza el comportamiento magnético de los dos iones de cobre en el trímero CuLaCu, donde el ion La^{3+} es diamagnético, y se comprueba que existe un acoplo entre sus espines, permitiendo la realización de puertas de dos qubits, también para este material. Incluyendo la información obtenida para este compuesto, se presenta por último un análisis del comportamiento magnético del trímero CuErCu constatando la existencia de un acoplo muy débil entre los iones cobre y el ion erbio y, por tanto, la posibilidad de realizar puertas cuánticas de tres qubits, como las puertas Fredkin y Toffoli.

Estudio de procesos de relajación y deposición en superficie

Esta última parte pretende aunar las dos partes anteriores depositando las moléculas estudiadas en la parte anterior sobre los dispositivos superconductores del principio, mediante la técnica de Dip-Pen Nanolitography (DPN). La intención última es comprobar si estas moléculas mantienen sus propiedades magnéticas al ser sometidas a los efectos de una superficie ajena a su estructura cristalina y comprobar si se trata de sistemas lo suficientemente coherentes como para realizar operaciones cuánticas sin que los estados se degraden demasiado rápido. En primer lugar, en este capítulo se presenta un estudio de los procesos de relajación de estas moléculas, en su estado original (capítulo

6), atendiendo al origen y las causas de estos procesos. Para ello se ofrecen los resultados en una serie de muestras en las que hay cada vez más niveles accesibles, partiendo de un dímero con un sólo espín magnético y sin apenas interacciones nucleares, ErLa, hasta llegar al caso de un dímero con dos espines magnéticos y una considerable contribución nuclear, Dy_2.

Una vez entendidos los procesos de relajación en las muestras cristalinas, se han depositado unas pocas monocapas de estas muestras sobre los SQUID utilizando la técnica DPN, con el fin de comprobar su integridad física (capítulo 7). En particular se describen experimentos para dos muestras diferentes, un imán molecular cuyo comportamiento es bastante conocido, el Mn_{12}, y un dímero de Dy_2. En este capítulo se muestran los resultados de las medidas de susceptibilidad ac en comparación con las medidas previas, hechas con medidas en microcristales.

Chapter 1

Introduction

Over the past decades we have assisted to an astonishing miniaturization of computer components. Whereas in 1971 a microchip had approximately 2300 transistors, today it contains more than one billion in the same space. Attending to Moore's law [1.1], in 2020 the basic components will reach the size of individual atoms.

In spite of this dramatic change in the size of computer elements, computation itself has been performed using the same underlying mathematical laws. These classical devices are based on the ability to store "0s" and "1s" and to manipulate them in a controlled manner, in close analogy to Turing's early model of computation [1.2]. However, a computer device is a physical system which is governed by physical laws. Therefore, to manage atom-sized components, quantum effects will necessarily have to be taken into account.

There are mainly two ways to face the emergence of quantum effects: trying to suppress them or getting profit of them. The second approach represents a new paradigm in computation, known as quantum computing.

First ideas about applying quantum mechanics on computation comes from the early 70s, when a group of physicists and mathematicians began to study the possibilities of certain quantum effects, such as reversibility or superposition, to improve classical computing [1.3–1.6]. It was in 1982 when Richard Feynman published the first abstract model of a quantum system that could be used to do computations [1.7] and, three years later, in 1985, David Deutsch described for the very first time an universal quantum Turing machine [1.8]. Quantum algorithms [1.9–1.11] and first proposals for experimental realization of them [1.12, 1.13] came in the 90s.

Quantum computing allows performing certain computational tasks in fewer steps than any classic computer. It linearises potential problems, going from

2^n steps to n steps [1.14]. For instance, concerning quantum simulations, each doubling of classical computational power permits only one additional spin-1/2 particle to be simulated whereas in quantum computing, only an additional "quantum bit" is required. It can also solve new tasks, such as teleporting information [1.15], breaking codes [1.10] or creating true random numbers [1.16], and improve some others, such as searching in databases [1.11].

The efficiency promised by quantum computing has stimulated the experimental search of multitude of candidates for successfully carrying out quantum operations. Among these candidates there are photons in cavities [1.17], ions trapped by electric fields and cooled by laser techniques [1.18], superconducting circuits [1.19, 1.20], quantum dots [1.21], NV centres [1.22], P defects in Si [1.23], topological excitations [1.24], single molecule magnets [1.25–1.27], etc.

As Richard Feynman said in 1959 [1.28], very small devices would not necessarily behave the same as bigger ones. It is then necessary to quantize them starting by the smallest computing unity: going from the bit to the qubit. Quantization is based on intrinsic discreteness of quantum world where any 2-state quantum system [1.29], such as a spin, the polarization of a linearly polarized photon, the direction of rotation of a circularly polarized photon or, simply, energy levels in an exited atom, appears as a natural quantum binary digit or a qubit.

As any 2-state quantum system, a qubit can exist in a superposition of states and therefore it can be either "0" and "1"

$$|\psi\rangle = a\,|0\rangle + b\,|1\rangle \tag{1.1}$$

with $a^2 + b^2 = 1$. Reading a qubit means obtaining $|0\rangle$ with a probability a^2 and $|1\rangle$ with a probability b^2.

After reading, the quantum state evolves to a frozen state $|0\rangle$ or $|1\rangle$. The question which arises then is if it is possible to read, copy, erase, negate a qubit without causing it to change. Entanglement appears as the way to measure qubits without "touching" them. For a 2-qubit system, we will have a state

$$|\Psi\rangle = c_0\,|00\rangle + c_1\,|01\rangle + c_2\,|10\rangle + c_3\,|11\rangle \tag{1.2}$$

This state is called entangled if and only if it does not exist a direct product of any two qubits which could reproduce the total state

$$|\Psi\rangle_{AB} \neq |\psi\rangle_A \otimes |\psi\rangle_B \tag{1.3}$$

for any $|\psi\rangle_A$ and $|\psi\rangle_B$.

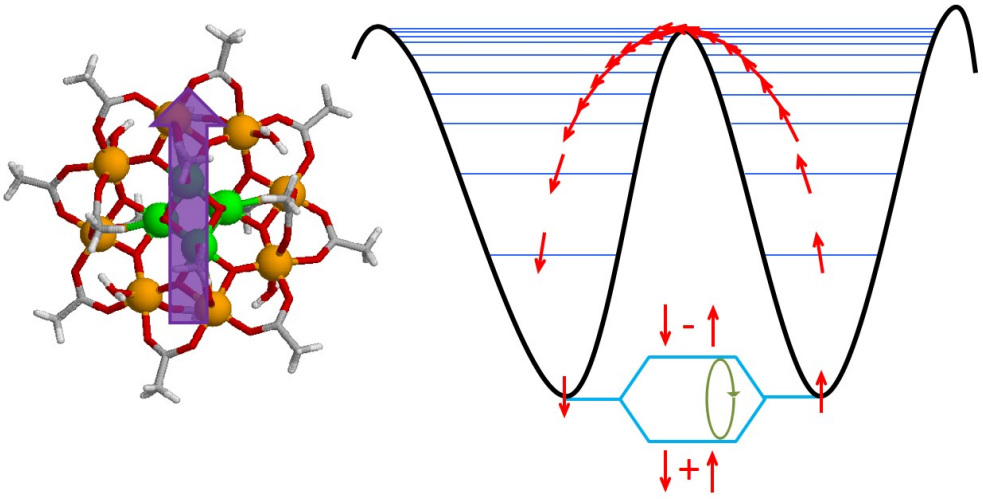

Figure 1.1: Example of experimental qubit, consisting of a single molecule magnet, Mn_{12}. All manganese atoms are strongly coupled and define a two state system.

If the qubits are entangled, the actions performed on one subset of qubits can have an impact on another "untouched" subset of qubits. For example, the entangled state

$$|\Psi\rangle = \frac{1}{\sqrt{2}} \left(|0\rangle_A \otimes |0\rangle_B + |1\rangle_A \otimes |1\rangle_B \right) \tag{1.4}$$

allows us to determine the value of B, without "touching" it, by measuring A.

Although we have already pointed out one of the conditions for having a qubit, the existence of a well-defined 2-level system, there exist other requirements. Qubits must be addressable [1.30], i.e. it is necessary to choose the one that is performing a given operation and be able to read out the answer. Moreover, a mechanism to initialize and manipulate each qubit is also needed [1.29]. Perhaps one of the most stringed conditions is related to quantum coherence. A good qubit candidate should have a long enough coherence time to perform operations before the state decays as a result of the interaction with its environment [1.29]. Finally, a good candidate must be integrated into an scalable architecture, able to perform complex computational tasks.

Single molecule magnets (SMM) have joined the list of qubit candidates for quantum computing in the last decade. These molecules consist of one or more strongly coupled magnetic atoms which define a molecular spin whose states can be used as the two states of a quantum bit (see Fig.1.1). The magnetic core is surrounded by non-magnetic atoms, mainly organic elements, which stabilize the molecule structure and isolate each molecular spin from its neighbours [1.31]. SMM are also highly reproducible providing as many qubits

as it is needed to perform more complexes quantum tasks, such as quantum gates, quantum processors and error correction mechanisms. The ability to chemically engineer the molecular structure, spin, anisotropy, etc. provides a very powerful method to define the basic qubit parameters and to optimize the spin coherence [1.32].

The study of these molecular materials also requires a parallel development of new devices, able to measure smaller and smaller amounts of SMM, in order to reduce to the limit unpleasant lattice effects which can affect the coherence and, hence, make possible quantum operations. Attempting to interact with just one of these SMM, being able to identify and address to each qubit from the ensemble, would be the final goal in this race [1.33].

A magnetic molecule, anchored onto a solid-state device, experiences a very different environment as that of a molecular crystal. This could also provoke changes in the characteristics of the molecule that make it suitable as a qubit. It is therefore interesting to study the magnetic behaviour of SMM deposited on a surface, in order to determine whether the molecule is sufficiently robust against the interaction with the substrates.

The main goal of this thesis has been to perform a detailed study of a special family of SMM, formed by lanthanide compounds. Lanthanide ions possess an angular momenta that presents a ground-state doublet which can be used as a quantum bit. The whole molecule has two or three of these ions which interact between them, giving the possibility to perform two and three qubit gates. As it has been mentioned above, this work is accompanied by a development of new magnetic sensors able to detect nanometric samples and a study of the interaction between SMM and device surfaces. The thesis is organised as follows:

Chapters 2 and 3 are devoted to describe the experimental techniques. The first one offers a detailed description of commercial and non-commercial equipments which existed previously to our thesis work. Chapter 3 deals with the development and characterization of a new generation of ultra high sensitivity microsusceptometers that allow susceptibility measurements of minute samples of molecular magnets. This chapter also describes an important modification over these microsusceptometers that permits detection in the nanoscale regime, by simply fabricating a nanoloop to enhance the flux coupling of the sample to the micrometric pickup loop.

In chapters 4 and 5 we delve into the possibility of performing quantum operations with the lanthanide compounds described above. In chapter 4 lanthanide compounds with two qubits (dimers) and their suitability as 2 -qubit gates are discussed. In particular we have focussed onto two dimers Tb_2 and ErCe. Tb_2 allows us to know whether a different coordination is enough to

make the qubits addressable and how. ErCe, on the contrary, allows us to add the possibility to deal with physically different qubits. The main goal of this chapter is to show that sample molecules can provide prototypes for the universal CNOT gate and the reversible gate SWAP.

Chapter 5 deals with molecular trimers, thus molecules that contain three qubits. The goal is to perform the universal 3-qubit gate CCNOT, also known as Toffoli. Our compounds use as qubits two Cu^{2+} and one Er^{3+} ions. We also evaluate the possibility of performing the 3-qubit gate CSWAP (or Fredkin) which is used in some quantum error correction schemes.

Chapter 6 describes further measurements performed on SMM, which provide information on quantum spin tunnelling processes and their relevance on the spin-lattice relaxation that ultimately determines the maximum achievable coherence time. This preliminary study will serve us to compare the results to those obtained in chapter 7, where we will dig into the robustness of the compounds when they are deposited onto microSQUID sensors.

Bibliography

[1.1] G. E. Moore, "Cramming more components onto integrated circuits," *Electronics*, vol. 38, no. 8, 1965.

[1.2] A. M. Turing, "On computable number, with an application to the entscheidungsproblem," *Proceedings of the London Mathematical Society*, vol. 42, no. 2, p. 230, 1936.

[1.3] S. J. Wiesner, "Conjugate coding," *SIGACT News*, vol. 15, no. 1, p. 78, 1983.

[1.4] A. S. Holevo, "Bounds for the quantity of information transmitted by a quantum communication channel," *Problems of Information Transmission*, vol. 9, no. 3, p. 177, 1973.

[1.5] R. S. Ingarden, "Comments on the kolmogorov-sinai-sasiada entropy and the quantum information theory," *Reports on Mathematical Physics*, vol. 10, no. 1, p. 131, 1976.

[1.6] Y. Manin, "Computable and uncomputable," *Sovetskove Radio*, 1980.

[1.7] R. Feynman, "Simulating physics with computers," *Internat. J. Theoret. Phys.*, vol. 21, p. 467, 1982.

[1.8] D. Deutsch, "Quantum theory, the church-turing principle and the universal quantum computer," *Proceedings of the Royal Society of London A*, vol. 400, p. 97, 1985.

[1.9] A. K. Ekert, "Quantum cryptography based on bell's theorem," *Phys. Rev. Lett.*, vol. 67, no. 6, p. 661, 1991.

[1.10] P. Shor, "Polynomial-time algorithms for prime factorization and discrete logarithms on a quantum computer," *SIAM Journal on computing*, vol. 26, no. 5, p. 1484, 1997.

[1.11] L. K. Grover, "Quantum mechanics helps in searching for a needle in a haystack," *Phys. Rev. Lett.*, vol. 79, no. 2, p. 325, 1997.

[1.12] J. I. Cirac and P. Zoller, "Quantum computations with cold trapped ions," *Phys. Rev. Lett.*, vol. 74, no. 20, p. 4091, 1995.

[1.13] D. Loss and P. DiVincenzo, "Quantum computation with quantum dots," *Phys. Rev. A*, vol. 57, no. 1, p. 120, 1998.

[1.14] D. R. Simon, "On the power of quantum computation," *SIAM Journal On Computing*, vol. 26, no. 5, p. 1474, 1997.

[1.15] M. Barrett, J. Chiaverini, T. Schaetz, J. Britton, W. M. Itano, J. D. Jost, E. Knill, C. Langer, D. Leibfried, R. Ozeri, and D. J. Wineland, "Deterministic quantum teleportation of atomic qubits," *Nature*, vol. 429, p. 737, 2004.

[1.16] Y. Jian, M. Ren, E. Wu, G. Wu, and H. P. Zeng, "Two-bit quantum random number generator based on photon number-resolving detection," *Review of Scientific Instruments*, vol. 82, no. 7, p. 073109, 2011.

[1.17] F. de Martini, V. Buzek, F. Sciarrino, and C. Sias, "Experimental realization of the quantum universal NOT gate," *Nature*, vol. 419, p. 815, 2002.

[1.18] D. Porras and J. I. Cirac, "Effective quantum spin systems with trapped ions," *Physical Review Letters*, vol. 92, no. 20, p. 207901, 2004.

[1.19] A. O. Niskamen, K. Harrabi, F. Yoshirara, Y. Nakamura, S. Lloyd, and J. S. Tsai, "Quantum coherent tunable coupling of superconducting qubits," *Science*, vol. 316, p. 723, 2007.

[1.20] J. H. Plantenberg, P. C. de Groot, C. J. P. M. Harmans, and J. E. Mooij, "Demonstration of controlled-NOT quantum gates on a pair of superconducting quantum bits," *Nature*, vol. 447, p. 836, 2007.

[1.21] R. Hanson and D. D. Awschalom, "Coherent manipulation of single spins in semiconductors," *Nature*, vol. 453, p. 1043, 2008.

[1.22] J. R. Weber, W. F. Koehl, J. B. Varley, A. Janotti, B. B. Buckley, C. G. V. de Walle, and D. D. Awschalom, "Quantum computing with defects," *Proc. Natl. Acad. Sci. U. S. A.*, vol. 107, no. 19, p. 8513, 2010.

[1.23] B. E. Kane, "A silicon-based nuclear spin quantum computer," *Nature*, vol. 393, p. 133, 1998.

[1.24] J. D. Sau, R. M. Lutchyn, S. Tewari, and S. D. Sarma, "Generic new platform for topological quantum computation using semiconductor heterostructures," *Phys. Rev. Lett.*, vol. 104, no. 4, p. 29, 2010.

[1.25] J. R. Friedman, M. P. Sarachik, J. Tejada, and R. Ziolo, "Macroscopic measurement of resonant magnetization tunneling in high-spin molecules," *Phys. Rev. Lett.*, vol. 76, p. 3830, 1996.

[1.26] J. M. Hernández, X. X. Zhang, F. Luis, J. Bartolomé, J. Tejada, and R. Ziolo, "Field tuning of thermally activated magnetic quantum tunnelling in Mn_{12} - ac molecules," *Europhys. Lett.*, vol. 35, no. 4, p. 301, 1996.

[1.27] L. Thomas, F. Lionti, R. Ballou, D. Gatteschi, R. Sessoli, and B. Barbara, "Macroscopic quantum tunneling of magnetization in a single crystal of nanomagnets," *Nature*, vol. 383, p. 145, 1996.

[1.28] R. P. Feynman, "Plenty of Room at the Bottom," (Pasadena), December 1959.

[1.29] E. Knill, "Quantum computing," *Nature*, vol. 463, no. 28, p. 441, 2010.

[1.30] J. M. Gambetta, A. D. Corcoles, S. T. Merkel, B. R. Johnson, J. A. Smolin, J. M. Chow, C. A. Ryan, C. Rigetti, S. Poletto, T. A. Ohki, M. B. Ketchen, and M. Steffen, "Characterization of addressability by simultaneous randrandom benchmarking," *Phys. Rev. Lett.*, vol. 109, no. 24, p. 240504, 2012.

[1.31] M. J. M. Pérez, *μSQUID susceptometry of molecular qubits*. PhD thesis, Universidad de Zaragoza, 2011.

[1.32] D. Aguilà, L. A. Barrios, F. Luis, A. Repollés, O. Roubeau, J. Teat, and G. Aromí, "Synthesis and Properties of a Family of Unsymmetric Dinuclear Complexes of Ln^{III} (Ln = Eu, Gd, Tb)," *Inorganic Chemistry*, vol. 49, p. 6784, 2010.

[1.33] M. Blencowe, "Quantum RAM," *Nature*, vol. 468, p. 44, 2010.

Chapter 2

Experimental Techniques

2.1 Introduction

In this thesis, magnetic properties of Single Molecule Magnets (SMM) need to be measured in order to determine their spin state and energy levels. For this purpose, both commercial equipments and non-commercial ones have been used. This chapter describes the most important of them and explain their relevance to our research.

Commercial systems present some advantages such as reliable and well-calibrated measurements and, often, a user-friendly software which allows to obtain data quickly. They also offer the possibility to carry out measurements under diverse conditions, such as different temperatures, applied magnetic fields, frequencies, excitations, etc. In this thesis we have used some commercial systems from the company Quantum Design [2.1], in particular the PPMS (Physical Properties Measurement System), for specific heat and magnetic measurements, and the MPMS (Magnetic Properties Measurement System), for magnetic susceptibility and magnetization measurements. Section 2.2 provides a detailed description of these systems.

There are however some measurements that need to be carried out under extreme experimental conditions non attainable by these commercial systems. In our case, exploring the magnetic behaviour at very low temperatures is of utmost importance. For this purpose, a dilution refrigerator from Leiden Cryogenics, previously adapted for magnetic susceptibility measurements, has been used. In section 2.3 some basic concepts of low temperatures measurements with dilution refrigerators are described.

Besides explaining how a dilution refrigerator works, it is also necessary to explain how it has been adapted to measure magnetic susceptibility. The

refrigerator has been modified to host a SQUID microsusceptometer on which the samples are placed. The development and improvement of these microsusceptometers is part of this thesis work and chapter 3 is entirely dedicated to it.

In the course of this thesis, some other techniques have been used, such as Focused Ion Beam (FIB) for modification of microsusceptometers, Dip-Pen nanolithography (DPN) for molecule deposition on substrates and chips and Electronic Paramagnetic Resonance (EPR) for the characterization of the magnetic energy levels of magnetic molecules. As these techniques have been used in collaboration with other research groups, we will not describe them in this chapter. We shall instead include some details wherever the relevant results are discussed.

2.2 Commercial systems

Magnetization, susceptibility and specific heat data provide a basic characterization of a magnetic material. Specific heat gives information about the lattice vibrations, the magnetic anisotropy and the couplings that electron spins have with other ones or with nuclear spins. On the other hand, magnetic measurements such as magnetization and dc susceptibility give complementary information about the spin state, the size of the magnetic anisotropy and energy level structures, whereas ac susceptibility adds information about spin dynamics.

In this section, we describe two commercial systems, PPMS and MPMS, used to perform physical measurements in a user-friendly manner. Although their measurement ranges do not cover all our needs, due to the necessity of exploring lower temperatures and higher frequencies, they nevertheless provide an important starting point. Both systems belong to the Physical Measurements Service from the Research Support Services of the University of Zaragoza [2.2].

2.2.1 PPMS: heat capacity measurements

PPMS is a versatile multi-measurement system that enables measuring diverse physical properties of a sample such as heat capacity, thermal and electrical conductance and also magnetic susceptibility and magnetization. It operates over a wide range of temperatures, from 350 mK (using a ^{3}He refrigerator inset) up to 1000 K (using an oven). It is also possible to apply magnetic fields up to 14 T. In this thesis we have only used this system to measure heat capacity so we will just explain how this option works.

Figure 2.1: PPMS (left) and MPMS (right) equipments.

Heat capacity is a very useful tool to study energy excitations in a given sample. Thus, it is possible to obtain from this quantity information about lattice vibrations. Besides, it provides information about magnetic energy levels and its dependence on the magnetic field as well as on the existence of hyperfine and spin-spin interactions [2.3].

The calorimeter used for performing all these measurements is included in a set-up which is inserted in an ^{3}He refrigerator. As shown in Fig. 2.2, the calorimeter consists of a platform where a sample holder, a heater and a thermometer are placed. The sample holder is made of sapphire, the thermometer is a semiconducting Cernox^{TM}(ceramic-oxynitride) thin film and the heater is a metallic film resistor. The platform is connected to a metallic frame by two pairs of superconducting wires made of NbTi. One pair provides electric current to the heater and the other one, connected to the thermometer, measures its resistance. A metallic cover shields the system from external radiation. The whole structure is then screwed to a probe (see Fig. 2.2) and introduced into the refrigerator.

As we usually measure powder samples, a previous process is necessary. First, the powder is pressed to form a thin pellet of about 1 mg. Then, with the help of a pick, we deposit a thin layer of Apiezon N whose heat capacity has been previously calibrated (1.00 μJ/μgK at 160 K [2.4]) onto the calorimeter platform, and place the sample on it.

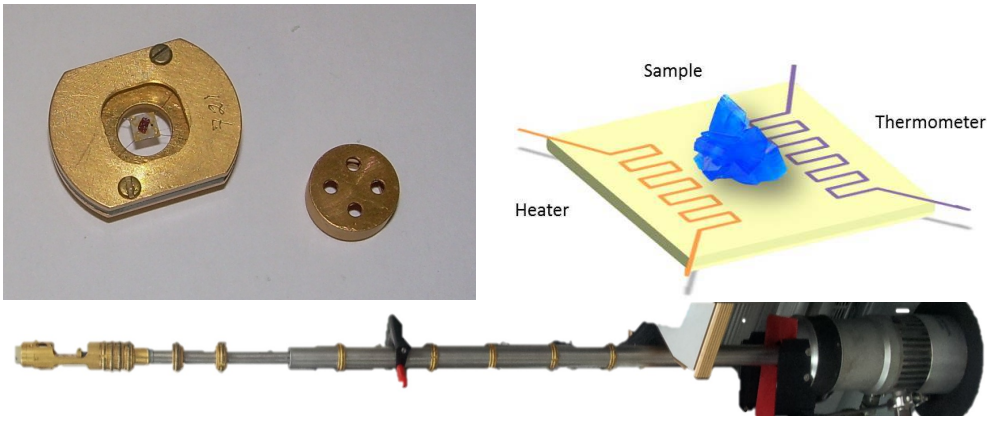

Figure 2.2: Picture of one of the calorimeter used (left) and its schematic representation (right). Down, probe where the calorimeter is placed.

The method used for measuring heat capacity is the semi-adiabatic relaxation method [2.5]. This experimental method consists of measuring the transient response of a thermal RC circuit, where RC is equivalent to a characteristic relaxation time τ and the voltage V is equivalent to the temperature T. It consists of the application of square power pulses P through the heater during a controlled period of time Δt (which corresponds to applying a voltage pulse in the equivalent electrical circuit). The evolution of the calorimeter temperature $T(t)$ is then monitored. Its variation with respect to the initial temperature T_0 shows first a transient decay towards the thermal Ohm law, according to the relation

$$T(t) - T_0 = \frac{P}{K}\left[1 - e^{\left(-\frac{t}{\tau}\right)}\right] \tag{2.1}$$

where K is the thermal conductivity of the NbTi wires and $\tau = C/K$ is a characteristic relaxation time. C is the heat capacity of the calorimeter, the Apiezon grease and the sample.

The metallic frame that holds the calorimeter is taken as a thermal bath at a constant temperature T_0. The pulse amplitude is set to induce a maximum temperature change in the calorimeter of about $0.05T_0$. Afterwards, the power is reduced to zero and the temperature evolution back to its initial value is also monitored (see Fig. 6). Fitting these two curves to Eq. (2.1) it is possible to obtain K and C in a much more sensitive manner than measurements performed in the stationary regime, due to the intrinsic accuracy of time measurements.The sensitivity of the system is 10 nJ/K at 2 K [2.1].

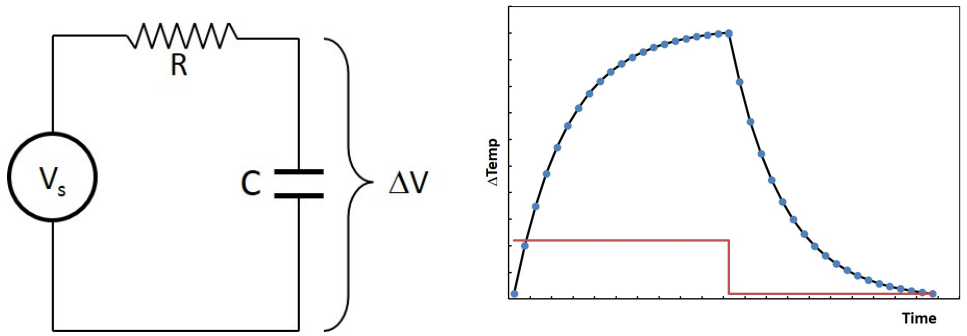

(a) (b)

Figure 2.3: a) Equivalent RC circuit of a calorimeter operating with the relaxation method. The voltage variation ΔV is equivalent to the temperature variation ΔT when a square power pulse P is applied, the same as a voltage pulse does in the electrical circuit. b) Example of the temperature evolution associated with a typical heat capacity measurement. The temperature increases exponentially (cf. Eq. (2.1)) while the heater is on and relaxes the same way when the heater switches off. Solid lines are experimental least square fits from which the characteristic relaxation rate, thus also the heat capacity, are determined.

2.2.2 MPMS: SQUID magnetometry

The MPMS is a commercial setup from Quantum Design specifically designed to perform magnetic measurements. This system works inside an ^{4}He refrigerator so its temperature range goes from 1.8 K to 400 K. It is also possible to apply magnetic fields up to 5 T and ac magnetic fields with amplitudes up to 4 Oe.

The main component of the MPMS is a rf SQUID (Superconducting Quantum Interference Device) sensor. The SQUID is used to amplify magnetic signals thanks to its behaviour as a very sensitive flux-to-voltage converter.

The SQUID amplifier is coupled to a second order superconducting gradiometer made of NbTi. A complete scheme of the measuring circuit is shown in Fig. 2.4. The sample has to be previously inserted into a straw which is introduced inside the coil and centred in such a way that it travels from 0.5 cm below the bottom coil to 0.5 cm above the top one.

There are two different methods of measurement, depending on the physical quantity of interest. For dc measurements (dc susceptibility and magnetization) the system fixes temperature and magnetic field and measures the output voltage $V(z)$ of the SQUID, as a function of the sample position z. The displacement of the sample induces a change of the magnetic flux across the pick up coils. The result can be fitted by approximating the sample to a point-

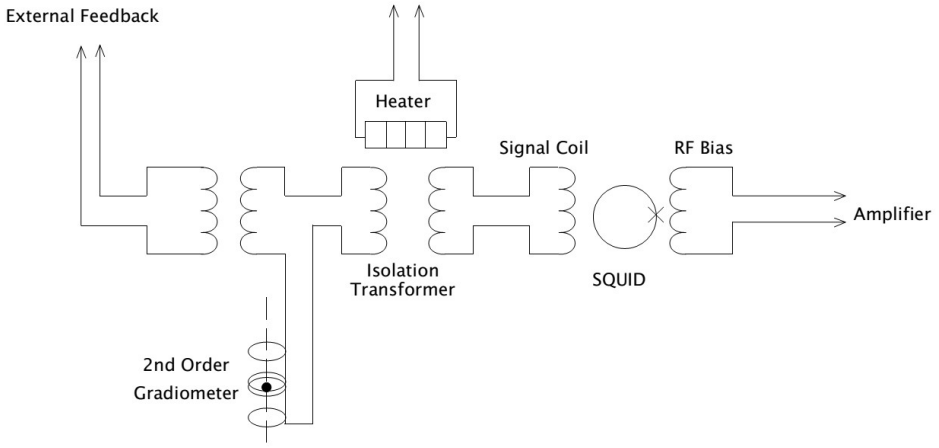

Figure 2.4: MPMS detection system. From [2.6].

like magnetic dipole Φ_{dip}, that generates a magnetic flux. The output voltage obeys the law:

$$V(z) = k\left[-\Phi_{dip}\left(z - z_0\right) + 2\Phi_{dip}\left(z\right) - \Phi_{dip}\left(z + z_0\right)\right] \tag{2.2}$$

where

$$\Phi_{dip}\left(z\right) = 2\pi m_z \frac{a^2}{\left(a^2 + z^2\right)^{3/2}} \tag{2.3}$$

k is the SQUID flux to voltage conversion gain, $2z_0 \cong 3$ cm is the distance between the gradiometer top and bottom coils, m_z is the sample magnetic moment and $a \cong 1$ cm indicates the maximal size of the sample to get a proper measurement (see Fig. 2.5). Fitting the data to this function allows to determine the magnetic moment m_z with a sensitivity of about 1×10^{-7} emu. The RSO option improves even further the sensitivity to 5×10^{-9} emu by performing an oscillation of z at a given frequency and detecting $V(z)$ with the help of a lock-in amplifier.

For ac measurements (ac susceptibility) the process is quite different. An ac magnetic field $h_{ac} = h_0 \cos \omega t$ is applied. The amplitude h_0 is typically 4 Oe and $f = \omega/2\pi$ can be varied from 1 mHz to 1 kHz. The output is an ac voltage with a given amplitude and phase. Comparing the input and output it is possible to obtain the real and imaginary components of the magnetic response. The sensitivity for this type of measurements is 10^{-8} emu. More details about ac susceptometry can be found in chapter 3.

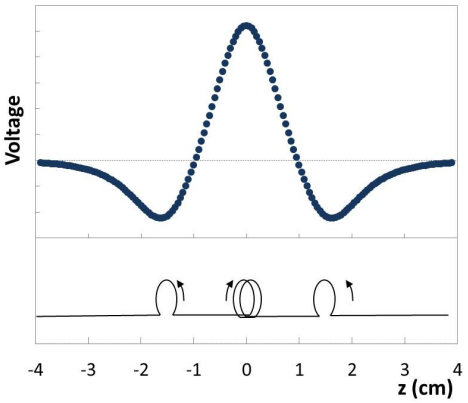

Figure 2.5: Example of a dc measurement. In the lower panel a scheme of the second order gradiometer as a function of z is also showed to compare the signal with the position of the coils.

2.3 Dilution Refrigerator

Some of the phenomena studied in this thesis take place at lower temperatures than commercial setups can attain. This is the reason why a different system, able to measure magnetic properties at such low temperatures, is necessary. A modified dilution refrigerator is a good solution for this purpose. But, to explain its operation, some previous concepts need to be explained before.

2.3.1 Early progress of low temperature physics and technologies

After the discovery of fire in the prehistoric age, humanity learnt how to use heat in their own profit. Activities such as cooking, tools production or pottery had to do with fire and ovens and therefore led to the development of heating systems. Cold, however, remained mysterious for a long time. People used it for keeping fresh foodstuffs for longer periods of time, but they were not able to "produce" cold. Actually, this was not a matter of scientific research until the beginning of the 19^{th} Century.

In the last decade of 1700's, Jacques Charles and Louis Gay Lussac studied the behaviour of gases when pressure, temperature and volume are changed. They predicted the existence of an absolute zero in temperature (at ∼-273 °C). This result strengthened the idea that heat and cold were of a different nature, considering that there exists a physical limit for cold whereas apparently such limit does not exist for high temperatures.

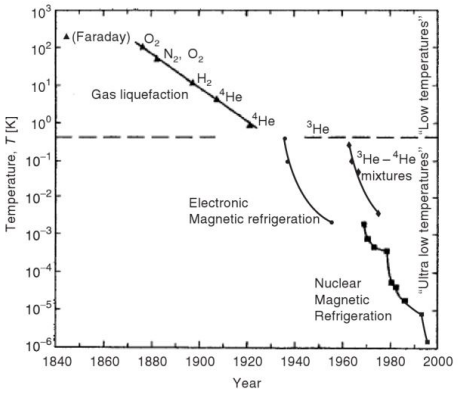

Figure 2.6: Historical development of refrigeration temperatures. [2.7]

In 1823, Michael Faraday was the first scientist who managed to liquefy a gas, Cl_2, by simply using isotheremal compression methods. He quickly realized that there were some gases, which he called permanent gases, that were impossible to liquefy just by increasing pressure. Charles Cagniard proposed then the idea of a critical temperature for each gas, below which it was possible to liquefy it. Therefore, permanent gases just had a lower critical temperature. The theory of Cargniard was confirmed forty years later, when Thomas Andrews could liquefy CO_2 (216 K) by cooling it below its critical temperature and applying pressure. In 1877, Raoul Pictet and Louis Paul Cailletet separately managed to liquefy O_2 (90 K) and N_2 (77 K) using different methods.

Storing all these liquid gases was also a challenge, especially for O_2, which is highly reactive. First warehouses, created by Zigmunt Wroblenski and Stanislav Olszewski, were often blocked by solidified vapour making them explosive. In 1893 James Dewar solved the storing problem by inventing a glass cryostat consisting of two flasks, placed one within the other and joined at the neck. The gap between the two flasks is evacuated of air, creating a vacuum which prevents heat transfer by conduction or convection. This cryostat, also called "dewar", allows to storage cryogenic liquids in a safe way.

By 1895, only two gases remained to be liquefied: H_2 and a recently discovered element, helium. This element had been detected in the Sun 25 years before. In 1895, Per Cleve and Nils Langlet found helium emanating from the uranium ore cleveite confirming its existence on Earth. In 1898 Dewar managed to liquefy H_2 (20 K) and ten years later, in Leiden, Heike Kamerlingh Onnes succeeded in helium liquefaction (at 4.2 K). The Leiden laboratory became pioneer in low temperatures research and kept working on achieving lower temperatures and studying material properties at low temperatures. This research led to the discovery of superconductivity in 1911 and superfluidity of

helium in 1920. In 1922 they had achieved 850 mK by pumping helium vapour pressure.

Once all of Faraday's permanent gases were liquefied, new methods were required to achieve even lower temperatures. In 1926 Peter Debye and William Giauque proposed a method based on the demagnetization of paramagnetic salts to cool down to 2 mK. Thirty years later, nuclear cooling allowed to reach the nK regime, although this temperature reflects only the state of only nuclear spins [2.8].

In the 60's, the dilution refrigerator was developed. This system cools down to 2 mK and it is independent of magnetic fields. In the 90's the lowest matter temperatures (in the range of nK) were achieved by laser cooling, although only for a few amount of atoms confined in vacuum [2.9, 2.10]. In this thesis we have used a dilution refrigerator from Leiden Cryogenics. Its operation is described in what follows.

2.3.2 Properties of ^{3}He - ^{4}He mixtures

As its own name suggests, dilution refrigerators are based on the properties of a mixture of ^{3}He and ^{4}He at low temperatures. We shall discuss some of these properties in this section, especially the ones that have more influence on the cooling process.

Solubility and phase diagram of ^{3}He - ^{4}He mixtures

For ^{3}He concentrations x lower than 67.5% on ^{4}He - ^{3}He, mixtures becomes superfluid below a temperature that decreases with x (see Fig. 2.7(a)). At even lower temperatures, a phase separation occurs. The lightest phase is made of pure ^{3}He, whereas the densest phase, which lies at the bottom, is composed by ^{4}He and a little concentration of ^{3}He, x. This concentration remains finite and reaches 6.6% at absolute zero.

It is then possible to use the transfer of ^{3}He from the pure phase to the diluted one using the mixing enthalpy ΔH as cooling power $\dot{Q}$,

$$\dot{Q} \propto x\Delta H \propto T^2 \tag{2.4}$$

where T is the temperature and $\Delta H \propto \int \Delta C dT$ with ΔC the difference between the specific heat of both phases. This temperature dependence is weaker than that of other refrigerators, such as the ^{3}He refrigerator, which is able to cool down to 300 mK. Consequently the cooling power decreases more slowly with T, as shown in Fig. 2.7(b).

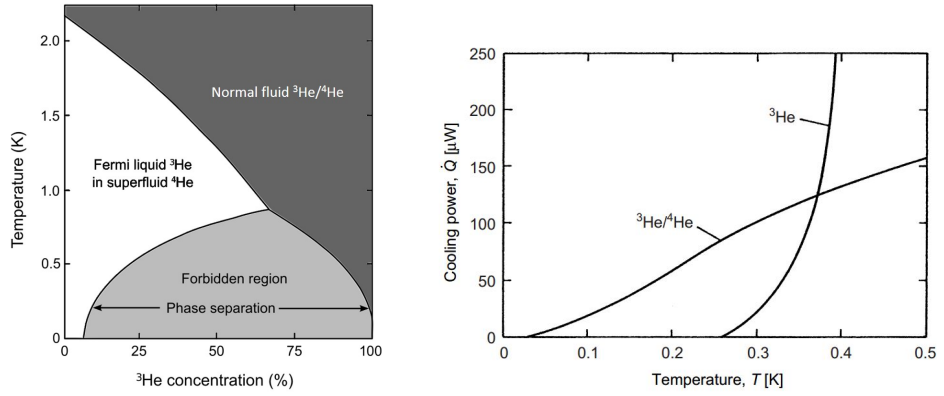

(a) (b)

Figure 2.7: a) Phase diagram of liquid ^{3}He-^{4}He mixtures at saturated vapour pressure as a function of ^{3}He concentration. b) Cooling power of a ^{3}He refrigerator and a ^{3}He-^{4}He dilution refrigerator. [2.7]

Finite solubility

To explain why there is not a completely separation between ^{3}He and ^{4}He even at absolute zero, it is important to point out that both are quantum liquids. ^{4}He is a boson and for $T < 0.5$ K almost all the atoms are in the ground energy state. It then behaves as a frictionless liquid. ^{3}He, on the contrary, has a nuclear spin $I = 1/2$ and behaves as a fermion. This means that there can not be two ^{3}He atoms in the same orbital with the same spin orientation.

To determine whether a ^{3}He atom which arrives to the interface prefers to move to the other phase or remains in ^{3}He, it is necessary to calculate the ^{3}He chemical potential in the two phases. For the pure phase

$$\mu_{3,\mathrm{c}} = -L_3/N_0 \tag{2.5}$$

where L_3 is the latent heat of vaporization for ^{3}He and N_0 is the number of atoms. For the diluted phase, the chemical potential depends on the energy binding $\epsilon_{3,\mathrm{d}}$ between different Helium atoms. Due to its lower mass, ^{3}He has larger zero point fluctuations and therefore a larger effective volume than ^{4}He. Consequently, ^{3}He atoms are, in average, more strongly bound when they are diluted in ^{4}He than they are in pure ^{3}He. When the density of ^{3}He in ^{4}He grows, their orbital energy increases up to $k_{\mathrm{B}}T_{\mathrm{F}}(x)$, where T_{F} is the Fermi temperature. Therefore,

$$\mu_{3,\mathrm{d}} = -\epsilon_{3,\mathrm{d}}(x) + k_{\mathrm{B}}T_{\mathrm{F}}(x) \tag{2.6}$$

An equilibrium is found when $\mu_{3,c} = \mu_{3,d}$ which gives a concentration of 6.6% at zero temperature. This fact is not understandable from classical thermodynamics, which would predict a complete phase separation.

2.3.3 The refrigeration circuit

This circuit, in which the ^{3}He-^{4}He mixture is enclosed, is at the heart of the dilution refrigerator (see Fig. 2.8). The goal is to achieve that ^{3}He from the pure phase passes continuously to the diluted phase by taking up mixture enthalpy from its surroundings and therefore cooling them. The circuit has three main parts: the mixing chamber, the still and the heat exchangers.

The mixing chamber

The mixing chamber is located at the bottom of the circuit and consists of a deposit where the two phases coexist. The diluted phase, which contains approximately a 6.6% of ^{3}He, is denser and lies at the bottom whereas the concentrated phase (100% ^{3}He) is at the top.

As we have said, to cool down it is necessary to keep a continuous flow of ^{3}He atoms $\dot{n}_3$ from the concentrated phase to the diluted one. The idea is to take some ^{3}He atoms off from the diluted phase, and then, as the ^{3}He concentration must remain constant, the pure phase will transfer some ^{3}He atoms to it in order to re-establish the equilibrium conditions.

Still

The still is a deposit connected to the diluted phase of the mixing chamber via a superleak ^{4}He vapour pressure and placed almost 40 cm above. It mainly contains mostly superfluid ^{4}He. ^{3}He atoms go from the mixing chamber to the still by the difference in osmotic pressure caused by the different temperatures and ^{3}He concentrations of these two reservoirs.

The still has to be at a temperature that ensures a sufficiently high ^{3}He vapour pressure, but a negligible part of ^{4}He, i.e. at 600-700 mK. At this temperature, although the liquid concentration of ^{3}He is less than 1%, its vapour pressure is more than a 90%. Then, we can pump this vapour (almost pure ^{3}He) to reduce the concentration of ^{3}He and cause the osmotic pressure. The ^{3}He is returned to the circuit by an external pump passing first an impedance to condensate it at 1.5 K, then another one in thermal contact with the still, to cool it down at 700 mK and finally the heat exchangers where it is cooled down thanks to the ^{3}He flow which ascends towards the still.

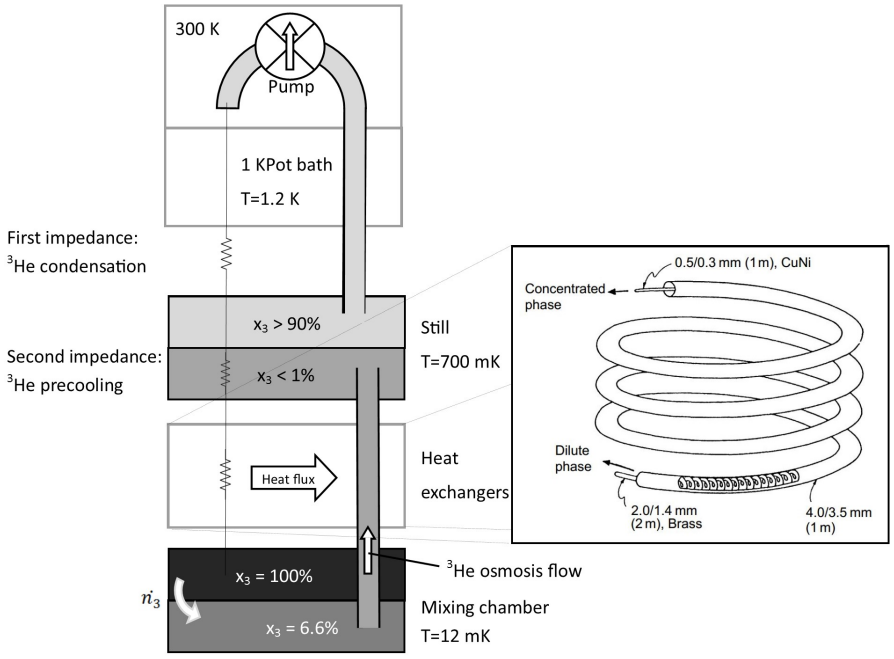

Figure 2.8: Left: Scheme of the dilution refrigerating mechanism. Right: Scheme of a concentric heat exchanger from [2.7]. Both circuits mix together in order to improve thermal contact and heat exchange.

Heat exchangers

The heat exchangers have the mission of cooling down the ^{3}He which returns to the mixing chamber. For this, the tube in which the ^{3}He goes out of the mixing chamber and the tube in which the ^{3}He comes back are linked to maximize the thermal contact between them. One of the most common designs consists of a spiral tube, where the coolest helium circulates, enclosed in a wider tube where the hottest helium comes back to the mixing chamber (see Fig. 2.8, right).

The cooling power depends directly on the temperature of the ^{3}He that enters the mixing chamber. Therefore the heat exchangers have to be as efficient as possible. For this, it is necessary that they have a small volume, small impedances and small thermal resistances. The cooling power is then determined by the temperature of the mixing chamber T_{mc} and the temperature of the ^{3}He coming from the heat exchanger T_{ex}:

$$\dot{n_3}\left(H_{3,\mathrm{d}}(T_{\mathrm{mc}}) - H_3(T_{\mathrm{mc}})\right) = \dot{n_3}\left(H_3(T_{\mathrm{ex}}) - H_3(T_{\mathrm{mc}})\right) + \dot{Q} \qquad (2.7)$$

Figure 2.9: Picture of Minikelvin 126-TOF model

$$\Longrightarrow \dot{Q} = \dot{n}_3 \left(95T_{\mathrm{mc}}^2 - 11T_{\mathrm{ex}}^2\right) \tag{2.8}$$

The maximum $\dot{Q}$ is achieved for $T_{\mathrm{ex}} \leq 3T_{\mathrm{mc}}$ and then $\dot{Q}_{\mathrm{max}} = 84\dot{n}_3 T_{\mathrm{mc}}$. $\dot{Q} = 0$, for $T_{\mathrm{ex}} = \sqrt{95/11}T_{\mathrm{mc}}$, determines the lowest attainable temperature.

2.3.4 Minikelvin 126-TOF model from Leiden Cryogenics

The dilution refrigerator used in this thesis is a Minikelvin 126-TOF model manufactured by Leiden Cryogenics. The refrigeration circuit stands out among the rest for two special features. On the one hand, whereas in the majority of refrigerators the sample is placed outside the mixing chamber, in thermal contact with it, in ours, the mixing chamber can be opened so that the sample and other measurement instruments can be placed inside. This has the advantage that the sample is in direct contact with the mixture and can be placed right at the boundary between both phases, where the temperature is the lowest. Thanks to this property, it is possible to perform experiments from the base temperatures, as low as 12 mK.

The second special feature is the possibility to change the concentration of ^{3}He in the mixture. Regular refrigerators usually have a deposit where the mixture is kept and it is just possible to decide how much mixture circulates through the circuit. However, in our model both gases are stored separately, and it is possible to choose the amount of each gas, and thus, its relative concentration. This allows us to adjust the position of the boundary level and to achieve a lower base temperature. It is also possible to measure with just ^{3}He, and so the system works as a ^{3}He refrigerator, or the same with ^{4}He.

The ^{3}He-^{4}He circuit is enclosed by two radiation shields and finally an hermetic stainless steal shield used to close the Inner Vacuum Chamber (IVC). The whole structure (mixture circuit and IVC) is introduced in a conventional

liquid He dewar. Liquid helium inside this dewar flows into the 1 K-pot through two pipes.

The inset is then connected by stainless steel gas lines to a gas handling structure, which contains the rest of the refrigerator parts. There are two pumps, one that pumps the 1 K-pot and another one that pumps to circulate the ^{3}He-^{4}He mixture. In order to increase the ^{3}He flow, a turbo pump is used in series with this dry rotary pump. The cabinet includes also a triple current source that generates the power required to warm up the mixing chamber, the still and the sorb pump, a vacuum gauge controller and a Nitrogen dewar used for cold trapping. It also has a control panel from where all valves can be activated or deactivated. Hidden inside the structure there are two reservoirs where the gases are stored. The upper one has a volume of 36 litres and contains ^{3}He whereas the lower one has a volume of 142 litres and contains ^{4}He.

The system has four thermometers to control the temperature in different parts of the refrigerator. It has three 10 kΩ RuO_2 thermometers placed at the 1 K-pot, the still and the sorb pump, and a Dale 1582 Ω thermometer placed at the mixing chamber. The resistances of the thermometers are measured with a low-power Oxford AVS-47 resistance bridge.

The dilution refrigerator is used for measurements of ac susceptibility, and it is optimized to host ultrasensitive SQUID microsusceptometers which will be described in more detail in chapter 3.

Bibliography

[2.1] Q. Design. `http://www.qdusa.com` (last view 01/04/2014).

[2.2] S. de Medidas Físicas Servicio de Apoyo a la Investigación. `http://sai.unizar.es/medidas/index.html` (last view 17/04/2014).

[2.3] M. Evangelisti, F. Luis, L. J. de Jongh, and M. Affronte, "Magnetothermal properties of molecule-based materials," *J. Mater. Chem*, vol. 16, p. 2534, 2006.

[2.4] Y. Moriya, H. Kawaji, T. Atake, M. Fukuhara, H. Kimura, and A. Inoue, "Heat capacity measurements on a thin ribbon sample of $Zr_{0.55}Al_{0.10}Ni_{0.05}Cu_{0.30}$ glassy alloy and Apiezon N high vacuum grease using a quantum design physical property measurement system," *Cryogenics*, vol. 49, no. 5, p. 185, 2009.

[2.5] R. Bachmann, R. Schwall, H. Thomas, R. Zubeck, C. King, H. Kirsch, F. Disalvo, T. Geballe, K. Lee, R. Howard, and R. Greene, "Heat-capacity measurements on small samples at low-temperatures," *Rev. Sci. Instrum.*, vol. 43, no. 2, p. 205, 1972.

[2.6] S. de Medidas Físicas Servicio de Apoyo a la Investigación, "Curso básico SQUID," October 2010.

[2.7] F. Pobell, *Matter and Methods at Low Temperatures*. Berlin: Springer, 3rd ed., 2007.

[2.8] N. Kurti, "Cooling by adiabatic demagnetization of nuclear spins," *Cryogenics*, vol. 1, no. 1, p. 2, 1960.

[2.9] A. Kastberg, W. D. Philips, S. L. Rolston, R. J. C. Spreeuw, and P. S. Jessen, "Adiabatic cooling of cesium to 700 nk in an optical lattice," *Phys. Rev. Lett.*, vol. 74, no. 9, p. 1542, 1995.

[2.10] W. D. Philips, "Laser cooling and trapping of neutral atoms," 1997. Nobel Lecture.

Chapter 3

Development and characterization of SQUID micro- and nanosusceptometers

3.1 Introduction

Nanoscopic magnetic materials offer a rich playground to explore the quantum-to-classical transition. Phenomena like spin quantum tunnelling [3.1–3.4], quantum coherence [3.5, 3.6], quantum spin entanglement [3.7, 3.8] and quantum spin relaxation [3.9, 3.10] have been discovered in chemically synthesized high spin molecular clusters that bridge the gap between macroscopic magnets and single paramagnetic ions. Some of the main goals of this thesis are the study of molecular compounds which could act as qubits or qugates. Magnetic susceptibility measurements can provide crucial information on how these high spin systems behave.

Quantum phenomena are often fragile, thus they are wrecked at high temperatures. It is therefore necessary to perform experiments close to the absolute zero, when zero-point fluctuations become dominant over thermal fluctuations. Besides, attaining a very high spin sensitivity is also desirable. It enables studying microscopic crystals, magnetically diluted samples or even small spin ensembles deposited onto solid substrates. Finally, magnetic sensors should also be able to explore the magnetic response within a broad band of characteristic time scales, to study the spin dynamics and the magnetic anisotropy. Commercial susceptometers can not properly satisfy all these conditions and, therefore, a development of new magnetic sensors which can be used at extremely low temperatures becomes necessary.

The integration of potential qubit candidates, such as molecular spins, into solid state devices can also provide a platform for the realization of a scalable quantum computation architecture [3.11]. In these applications, it is of utmost importance to maximize the magnetic coupling between the sample and the device. A rational approach to this goal is to decrease the size of the device, to a scale as close as possible to that of the sample. In the last few years, there have been several attempts to develop sensors which fulfil these conditions. Two examples are micro-Hall measurements and magnetic sensors based on Nitrogen Vacancy centres whose spin state can be read-out by optical means. The one we deal with in this thesis is the use of Superconducting Quantum Interference Devices (SQUID) as susceptometers.

SQUIDs are highly sensitive flux-to-voltage transducers able to measure the magnetic response of a sample (in terms of flux variations) to an ac magnetic field, and it is possible to do it for a wide range of frequencies, from mHz up to MHz. Due to the fact that SQUIDs are superconducting devices, they can only be used below their critical temperature, being possible to do it down to very low temperatures, down to absolute zero.

In this chapter, we describe the development of a new generation of μ-SQUID ac susceptometers. In sections 3.2 and 3.3 we explain basic concepts of a SQUID operation and describe some of their applications, in particular magnetic susceptometry. In section 3.4 we review previous work on SQUID miniaturization. The following sections are dedicated to the development and characterization of new devices. Our goal has been to develop SQUID sensors which meet the conditions described before: high sensitivity, broad frequency bandwidth and low temperature operation. In particular we have characterized for the first time on-chip SQUID microsusceptometers down to very low temperatures and we have proposed and carried out some improvements on these sensors. They are also user-friendly thanks to a commercial readout electronics that operates with broad bandwidths [3.12].

3.2 SQUIDs and their applications

Superconducting quantum interference devices, or SQUIDs, are among the main applications of superconductivity in science and technology. Its working principles are based on two consequences of the macroscopic quantum behaviour of superconductors [3.13]: Josephson effect [3.14] and flux quantization [3.15].

A dc-SQUID consists of two resistively – shunted Josephson junctions connected in parallel within a superconducting loop with inductance L and biased

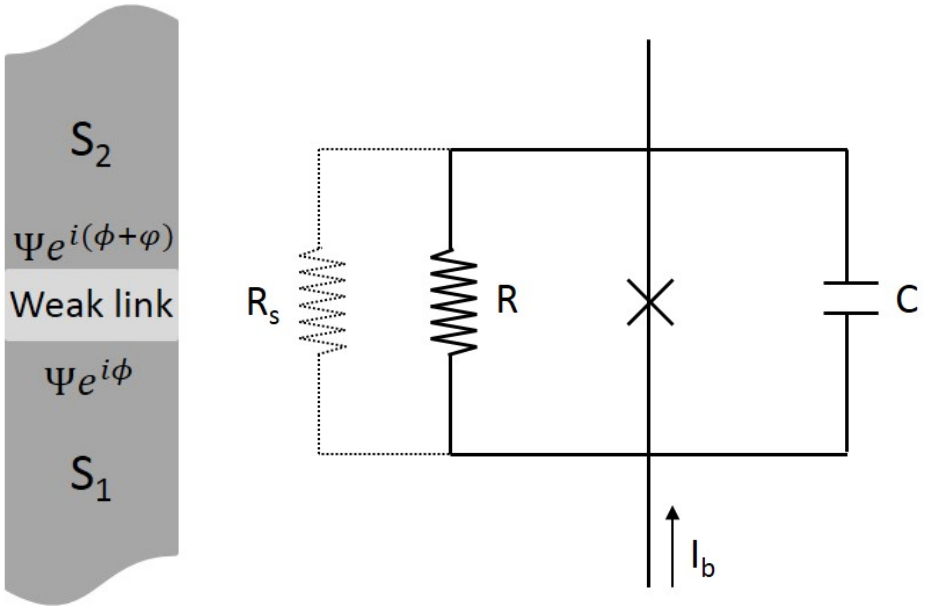

(a) (b)

Figure 3.1: a) Scheme of a Josephson junction. The weak link generates a change in the phase when a bias current passes through it. b) Solid lines. RCSJ electrical equivalent circuit for a Josephson junction. Dotted lines correspond to an extra shunt resistance that avoids I-V curve from hysteretic behaviour.

by an external dc source I_b. It was developed in 1964 by Jaklevic, Lambe, Silver and Mercereau [3.16]. To completely understand how a dc-SQUID works it is necessary to describe first the behaviour of a Josephson junction.

3.2.1 Quantum behaviour of a Josephson junction

A Josephson junction consists of two superconductors, separated by a weak link (see Fig. 3.1(a)), which can consist of an insulating barrier, a short section of non-superconducting metal or a physical constriction. When a bias current I_b passes through the weak link the function wave that defines the superconducting Cooper pairs behaviour $\Psi e^{i\phi}$ changes. Those changes are known as Josephson effects in honour of their discoverer, and are two:

dc Josephson effect

When a dc current $I_b < I_c$ passes through the Josephson junction (where I_c is the critical current), the phase of the Cooper pairs wave function obtains an additional contribution φ that depends on I_b as

$$I_b = I_c \sin \varphi \tag{3.1}$$

although no voltage drop is observed. This is called the dc Josephson effect.

φ grows with I_b until $I_b = I_c$ when a voltage drop appears and the link starts behaving as a resistance.

ac Josephson effect

If $I_b > I_c$ there is a fixed voltage drop V across the junction. On this case, the phase varies with time as

$$\dot{\varphi} = \frac{2e}{\hbar} V \tag{3.2}$$

an a local ac current

$$I_{ac} = I_c \sin\left(\frac{2e}{\hbar} V t\right) \tag{3.3}$$

appears. The frequency of this current is approximately 50 GHz for $V = 100\ \mu$V (484 THz/V).

Josephson effects in a Josephson junction can be modelled by a resistively-and-capacibility-shunted-junction equivalent electrical circuit (RCSJ model) as shown in Fig. 3.1(b) in solid lines. For $I_b < I_c$ the junction behaves as an ideal junction and $V = 0$, although there exists a phase shift φ between both sides of the link. For $I_b > I_c$ an ac current appears that circulates by the RC circuit,

$$I_b = I_c \sin \varphi + \frac{V}{R} + C\frac{dV}{dt} \tag{3.4}$$

with V depending on φ according to Eq. (3.2).

$I_b(V)$ can be solved for a general case by numerical analysis. It shows an hysteretical path that corresponds, in the equivalent circuit, to the effect of the capacitor C as shown in Fig. 3.2(a). This hysteresis therefore can be avoided

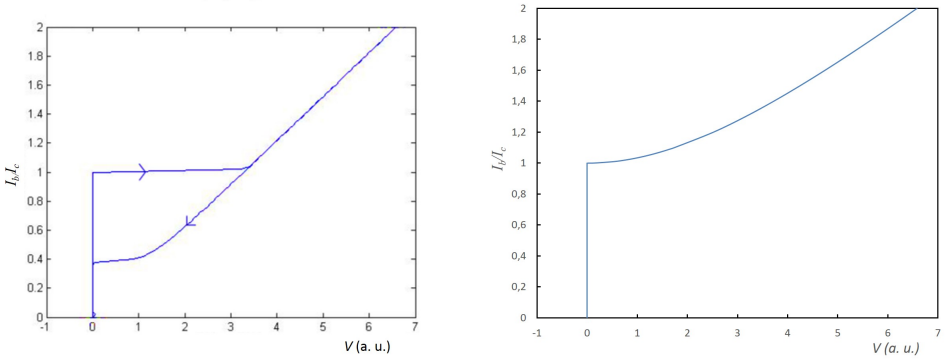

(a) (b)

Figure 3.2: a) I-V characteristics for a single Josephson junction with non negligible capacitance C. For increasing I_b V keeps constant up to I_c and has afterwards a linear behaviour with bias current. For decreasing current, the linear behaviour continues below I_c in an hysteretic path. Graph from [3.17]. b) I-V characteristics for a single Josephson junction with $C = 0$.

minimizing the capacitor contribution. In the ideal case, for $C = 0$, Eq. (3.4) is analytical and can be solved as,

$$\begin{aligned} V &= 0 & I_b &< I_c \\ V &= R(I_b^2 - I_c^2)^{1/2} & I_b &> I_c \end{aligned} \tag{3.5}$$

as shown in Fig. 3.2(b).

In the real case, as C depends mainly on the geometry and the type of the junction, its effect can be minimized by adding an additional shunt resistance R_s in parallel to the Josephson junction as it is shown in Fig. 3.1(b) in dotted lines.

3.2.2 dc SQUID

A dcSQUID is formed by two Josephson junctions connected in parallel. It is therefore a superconducting ring with two RCSJ junctions. The equivalent circuit is shown in Fig. 3.3(a). If both junctions are identical, the critical current is $2I_c$ and they will present the same behaviour. For a given voltage ($I_b \geq 2I_c$), two identical ac currents as in Eq. (3.3) circulate by the ring in opposite senses.

If a magnetic flux $\phi \neq N\phi_0$, with $N = 0, 1, 2, ...$ and $\phi_0 = \frac{h}{2e}$ the magnetic flux quantum, passes through the ring, the phase changes differently in both

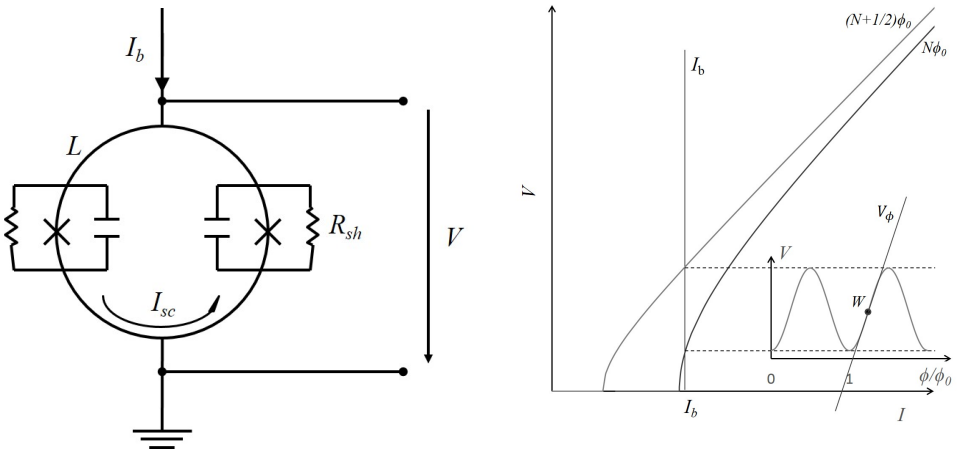

Figure 3.3: a) Scheme of a typical dc-SQUID. R_{sh} is the equivalent resistance of R and R_s from Fig. 3.1(b) in parallel. b) I-V characteristics depending on ϕ_0. For a constant I_b, voltage drop varies periodically with the applied field. Optimized transfer equation occurs maximizing the V-ϕ slope and choosing it as a working point W.

branches and current does not distribute equally through the two junctions. Wave function inside the superconductor must be however continuous and therefore phase imbalance generates a net current I_{sc}, circulating by the ring, that corresponds to an interference between the two ac currents and causes a voltage drop in the I-V curve (Fig. 3.3(b)). Hence, the maximum drop correspond to an applied flux $\phi = \left(N + \frac{1}{2}\right)\phi_0$ and V varies periodically with the applied flux, being ϕ_0 the period. The SQUID turns, then, into a flux-to-voltage transducer.

The amplitude of the voltage modulation depends on the bias current I_b, which can be chosen to maximize it. Then, we can define the transfer coefficient V_ϕ as the maximum variation of voltage with respect to flux changes, i.e.

$$V_\phi = \left|\frac{\delta V}{\delta \phi}\right|_{max} \tag{3.6}$$

The point in the $V-\phi$ characteristic where this occurs is called working point, W.

V_ϕ can also be increased by including an Additional Positive Feedback (APF) [3.18]. It consist of a resistance R_a and a coil L_a in series, which are connected in parallel with the SQUID, as shown in Fig. 3.4(a). APF induces an additional flux in the SQUID that affects differently to the Josephson junctions. Due to this, the $V-\phi$ characteristics becomes strongly asymmetric. It gets

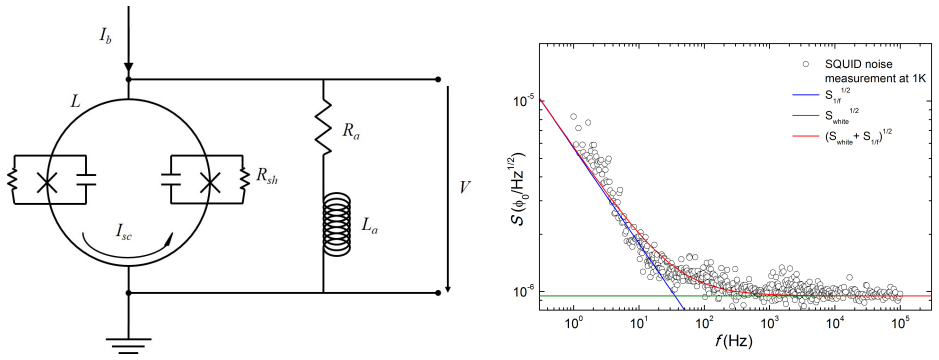

(a) (b)

Figure 3.4: a) dc SQUID with Additional Positive Feedback (APF). b) Example of flux noise measured for a microSQUID at 1 K. Lines indicate the two noise contributions: the white noise, which is independent on frequency and the Flicker noise, proportional to f^{-1}.

steeper at one side, increasing therefore V_ϕ at the working point, while it gets flatter at the opposite side.

3.2.3 Noise in a dc SQUID

A dc SQUID has three sources of noise that are uncorrelated: current noise, voltage noise and Flicker noise.

The resistance R_s in parallel with the Josephson junction introduces a white current noise associated to thermal fluctuations whose spectral density can be described as

$$S_\mathrm{I} = \frac{8k_\mathrm{B}T}{R_\mathrm{s}} \tag{3.7}$$

where k_B is the Boltzmann constant and T is the temperature. Current noise is coupled to the microSQUID in terms of magnetic flux as,

$$S_{\phi_\mathrm{I}} = S_\mathrm{I} M_\mathrm{in}^2 \tag{3.8}$$

where M_in is the mutual inductance between the SQUID loop and the input coil.

The presence of magnetic flux noise introduces a voltage noise whose spectral density is

$$S_\mathrm{V} = S_{\phi_\mathrm{V}} V_\phi^2 \tag{3.9}$$

where $S_{\phi_\mathrm{V}} \approx 16k_\mathrm{B}TL^2/R_\mathrm{s}$ is the flux noise spectral density.

S_{I} and S_{V} are independent of frequency and give them rise to a white noise.

The third noise source is commonly known as Flicker noise or $1/f$ noise. There is no a clear explanation for the origin of this noise. It is normally associated with the vortex movement which creates changes in the energy barrier of the Josephson junctions, causing local fluctuations on the tunnelling process. It could be also caused by unpaired electrons which are trapped in the Nb wires.

Flicker noise is dependent on a distribution of activation energies and therefore, a statistical treatment is necessary. Then

$$S_{\phi_{\mathrm{F}}}(T,f) \propto \frac{k_B T}{f} D(\tilde{E}) \tag{3.10}$$

where $D(\tilde{E})$ is the distribution of activation energies. It also depends on the frequency as $1/f$.

As the noises are uncorrelated, it is possible to add directly all the contributions,

$$S_\phi = \frac{S_{\mathrm{V}}}{V_\phi^2} + S_{\mathrm{I}} M_{\mathrm{in}}^2 + S_{\phi_{\mathrm{F}}}(T,f) \tag{3.11}$$

Fig. 3.4(b) shows an example of noise measurement.

There is also an extra source of noise which is extrinsic to the SQUID itself and which arises from the room temperature electronics and feedback loops (FLL). This noise contribution has two components, voltage noise and current noise. Both, SQUID noise and electronics noise, are not correlated and therefore,

$$S_{\mathrm{T}} = S + S_{\mathrm{FLL}} \tag{3.12}$$

In terms of flux noise density the total measured noise $S_{\phi_{\mathrm{T}}}$ can be written as

$$S_{\phi_{\mathrm{T}}} = S_\phi + \frac{S_{\mathrm{V_{FLL}}}}{V_\phi^2} + S_{\mathrm{I_{FLL}}} M_{\mathrm{d}}^2 \tag{3.13}$$

where S_ϕ is the intrinsic SQUID flux noise (described in Eq. (3.11)), $S_{\mathrm{V_{FLL}}}$ and $S_{\mathrm{I_{FLL}}}$ are the electronics voltage and current noise contribution, V_ϕ is the transfer function described in section 3.2.2 and M_{d} is a virtual inductance which acts as a transfer function for current noise, in a similar way to V_ϕ.

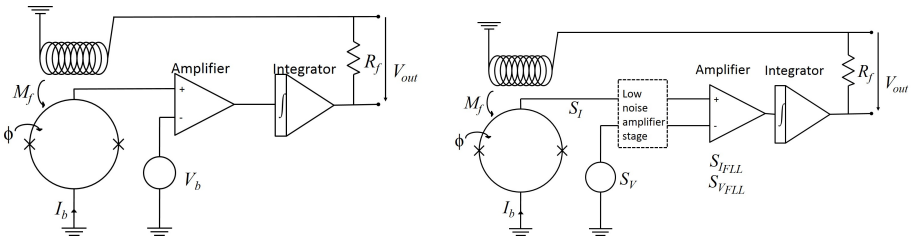

(a) (b)

Figure 3.5: a) Circuit of the SQUID with a flux locked loop. The feedback circuit maintains the flux constant inside the SQUID loop. The output voltage is proportional to the external flux seen by the SQUID. b) Noise sources of the circuit. If an amplifier stage is added before reaching the electronics noise, the intrinsic signal increases and electronic noise is not affected. The transfer function V_ϕ also increases and therefore, the electronics noise in terms of flux is reduced.

3.2.4 SQUID read out

As it is shown in section 3.2.2, a SQUID is a device that transforms minute magnetic flux changes into easily measurable voltage changes. Its ability to detect flux variations below a flux quantum makes the device highly sensitive. However, the periodicity of the curve $V - \phi$ is unpractical.

To solve this, a Flux Locked Loop (FLL) can be added to the device. This FLL mode linearises the transfer function V_ϕ and removes any ambiguity from the system readout. It consists of a simple feedback circuit, shown in Fig. 3.5(a), which keeps the magnetic flux inside the loop constant.

Once the SQUID is biased to maximize the amplitude of the voltage modulation, we can use as working point the steepest point of the periodic signal $V - \phi$. For small variations of the flux the signal obtained is approximately linear. This variation is amplified and integrated at room temperature and sent back to the SQUID using a feedback resistance R_f and a feedback coil, magnetically coupled to the SQUID by a mutual inductance M_f, cancelling the flux signal that originally arrived to the loop. The output voltage V_out can be related to the flux ϕ via the following expression

$$\phi - \frac{V_\mathrm{out}}{R_\mathrm{f}} M_\mathrm{f} = 0 \Longrightarrow \phi = G V_\mathrm{out} \tag{3.14}$$

thus setting a linear relation between the flux and the output voltage. $G = M_\mathrm{f}/R_\mathrm{f}$ is the FLL gain.

In some cases the noise of the room temperature amplifier is higher than the SQUID noise which is not desirable. As follows from Eq. (3.13), it is possible to reduce the contribution of the electronics to the noise by increasing

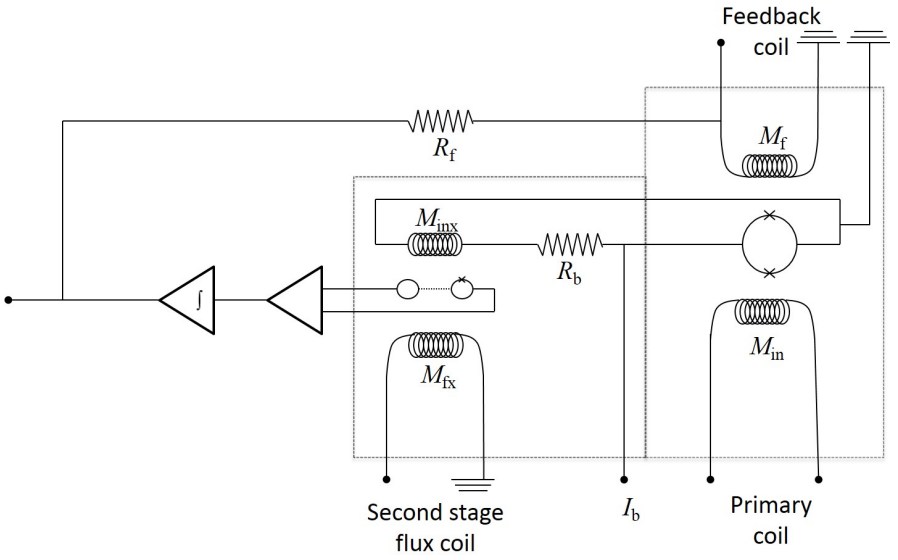

Figure 3.6: Circuit of a two - stage configuration. The voltage drop of the front-end SQUID is transformed into a flux through an intermediate coil and it is coupled to an array of SQUIDs in series which amplify the signal.

the value of V_ϕ. For this, an extra amplifying stage is allocated between the SQUID and the room temperature amplifier, as it is shown in Fig. 3.5(b). This stage is typically an array of SQUIDs, inductively coupled to the first one by an extra coil.

This is commonly called a two - stage configuration and it works as shown in Fig. 3.6. The voltage drop coming from the main SQUID is converted into a current and made it pass through a coil that generates a new flux. This flux passes through an array of SQUIDs, placed in series, which amplify the voltage signal before arriving the room temperature electronics.

As the transfer function V_ϕ is directly proportional to the voltage signal, it is also amplified and therefore, the flux noise contribution of the electronics can be much smaller than the intrinsic SQUID noise.

3.2.5 SQUID applications

A dc-SQUID is basically a flux to voltage transducer. Therefore, its main use is as a sensitive magnetic flux detector. As we have already seen in section 2.2.2, SQUIDs are commonly used in commercial magnetometers and susceptometers, although it is also possible to find gradiometers, voltmeters and amperemeters that integrate SQUIDs as part of their detection circuits.

They can also be used as low noise current amplifiers, as happens in transition-edge bolometers [3.20] for X-ray detection. In geophysics, they are used to map the Earth magnetic field and in spatial science, SQUIDs are also useful for detecting gravitational waves in gravity wave antennas [3.21]. In biomagnetism, SQUIDs are used in new diagnosis tools such as magnetocardiography (MCG) [3.22], where pathological heart signals can be detected with high precision in 3 dimensions, or magnetoencephalography (MEG) [3.23], where SQUIDs are used to map the brain activity by detecting the tiny magnetic fields created by the interneuronal electrical currents [3.24].

SQUIDs have also application as material properties analysers. For instance, it is possible to identify structural or material defects by measuring changes in magnetic flux via non-destructive evaluation (NDE) [3.25]. Likewise, it is also possible to use them for magnetic microscopy [3.26].

In this thesis, we have focused on using a microSQUID loop as an integrated magnetic susceptometer, in which the SQUID loop acts as a pickup coil that detects the magnetic flux generated by a magnetic specimen.

3.3 Micro-SQUID susceptometry

3.3.1 Magnetic susceptometry

Magnetic susceptibility χ is a physical quantity that measures the magnetization M changes of a material in response to small changes in the applied magnetic field H. It can be expressed as

$$\chi = \frac{\partial M}{\partial H} \tag{3.15}$$

A convenient experimental method to detect χ is ac susceptometry, It consists on the application of an oscillatory magnetic field $h = h_0 \sin \omega t$ to the sample and the synchronous detection of the ensuing magnetic flux changes. By varying ω, this technique provides also detailed information about the non-equilibrium physics and the spin dynamics of a sample. In general, it is possible to write the change in the magnetization as the sum of two components:

$$\Delta M \approx h_0 \cos \omega t + h_0 \sin \omega t \tag{3.16}$$

The first, or in-phase component, is proportional to the real susceptibility χ', whereas the second, out-of-phase component, is proportional to the imaginary susceptibility χ''.

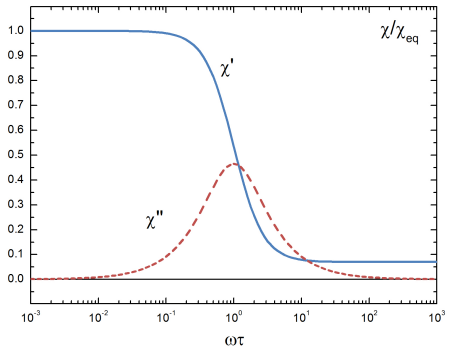

Figure 3.7: Typical normalized ac-susceptibility curve for a paramagnetic spin system with one relaxation time.

These two quantities can be related to relaxation times. To give a typical example, Fig. 3.7 shows the frequency magnetic response of a paramagnetic spin system with a relaxation time τ. Susceptibility response corresponds to the Debye curves:

$$\chi' = \chi_S + \frac{\chi_T - \chi_S}{1 + (\omega\tau)^2}$$
$$\chi'' = \omega\tau \frac{\chi_T - \chi_S}{1 + (\omega\tau)^2} \tag{3.17}$$

where χ_S is the adiabatic (or infinite-frequency) susceptibility and χ_T the equilibrium susceptibility.

As highly sensitive flux-to-voltage converters, SQUIDs can enhance the detection sensitivity of magnetic susceptibility measurements, thus allowing to measure smaller and smaller signals. Their use as flux to voltage transducers is described in this section.

Besides its role as amplifier, a SQUID can also be used as a susceptometer itself. The development of this utility has been thoroughly studied in this thesis and it is explained in detail on the following sections.

3.3.2 Use of a SQUID as external detector of the susceptometer: basic operation

A susceptometer consists mainly of two separated circuits. The first one generates the magnetic field excitation. It can be an external magnet or an

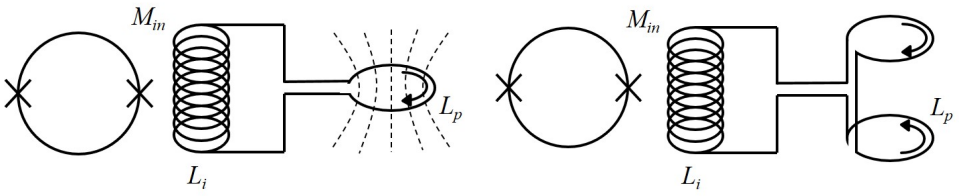

(a) Simplest fluxmeter (b) First order gradiometer

Figure 3.8: a) Basic configuration of a SQUID susceptometer. The flux that crosses the pickup coil (L_{p}) induces a current that travels through the coil (L_{i}). The induced magnetic field, proportional to the external flux, is coupled to the SQUID loop (M_{in}) that gives a response in terms of voltage. b) First order axial gradiometer. The opposite sense of the turns guarantees the isolation from the magnetic Earth field.

integrated circuit and it is usually named primary circuit. The second circuit is the part of the susceptometer which detects changes in the sample magnetization induced by the ac magnetic field. It is called secondary or pickup circuit and it normally consists of a gradiometer coupled to a SQUID.

Primary circuit

As it is said above, the primary circuit is any agent that generates a local magnetic field whose flux pass through the pickup coil. In this thesis we work mainly with on-chip ac susceptometers. The primary circuit consists of two identical coils connected between them that generate two identical magnetic fields, h_1 and h_2, which pass trough the two gradiometric turns of the pickup circuit.

Pickup circuit

The simplest configuration for a pickup circuit (Fig. 3.8(a)) consists of a superconducting coil with a single turn (called pickup coil). In the presence of a magnetic flux, an electrical current is induced in the pickup coil. This current flows through another coil which inductively couple to the SQUID loop. The SQUID then converts the flux into voltage and its magnitude is read. This simple system has its disadvantages due to the fact that the pickup coil is sensitive to any background magnetic field.

To solve this problem, more sophisticated coil designs are used, such as gradiometers, which have turns wound in opposite senses in order to cancel the flux from any uniform magnetic field, like the Earth magnetic field. Therefore, if the magnetic permeability of the medium filling both coils is the same, the

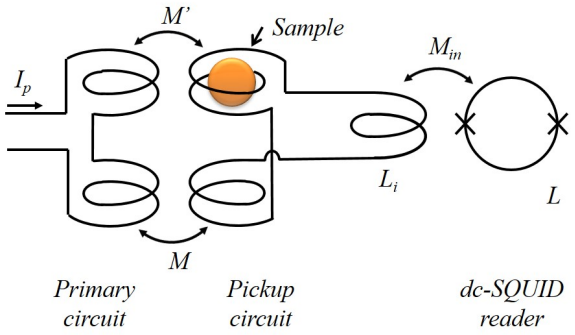

Figure 3.9: Scheme of a first order susceptometer coupled to a dc-SQUID. The current through the primary coil generates an oscillatory magnetic field that produces a coupled flux in the pickup coils. The induced current generates a voltage drop proportional to the susceptibility of the sample, which is placed in just one of the two pickup coils.

total induced flux vanishes. However, if a sample is placed inside one of the pickup coils, the net flux differs from zero (see Fig. 3.9). Figure 3.8(b) shows the basic configuration of a first order gradiometer.

It is possible to relate the SQUID flux to the coupled one just knowing the value of the inductances (L_p for the pickup coil and L_i for the intermediate coil) and the mutual inductance M_in between the intermediate coil and the SQUID loop:

$$\phi = \frac{M_\mathrm{in}}{L_\mathrm{p} + L_\mathrm{i}} \phi_\mathrm{ext} \tag{3.18}$$

If the FLL mode is set, ϕ_ext is proportional to V_out. Using Eq. (3.14) leads to

$$V_\mathrm{out} = \frac{R_\mathrm{f}}{M_\mathrm{f}} \frac{M_\mathrm{in}}{L_\mathrm{p} + L_\mathrm{i}} \phi_\mathrm{ext} \tag{3.19}$$

3.4 Previous examples and designs of μSQUID susceptometers and magnetometers

The interest for miniaturizing SQUIDs dates from the 80's, when the first micrometric SQUID susceptometers were fabricated [3.27] by M. B. Ketchen and co-workers. The SQUID loop of this device had 15 μm diameter and a flux sensitivity of about 10^{-6} $\phi_0/\mathrm{Hz}^{1/2}$. Since then, many groups have worked on this topic. In 1995 an ultra-sensitive microSQUID was developed by W. Wernsdorfer and co-workers at the Néel Laboratory in Grenoble [3.28]. This

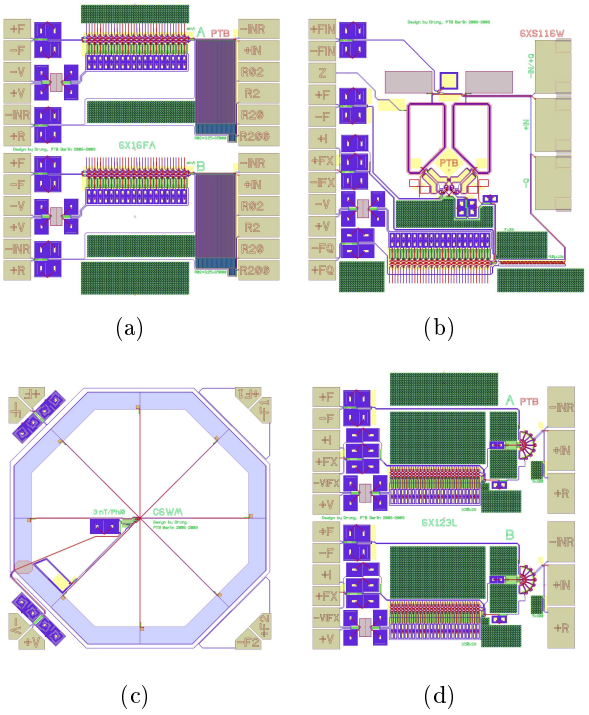

Figure 3.10: Different examples of chips fabricated at PTB-Berlin. a) 16-array SQUIDs, which can be used as a low noise amplifier stage. b) One single SQUID coupled to a 16-array amplifier stage. c) Magnetometer SQUID. It is the most widely used of all the devices and it has been integrated in biomagnetic sensors. d) The "fan" model. Two simple fan-shaped SQUIDs coupled to both 16-array stages. The size of all chips is 3x3 mm^2.

SQUID had 1 μm diameter and a flux sensitivity of 10^{-4} $\phi_0/\mathrm{Hz}^{1/2}$. It was in the 2000's when first nanometric SQUIDs were fabricated. Thus, in 2003, a 100 nm SQUID loop was first reported [3.29] and in 2006 it was improved by using carbon nanotubes as Josephson junctions which reduced the thickness of the Josephson junctions down to 1 nm [3.30].

Since 2007, our group has been working in collaboration with D. Drung and co-workers from the Physikalish - Technische Bundesanstalt (PTB) on Berlin in the fabrication and testing of micro- and nanoSQUID susceptometers. In this section we present a short overview of the work previously done on this topic.

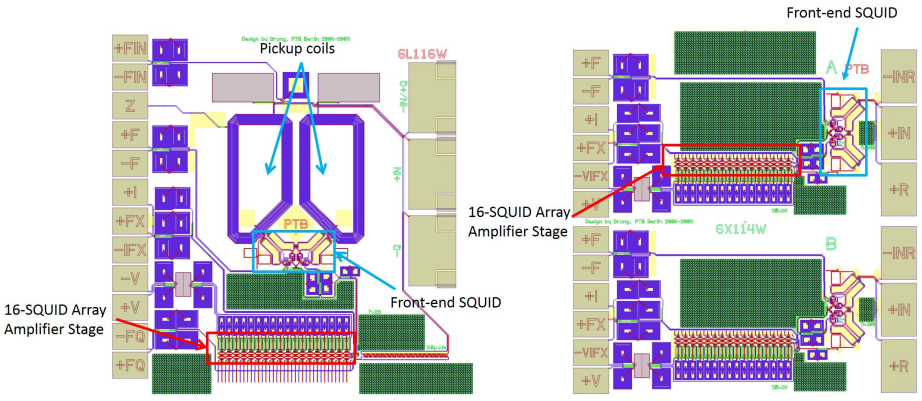

Figure 3.11: Models #32 - L116W and #33 - X114W used for first and second generation susceptometer modification respectively. Both SQUIDs are coupled to a SQUID array amplifier stage. The right one does not have an intermediate loop and it occupies just one half of the chip.

3.4.1 Development of microSQUIDs ac susceptometers. Previous work and background

The department of Cryophysics and Spectrometry from the PTB - Berlin [3.31] works on the development of highly sensitive on-chip SQUID sensors and its electronic read-out since the early 90's. It works together with a spin off company, Magnicon GmbH [3.32], which commercializes these devices and the readout electronics, used mainly in for commercial equipments such as those described in section 3.2.5.

Sensors are typically fabricated on 3" silicon wafers by optical lithography. They are built with different layers of SiO_2 insulators, Nb wires and $Nb/Al/AlO_x/Al/Nb$ Josephson junctions. Therefore, they work at temperatures of liquid helium and below ($T < 4.2$ K). They are fabricated in different configurations, depending on their possible future usage. Thus, there exists single SQUID loops, SQUID loops linked to pickup coils, SQUIDs arrays in parallel and combinations of some of them. Some examples are shown in Fig. 3.10.

Originally, the design of these chips did not include any susceptometer device. In 2007, M. José Martínez, as part of her thesis work [3.33], worked with the idea of turning one of these PTB chips into a susceptometer by using focused ion beam etching (FIB) and FIB induced deposition (FIBID). She developed two generations of sensors that are briefly described below and which have been the starting point for the present work.

First generation susceptometers

The chips were similar to those shown in Fig. 3.10(b), more precisely, models #32 - L116W and #42 - XL116W, whose main difference is the input inductance (400 nH for model #32 and 1050 nH for model #42). These chips have a two stage configuration so that the signal measured in so-called front-end SQUID (see Fig. 3.11)is amplified by a 16-SQUIDs array. The primary circuit is a 30-turn input double transformer loop and it is deposited on top of two single-turn pickup coils. The active area of each one of the pickup coils is 367 μm $\times$ 920 μm [3.33]. Pickup coils are inductively coupled to the SQUID loop through a second transformer.

The input coils were fabricated in a gradiometric fashion, although the turns were not in opposite directions, so they did not act as susceptometers but as simple transformers. The modification was, then, quite simple, at least in theory. It would be enough to change the direction of one of the two turns of the primary coil, as it is shown in Fig. 3.12(a).

The experimental technique used to perform these changes was the combined FIB etching/ FIBID system. By using FIB etching it is possible to cut the lines of the superconducting primary coil. Then, thanks to FIBID of new superconducting leads, a new circuit that connects the two parts of the primary circuit in the opposite direction can be made [3.34] (see Fig. 3.12(b)).

It is also important to underline that the primary circuit is superconductor, so a superconducting material has to be deposited. In 2004 a new material which fulfils this condition was discovered [3.35]. It consists of an amorphous material made of 40% of W, 40% of C and 20% of Ga, called W-FIBID and it is deposited by means of FIBID. Although the critical temperature for superconductivity of each of its components is very low (10 mK for metallic W and 1.09 K for metallic Ga), this compound shows a critical temperature that ranges between 5.2 K and 6.2 K depending on the deposition conditions [3.36]. Therefore, it is also possible to use the SQUIDs, which have been modified with W-FIBID, at liquid helium temperatures [3.37].

One of these first generation SQUIDs, called H32, has been regularly used for measurements reported on this work and we will describe its particular characteristics in the next section.

Second generation susceptometers

Next step in the miniaturization process, which implies a sensitivity enhancement, is just suppressing the intermediate circuit and directly coupling the sample to the SQUID loop [3.38]. To carry this out, our group took profit of

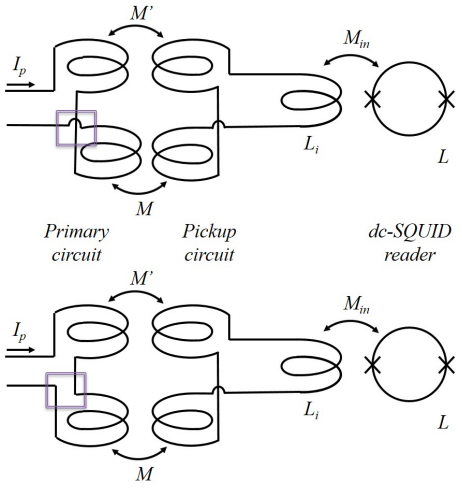

(a)

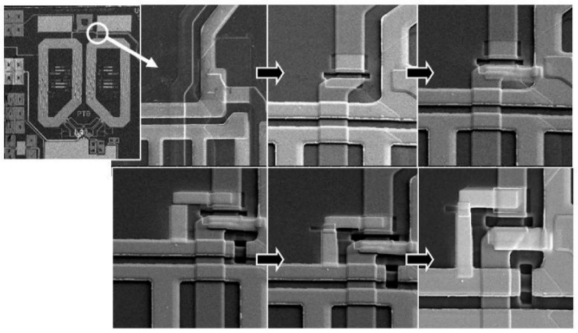

(b)

Figure 3.12: a) First generation susceptometer. The primary circuit is modified in order to have turns in opposite directions. b) SEM images of the process of circuit editing taken from [3.34].

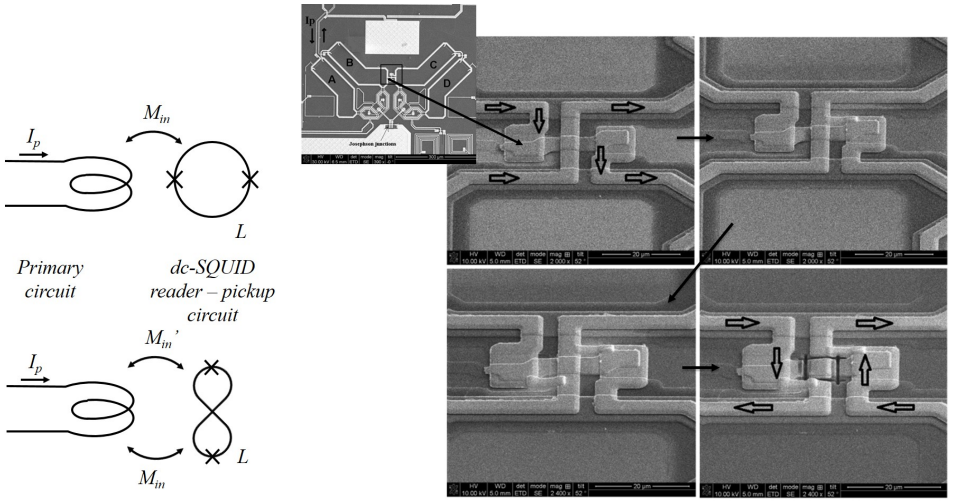

(a) (b)

Figure 3.13: Second generation susceptometer. Here, the intermediate loop is suppressed and changes are made on the SQUID loop itself. Left. SEM images of the process taken from [3.38].

the gradiometric design of the SQUID loop itself from the model #33 - X114W. Instead of being circular, this SQUID has a four-banana shape (see Fig. 3.11). The susceptometer is simply achieved by changing the current sense of two of the banana-shaped coils that couple flux to the SQUID in the original sense and that, in this manner, are turned into a primary loop, generating a quasi - homogeneus ac magnetic field. The idea and the technique are just the same as were used in the first generation. FIB/FIBID steps are illustrated in Fig. 3.13.

3.5 Characterization of H32 microSQUID susceptometer

The H32 device is a first generation susceptometer whose critical current is about 8 μA. It has two pickup coils, each with a sensing area of about 0.34 mm^2 coupled inductively to the SQUID via a flux transformer. The main SQUID is coupled to an array of 16 SQUIDs, which acts as an amplifier (see section 3.2.4 and Fig. 3.14).

In the linear regime the maximum transfer function, defined by Eq. (3.6), is $V_\phi \approx 3000\ \mu\mathrm{V}/\phi_0$ and the mutual inductance between the pickup coil and

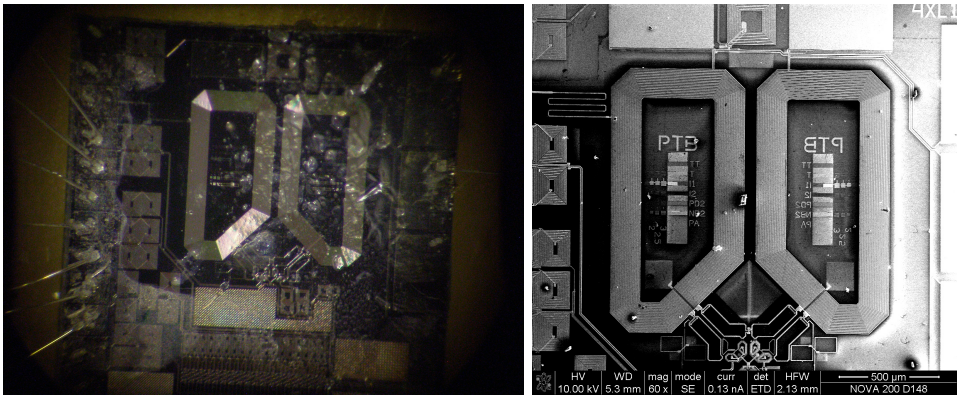

(a) (b)

Figure 3.14: a) Picture of the H32 SQUID microsusceptometer. The pickup coils are the trapezoidal-shaped ones whereas the SQUID is formed by four wings. The second stage, formed by 16 SQUIDs in series, are placed just below. b) SEM image of the device.

the feedback coil is $M_{\mathrm{f}}^{-1} = 41.3\ \mu\mathrm{A}/\phi_0$. There is a more detailed description in [3.33].

The chip is glued on a chip carrier which can be plugged either in a dipstick, to introduce it directly in a transport dewar, or inside the mixing chamber of a dilution refrigerator. The wires pass through the dipstick or the refrigerator system and are connected to the SQUID electronics XXF, commercialized by Magnicon GmbH.

This electronics consists of a FLL box, where the feedback resistances are placed. There exists several feedback resistances R_{f}, from 0.7 kΩ to 100 kΩ, which change the amplitude of the signal. It is also possible to change the Gain Bandwidth Product (GBW) of the amplifier, from 0.23 GHz to 7.20 GHz, to broaden or narrow the bandwidth. The FLL box is plugged to an additional box which connects the system to a relatively user-friendly computer software, also developed by PTB. Both, the FLL box and the connector box work at room temperature.

As it is said above, for measuring ac susceptometry it is necessary to apply an ac magnetic field through the primary coil and collect the output from the SQUID. In this case it will be amplified from the second stage. The amplitude gain and the phase shift between both signals are then measured by a Lock In amplifier, controlled by the computer and transformed into a complex number which is proportional to the complex susceptibility.

3.5.1 Background signal

In an ideal bare susceptometer, the background flux should be zero due to its gradiometric design. Nevertheless, the detected flux differs from zero due to a non perfect fabrication or even to environmental factors. It is then necessary to measure this background signal as a function of frequency and temperature, so that it could be properly subtracted.

In addition, if the measurement is performed in the FLL mode, the feedback resistance R_f and the GBW of the feedback loop can also affect the signal. Actually, Eq. (3.19) shows that the signal just scales with R_f. However the mutual inductance M_f can also be affected by frequency and its dependence could be more complicated.

Background depending on FLL conditions

Figure 3.15 shows measurements of the background signal, performed for different values of the FLL parameters, R_f and GBW. It is easy to see that the signal, which would ideally be independent of frequency, deviates mores the higher the frequency and that it also changes depending on the GBW, especially for high feedback resistances. On the other hand, the higher the feedback resistance, the more sensitivity the device shows.

This turns into a conflict and a compromise need to be achieved. On the one hand, the bigger the resistance the bigger the output signal becomes. On the other hand, the signal is more unstable and depends much more on the GBW, especially at high frequencies.

In this work we have mainly used the largest GBW, 7.20 GHz and 10 kΩ or 30 kΩ depending on the sensitivity that was required for each particular experiment.

Temperature dependence of the background signal

As this device is thought to be used at temperatures which range from 4.2 K down to a few mK, it is also of our interest to determine whether the signal of the empty susceptometer depends on the temperature or not.

For this purpose, we performed a measurement of the empty sensor using the dilution refrigerator. As it can be seen in Fig. 3.16 the signal remains approximately constant between 10 mK and 4.2 K, thus considerably simplifying the data treatment. The measurement was performed using 10 kΩ as

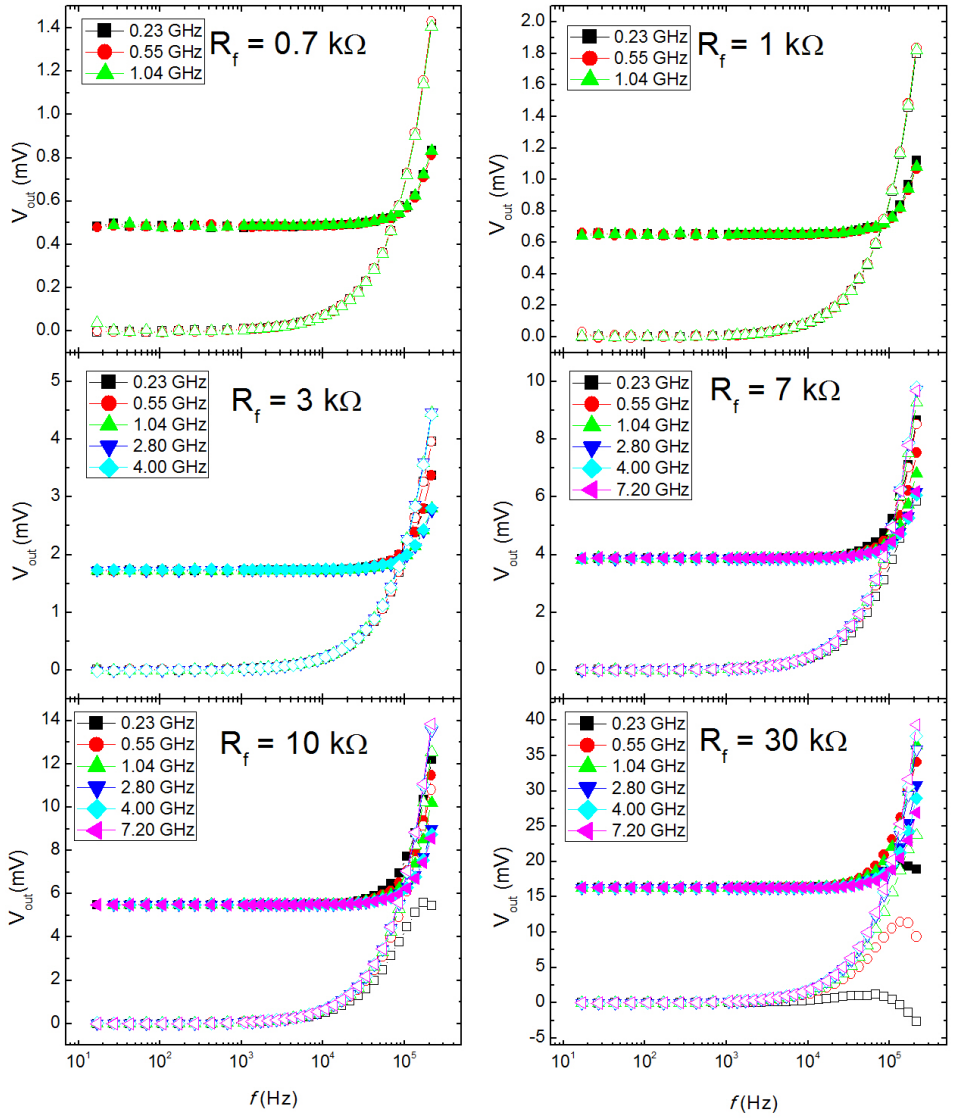

Figure 3.15: Background signal for different feedback resistances and bandwidths. The input current is 10 μA which corresponds to an induced field of 1.2 μT. The full symbols correspond to the real part of the response whereas the empty ones correspond to the imaginary part.

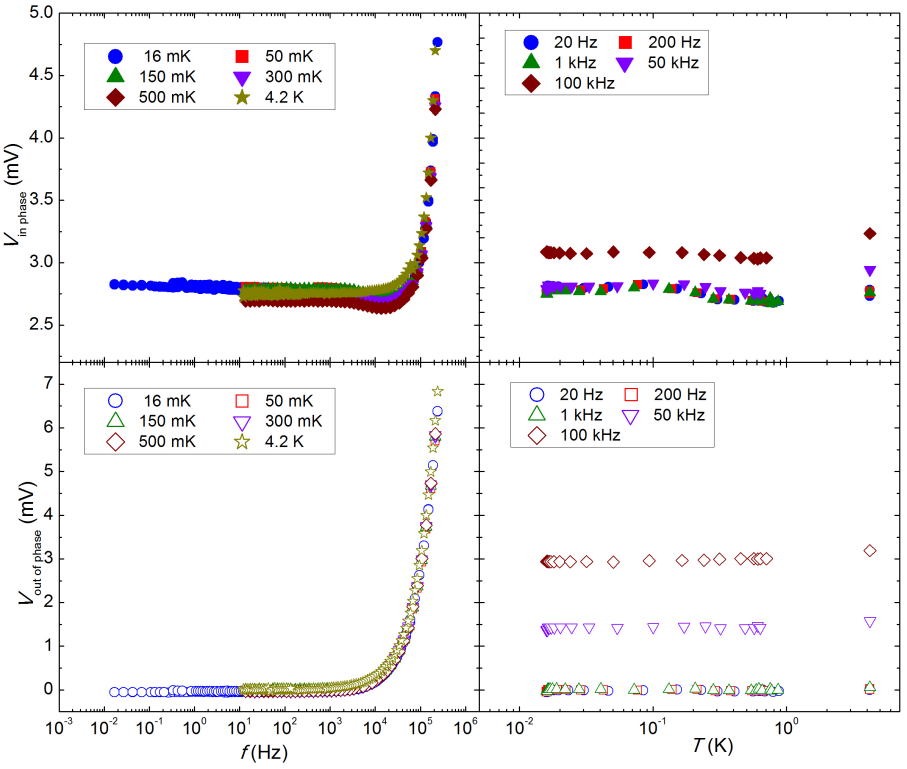

Figure 3.16: Background signal as a function of frequency for different temperatures from 4.2 K down to 15 mK and as a function of temperature for different frequencies.

feedback resistance and 7.20 GHz as GBW. The input excitation was 5 μA, corresponding to an induced field of 0.6 μT [3.33].

3.5.2 Scaling function

Once we fix the feedback resistance and the GBW the only dependence we have to take into account is the frequency dependence, since there is no dependence on temperature. There must therefore exist a complex function $F^*(f)$ which depends on the frequency and satisfies

$$V_{\text{out}}(f) = F^*(f) \cdot V(f) \tag{3.20}$$

where V_{out} is the measured signal and V is the intrinsic signal. The goal of the calibration process is to determine $F^*(f)$ and then be able to extract the intrinsic signal of the bare sensor and of any sample placed on it.

For the background signal of the sensor V_{B} we will have

$$V_{\text{out}_{\text{B}}}(f) = F^*(f) \cdot V_{\text{B}}(f) \tag{3.21}$$

whereas when a sample is placed onto one of the coils we will have

$$V_{\text{out}}(f) = F^*(f) \cdot (V_{\text{B}}(f) + V_{\text{S}}(f)) \tag{3.22}$$

where $V_{\text{out}_{\text{B}}}$ and V_{out} are the measured signals for background and sample respectively and V_{S} is the intrinsic contribution associated with the sample itself.

To obtain V_{S} two steps are therefore necessary. First we can simply subtract Eq. (3.21) from Eq. (3.22) and then calculate the inverse of the transformation function:

$$V_{\text{S}} = F^{*-1} \cdot V_{\text{out}_{\text{S}}} \tag{3.23}$$

where $V_{\text{out}_{\text{S}}} = V_{\text{out}} - V_{\text{out}_{\text{B}}}$ is the measured signal once subtracted the background contribution.

Use of $\mathbf{K_{12}GdW_{30}}$ as calibrating sample

To determine the function F^{*-1} a sample of $K_{12}GdW_{30}$ was used as calibrating sample. $K_{12}GdW_{30}$ is a potassium salt of a special kind of molecules based on polyoxometalates or POM (see Fig. 3.17(a)) whose complete formula is $[Gd(P_5W_{30}O_{110})]^{12-}$. They were synthesized by AlDamen *et al.* in 2009 [3.39–3.41]. The molecular structure consists of a polyoxometalate structure which encapsulates a single lanthanide ion, Gd^{3+} in this case. This molecule is paramagnetic and its magnetic anisotropy is almost exclusively determined by Coulomb interaction between ions.

Previous measurements of this compound [3.41] have shown that its magnetic anisotropy is very low. This means that for Helium temperatures, the ac susceptibility should be independent of frequency and can be used for calibrating our microSQUID susceptometer. We have separately measured the sample in both coils and compared the results as shown in Fig. 3.18.

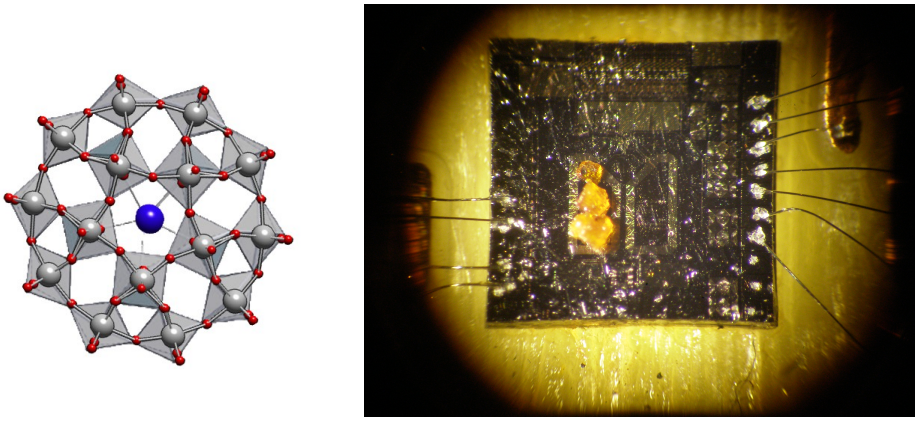

(a) (b)

Figure 3.17: a) Molecular structure of a GdW_{30} ion. The blue atom is the lanthanide which is surrounded by 30 atoms of tungsten. b) Crystal of $K_{12}GdW_{30}$ placed on one of the two coils of the H32 susceptometer.

According to Eq. (3.22) it is possible to obtain $V_{\text{out}_S} = F^* V_S$ by three independent ways,

$$V_{\text{out}_S} = 0.5 \cdot (V_{\text{out}_2} - V_{\text{out}_1}) \tag{3.24}$$

$$V_{\text{out}_S} = V_{\text{out}_2} - V_{\text{out}_B} \tag{3.25}$$

$$V_{\text{out}_S} = V_{\text{out}_B} - V_{\text{out}_1} \tag{3.26}$$

where V_{out_1} and V_{out_2} are the measurements with the sample placed on coil 1 and coil 2, respectively. Figure 3.18(a) shows V_{out_1} and V_{out_2}, and the V_{out_S} that results of applying the previous equations to these data. The three results agree well between them.

As we know that V_S must be real and independent of frequency, if we transform the complex signal into module-phase components, we find that the function F^{*-1} must be mainly a phase shift, which depends on frequency. Fitting the phase part to a logistic function, we obtain that

$$F^{*-1} = e^{i\phi(f)} \longrightarrow \phi(f)[deg] = -55.833 + \frac{55.818}{1 + \frac{f}{1.295 \cdot 10^6}} \tag{3.27}$$

that must be subtracted from the measured phase. Figure 3.18(b) shows the fit of Eq. (3.27) to the phase shift measured experimentally and the intrinsic signal of the $K_{12}GdW_{30}$ crystal after data treatment. The differences between

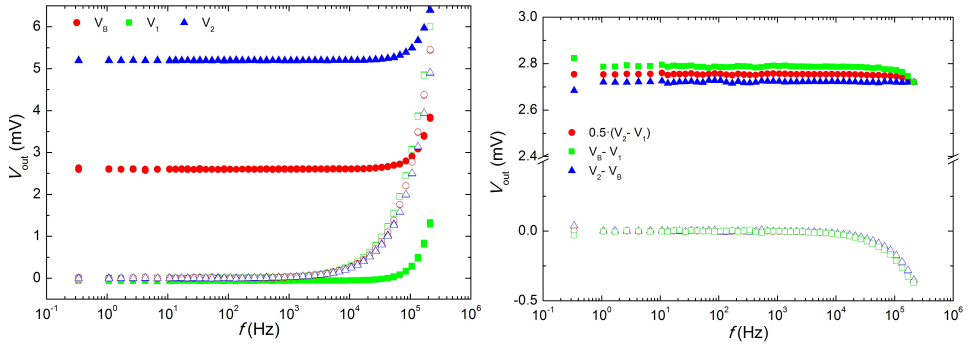

(a)

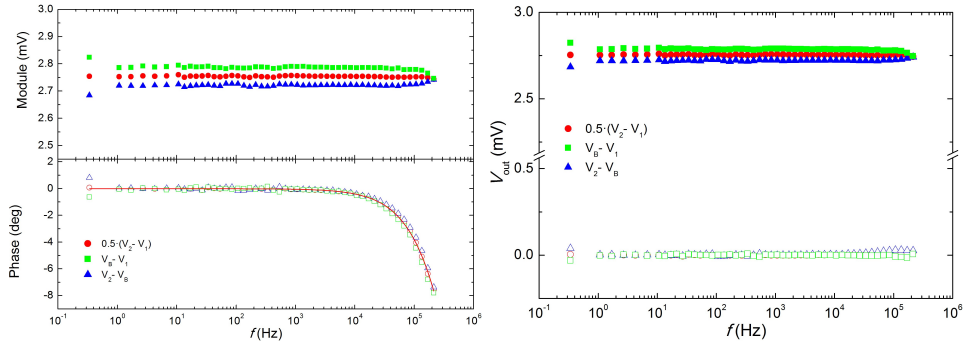

(b)

Figure 3.18: a) Left. Crystal of $K_{12}GdW_{30}$ measured on the two coils of the H32 susceptometer and the background signal when the device is empty. Right. Measurement after background extracting following Eqs. from (3.24) to (3.26). b) Left. Module-Phase representation: Although the module (in full symbols) is constant, there exists a contribution corresponding to a phase mismatch. The red line corresponds to the fitting curve. Right. Definitive measurement after applying all the data treatment.

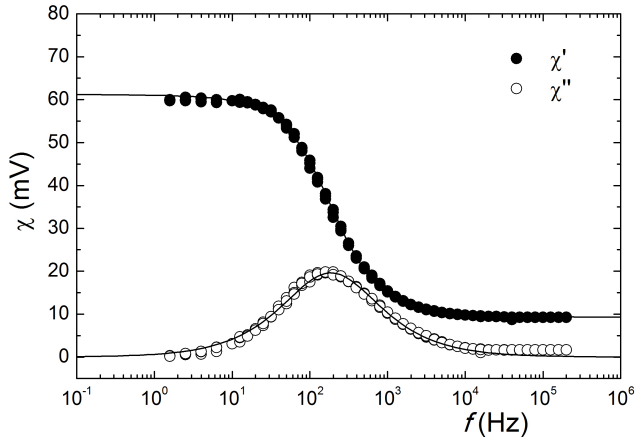

Figure 3.19: Fe_4 crystal measured at 1.7 K with H32 device and treated with the scaling function. The sample shows a relaxation time of 855 μs and fits according to two Cole-Cole functions which describe relaxation processes [3.42, 3.43].

the absolute value of the real part are probably due to a little loss of mass in the second measurement, occurred during the transference from one coil to the other.

Once we have obtained the scaling function, for future unknown samples it is just necessary to apply Eq. (3.25) or (3.26) depending on the side the sample is placed, and use the shift correction to the result.

As an example, Fig. 3.19 shows the data of a Fe_4 crystal after applying the scaling function. The results agree with the Cole-Cole relaxation model [3.42, 3.43], valid for a spin system with a certain distribution of spin-lattice relaxation times (see chapter 6 below):

$$\chi^* = \chi_S + \frac{\chi_T - \chi_S}{1 + (i\omega\tau)^\beta} \tag{3.28}$$

where $\chi^* = \chi' - i\chi''$ is the complex susceptibility, τ is the average relaxation time, ω the applied frequency, β determines dispersion of relaxation times (zero for $\beta = 1$, maximum for $\beta \to 0$), χ_S is the adiabatic susceptibility and χ_T is the thermal equilibrium susceptibility.

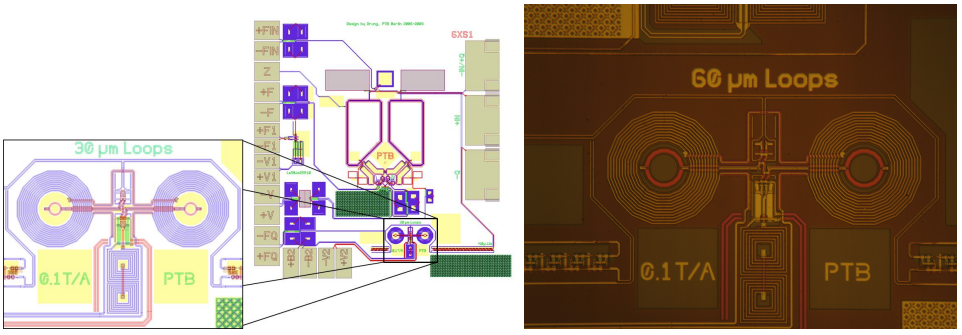

(a) (b)

Figure 3.20: a) Third generation susceptometer with 30 μm loops. The device occupies a tiny area on the right corner at the bottom of the chip. b) Microscope image of a 60 μm loops device.

3.6 Third generation of micro SQUID: Characterization and development of 30 μm and 60 μm loop SQUID susceptometers

3.6.1 Introduction: common characteristics

Building on the idea of the second generation susceptometers, researchers at PTB designed a new chip (see Fig. 3.20). These third generation devices don't need to be modified since they have been directly built as susceptometers. They are even smaller than those of the first and second generations. There exist two models: one with 30 μm diameter SQUID-loops (the #01 susceptometer) and another one with 60 μm diameter SQUID-loops (the #02 susceptometer). We have mainly worked with the first ones, which are also the smallest ones.

The device consists of a SQUID with two loops each surrounded by a coil that creates a local ac magnetic field. This magnetic field is related to the current flowing in the coil by a proportionality constant, 0.1 T/A. The circuit is completed with a FLL circuit. Figure 3.21 shows a schematic circuit of the susceptometers. There are six electrical contacts: $+V/-V(GND)$ for SQUID biasing, $+IN/-IN$ for field coil current setting and $+F/-F$ for feedback coil current setting.

The chip is glued onto a chip carrier which is then connected to the electronics as described in section 3.14.

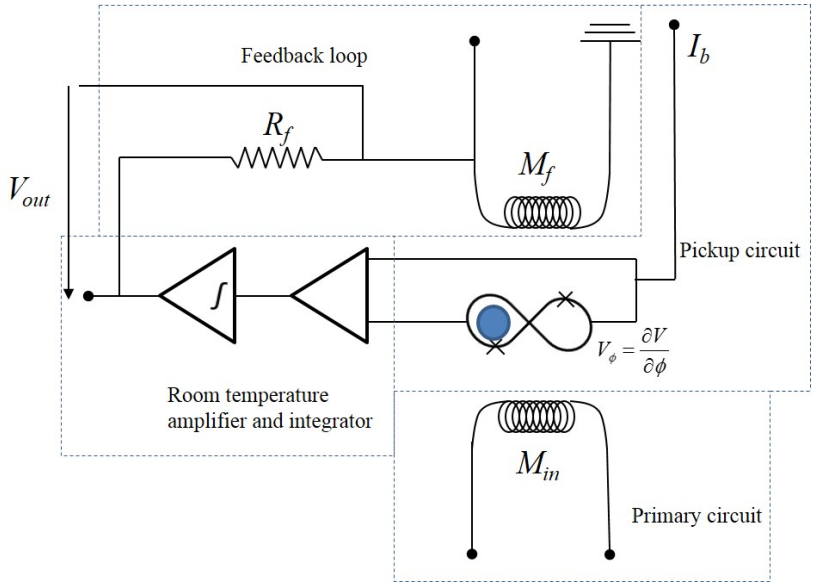

Figure 3.21: SQUID susceptometer circuit. The integrator and the amplifier stages are included in a special electronics at room temperature. The feedback resistance is also at room temperature and it is possible to tune it. The sample is placed in one of the two SQUID loops.

3.6.2 Measurement of basic characteristics

As it has already been said, this third generation susceptometers are still in an experimental phase, so PTB uses to make modifications on each fabrication run, varying the thickness of the different layers. The fabrication of these chips is done on 3 inch wafers together with many other different chips, as shown in section 3.4. Chips are organized within the wafer in two groups of 25 devices which are repeated along the wafer. This means that each susceptometer has different properties due to the different wafers and the chip position on it. This is specially important for tuning the susceptometer at a good operation point, eg., the current bias which optimizes the SQUID response.

The specific code of the chips indicates the number of the wafer and the position within the wafer. For instance, the chip C628_M01 is the model 01, belonging to the wafer number C628 and placed at the position M inside the wafer. Fig. 3.22 shows the position of the different chips in the wafer. The models 01 and 02 belongs to the susceptometers we have described above. In this section we present a study of all the differences among a set of eight 30 μm SQUID-loop susceptometers, studied at 4.2 K. In particular a comparative of M_{f}, M_{in}, V_ϕ and the bias parameters is presented.

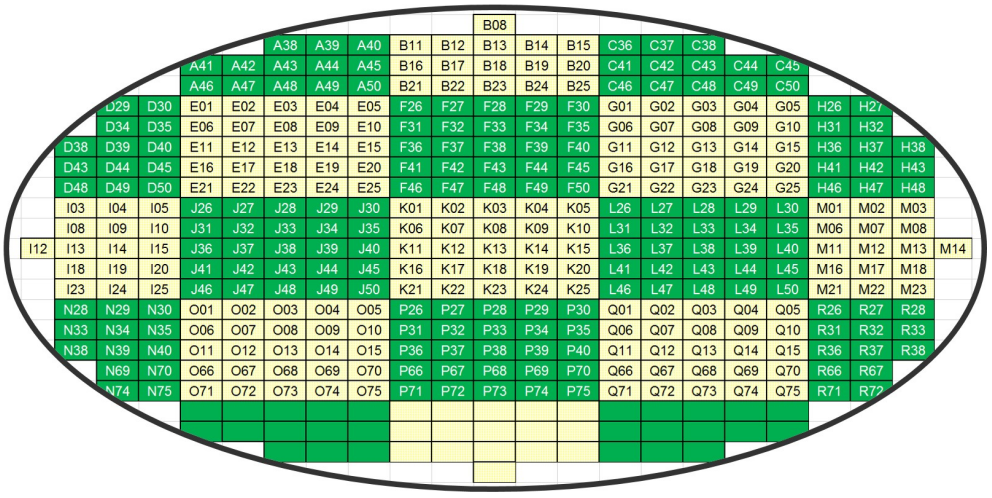

Figure 3.22: Diagram of the position of the chips on the wafer. There are two different groups of 25 chips (in yellow and green) which are alternatively repeated.

Mutual inductance

The mutual inductance M_{f}^{-1} is the coupling between the feedback coil and the SQUID loop. This coupling is weaker than that of the previous models due to the smaller size of the coils. Due to the limit of 250 μA in the maximum current from Magnicon electronics, it is necessary to use an external current source to induce several flux quanta. The mutual inductance can be directly calculated by monitoring the $V - \phi$ curve (see Fig. 3.23(b)) as

$$M_{\mathrm{f}}^{-1} = \frac{V/R}{n\phi_0} \tag{3.29}$$

where V is the voltage (in the y axis) for an integer number n of flux quanta ϕ_0 and $R = 2$ kΩ is the resistance which converts the applied voltage into current.

The average value for this magnitude is $\bar{M}_{\mathrm{f}}^{-1} \approx 580$ μA/ϕ_0. It is one of the most stable parameters (see table 3.1) except for the wafer C633 where it was found to be ≈ 720 μA/ϕ_0.

Another mutual inductance M_{in} determines the coupling between the field coil and the SQUID loop. If the balance between the two SQUID loops was perfect, M_{in} would vanish because the two SQUID loops are coiled in opposite senses and the couplings are mutually cancelled. As it is shown in the table, this parameter is at least ten times smaller than the feedback inductance. Due to this fact, the V-ϕ curve then shows only one flux quantum or even less and the measurement is less accurate.

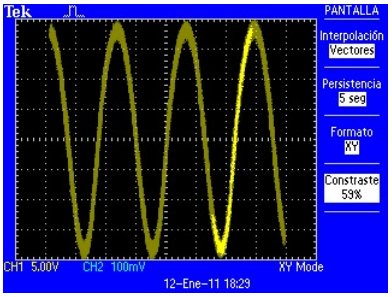

(a)

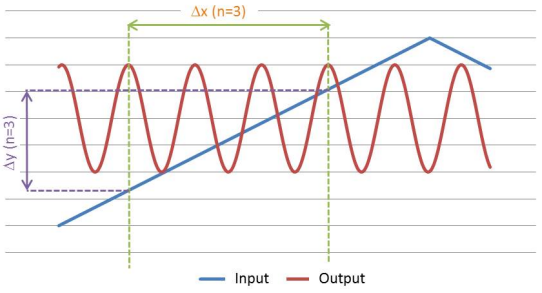

(b)

Figure 3.23: a) $V-\phi$ curve. It shows the periodic voltage answer of the SQUID loop when a flux is coupled to it. b) M_{f}^{-1} determination. In blue, the input current excitation. In red, the periodic SQUID response. Each period corresponds to a flux quantum.

Chip name	M_{f}^{-1} (μA/ϕ_0)	M_{in}^{-1} (μA/ϕ_0)	$I_{\mathrm{b_{max}}}$ (μA)	ΔV_{max} (μV)	V_ϕ (μV/ϕ_0)	M_{d}^{-1} (μA/ϕ_0)
C628_M01	551.0	9600	10.9	28.5	90.8	26.8
C629_K01	558.6	4300	7.09	16.5	59.1	12.6
C629_Q01	580.0	4700	9.36	7.25	22.9	3.40
C632_K01	571.3	8800	8.90	17.3	66.8	18.8
C633_K01	752.2	11800	8.50	12.5	84.5	17.9
C633_M01	710.9	20600	13.1	31.5	103	19.2
C635_E01	590.4	9700	9.50	7.89	82.2	24.6
C636_K01	593.8	8800	8.90	22.1	78.0	18.6

Table 3.1: Summary of the main characteristics for 30 μm susceptometers.

Bias parameters

The amplitude of the $V-\phi$ curve depends on the bias current I_{b}. To maximize the response in the linear regime, the sharpest slope is needed, so the amplitude must be maximized. The optimum I_{b} must be slightly higher than the critical current I_0. It can then depend on the chip fabrication parameters that ultimately determine the properties of the junctions.

As it can be seen in the table 3.1, I_{b} is 9.5 μA on average whereas the maximum amplitude varies widely from 7.3 μV up to 31.5 μV. These variation could exist due to the chips position inside the wafer or another factors, such as the oxidation time for the Josephson junctions, although there is not enough data to define a standard.

Transfer function

The transfer function V_ϕ relates the coupled flux with the SQUID voltage V by Eq. (3.6). This is the intrinsic gain of the SQUID. In FLL mode, the measured output also depends on the feedback resistance and the feedback coil, as shown in Eq. (3.14).

To measure V_ϕ, we apply a little voltage variation δV trough the SQUID. This voltage induces a little flux variation $\delta\phi$. Measuring the voltage response δV_{out} we can determine this variation by Eq. (3.14)

$$\delta\phi = G\delta V_{\text{out}} = \frac{M_{\text{f}}}{R_{\text{f}}}\delta V_{\text{out}} \tag{3.30}$$

V_ϕ can be therefore calculated as

$$V_\phi = \frac{\delta V}{\delta\phi} \tag{3.31}$$

The fifth column of table 3.1 shows the experimental data of the transfer coefficient, measured in FLL mode for a feedback resistance of 1 kΩ. V_ϕ varies from 22.9 μV/ϕ_0 to 103 μV/ϕ_0. As shown in section 3.2.3, V_ϕ plays an important role in reducing flux noise associated to the voltage electronics noise.

In the same way, current electronic noise can be translate into flux noise by M_{d}, a virtual inductance which acts as a transfer function for current:

$$M_{\text{d}}^{-1} = \frac{\delta I_{\text{b}}}{\delta\phi} \tag{3.32}$$

To measured it, a little bias current variation δI_{b} is applied. In FLL it produces a voltage output that can be translated into flux by Eq. (3.30) and hereafter, obtaining M_{d}. Measured values for M_{d}^{-1} are shown on the last column of table 3.1, varying from 3.4 μA/ϕ_0 and 26.8 μA/ϕ_0.

3.6.3 Noise measurements

To estimate the sensitivity of the sensor, a full characterization of the noise spectrum is needed. As we have seen in section 3.2.3, a SQUID device has several contributions to this spectrum: a white flux noise , which do not depend on frequency, and the Flicker noise $S_{\text{F}}(f)$, which is inversely proportional to frequency. There is also an extra contribution $S_{\phi_{\text{FLL}}}$ to the noise spectrum when we work in FLL mode, which comes from the electronics and has voltage and

Chip name	$S_{\phi_T}^{1/2}$ $(\mu\phi_0/\mathrm{Hz}^{1/2})$	$S_{V_{FLL}}^{1/2}/V_\phi$ $(\mu\phi_0/\mathrm{Hz}^{1/2})$	$S_{I_{FLL}}^{1/2} M_d$ $(\mu\phi_0/\mathrm{Hz}^{1/2})$
C628_M01	4.10	3.63	0.10
C629_K01	6.08	5.58	0.22
C629_Q01	13.5	14.4	0.82
C632_K01	5.25	4.94	0.15
C633_K01	4.30	3.91	0.16
C633_M01	3.75	3.21	0.15
C635_E01	4.66	4.01	0.11
C636_K01	4.67	4.23	0.15

Table 3.2: Noise measurements of the 30 μm susceptometers on one stage configuration at 1 kHz. The second column is a theoretical estimation of voltage noise contribution using the experimental reference $S_{V_{FLL}}^{1/2} = 0.33$ nV/Hz$^{-1/2}$ and V_ϕ value for each susceptometer. The third column shows the same for the current noise contribution taking the experimental reference $S_{I_{FLL}}^{1/2} = 2.8$ pA/Hz$^{-1/2}$ and M_d value for each susceptometer.

current noise contributions. As these noise contributions are not correlated, the total noise is just the sum of them:

$$S_{\phi_T} = S_\phi + S_{I_{FLL}} M_d^2 + S_{V_{FLL}}/V_\phi^2 \tag{3.33}$$

The intrinsic electronics noise was characterized in 2006 [3.44] and it is shown in figure 3.24(a). The voltage noise spectrum is approximately constant and can be approximated as $S_{V_{FLL}}^{1/2} = 0.33$ nV/Hz$^{-1/2}$. The current noise spectrum is $S_{I_{FLL}}^{1/2} = 2.8$ pA/Hz$^{-1/2}$.

Table 3.2 compares the noise measured for each susceptometer at 1 kHz (out of the Flicker noise influence) with the noise contribution expected from the electronics. As it can be seen, the voltage electronics noise becomes dominant and the intrinsic susceptometer noise contribution lies within the experimental uncertainties. This fact complicates the detection of the intrinsic noise contributions. Current noise contribution, on the contrary is much smaller and it will be neglected hereafter.

According to Eq. (3.33), V_ϕ largely influences $S_{\phi_T}^{1/2}$: the bigger V_ϕ, the smaller the electronics contribution. As we have already said, V_ϕ is the flux to voltage transfer coefficient and it is possible to enhance it by including a low noise amplifier stage, such as an amplifier SQUID array, between the SQUID and the electronics. This method is discussed in the following subsection.

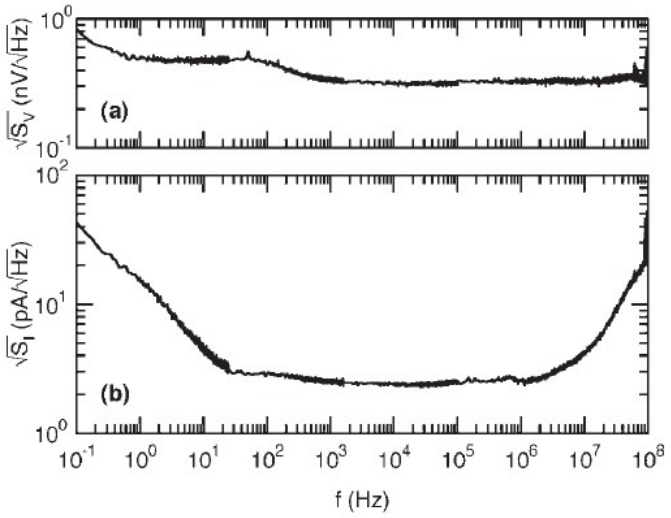

(a)

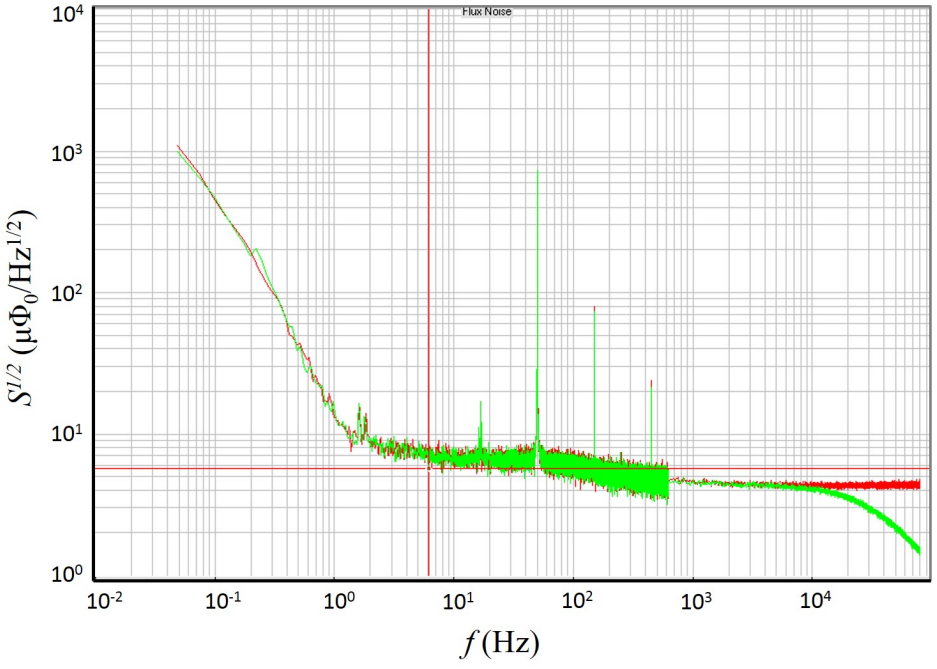

(b)

Figure 3.24: a) Intrinsic electronics voltage and current noise spectra from [3.44]. The voltage noise is approximately constant over 1 Hz. b) Noise spectrum from C632_K01 device, measured at two different feedback resistances: 1 kΩ in red and 10 kΩ in green.

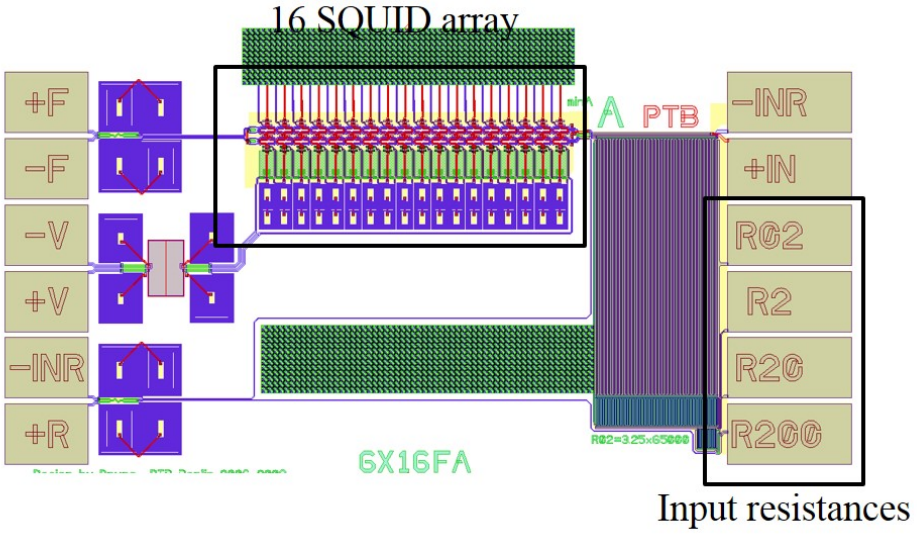

Figure 3.25: 16-SQUID array from PTB.

Noise reduction: Second stage

To reduce the electronics contribution, we need to amplify the SQUID output as much as possible before arriving to the room temperature amplifier. To achieve this, a SQUID array was coupled to the susceptometer output. This array is shown in Fig. 3.25. It consists of 16 identical SQUIDs connected in series. They detect the flux created by a coil and give a voltage signal which is the sum of the output signal of the 16 detectors, giving therefore a 16 times larger signal than a single SQUID would give. The transfer function V_ϕ of the array itself is, at least 10 times higher than that of the susceptometer and therefore, its intrinsic contribution to the noise spectral density is negligible.

To couple the susceptometer and the array, the output voltage of the SQUID susceptometer passes through a resistance R_b which can be chosen from 0.2 Ω up to 200 Ω and the ensuing dc current passes through a coil which creates the flux. The whole circuit is similar to that shown in Fig. 3.6.

In table 3.3 the results of noise measurements in the two-stage configuration are shown. Four different arrays have been used to show that their contribution to noise is negligible whereas the total transfer function V_ϕ increases up to 3200 $\mu\mathrm{V}/\phi_0$. The table shows that the electronics noise contribution is much lower than that given in table 3.2, being in some cases lower than a 1 %, and therefore enable us to measure almost directly the intrinsic susceptometer noise. On average, we find $S_\phi^{1/2} \approx 1.7 \pm 0.2\ \mu\phi_0/\mathrm{Hz}^{1/2}$. This value is similar to

Suscep. chip	Array chip	V_ϕ (μV/ϕ_0)	$S_{\phi_T}^{1/2}$ ($\mu\phi_0$/Hz$^{1/2}$)	$S_{V_{FLL}}^{1/2}/V_\phi$ ($\mu\phi_0$/Hz$^{1/2}$)	$S_\phi^{1/2}$ ($\mu\phi_0$/Hz$^{1/2}$)
C628_M01	C633_L40	308.6	2.273	1.069	2.006
C629_K01	C633_D40	2679.8	1.568	0.123	1.563
C629_Q01	C633_D40	2206.6	1.925	0.150	1.919
C632_K01	C633_L40	306.0	2.377	1.078	2.119
C633_K01	C633_D40	1475.8	1.536	0.224	1.520
C633_M01	C633_D40	2203.6	1.388	0.150	1.380
C635_E01	C635_B15	3194.0	1.515	0.103	1.511
C636_K01	C636_A39	1735.5	1.655	0.190	1.644

Table 3.3: Noise measurements of the 30 μm susceptometers on two-stage configuration.

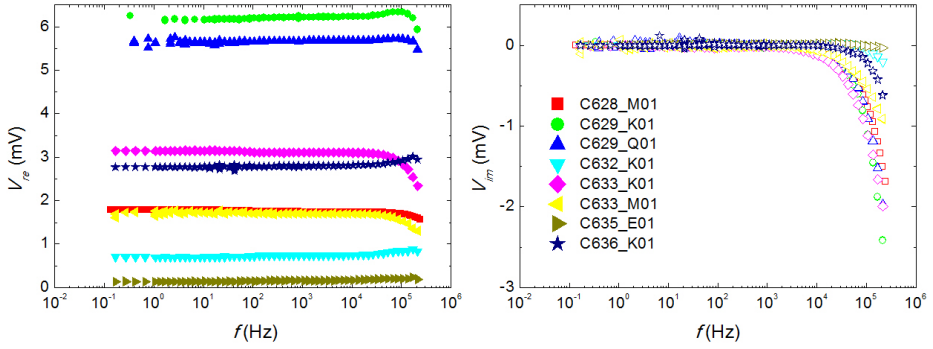

Figure 3.26: Background signal of some of the 30 μm susceptometers for an input current of 50 μA, a feedback resistance of 1 kΩ and a GWB product of 7.20 GHz. Full symbols correspond to the real part of the signal whereas the empty ones correspond to the imaginary part.

the noise of the H32 device, already shown in Fig. 3.4(b), which is $S_{\phi_{(H32)}}^{1/2} \approx 0.9$ $\mu\phi_0$/Hz$^{1/2}$ [3.33].

3.6.4 Background signal

Although the chips are designed to be as symmetric as possible, the total flux detected by a bare sensor differs from zero. As in the case of the H32 sensor, this fact can be related to a non perfect fabrication.

The magnitude of the background signal depends also on the sensitivity of the sensors and on the structural differences. Figure 3.26 shows the background signal for some sensors. As it happened with the H32 sensor, the signal also

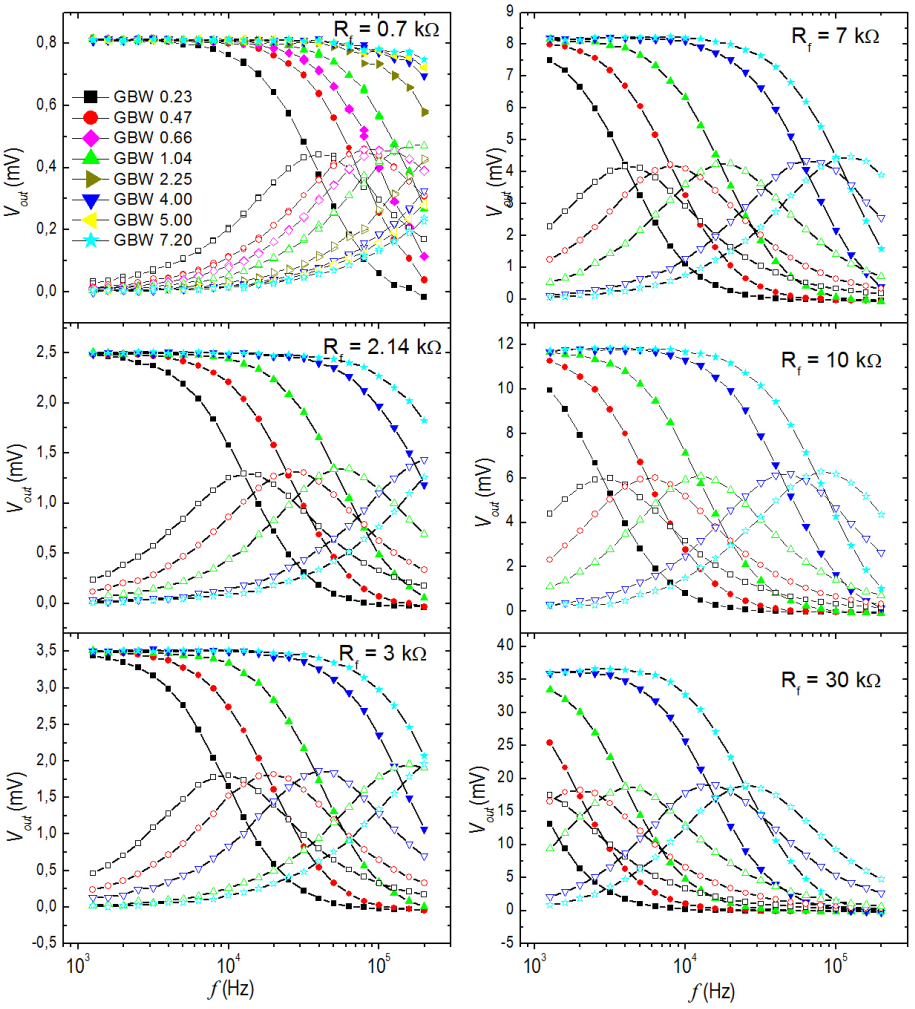

Figure 3.27: Background signal of a 30 μm susceptometer for different feedback resistances and GBW. Full symbols correspond to the real part whereas empty symbols correspond to the imaginary part. The input current is 25 μA.

changes with the FLL conditions. Figure 3.27 shows these variations for one of the chips. The background signal depends strongly on the feedback resistance at high frequencies. This is why it is not possible to use R_f as large as those used with the H32 sensor. Resistances of about 1 kΩ have been selected for susceptibility measurements.

Scaling function

The diverse responses found for different sensors makes it necessary to study their background signal one by one, instead of obtaining a general formula, in a similar way to the work described in section 3.5.2.

This time we have used as calibrating sample a crystal of Er_2 dimers, which consist of two Er^{3+} ions shielded by an organic structure. This molecule will be studied in more detail in chapters 4 and 6. For calibration, only the fact that χ is independent on $\omega = 2\pi f$ at $T = 4.2$ K is relevant.

As an example, we present in detail the results obtained for the device C636_K01. We compare measurements of the empty susceptometer and of the device with the sample on both coils. Figure 3.28(a) shows the sample placed on both coils and Fig. 3.28(b) shows the measurements results.

Applying Eqs. (3.24) to (3.26), it is possible to subtract the background signal. The resulting V_{out} vs. ω is nearly flat, as it was expected to be, except at high frequencies (Fig. 3.28(c)). As in the case of H32 susceptometer, the Module - Phase representation shows that the origin of this behaviour is a phase shift. Fitting then the phase signal (see Fig. 3.28(d)), we obtain that

$$F^{*-1} = e^{i\phi(f)} \tag{3.34}$$

where

$$\phi(f)[deg] = -360 + \frac{359.98}{1 + \frac{f}{4 \cdot 10^6}} \tag{3.35}$$

that must be subtracted from the experimental phase. The final results, shown in Fig. 3.28(e), have different values for the real part, depending on the location of the sample. This is normal, taking into account that little losses of mass could occur when the sample is transferred from one coil to the other.

Comparing to the H32 background signal (shown in Fig. 3.18), it is possible to conclude that both types of devices have similar background signals and therefore, to subtract it properly, a phase correction is necessary.

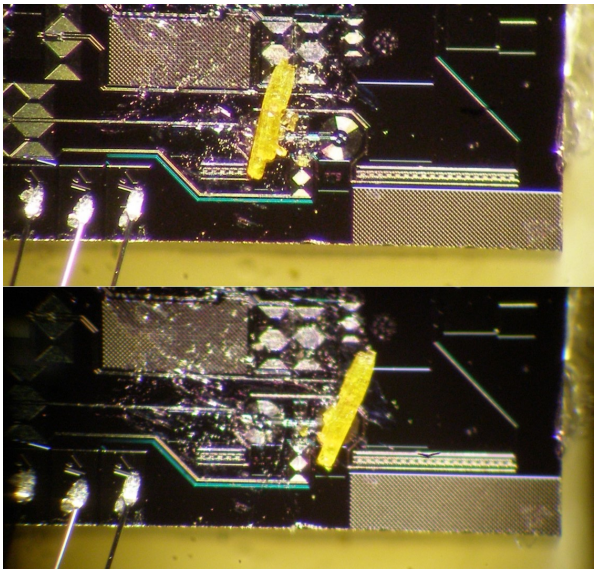

(a)

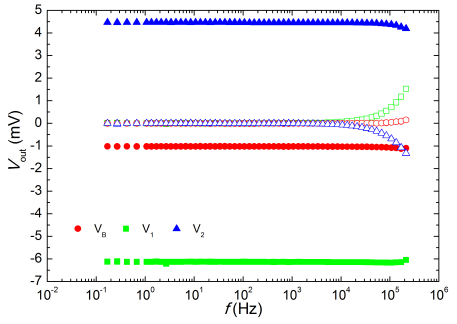

(b)

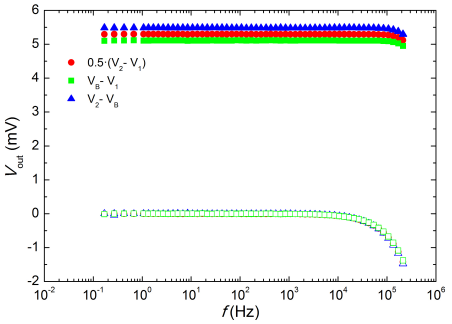

(c)

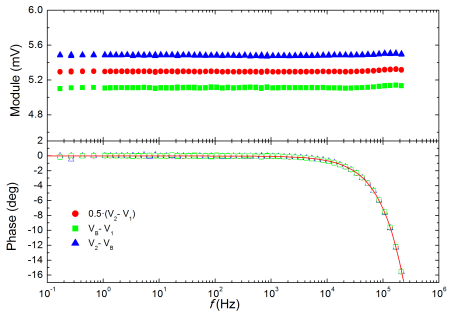

(d)

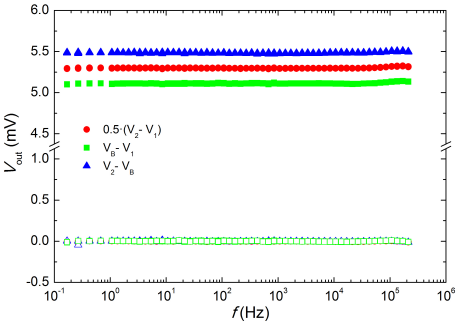

(e)

Figure 3.28: a) Picture of the C636_K01 susceptometer with a crystal of Er_2 placed on the coils. b) Crystal of Er_2 measured on the two coils of the C636_K01 susceptometer and the background signal when the device is empty. c) Measurement after background extracting following Eqs. from (3.24) to (3.26). d) Module-Phase representation which shows a phase contribution. e) Definitive measurement after applying all the data treatment.

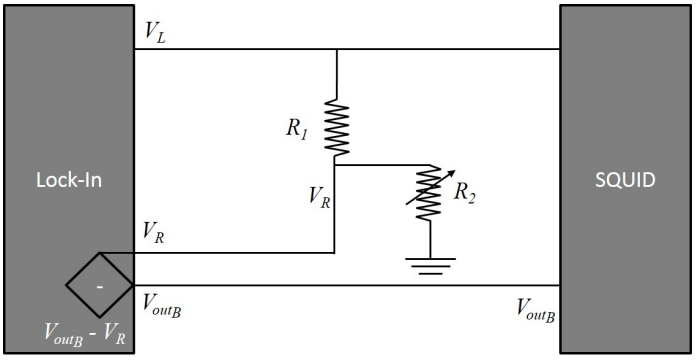

Figure 3.29: Scheme of the voltage divider placed between the output and input signals.

3.6.5 Background signal compensation

Reducing the background signal without changing the FLL mode parameters improves the sensitivity of the measurement as it enables increasing the lock-in sensitivity. It does not improve the intrinsic sensitivity of the device, which comes from the geometric design, but allows us to measure more precisely. Here, we present two different experimental methods that we have explored to reduce the background signal: external compensation and area compensation. The first one has nothing to do with the sensor itself whereas the second one implies a SQUID modification.

Current compensation

The lock-in amplifier used in this thesis is the model 7265 from Signal Recovery. It has the possibility to subtract two input signals. The lock-in measures the amplitude gain and the phase shift of the output with respect to the excitation signal. Our goal is to reduce the amplitude of the bare sensor output signal without affecting the phase shift. The best way to do it is by subtracting a signal proportional to the excitation one, i.e., a signal with the same phase as the excitation signal and the same amplitude as the background signal at the non-dependent on frequency region.

This can be easily achieved with a tunable voltage divider (see Fig. 3.29), where it is possible to subtract from the background $V_{\mathrm{out_B}}$ a signal V_{R} which is proportional to the excitation signal, V_{L}. The resistances R_1 and R_2 of the circuit shown in Fig. 3.30(a) can be chosen to tune V_{R}, considering that

$$V_{\mathrm{R}} = \frac{R_2}{R_1 + R_2} V_{\mathrm{L}} \tag{3.36}$$

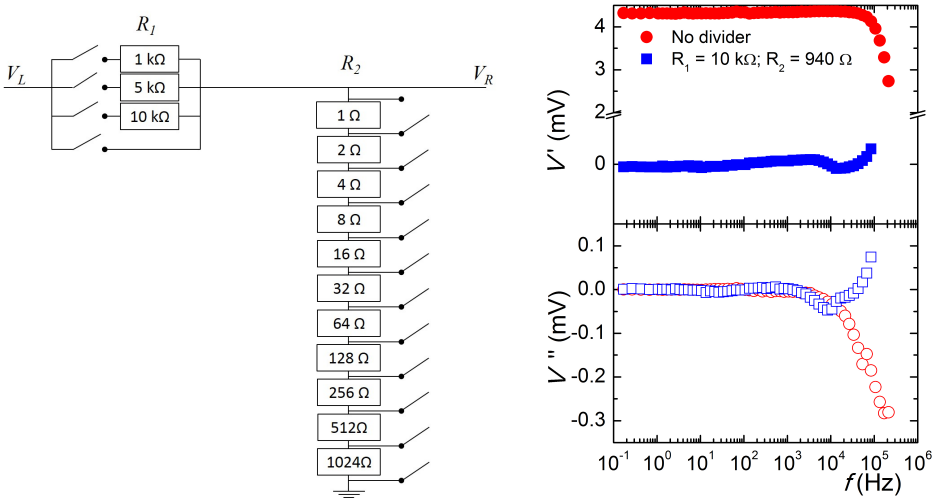

(a) (b)

Figure 3.30: a) Circuit scheme of the "binary" voltage divider, made of SMD resistances. b) C636_K01 background signal measured without voltage divider and with it.

Then, if the background signal shows an amplitude $V_{\mathrm{out_B}}$ and a mismatch $\phi(f)$ and the excitation signal shows an amplitude V_{L} and no mismatch, it is possible to tune the voltage divider so that $V_{\mathrm{R}} = V_{\mathrm{out_B}}$. The result is a new background signal with null amplitude at low frequency and some phase shift.

To carry out this experiment we have fabricated a voltage divider using Surface Mounted Devices (SMD) resistances, which are more robust with respect to frequency and temperature changes. The divider is highly tunable as shown in Fig. 3.30(a). The R_1 resistance can be chosen between 1 kΩ, 5 kΩ, 10 kΩ or any combination in parallel of them. R_2 is a "binary" resistance from 1 Ω to 2047 Ω consisting of eleven resistances, 1, 2, 4, 8, 16, 32, 64, 128, 256, 512 and 1024 Ω, in series which can be independently connected or short-circuited.

For each susceptometer, a proper set of R_1 and R_2 values must be chosen, depending on the magnitude of the background signal. We next describe the results obtained for C636_K01 μSQUID. This device shows a background signal of about $V_{\mathrm{out_B}} = 4.3$ mV when an excitation of $V_{\mathrm{L}} = 50$ mV is applied. Therefore we must tune the voltage divider to transform V_{L} into $V_{\mathrm{R}} \approx V_{\mathrm{out_B}}$. Considering our divider, we have six solutions for Eq. (3.36), tabuled on table 3.4.

Among these solutions, we have chosen the third option ($R_1 = 10$ kΩ and $R_2 = 940$ Ω) because it allows more accuracy in R_2. Measurement results are

R_1 configuration	R_1 (kΩ)	R_2 (Ω)
1 kΩ	1	94
5 kΩ	5	470
10 kΩ	10	940
1 kΩ || 5 kΩ	0.83	78
1 kΩ || 10 kΩ	0.91	85
5 kΩ || 10 kΩ	3.33	313
1 kΩ || 5 kΩ || 10 kΩ	0.77	72

Table 3.4: Solutions for Eq. (3.36).

shown in Fig. 3.30(b). As expected, the in-phase V' signal has been reduced from 4.3 mV to 22 μV, which means that it is possible to improve the lock-in sensitivity 200 times.

On the other hand, despite the small dependence of the SMD resistances on frequency, it is possible to observe a change in the shape of the signal, which implies an additional treatment for background subtraction.

Area compensation

The other method to reduce the background signal is trying to compensate it with an areal compensation. This consists in increasing the effective area of one of the pick-up coils by using FIB etching. The mismatch is then compensated in order to null the background signal. We performed this modification on chip C602_Q01 ($M_{\mathrm{f}}^{-1} = 480$ μA/ϕ_0).

To determine which one of the two pick-up coils must be increased, measurements with an aluminium sample in both coils have been done in order to see which one plays in favour of the background signal. As it is shown in Fig. 3.31(a) the aluminium susceptibility is added to the background when it is measured in coil 1, whereas it is subtracted from the background when it is measured in coil 2. This means that the flux coupled to the coil 1 is larger and that, therefore,the coil 2 effective area must be increased.

To calculate how much the coil area must be increased, we calculate first the flux needed to compensate the flux signal of the background. For an input current $I_{\mathrm{p}} = 25$ μA, and a feedback resistance $R_{\mathrm{f}} = 700$ Ω we obtain a background signal $V_{\mathrm{out_B}} = 0.78$ mV. This is equivalent to a flux imbalance of

$$\Delta\phi = \frac{M_{\mathrm{f}}}{R_{\mathrm{f}}} V_{\mathrm{out_B}} = 2.32 \cdot 10^{-3} \phi_0 \tag{3.37}$$

where $\phi_0 = 2.0678 \cdot 10^{-15}$ Wb is the magnetic flux quantum.

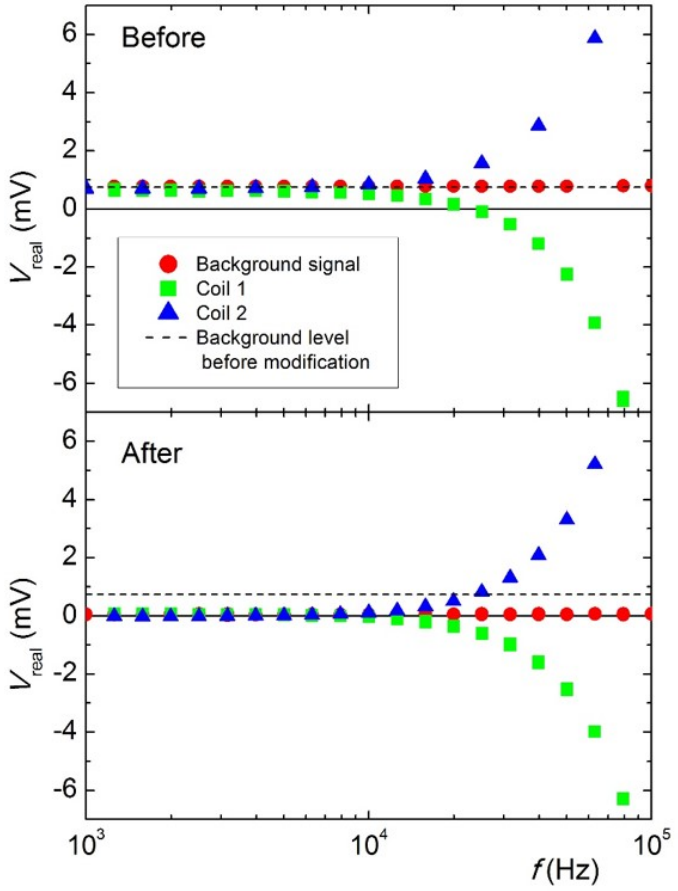

(a)

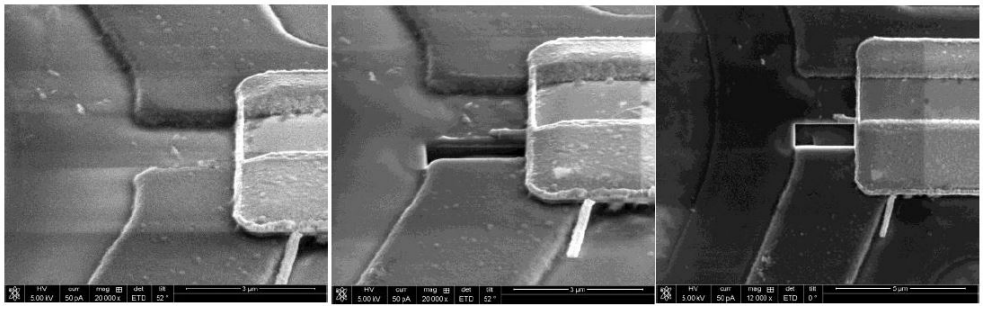

(b)

Figure 3.31: a) Measurement of Aluminium performed in both coils of the C602_Q01 susceptometer. The top graphics shows the measurements before the area compensation and the bottom one shows the measurements afterwards. The input excitation is 25 μA. The FLL conditions are $R_f = 700\ \Omega$ and $GBW = 7.20$ GHz. b) FIB process of increasing effective area. The chosen place to etch does not affect the circular shape of the coil.

On the other hand, the magnetic flux that passes through the whole area of the coil can also be calculated. Taking into account that the magnetic field created by the field coil is 0.1 T/A the applied magnetic field is $B_p = 0.1 \cdot I_p$ =2.5 μT. As the coil radius $r = 15$ μm is known, the total flux ϕ through the coil is

$$\phi = B_p \cdot A = B_p \cdot \pi r^2 = 1.77 \cdot 10^{-15} \text{ Wb} = 0.85 \ \phi_0. \tag{3.38}$$

As B_p is constant, flux and area are proportional, and therefore we must remove an area A_{rem} of

$$A_{rem} = \frac{\Delta\phi}{\phi} V_{out_B} = 1.93 \ \mu m^2 \tag{3.39}$$

In order to ease the process, a 0.88 μm $\times$ 2.25 μm rectangular geometry has been chosen. Fig. 3.31(b) shows some SEM images of the etching process.

After the area compensation, we carried out again the same measurements as we did before. As it can be seen in Fig. 3.31(a), the background signal has been reduced from 0.78 mV to 0.054 mV and the signal shape has not changed, thus allowing us to use the same data treatment.

After this success we tried to reduce even more the background imbalance by removing another smaller area, but these chips are very susceptible to electrostatic discharges and the device broke up. For this reason, a very strict protocol is needed to avoid electrostatic discharges and still some of the chips were unavoidably damaged.

3.7 Fabrication and characterization of nanosusceptometers

3.7.1 Introduction

In the last years there has been a growing interest in the investigation of nano scale samples. For this reason, fabrication of nanometric devices appears as a natural way of studying these new materials. For magnetic measurements, the natural choice is the use of a nanoSQUID sensors, consisting of devices whose SQUID loop is in the nanometric regime [3.45].

NanoSQUIDs present several benefits, as compared with bigger devices. On the one hand, as the coil fits the sample better, their mutual coupling is enhanced. On the other hand, the inductance of the SQUID ring and the capacitance of the Josephson junctions are lowered, which could theoretically

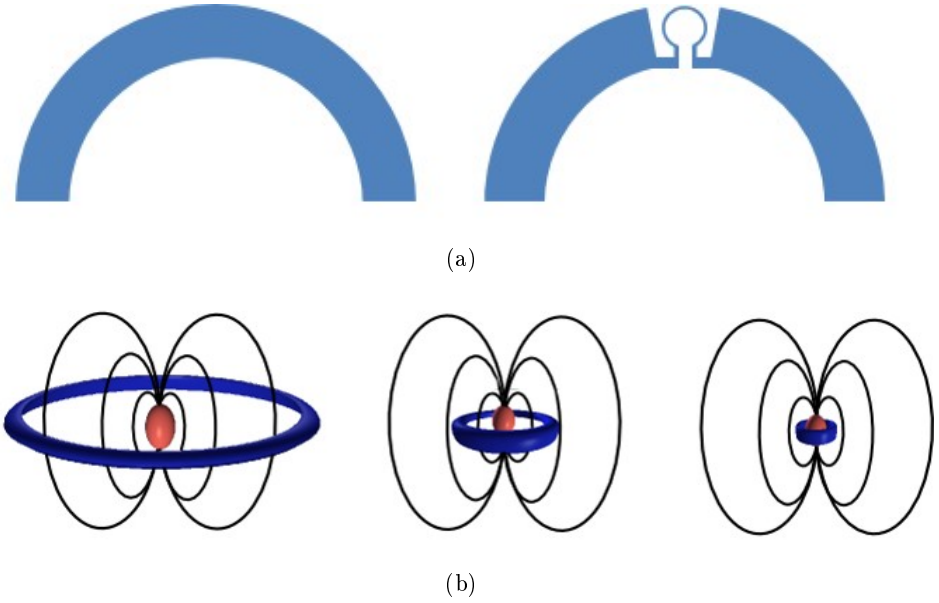

Figure 3.32: a) Scheme of nanoloop fabrication. The left coil is the original one whereas the right coil is the modified one. b) The magnetic field lines are better coupled to the coil when the coil fits the sample.

reduce the noise level down to 10 n$\phi_0/\sqrt{\text{Hz}}$. Unfortunately, there exist many limitations to the fabrication of suitable Josephson junctions because conventional techniques are not optimized for nanometric scale and this fact turns into a higher noise, similar to that of microSQUIDs [3.46]. Besides nanoSQUIDs do not usually have a feedback coil because it is more difficult to achieve a good coupling between the nanoloop and the feedback coil, and this makes it impossible to perform linear measurements in a FLL regime [3.47].

These disadvantages made us think of a new way of measuring nanosamples without using a nanoSQUID. Our idea was to upgrade a conventional microSQUID, as those described in previous sections, and to adapt it to measure nanosamples.

3.7.2 Basic concept

The aim is to fabricate a nanoloop in series to one of the 30 μm SQUID loop. A schematic picture of this idea is shown in Fig. 3.32(a). The left coil is the original microloop and the right one shows a nanoloop, integrated in series into the microloop. The hypothesis is that the coupling between a sample placed inside the nanoloop and the nanoloop itself must be much better that

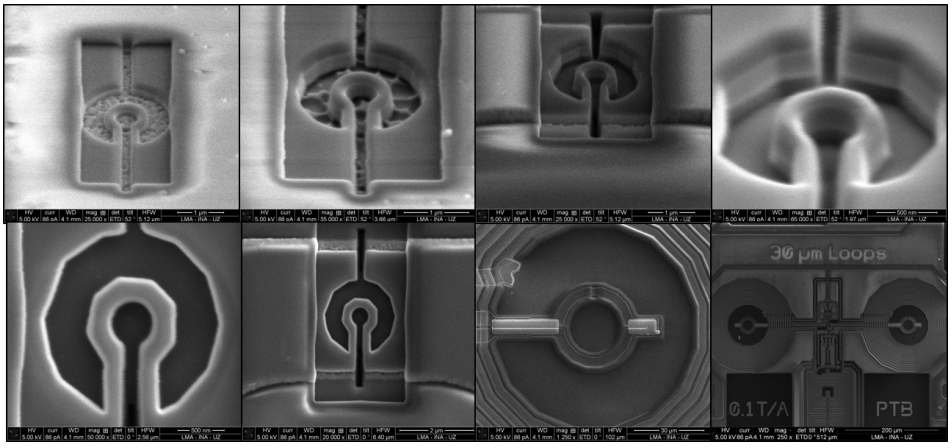

Figure 3.33: SEM images of the nanoloop fabrication process. The inner diameter is 430 nm long.

the coupling between the same sample and the whole microloop as shown in Fig. 3.32(b).

To calculate this coupling, we can suposse the magnetic flux created by a punctual magnetic sample whose magnetic moment is $\mu = IA$ by modelling it as a planar current loop I with an area A. Then, the flux ϕ, that this sample couples to the pickup coil of the device $\phi = MI$, where M is the mutual inductance between the sample and the pickup coil. Coupled flux is related to the magnetic moment as

$$\phi = \frac{M}{A}\mu \tag{3.40}$$

On the other hand, the magnetic field B_p at the dipole position, which is generated by a current I_p circulating through the pickup loop, can be related to the dipole by the Lorentz reciprocity theorem, which says that sources and fields can be interchanged as follows

$$B_\mathrm{p}A = MI_\mathrm{p} \tag{3.41}$$

Then we can find a relation between the magnetic moment and the coupled flux as

$$\phi = \frac{B_\mathrm{p}}{I_\mathrm{p}}\mu \tag{3.42}$$

The transfer function $B_\mathrm{p}/I_\mathrm{p}$ depends only on the pickup loop characteristics and is a figure of merit for the coupling between the magnetic dipole and the pickup coil. COMSOL simulations were done by D. Drung *et al.* [3.48] for a nanoloop with an inner diameter of 300 nm and an outer diameter of 500 nm. They obtain that $B_\mathrm{p}/I_\mathrm{p}$ is predicted to be about ten times larger inside the nanoloop, ∼6 T/A, than outside it ∼0.55 T/A.

3.7.3 Experimental realization

To verify this sensitivity enhancement, we have chosen the C632_K01 device and modified one of their pickup coils using focused ion beam (FIB) to fabricate the nanoloop. The system used for this has been the Dual-Beam Helios 600, located in the Institute of Nanoscience of Aragón (INA). It allows to "print" a pattern over a subtract by etching. The zone to be eroded is bombarded with Ga^+ ions causing the vaporization of superconducting material. Figure 3.33 shows the etching process in which a nanoloop of 430 nm inner diameter and 950 nm outer diameter has been fabricated.

3.7.4 Nanoloop characterization

The fabrication of a coil has similar effects on the SQUID characteristics to those found when we tried to tune the effective area of one of its loops (in section 3.6.5). It does not affect the main characteristics, except for the mutual inductance between the primary coil and the pickup coil, M_{in} that, according to section 3.6.2 depends on the imbalance of the areas. The background signal, therefore, changes due to the new ratio between the areas of both SQUID loops, as it can be seen in Fig. 3.34. In this case, the area increment has even changed the sign of the background signal, and this must be taken into account when samples are measured.

3.7.5 Measurement of a Permalloy sample

In order to test whether the nanoloop was able to detect any signal we have fabricated a sufficiently small test sample consisting on a 125 nm thick Permalloy layer. To achieve this, we used again the dual-beam Helios 600 from INA. This time we used electron-beam evaporation to deposit a Permalloy layer on a 50 nm silicon nitride support film, which does not have magnetic response. Then, a small piece of this film was cut with the focused ion beam and moved to the nanoloop using an Omniprobe manipulator included in the system. Fig. 3.35(a) shows some SEM images of how the Permalloy layer is placed on the nanoloop.

The results of the measurement at 4.2 K, after properly subtracting the background due to the empty susceptometer, are shown in Fig. 3.35(b). They show a weak, close to logarithmic dependence on frequency below 10 kHz with a roll-off above this frequency for the real part and a increasing imaginary signal, in agreement with Kramers-Kronig relations. This behaviour has also been observed for other soft magnetic materials such as Co based amorphous alloys and it can be explained as a broad distribution of magnetic relaxation

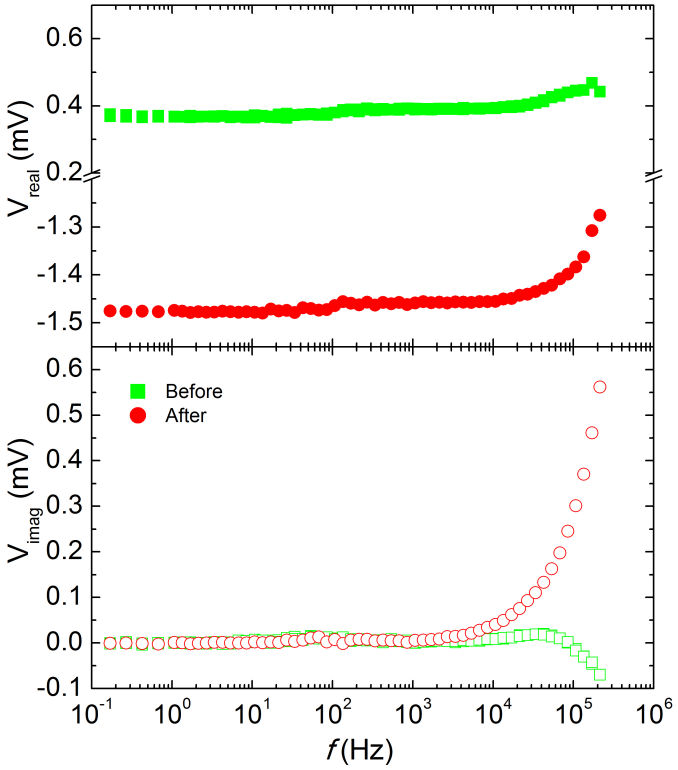

Figure 3.34: Background signal of the C632_K01 susceptometer before and after fabricating the nanoloop.

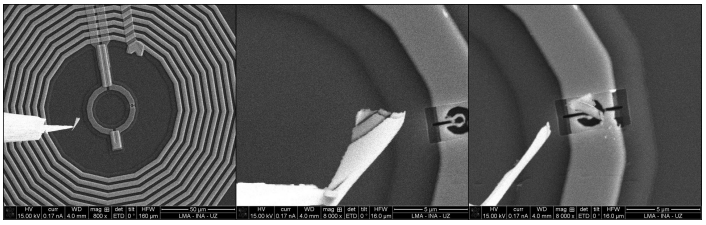

(a)

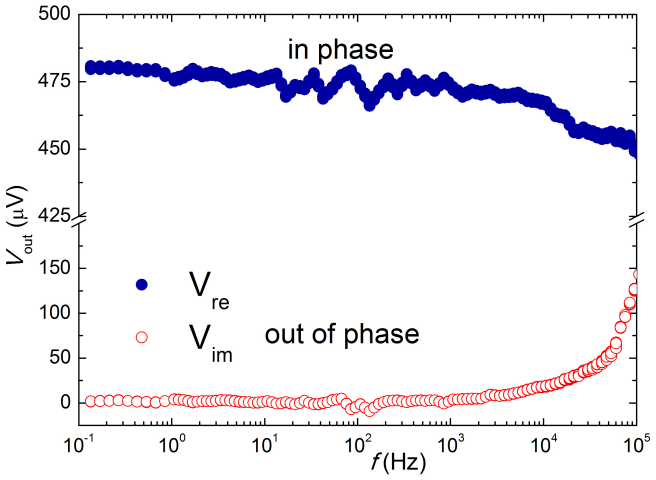

(b)

Figure 3.35: a) SEM pictures of the placing of a Permalloy layer on the nanoloop, using an Omniprobe manipulator. b) Permalloy susceptibility for an input excitation of 2.5 mA. It shows a similar behaviour for other amorphous alloys.

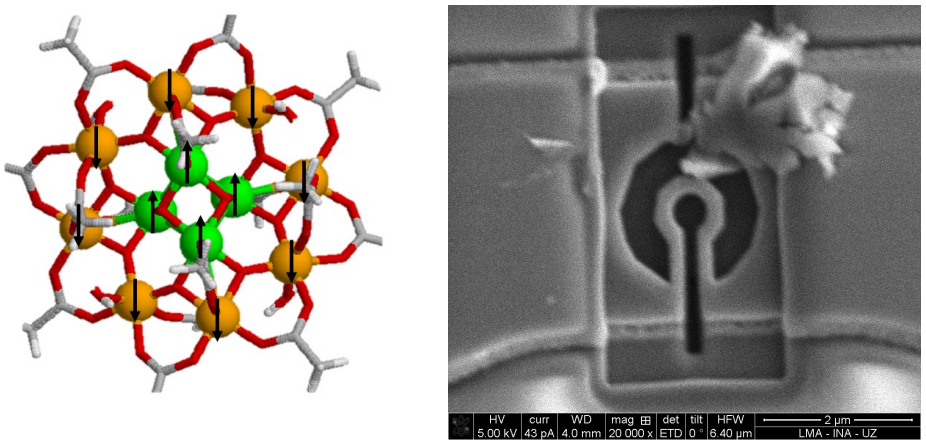

(a) (b)

Figure 3.36: a) Mn_{12}ac molecule. b) Mn_{12} nanocrystal placed on the nanoloop.

times [3.49]. This distribution can be caused by the depinning, either by thermal activation [3.50] or quantum tunnelling [3.51] of magnetic vortexes [3.52].

The coincidence with other samples reveals that the nanosample behaviour remains similar to the bulk sample and, more importantly for us, that our nanoloop is able to detect it.

3.7.6 Measurement of a Mn_{12} microcrystal

We have also performed another measurement on a sample one of magnetic molecules, a crystal of Mn_{12}ac. Mn_{12} [3.2,3.3,3.53] is probably the most studied SMM together with Fe_8. Mn_{12}ac was synthesized for the first time in 1980 by T. Lis [3.54]. It consists of a core formed by eight Mn^{3+} ions and Mn^{4+} ions. The innermost Mn^{3+} ions are mostly coupled antiferromagnetically to the outermost ones, as shown in Fig. 3.36(a), leading to a molecular spin S=10 ground state. In 1991 [3.55], ac magnetic susceptibility measurements on this SMM showed a non-zero imaginary component below 5 K. This phenomenon was interpreted as evidence for slow magnetic relaxation, or magnetic memory, due to the fact that the spin reversal characteristic time becomes comparable to or larger than ω^{-1} at such temperatures.

Here we have looked for this phenomenon in a microscopic Mn_{12}ac crystal and in a nanoscopic one to test whether this property is kept for such as small sample. We have performed measurements in a normal 30 μm susceptometer (model C629_Q01) and in the nanoloop, in order to compare both results. As

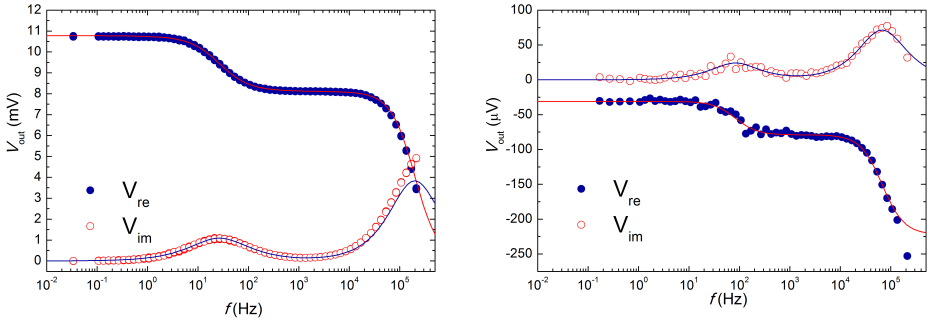

(a) (b)

Figure 3.37: a) Mn_{12} crystal measured in bulk with the C629_Q01 device. The susceptibility shows two thermal relaxation processes at 167 Hz and 1.25 MHz. b) Mn_{12} nanocrystal measured in the nanoloop. It also shows two relaxation processes at 518 Hz and 385 kHz as described in section 3.3. Both measurements have been done using an input excitation of 25 μA.

it can be seen in Fig. 3.37(a) the Mn_{12}ac we have used presents two species with different relaxation times, one faster, with a characteristic time $\tau_{\text{fast}} = 0.8$ μs, and another one slower, with a characteristic time $\tau_{\text{slow}} = 6$ ms.

Then, we have deposited a crystal of Mn_{12} on the nanoloop, using the same technique as in the case of Permalloy (see Fig. 3.36(b)). The results are shown in Fig. 3.37(b) and show that both relaxation processes seen in the bulk material also appear in this measurement. The characteristic times nevertheless vary: the faster relaxation seems to be approximately 3 times slower $\tau_{\text{fast}} \approx 2.3$ μs whereas the slower relaxation is approximately 3 times faster $\tau_{\text{slow}} \approx 1.93$ ms than in the bulk material, although both keep their order of magnitude.

Therefore, Mn_{12} keeps its condition of single molecule magnet also for nanometric crystals, and the nanoloop is able to detect it.

3.8 Summary and conclusions

In this chapter we have studied the properties of microSQUID susceptometers and their suitability as high sensitive sensors. Besides we have dug into ways to improve this sensitivity, specially for measurement of nanometric samples. We have arrived to the following conclusions.

First, we have begun by characterizing the H32 susceptometer, which belongs to the previous generation. This susceptometer has a robust background

signal that varies only with frequency above 10 kHz and it is independent on the temperature. Using the SMM GdW_{30} as calibrating sample we have determined the transformation function for data treatment. This function is just a phase shift correction,

$$F^{*-1} = e^{i\phi(f)} \longrightarrow \phi(f)[deg] = -55.833 + \frac{55.818}{1 + \frac{f}{1.295 \cdot 10^6}} \tag{3.43}$$

In second place, we have characterized a set of new 30 μm loop susceptometers. Concerning their specific characteristics, we have seen that they depend on the fabrication settings. Noise measurements reveal a dominant contribution of the electronics noise and to resolve the intrinsic noise of the 30 μm susceptometric devices a two-stage configuration has been proposed, using a low noise amplifier which reduces the electronics noise contribution. Thanks to that it has been possible to determine the intrinsic microSQUID noise. We have obtained that the microSQUID susceptometer noise is 1.7 ± 0.2 $\mu\phi_0/\mathrm{Hz}^{1/2}$.

The frequency dependence of the background signal of these devices depends much more on the FLL conditions than the dependence we have observed in H32. For background signal treatment we have used another SMM, Er_2, as calibrating sample, concluding that the data treatment is similar to the H32 data treatment but changing the phase shift function constants.

In order to improve the sensitivity of the Lock In used for measurements we have successfully carried out two methods to reduce the background level.

The first method consists on placing a voltage divider to reduce the amplitude of the read background signal. For this purpose, we have fabricated a voltage divider made of SMD resistors, with R_1 between 777 Ω and 10 kΩ and R_2 between 1 Ω and 2047 Ω. Results show a reduction 200 times smaller of the background level, although the dependence on the frequency changes.

The second method we have carried out is to compensate the background signal by increasing one of the effective areas of the pickup coils. Results are much better than in previous method because it does not change the frequency dependence of the background signal. Nevertheless, this method is very sensitive to electrostatic discharges and the risk of irreversible damage is quite high despite its good results in background level reduction.

To end with, we have upgraded the microSQUID susceptometer to measure nanometric samples. We have theoretically calculated that it is not necessary to miniaturize the whole SQUID, but only the coil that is used to couple the flux. In this way, the sensitivity in the the coil center is improved up to ten times, from ~ 0.55 T/A to ~ 6 T/A.

We have then fabricated a nanoloop in series to the microloop for this purpose using focused ion beam. We have found that the flux noise of the device does not change significantly in this new configuration.

To determine the well-working of the nanoloop we have performed two measurements at 4.2 K, the first one using a 125 nm thick Permalloy layer and the second one using a Mn_{12}ac nanocrystal. In both cases we have demonstrated that the nanoloop coil is able to detect both samples and, moreover, they show similar behaviours to those measured for bulk samples in bigger susceptometers.

Bibliography

[3.1] D. D. Awschalom, J. F. Smyth, G. Grinstein, D. P. DiVincenzo, and D. Loss, "Macroscopic quantum tunneling in magnetic proteins," *Phys. Rev. Lett.*, vol. 68, p. 3092, 1992.

[3.2] J. R. Friedman, M. P. Sarachik, J. Tejada, and R. Ziolo, "Macroscopic measurement of resonant magnetization tunneling in high-spin molecules," *Phys. Rev. Lett.*, vol. 76, p. 3830, 1996.

[3.3] J. M. Hernández, X. X. Zhang, F. Luis, J. Bartolomé, J. Tejada, and R. Ziolo, "Field tuning of thermally activated magnetic quantum tunnelling in Mn_{12} - ac molecules," *Europhys. Lett.*, vol. 35, no. 4, p. 301, 1996.

[3.4] L. Thomas, F. Lionti, R. Ballou, D. Gatteschi, R. Sessoli, and B. Barbara, "Macroscopic quantum tunneling of magnetization in a single crystal of nanomagnets," *Nature*, vol. 383, p. 145, 1996.

[3.5] S. Bertaina, S. Gambarelli, T. Mitra, B. Tsukerblat, A. Müller, and B. Barbara, "Quantum oscillations in a molecular magnet," *Nature*, vol. 453, p. 203, 2008.

[3.6] S. Ghosh, R. Parthasarathy, T. F. Rosenbaum, and G. Aeppli, "Coherent spin oscillations in a disordered magnet," *Science*, vol. 296, no. 5576, p. 2195, 2002.

[3.7] F. Luis, A. Repollés, M. J. Martínez-Pérez, D. Aguilà, O. Roubeau, D. Zueco, P. J. Alonso, M. Evangelisti, A. Camón, J. Sesé, L. A. Barrios, and G. Aromí, "Molecular prototypes for spin-based CNOT and SWAP quantum gates," *Phys. Rev. Lett.*, vol. 107, no. 11, p. 117203, 2011.

[3.8] G. A. Timco, S. Carretta, F. Troiani, F. Tuna, R. J. Pritchard, C. A. Muryn, E. J. L. McInnes, A. Ghirri, A. Candini, P. Santini, G. Amoretti, M. Affronte, and R. E. P. Winpenny, "Engineering the coupling between molecular spin qubits by coordination chemistry," *Nat. Nanotechnol.*, vol. 4, p. 173, 2009.

[3.9] W. J. de Haas and F. K. du Pré, "Paramagnetic relaxation in iron ammonium alum at low temperatures," *Physica*, vol. 5, no. 6, p. 501, 1938.

[3.10] A. Repollés, A. Cornia, and F. Luis, "Spin-lattice relaxation via quantum tunneling in diluted crystals of Fe_4 single-molecule magnets," *Phys. Rev. B*, vol. 89, no. 5, p. 054429, 2014.

[3.11] M. Jenkins, *Coupling Quantum Circuits to Magnetic Molecular Qubits.* PhD thesis, Universidad de Zaragoza, 2015.

[3.12] D. Drung, C. Assmann, J. Beyer, A. Kirste, M. Peters, F. Ruede, and T. Schurig, "Highly sensitive and easy-to-use SQUID sensors," *IEEE Trans. Appl. Supercond.*, vol. 17, no. 2, p. 699, 2007.

[3.13] J. Clarke and A. I. Braginski, eds., *The SQUID Handbook. Vol. 1 Fundamentals and technology of SQUID and SQUID system.* Weinheim: Wiley, 1st ed., 2004.

[3.14] B. D. Josephson, "Possible new effects in superconductive tunnelling," *Phys. Lett.*, vol. 1, no. 7, p. 251, 1962.

[3.15] F. London, *Superfluids. Volume 1, Macroscopic theory of superconductivity.* New York: Wiley, 2nd ed., 1961.

[3.16] R. C. Jaklevic, J. Lambe, A. H. Silver, and J. E. Mercereau, "Quantum interference effects in Josephson tunneling," *Phys. Rev. Lett.*, vol. 12, p. 159, 1964.

[3.17] B. Ahlgren and D. Byström, "A study of josephson junction characteristics," Master's thesis, Royal Institute of Technology (KTH), Sweden, 2011.

[3.18] H. Weinstock, ed., *SQUID Sensors: Fundamentals, Fabrication and Applications.* Springer Science & Business Media, 2012.

[3.19] D. Drung, "High-T_c and low-T_c dc SQUID electronics," *Supercond. Sci. Technol.*, vol. 16, p. 1320, 2003.

[3.20] J. Clarke and A. I. Braginski, eds., *The SQUID Handbook. Vol. 2 Applications of SQUID and SQUID Systems.* Weinheim: Wiley, 1st ed., 2004.

[3.21] I. Jin, A. Amar, T. R. Stevenson, F. C. Wellstood, A. Morse, and W. W. Johnson, "35 lambda two-stage SQUID system for gravity wave detection," *IEEE Trans. Appl. Supercond.*, vol. 7, p. 2742,

[3.22] H. Koch, "SQUID magnetocardiography: Status and perspectives," *IEEE Trans. Appl. Supercond.*, vol. 11, no. 1, 1, p. 49, 2001.

[3.23] V. S. Zotev, A. N. Matlachov, P. L. Volegov, H. J. Sandin, M. A. Espy, J. C. Mosher, A. V. Urbaitis, S. G. Newman, and R. H. Kraus, Jr., "Multi-channel SQUID system for MEG and ultra-low-field MRI," *IEEE Trans. Appl. Supercond.*, vol. 17, no. 2, 1, p. 839, 2007.

[3.24] R. Gross and A. Marx, "Applied superconductivity: Josephson effects and superconducting electronics." Lecture Notes, 2009. Walther Meissner Institut.

[3.25] W. G. Jenks, S. S. H. Sadeghi, and J. P. Wikswo, "SQUIDs for non-destructive evaluation," *J. Phys. D: Appl. Phys.*, vol. 30, no. 3, p. 293, 1997.

[3.26] R. C. Black, A. Mathai, F. C. Wellstood, E. Dantsker, A. H. Miklich, D. T. Nemeth, J. J. Kingston, and J. Clarke, "Magnetic microscopy using a liquid-nitrogen cooled $YBa_2Cu_3O_7$ superconducting quantum interference device," *Appl. Phys. Lett.*, vol. 62, no. 17, p. 2128, 1993.

[3.27] M. B. Ketchen, T. Kopley, and H. Ling, "Miniature SQUID susceptometer," *Appl. Phys. Lett.*, vol. 44, no. 10, p. 1008, 1984.

[3.28] W. Wernsdofer, K. Hasselbach, D. Mailly, B. Barbara, A. Benoit, L. Thomas, and G. Suran, "dc-SQUID magnetization measurements of single magnetic particles," *J. Magn. Magn. Mater.*, vol. 145, no. 1-2, p. 33, 1995.

[3.29] S. K. H. Lam and D. L. Tilbrook, "Development of a niobium nanosuperconducting quantum interference device for the detection of small spin populations," *Appl. Phys. Lett.*, vol. 82, p. 1078, 2003.

[3.30] J. P. Cleziou, W. Wernsdorfer, V. Bouchiat, T. O. uhu, and M. Monthioux, "Carbon nanotube superconducting quantum interference device," *Nat. Nanotechnol.*, vol. 1, no. 1, p. 53, 2006.

[3.31] P.-T. B. Cryophysics and Spectrometry.
`http://www.ptb.de/cms/en/fachabteilungen/abt7/fb-72.html` (last view: 11/06/2014).

[3.32] M. GmbH.
`http://www.magnicon.com/` (last view: 11/06/2014).

[3.33] M. J. M. Pérez, *μSQUID susceptometry of molecular qubits.* PhD thesis, Universidad de Zaragoza, 2011.

[3.34] M. J. Martínez-Pérez, J. Sesé, R. Córdoba, F. Luis, D. Drung, and T. Schurig, "Circuit edit of superconducting microcircuits," *Supercond. Sci. Technol.*, vol. 22, no. 12, p. 125020, 2009.

[3.35] E. S. Sadki, S. Ooi, and K. Hirata, "Focused-Ion-Beam-Induced deposition if superconducting nanowires," *Appl. Phys. Lett.*, vol. 85, p. 6206, 2004.

[3.36] J. M. de Teresa, A. Fernández-Pacheco, R. Córdoba, J. Sesé, R. Ibarra, I. Guillamon, H. Suderow, and S. Vieira, "Transport properties of superconducting amorphous W-based nanowires fabricated by Focused-Ion-Beam-Induced-Deposition for applications in nanotechnology," in *Symposium CC - Nanoscale Functionalization and New Discoveries in Modern Superconductivity*, vol. 1180 of *MRS Proceedings*, 2009.

[3.37] S. K. Tripathi, N. Shukla, and V. N. Kulkarni, "Exploring a new strategy for nanofabrication: deposition by scattered Ga ions using Focused Ion Beam," *Nanotechnology*, vol. 20, no. 7, 2009.

[3.38] M. J. Martínez-Pérez, J. Sesé, F. Luis, R. Córdoba, D. Drung, T. Schurig, E. Bellido, R. de Miguel, C. Gómez Moreno, A. Lostao, and D. Ruiz-Molina, "Ultrasensitive broad band SQUID microsusceptometer for magnetic mmeasurement an very low temperatures," *IEEE Trans. Appl. Supercond.*, vol. 21, no. 3, p. 345, 2011.

[3.39] M. A. AlDamen, S. Cardona-Serra, J. M. Clemente-Juan, E. Coronado, A. Gaita-Arino, C. Martí-Gastaldo, F. Luis, and O. Montero, "Mononuclear lanthanide single molecule magnets based on the polyoxometalates $[Ln(W_5O_{18})_2]^{9-}$ and $[Ln(\beta_2\text{-}SiW_{11}O_{39})_2]^{13-}$ (Ln(III) = Tb, Dy, Ho, Er, Tm, and Yb)," *Inorg. Chem.*, vol. 48, no. 8, p. 3467, 2009.

[3.40] S. Cardona-Serra, J. M. Clemente-Juan, E. Coronado, A. G.-A. no, A. Camón, M. Evangelisti, F. Luis, M. J. Martínez-Pérez, and J. Sesé, "Lanthanoid Single-Ion Magnets Based on Polyoxometalates with a 5-fold Symmetry: The series $[LnP_5W_{30}O_{110}]^{12-}$ (Ln^{3+}=Tb, Dy, Ho, Er, Tm and Yb)," *J. Am. Chem. Soc.*, vol. 134, no. 36, p. 14982, 2012.

[3.41] M. J. Martínez-Pérez, S. Cardona-Serra, C. Schlegel, F. Moro, P. J. Alonso, H. Prima-García, J. M. Clemente-Juan, M. Evangelisti, A. Gaita-Arino, J. Sesé, J. van Slageren, E. Coronado, and F. Luis, "Gd-based single-ion magnets with tunable magnetic anisotropy: Molecular design of spin qubits," *Phys. Rev. Lett.*, vol. 108, no. 24, 2012.

[3.42] K. S. Cole and R. H. Cole, "Dispersion and Absorption in Dielectric - I Alternating Current Characteristics," *J. Chem. Phys.*, vol. 9, p. 341, 1941.

[3.43] K. S. Cole and R. H. Cole, "Dispersion and Absorption in Dielectrics - II Direct Current Characteristics," *J. Chem. Phys.*, vol. 10, p. 98, 1942.

[3.44] D. Drung, C. Hinnrichs, and H. J. Barthelmess, "Low-noise ultra-high-speed dc SQUID readout electronics," *Supercond. Sci. Technol.*, vol. 19, no. 5, p. S235, 2006.

[3.45] C. P. Foley and H. Hilgenkamp, "Why nanoSQUIDs are important: an introduction to the focus issue," *Supercond. Sci. Technol.*, vol. 22, no. 6, 2009.

[3.46] L. Hao, J. C. Macfarlane, J. C. Gallop, D. Cox, J. Beyer, D. Drung, and T. Schurig, "Measurement and noise performance of nano-superconducting-quantum-interference devices fabricated by Focused Ion Beam," *Appl. Phys. Lett.*, vol. 92, no. 19, 2008.

[3.47] C. Granata, E. Espósito, A. Vettoliere, L. Petti, and M. Russo, "An integrated superconductive magnetic nanosensor for high-sensitivity nanoscale applications," *Nanotechnology*, vol. 19, no. 27, 2008.

[3.48] D. Drung, J. H. Storm, F. Ruede, A. Kirste, M. Regin, T. Schurig, A. M. Repollés, J. Sesé, and F. Luis, "Thin-film microsusceptometer with integrated nanoloop," *IEEE Trans. Appl. Supercond.*, vol. 24, no. 4, p. 1600206, 2014.

[3.49] S. Vitale, R. Tommasini, M. Cerdonio, M. Bonaldi, A. Cavalleri, and G. Durin, "Magnetic viscosity, thermal relaxation and thermal equilibrium moise in Co based amorphous alloys at millikelvin temperatures.," *J. Appl. Phys.*, vol. 72, p. 4820, 1992.

[3.50] J. A. J. Burgess, D. C. Fortin, J. E. Losby, D. Grombacher, J. P. Davis, and M. R. Freeman, "Thermally activated decay of magnetic vortices," *Phys. Rev. B*, vol. 82, p. 144403, 2010.

[3.51] R. Zarzuela, S. Vélez, J. M. Hernandez, J. Tejada, and V. Novosad, "Quantum depinning of the magnetic vortex core in micron-size permalloy disks," *Phys. Rev. B*, vol. 85, p. 180401, 2012.

[3.52] T. Shinjo, T. Okuno, R. Hassdorf, K. Shigeto, and T. Ono, "Magnetic vortex core observation in circular dots of permalloy," *Science*, vol. 289, no. 5481, p. 930, 2000.

[3.53] J. M. Hernández, X. X. Zhang, F. Luis, J. Tejada, J. R. Friedman, M. P. Sarachik, and R. Ziolo, "Evidence for resonant tunneling of magnetization in Mn_{12} acetate complex," *Phys. Rev. B*, vol. 55, p. 5858, 1997.

[3.54] T. Lis, "Preparation, structure, and magnetic-properties of a dodecanuclear mixed-valence manganese carboxylate," *Acta Crys. B*, vol. 36, no. SEP, p. 2042, 1980.

[3.55] A. Caneschi, D. Gatteschi, R. Sessoli, A. l. Barra, L. C. Brunel, and M. Guillot, "Alternating-current susceptibility, high-field magnetization, and millimeter band EPR evidence for a ground S = 10 state in $[Mn_{12}O_{12}(CH_3COO)_{16}(H_2O)_4]_2{\cdot}CH_3COOH{\cdot}4H_2O$," *J. Am. Chem. Soc.*, vol. 113, no. 15, p. 5873, 1991.

Chapter 4

Realization of molecular CNOT and SWAP quantum gates

4.1 Introduction

As we have said in the general introduction, qubits are the basic components for quantum computing. They differ from classical bits in that, whereas the bit can only take the states "0" or "1", the qubit can also take a superposition of both:

$$|\psi\rangle = a\,|0\rangle + b\,|1\rangle \tag{4.1}$$

with a and b complex numbers fulfilling $|a|^2 + |b|^2 = 1$.

Once the qubit is defined, the next step is how to operate with one or several of them. In the same way as the logical gates "AND", "OR" and "NOT" form the basis for classical operations over bits, quantum computing has its own set of universal quantum gates (qugates). They must take into account that qubits are not boolean and, then, they must include how to operate with state superpositions. In this chapter, we will study two qugates which operate over two qubits, "SWAP" and "CNOT" whose icons are shown in Fig. 4.1(a).

In a two-qubit system, we can consider the total state as a superposition of the four possible combinations:

$$|\Psi\rangle = c_0\,|00\rangle + c_1\,|01\rangle + c_2\,|10\rangle + c_3\,|11\rangle \tag{4.2}$$

where $c_0^2 + c_1^2 + c_2^2 + c_3^2 = 1$.

The SWAP gate simply exchanges the qubit values. For instance, the states $|00\rangle$ and $|11\rangle$ will not change, whereas the state $|01\rangle$ will be exchanged by $|10\rangle$ and viceversa. This can be expressed as a quantum operator:

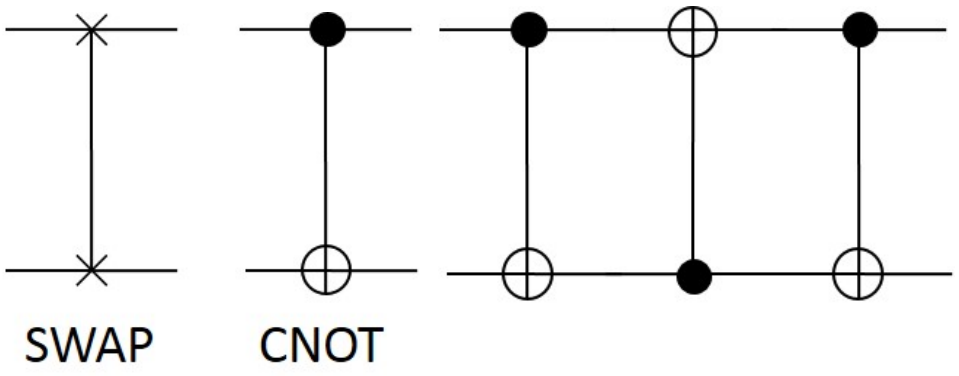

(a) (b)

Figure 4.1: a). SWAP and CNOT icons, commonly used in quantum circuit diagrams. b). SWAP gate obtained from three CNOT gates.

$$\text{SWAP} = \begin{pmatrix} 1 & 0 & 0 & 0 \\ 0 & 0 & 1 & 0 \\ 0 & 1 & 0 & 0 \\ 0 & 0 & 0 & 1 \end{pmatrix}$$

The CNOT gate, or controlled-not gate flips the value of the second qubit if and only if the first one is in state "1". Then, the state $|01\rangle$ will remain unchanged whereas the state $|10\rangle$ will cause the flipping of the second qubit, resulting in the output $|11\rangle$. As an operator:

$$\text{CNOT} = \begin{pmatrix} 1 & 0 & 0 & 0 \\ 0 & 1 & 0 & 0 \\ 0 & 0 & 0 & 1 \\ 0 & 0 & 1 & 0 \end{pmatrix}$$

Both are reversible gates which means that there is always a unique input associated with a unique output and viceversa. The CNOT gate is also a universal two-qubit gate and, therefore, every other two-qubit gate can be obtained from a combination of several CNOT gates [4.1]. As an example, Fig. 4.1(b) shows how to obtain a SWAP gate by using three CNOT gates.

In this chapter we propose Single Molecule Magnets as experimental candidates to carry out the quantum gates SWAP and CNOT.

4.2 Experimental requirements for the realization of quantum gates

Going from quantum computing theory to experimental realization is not easy. It implies managing quantum systems in a controlled manner without disturbing their integrity. To carry out quantum gates for two qubits, a viable proposal should fulfil at least three conditions that we describe below.

4.2.1 Two well defined and coherent qubits

A well defined qubit is a physical system which has two well defined physical states that can act as $|0\rangle$ and $|1\rangle$. A coherent superposition state can be described as a quantum state which keeps well defined amplitudes and phases between the different basis states taking part of the superposition. However, after some time, the state starts to decay. This is normally caused by external interferences such as interaction with the surrounding particles or with the lattice vibrations.

To perform quantum computing, the coherence time of a qubit state (or a entangled state of several qubits) must be longer than the time needed for operating with it. Otherwise it would be impossible to trust the results. In other words, the quantum state must be stable enough to work with it.

4.2.2 Coupling between qubits

Quantum gates normally operate over several qubits. SWAP and CNOT gates, for instance, work over two qubits. To carry out these operations, both qubits must be able to interact with one another.

If we consider two qubits A and B, we can write their quantum state as

$$|\psi\rangle_A = a_0 |0\rangle + a_1 |1\rangle \tag{4.3}$$

$$|\psi\rangle_B = b_0 |0\rangle + b_1 |1\rangle \tag{4.4}$$

where $a_0^2 + a_1^2 = 1$ and $b_0^2 + b_1^2 = 1$.

The quantum state of the whole system can be written in the basis $\{|00\rangle, |01\rangle, |10\rangle, |11\rangle\}$ as

$$|\Psi\rangle = c_0 |00\rangle + c_1 |01\rangle + c_2 |10\rangle + c_3 |11\rangle \tag{4.5}$$

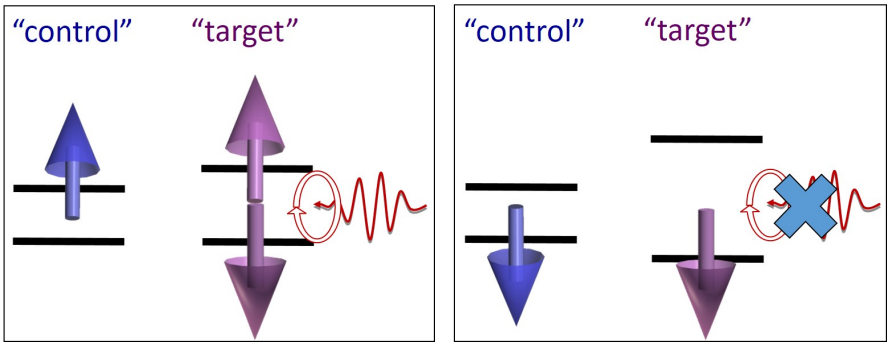

(a) (b)

Figure 4.2: Example of addressability. Thanks to the enranglement, the energy gap of the target qubit depends on the state of the control qubit. a) When the control qubit is $|\uparrow\rangle$ a concrete excitation produces transitions on the target qubit. b) If the control qubit is $|\downarrow\rangle$ the same excitation will not have any effect over the target qubit. Addessability allows also to change the roles and, for another excitation, to use the target qubit as a control qubit and vice versa.

where $c_0^2 + c_1^2 + c_2^2 + c_3^2 = 1$.

$|\Psi\rangle$ is called a "entangled" state if and only can not be written as a product $|\psi_A\rangle \otimes |\psi_B\rangle$. Entangled states let us perform changes over one qubit without acting directly over it. For instance, for the entangled state $|\Psi\rangle = 1/\sqrt{2}\,(|00\rangle + |11\rangle)$ it is possible to set the state of the second qubit just by reading the first one.

Quantum gates are operations over several qubits. Therefore they necessarily give rise to entangled states as part of their operation. For instance, a CNOT operation over an initial state $\frac{1}{\sqrt{2}}\,(|01\rangle + |11\rangle)$, which is not entangled, gives rise to $\frac{1}{\sqrt{2}}\,(|01\rangle + |10\rangle)$, which is entangled.

4.2.3 Addressable qubits

Qubits inside a quantum gate must be distinguishable due to their different functions. For example, qubits in a CNOT have two roles: the first one is called the control qubit and it will always remains unchanged whereas the second one is the target qubit and it could change depending on the state of the control qubit (see Fig. 4.2). These roles could be exchanged depending on the quantum circuit, as we can see in Fig. 4.1(b), and that is why it is so important to know exactly which qubit is being used as control and which one as target during each step.

4.3 Experimental candidates for quantum gates

Over the past two decades numerous experimental candidates have been proposed for the realization of quantum gates realization. We describe here some of them.

4.3.1 NMR on solutions of cytosine in D_2O

One of the first experimental implementations consisted of the application of nuclear magnetic resonance (NMR) to a solution of pyrimidine base cytosine in D_2O [4.2]. There, the rapid exchange of the two amine protons and the single amide proton, together with the solvent deuteron, forms an isolated system of two-coupled spins each of them acting as a qubit.

Operating at radio-frequencies it is possible to make transitions between energy levels using selective pulses and pass from the input state to the desired output state. The read out is carried out by NMR which is a non - invasive technique.

The imperfect selective pulses, together with the almost impossible initialization of the nuclear spin states are the main disadvantages of this proposal.

4.3.2 Optical cavities

Optical cavities use the polarization states of a single photon as qubit states [4.7]. Each photon is isolated in an optical net of cavities, created by the interference of two laser beams. The qubit is first encoded in a polarization state. Then it is injected as the input state into an optical parametric amplifier and excited by a pulsed ultraviolet laser beam. Qugate operation works via stimulated emission.

4.3.3 Ionic traps

This method uses ions trapped by electric and/or magnetic forces into 1D or 2D arrays (or Paul traps) and cooled by laser beams [4.8]. Under these conditions, ions have stable energy levels, which can be treated as effective spins. Two electronic or hyperfine states can be used to store a bit of quantum information. This information can be processed by resonant laser or radiofrequency pulses, focused on a given ion and transferred by inducing a collective movement of some ions in the trap, which modify their mutual Coulomb forces.

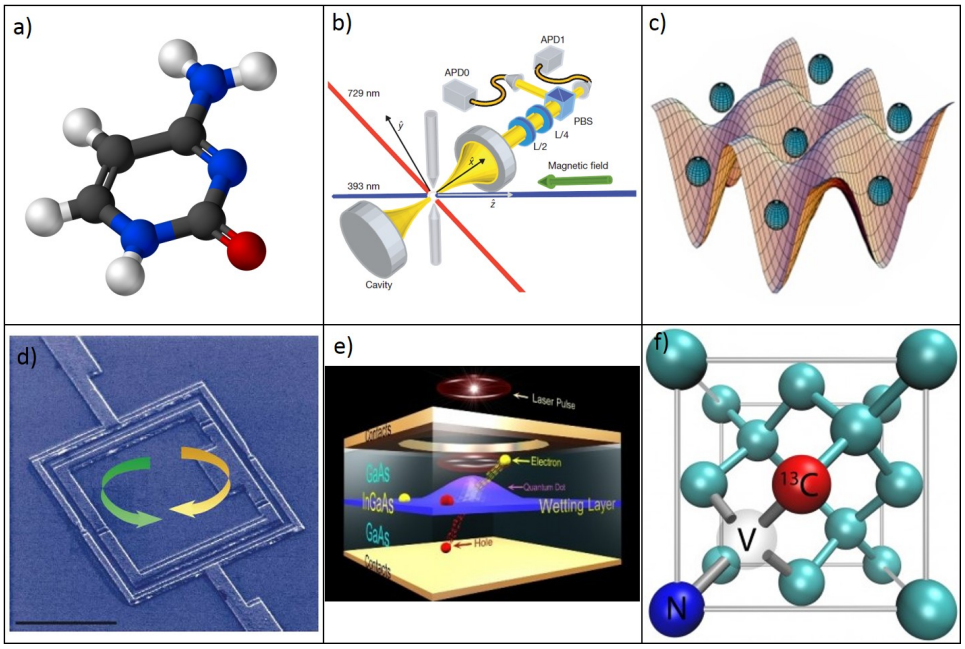

Figure 4.3: a). Cytosine molecule used in NMR quantum computers. Image from [4.3]. b). Confinement of a photon into an optic cavity. Image from [4.4]. c). Picture of ions trapped into electromagnetic Paul traps. Imagen from Ivan H. Deutsch. d). Superconducting qubit. Image from [4.5]. e). Picture of a quantum dot, made of InGaAs into a GaAs structure. f). Nitrogen-vacancy center. Image from [4.6].

If the radial trapped frequency is large enough, spin-spin interaction can be controlled with laser beams. Qubits can be initialized by exciting the trap with lasers, propagating along a certain direction α. Entanglement will depend on the alignment of α with the effective spins.

Using this method, it has been possible to entangle up to six qubits [4.9], made of Be^{2+} ions and simulate a quantum magnet with two trapped Mn^{+} ions in a lineal Paul trap [4.10].

4.3.4 Superconducting qubits

The macroscopic quantum behaviour of superconductors makes it possible the realization of coherent qubits in artificially fabricated superconducting structures [4.11]. They consist of superconducting loops interrupted by Josephson junctions (typically one or three junctions [4.12]) in the same way as SQUID sensors. The two lowest energy states have supercurrents rotating in opposite directions and can be used as qubit states.

The energy gap can be controlled by the coupled magnetic flux and it is possible to change the qubit state by applying resonant microwave pulses. Using quantum electrodynamic devices (QED), consisting of resonant cavities [4.5], operations can be performed on individual superconducting qubits. Coherence times are in the order of ms. Using the same architecture, different superconducting qubits can be coherently coupled via radiofrequency photon buses [4.13].

4.3.5 Semiconductor quantum dots

Quantum dots are based on charge carriers confined in the three dimensions by electrical gating and/or etching techniques [4.14]. The dimension of these dots is on the order of the Fermi wavelength (about 10 nm) which produces discrete energy levels for the electrons or holes allocated into them. The most common material for the fabrication of these "qubits" is GaAs.

The number of electrons into each dot is tunable from zero to some of them. The use of just one electron per dot allows a pure 1/2 spin. Entanglement is created by Coulomb interaction and Pauli exclusion principle. The electronic wavefunctions of the dots overlap strongly due to this interaction [4.15].

Quantum dots are also very easy to excite optically and the states can be measured with non - invasive spectroscopic methods. Coherent times are of the order of ms whereas operation times only require ps.

4.3.6 Nitrogen-vacancy centers in diamond

Another solid state proposal takes advantage of some special characteristics of diamond whose energy gap between the lattice ground energy level and the first excited is enormous. A nitrogen-vacancy center consists of a carbon vacancy and an adjacent substitutional nitrogen impurity [4.16]. An unpaired paramagnetic electron is then captured from the bulk and can be used as a qubit.

The spin can be polarized by optical pumping. It also exists a fluorescent transition between the spin states, that can be measured giving access to reading-out the qubit state. The wide band gap in the lattice allows also a very high coherence time due to the weak spin-lattice interaction.

4.3.7 Single Molecule Magnets

Single Molecule Magnets (SMM) [4.17] are molecular nanomagnets composed of a discrete number of spins which are paramagnetic at room temperature although they can store information at low temperatures. Its chemical structure consists of very few atoms, isolated from the environment by a shield of organic ligands. Spins themselves can act as qubits that can flip by tunneling [4.18–4.20]. This quantum phenomenon in mesoscopic size objects was observed for the very first time in a Mn_{12} SMM.

Tunneling is associated to discrete energy levels, i.e. to different quantum states. Applying a magnetic field, it is then possible to manipulate the qubit to be in state $|0\rangle$, $|1\rangle$ or in a superposition of both.

The molecule that aroused the interest for SMM was the Mn_{12} acetate cluster, already described in section 3.7.6, which shows magnetic hysteresis at low temperatures [4.21] and, therefore, the possibility of storing information. Suitable qubit candidates must have a high magnetic anisotropy so that, at low temperatures, only the ground state and a first excited state are populated. In this thesis we have studied the suitability of some of these molecules to build qubits and qugates.

4.4 Synthesis and main characteristics of spin dimers

Among the large amount of different single molecule magnets, we have chosen a small family of compounds, based on pairs of lanthanide ions, to carry out quantum operations with them. We will call them spin dimers, or just dimers,

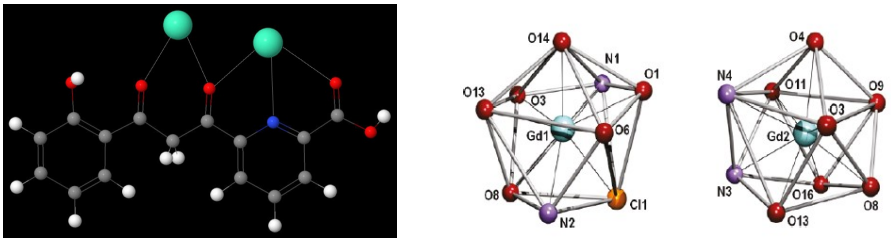

(a) (b)

Figure 4.4: a). H_3L ligand formed by carbon (in grey), hydrogen (in white), oxygen (in red) and nitrogen (in blue). Lanthanides (in turquoise) are placed where it is shown. b). Local coordination of the lanthanides inside the dimer. Both sites have different composition and size. The right pocket is bigger than the left one.

and label them as LnLn', where Ln is substituted by the corresponding lanthanide.

4.4.1 Synthesis and architecture of spin dimers

Lanthanides have unique spectroscopic and electronic properties which make them suitable candidates to act as qubits. Although their spin differs from 1/2, most of them have a strong anisotropy and, at sufficiently low temperatures, magnetic clusters made of lanthanides present a ground-state doublet, well separated from the excited levels. This fact provides a good definition of qubits for these magnetic clusters.

In this chapter we are interested in two-qubit gates and, therefore, it is necessary to count on a non-magnetic molecular architecture which can host two dissimilar qubits exhibiting weak interaction. The group of Guillem Aromí and David Aguilà from the Department of Inorganic Chemistry of the University of Barcelona has developed a new organic ligand that fulfils this condition [4.22]. The ligand (6-3-oxo-3-(2-hydroxyphenyl) - propionyl)- 2 - pyridinecarboxilic acid, commonly named H_3L, is designed to allocate two lanthanides in an asymmetrical configuration, as shown in Fig. 4.4(a).

Dimers are synthesized using H_3L ligands and LnX_3 salts, where Ln^{3+} is a lanthanide ion and X^- can be either Cl^- or NO_3^-. Independently of the salt anion, all the compounds have very similar molecular structures, consisting of an organic shield with two 9-coordinated pockets where the two lanthanides are allocated. As it can be observed in Fig. 4.4(b), the first pocket has an irregular shape and it contains the Cl^- or NO_3^- coming from the lanthanide salt. The second one can be identified with a distorted capped square antiprism where there is a water molecule instead of the salt anions.

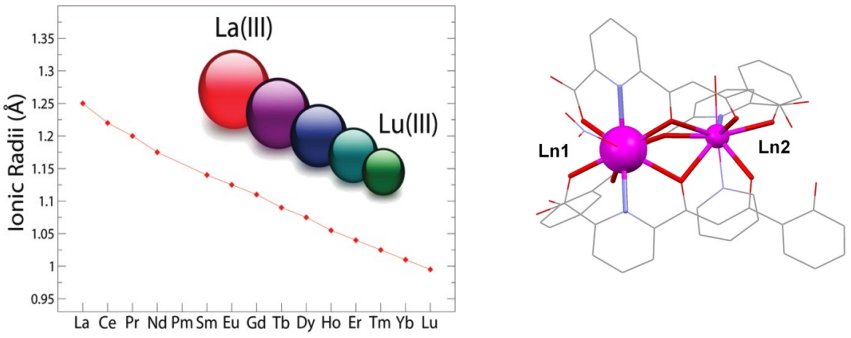

(a) (b)

Figure 4.5: a). Ionic radii of the lanthanide series. It allows to know previously where each ion will be allocated: the largest ion will be placed in the biggest pocket whereas the smallest one will be in the smallest pocket. b). Molecular structure of the dimers described in this chapter.

The asymmetry of the pockets also determines their size and, therefore, one is larger than the other. Considering that the ionic radii of the complete series of lanthanide decrease with the atomic number (see Fig. 4.5(a)) and that no lanthanide ion is equal in size to any other, it is possible to create heteronuclear dimers and selectively choose the position of different lanthanides on intended locations within the same molecule.

Lanthanides are linked to the organic ligand shield by three oxygen atoms and hydrogen bonds. Figure 4.5(b) shows the structure of the whole molecule.

4.4.2 Study of lattice and non magnetic behaviour. Heat capacity measurements

The versatile design of lanthanide dimers allows us to prepare molecules with a large number of combinations of two $4f$ metals in function of our interests. Thus, it is possible to study the non magnetic behaviour of the cluster by choosing two non-magnetic elements, such as a YLa dimer, or the magnetic behaviour of just one qubit by combining it with Lanthanum, Lutetium or Yttrium, also non-magnetic.

Specific heat data c_p measured at zero field on powder samples, enables us to explore if the molecular structure remains the same for all these situations. Figure 4.6 shows c_p measurements for a wide variety of dimers, including "homonuclear" dimers (Ce_2, Gd_2, Er_2 and Tb_2), "heteronuclear" dimers (ErCe), dimers with just one magnetic ion (ErLa and YCe) and the non-magnetic dimer (YLa).

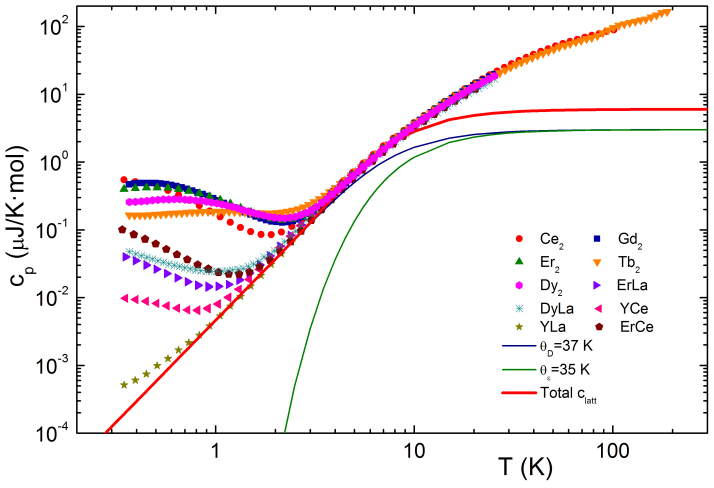

Figure 4.6: Specific heat of several dimers measured at zero field. The non-magnetic dimer YLa owns its specific heat just to the lattice vibrations and can be subtracted from the specific heat of the other compounds in order to obtain the magnetic specific heat, associated to electronic and nuclear spin levels. Lines correspond to the fit of Debye and Eistein models to account for the lattice contribution.

At temperatures above 3 K, c_{p} is dominated by the specific heat c_{latt} arising from lattice vibrations and all measurements are coincident, as it is expected for molecules with approximately the same structure. c_{latt} can be fitted using a model that includes a Debye function,

$$c_{\mathrm{D}} = 9\left(\frac{T}{\theta_{\mathrm{D}}}\right)^3 \int_0^{T/\theta_{\mathrm{D}}} \frac{x^4 \mathrm{e}^x dx}{(\mathrm{e}^x - 1)^2} \tag{4.6}$$

where T is the temperature and $\theta_{\mathrm{D}} = 37$ K is the Debye temperature, and an Einstein function,

$$c_\epsilon = 3\left(\frac{\theta_\epsilon}{T}\right)^3 \frac{\mathrm{e}^{\theta_\epsilon/T}}{\left(\mathrm{e}^{\theta_\epsilon/T} - 1\right)^2} \tag{4.7}$$

where $\theta_\epsilon = 35$ K is the Einstein temperature. These models account for the specific heat arising from acoustic phonon modes (Debye model) and internal vibrational modes (Einstein model) of each molecule.

Below 3 K, the specific heat shows additional contributions which can be associated with electronic and nuclear spin levels. In "homonuclear" dimers, Schottky anomalies, typical of two-level systems, are clearly observed. In the others, specific heat grows when temperature goes down but no peaks can be observed. YLa, does not grow, as it is supposed to do for a non magnetic clus-

ter. The data for YLa correspond, therefore, to the pure lattice contribution and will be used to extract the magnetic contribution c_{m} of the rest of dimers by simply subtracting it,

$$c_{\mathrm{m}} = c_{\mathrm{p}} - c_{\mathrm{YLa}} \tag{4.8}$$

In the remainder of this chapter we focus on two specific dimers: Tb_2 to study a qugate where qubits are distinguishable due to the asymmetric structure and ErCe to study a qugate with different lanthanide ions as qubits.

4.5 Theoretical model

4.5.1 Spin Hamiltonian

To study these dimers, we have used a general spin Hamiltonian for two angular momenta $\vec{J}_1$ and $\vec{J}_2$, coupled via an exchange interaction that is weaker than the crystal field interaction. To formulate this, we need a Hamiltonian which includes local terms for each ion $\mathcal{H}_i$ and another accounting for the interaction between them $\mathcal{H}_{12}$:

$$\mathcal{H} = \mathcal{H}_1 + \mathcal{H}_2 + \mathcal{H}_{12} \tag{4.9}$$

Using the fact that $\mathcal{H}_{12} \ll \mathcal{H}_1, \mathcal{H}_2$, we can apply perturbation theory and consider in zero-order approximation the Hamiltonian of each ion, which has three terms: the crystal field term, the Zeeman term and the hyperfine interaction term.

Crystal field interaction term

This term is related to the anisotropy of each single ion, which mainly depends on the crystal lattice that surrounds it. It can be expressed as

$$\mathcal{H}_{\mathrm{cf}_i} = \sum_{p} \sum_{q=-p}^{p} B_p^q(r) O_p^q(\vec{J}_i) \tag{4.10}$$

where B_p^q are the anisotropy parameters and O_p^q, also called Stevens's operators [4.23], are q-order polynomials of J_x, J_y and J_z operators. B_p^q parameters depend on the molecular symmetry and structure. In the simplest cases, only the parameters B_2^0 and B_2^2 are non-zero or, at least, totally dominant over the

rest of parameters. Then we can rewrite the spin Hamiltonian in a simpler form,

$$\mathcal{H}_{\mathrm{cf}_i} = D\left(J_{iz}^2 - \frac{1}{3}S(S+1)\right) + E\left(J_{ix}^2 + J_{iy}^2\right) \tag{4.11}$$

where $D = 3B_2^0$ and $E = B_2^2$, $i = 1, 2$.

Zeeman interaction term

It describes the interaction of the ion magnetic moment with an external magnetic field $\vec{H}$:

$$\mathcal{H}_{\mathrm{Ze}_i} = -g_J\mu_{\mathrm{B}}\vec{H}\vec{J}_i = -g_J\mu_{\mathrm{B}}\left(H_xJ_{ix} + H_yJ_{iy} + H_zJ_{iz}\right) \tag{4.12}$$

where $\mu_{\mathrm{B}} = 9.274 \times 10^{-24}$ J/T is the Bohr magneton.

Hyperfine interaction term

It describes the interaction between the electronic spin $\vec{J}$ and the nuclear spin $\vec{I}$,

$$\mathcal{H}_{\mathrm{hf}_i} = A_J\vec{J}_i\vec{I}_i \tag{4.13}$$

where A_J is the hyperfine interaction constant.

Spin-spin coupling term

It consists of a term that describes the coupling between both ions,

$$\mathcal{H}_{12} = \vec{J}_1\widetilde{C}\vec{J}_2 \tag{4.14}$$

where $\widetilde{C}$ is a second rank tensor.

The total Hamiltonian can therefore be written as

$$\mathcal{H} = \mathcal{H}_1 + \mathcal{H}_2 + \mathcal{H}_{12} \tag{4.15}$$

where

$$\mathcal{H}_i = \mathcal{H}_{\mathrm{cf}_i} + \mathcal{H}_{\mathrm{hf}_i} + \mathcal{H}_{\mathrm{Ze}_i} \tag{4.16}$$

with $i = 1, 2$, is the spin Hamiltonian for a single qubit. We consider now the difference between Kramers and no-Kramers ions.

4.5.2 Kramers ions

If both ions are Kramers the levels are at least double degenerated at zero field. If there are not additional degeneracies, the ground level defines a two dimensional subspace. For any state Φ of this subspace, the pair $\{\Phi, T\Phi\}$, where T is the time-reversal operator, defines a suitable basis. If the energy splitting Δ between the ground and first excited Kramer doublets is large enough in comparison to the thermal energy and the Zeeman splitting, the magnetic response of each free ion can be described with an effective spin $S = 1/2$ in a magnetic field using an anisotropic $\widetilde{g}$ tensor,

$$\mathcal{H}_S = \mu_{\mathrm{B}} \vec{H} \widetilde{g} \vec{S} \tag{4.17}$$

This Hamiltonian replaces both terms, $\mathcal{H}_{\mathrm{cf}}$ and $\mathcal{H}_{\mathrm{Ze}}$.

For two lanthanide Kramers ions, named "1" and "2", with a weak interaction between them, the solutions in zero-order approximation would be $|\psi\rangle = |\Phi_1\rangle \otimes |\Phi_2\rangle$, where $\mathcal{H}_i |\Phi_i\rangle = E_i |\Phi_i\rangle$ $(i = 1, 2)$ and have energies $E = E_1 + E_2$. We can define a suitable basis for the system of two ions as

$$\begin{pmatrix} \Phi_1 \\ T\Phi_1 \end{pmatrix} (\Phi_2 \; T\Phi_2) = \{|\Phi_1\rangle \otimes |\Phi_2\rangle, |\Phi_1\rangle \otimes |T\Phi_2\rangle, |T\Phi_1\rangle \otimes |\Phi_2\rangle, |T\Phi_1\rangle \otimes |T\Phi_2\rangle\} \tag{4.18}$$

Mutual interaction term

Let us consider now the mutual interaction Hamiltonian, which can be dipole-dipole interaction and/or exchange interaction, as a first order perturbation of the two free ions Hamiltonian,

$$\mathcal{H}_{12} = \vec{J}_1 \widetilde{C} \vec{J}_2 \tag{4.19}$$

where $\widetilde{C}$ is a second rank tensor that relates both doublets.

By using first-order perturbation theory, the energy eigenstates of the whole Hamiltonian can be written as a linear combination of the states of the basis given in Eq. (4.18). These states are used for describing a system with two effective spins $S_1 = S_2 = 1/2$ and, therefore, it would be useful to write $\mathcal{H}_{12}$ in terms of them. Considering the correspondence $g_J \vec{J} = \widetilde{g} \vec{S}$ we can rewrite,

$$\mathcal{H}_{S_{12}} = \vec{S}_1 \widetilde{D} \vec{S}_2 \tag{4.20}$$

where

$$\widetilde{D} = \frac{\widetilde{g}_1 \widetilde{C} \widetilde{g}_2}{g_{J1} g_{J_2}} \tag{4.21}$$

is a coupling tensor [4.24].

The whole Hamiltonian can then be written in terms of two effective spins $S = 1/2$ and their respective anisotropic $\widetilde{g}$ tensors,

$$\mathcal{H} = \mathcal{H}_1 + \mathcal{H}_2 + \mathcal{H}_{12} = \mu_{\mathrm{B}} \vec{H} \widetilde{g_1} \vec{S}_1 + \mu_{\mathrm{B}} \vec{H} \widetilde{g_2} \vec{S}_2 + \vec{S}_1 \widetilde{D} \vec{S}_2 \tag{4.22}$$

$\widetilde{D}$ is normally a non-symmetric tensor. Nevertheless, if we consider that $\widetilde{C}$ is an scalar, it becomes symmetric.

We will also consider that the principal axes of $\widetilde{g_1}$ and $\widetilde{g_2}$ can be misaligned, as a result of the different local coordination of the two lanthanide sites. EPR spectra provide information about the principal values of $\widetilde{g}$ [4.25]. Unfortunately, only absolute values can be obtained from conventional EPR experiments. The sign of the product of the three principal values can be determined by using polarized microwaves [4.26] although other measurements and simulations will be necessary to assign the sign of each value.

4.5.3 Non-Kramers ions

For a non-Kramers ion, all states can be nondegenerate. For the ground state doublet it can be shown that the g-factor matrix can only have one non-zero principal value, g_z [4.26,4.27]. The same argument is also valid for the hyperfine interaction. Thus, we can rewrite,

$$\mathcal{H}_{\mathrm{hf}_i} = A_J J_{iz} I_{iz} \tag{4.23}$$

$$\mathcal{H}_{\mathrm{Ze}_i} = -g_z \mu_{\mathrm{B}} J_{iz} H_{iz} + \Delta J_x \tag{4.24}$$

Here, the z axes of both ions might not be aligned, as shown in Fig. 4.7, and, therefore, the projection of $\vec{H}$ over each one can be different. In spherical coordinates, an applied field in an arbitrary direction (θ, ϕ) with respect to the general frame (xyz) will be "seen" by the individual frames $(xyz)_1$ and $(xyz)_2$ as:

$$\begin{aligned} \vec{H}_1 &= H(\sin\theta\cos\phi, \sin\theta\sin\phi, \cos\theta) \\ \vec{H}_2 &= H(\sin\theta\cos\phi, \sin\theta\sin\phi - \cos\theta\sin\delta, \cos\theta\cos\delta + \sin\theta\sin\phi\sin\delta) \end{aligned} \tag{4.25}$$

Δ is a numerical coefficient related to a zero-field, or quantum tunnel, splitting. Although $\Delta \neq 0$ we consider in the further discussion that it can be neglected, leading to

$$\mathcal{H}_{\mathrm{cf}_i} = -D J_{iz}^2 \tag{4.26}$$

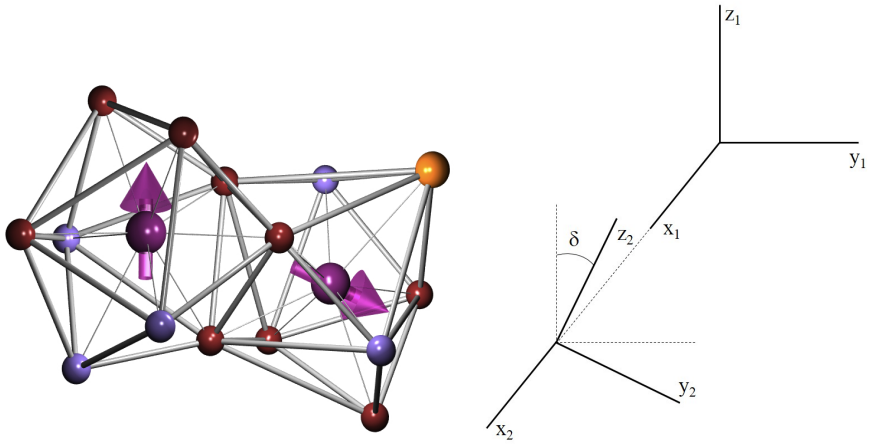

(a) (b)

Figure 4.7: a). Dimer structure considering the misalignment of the z axes. b). Reference frame for theoretical calculations. y and z axis of the second atom are rotated in the xy plane.

This simplified version of the spin Hamiltonian for a non-Kramers ion is diagonal and can be solved analytically. It is not trivial, however, that the exchange Hamiltonian $\mathcal{H}_{12}$ can be simplified in terms of J_z. For simplicity we consider $\widetilde{C}$ as an scalar and therefore,

$$\mathcal{H}_{12} = -2J_{\text{ex}}\vec{J}_1\vec{J}_2 \tag{4.27}$$

where $\widetilde{C} = -2J_{\text{ex}}$.

$\mathcal{H}$ can also be rewritten as a Hamiltonian with an effective spin $S = 1/2$ by simply rescaling D, J_{ex}, A_J and g_z, all of them scalar values.

4.5.4 Partition function and observables

We are interested in obtaining magnetic susceptibility, magnetization and specific heat from $\mathcal{H}$. Any of them can be extracted from partial derivatives of the partition function $\mathcal{Z}$, defined as

$$\mathcal{Z} = \text{Tr}\left(\text{e}^{-\beta\mathcal{H}}\right) = \sum_n \text{e}^{-\beta E_{\text{n}}} \tag{4.28}$$

where $\beta = 1/k_{\text{B}}T$, being $k_{\text{B}} = 1.38 \cdot 10^{-23}$ J/K the Boltzmann constant, and E_{n} are the eigenvalues of $\mathcal{H}$, i.e. $\mathcal{H}\left|\epsilon_{\text{n}}\right\rangle = E_{\text{n}}\left|\epsilon_{\text{n}}\right\rangle$.

Magnetization can, therefore, be extracted from $\mathcal{Z}$, as

$$M = \frac{1}{\beta}\frac{\partial \ln \mathcal{Z}}{\partial H} = \frac{1}{\beta \mathcal{Z}}\frac{\partial \mathcal{Z}}{\partial H} \tag{4.29}$$

Linear magnetic susceptibility is obtained from magnetization,

$$\chi = \frac{\partial M}{\partial H} = \frac{1}{\beta}\left[\frac{1}{\mathcal{Z}}\frac{\partial^2 \mathcal{Z}}{\partial H^2} - \left(\frac{\partial \mathcal{Z}}{\partial H}\right)^2\right] \tag{4.30}$$

Specific heat can be calculated as

$$c = \frac{1}{\beta}\frac{\partial^2 (T \ln \mathcal{Z})}{\partial T^2} = \frac{1}{\beta}\frac{\partial}{\partial T}\left(\ln \mathcal{Z} + \frac{T}{\mathcal{Z}}\frac{\partial \mathcal{Z}}{\partial T}\right) = \frac{1}{\beta \mathcal{Z}}\left[2\frac{\partial \mathcal{Z}}{\partial T} + T\frac{\partial^2 \mathcal{Z}}{\partial T^2} - \frac{T}{\mathcal{Z}}\left(\frac{\partial \mathcal{Z}}{\partial T}\right)^2\right] \tag{4.31}$$

For powdered samples, it is also necessary to average all these quantities,

$$\overline{A} = \frac{\int_0^{\pi}\int_0^{2\pi} A \sin\theta d\phi d\theta}{\int_0^{\pi}\int_0^{2\pi} A \sin\theta d\phi d\theta} = \frac{1}{4\pi}\int_0^{\pi}\int_0^{2\pi} A \sin\theta d\phi d\theta \tag{4.32}$$

due to the aleatory distribution of the anisotropy axis for each molecule.

High temperature approximation

At sufficiently high temperatures, when $k_{\mathrm{B}}T \gg \left|\widetilde{C}\right| J^2, A_J IJ$ the two ions are uncoupled and hyperfine couplings are negligible. Then, the Hamiltonian can be approximated to

$$\mathcal{H}_{\mathrm{HT}} = \mathcal{H}_{\mathrm{cf}} + \mathcal{H}_{\mathrm{Ze}} \tag{4.33}$$

For free Kramers ions, the dependence of the susceptibility on temperature can be described using Van Vleck's general formalism [4.28,4.29]. χT increases with increasing T, showing the gradual population of the excited Kramers doublets. When only the ground and first excited doublets are populated, Van Vleck's expression can be written in terms of the energy gap Ω between both energy levels as [4.30],

$$\chi T \approx \frac{N_{\mathrm{A}}\mu_{\mathrm{B}}^2 S^2}{k_{\mathrm{B}}}\left[C_0 + C_1\frac{2}{\beta\Omega}\tanh\left(\frac{\beta\Omega}{2}\right) + C_2\tanh\left(\frac{\beta\Omega}{2}\right)\right] \tag{4.34}$$

where C_0,C_1 and C_2 are numerical coefficients that depend on the electronic structure of each doublet, $N_{\mathrm{A}} = 6.022 \times 10^{23}$ is the Avogadro number and $\beta = (k_{\mathrm{B}}T)^{-1}$.

For free non-Kramers ions, the Hamiltonian is diagonal and the averaged susceptibility can be written as the analytical formula [4.28],

$$\overline{\chi} = \frac{2N_{\mathrm{A}}g^2\mu_{\mathrm{B}}^2 J}{3k_{\mathrm{B}}T}\left(J + \frac{2}{\beta\Omega}\frac{1-\mathrm{e}^{-\beta\Omega}}{1+\mathrm{e}^{-\beta\Omega}}\right) \tag{4.35}$$

with $\Omega = D\,(2J-1)$. This expression has only one free parameter, which is the magnetic anisotropy constant D, defined above (see Eq. (4.11)).

For specific heat, at high temperatures it coincides with the lattice specific heat, as we have already pointed out in section 4.4.2.

Low temperature approximation

In the low temperature regime, only the ground state doublet is populated, and therefore, only two energy eigenstates must be taken into account, in order to calculate susceptibility and specific heat.

For Kramers ions, the resulting Hamiltonian is not diagonal due to the existence of non-zero g_x and g_y. The susceptibility can be approximated to

$$\chi = \frac{N_{\mathrm{A}}\mu_{\mathrm{B}}^2}{k_{\mathrm{B}}T}\left\langle g^2\right\rangle S^2 \tag{4.36}$$

where $\left\langle g^2\right\rangle = \frac{g_x^2+g_y^2+g_z^2}{3}$.

For non-Kramers ions and for not too large magnetic field, only states with $J_{\mathrm{z}} = \pm J$ are populated. Therefore $\mathcal{H}_{\mathrm{cf}} = -2DJ^2$ is constant and can be removed from the total Hamiltonian. The only states that remain are the states $|\pm J\rangle\,|m_{I_z}\rangle$, where m_{I_z} is the projection of the nuclear spin over the z axis.

The Hamiltonian can be then rewritten as

$$\mathcal{H}_{LT} = -g\mu_{\mathrm{B}}J\,(h_{z,1}\sigma_{z,1} + h_{z,2}\sigma_{z,2}) - 2J_{\mathrm{ex}}J^2\sigma_{z,1}\sigma_{z,2} + A_J J\,(\sigma_{z,1}I_{z,1} + \sigma_{z,2}I_{z,2}) \tag{4.37}$$

with $\sigma_{z,j}$ the standard Pauli matrix $\sigma_z\,|\pm J\rangle = \pm\,|\pm J\rangle$ and $h_{z,1}$, $h_{z,2}$ the external magnetic field projection over z_1 and z_2 respectively (third coordinate from Eqs. (4.25)).

$\mathcal{H}_{\mathrm{LT}}$ is diagonal in the basis $\left\{|\pm J,\pm J\rangle\left|m_{I_z},m'_{I_z}\right\rangle\right\}$ and, therefore, the partition function is immediate

$$\mathcal{Z}=\sum_{\substack{j_1,\,j_2\\ m_{I_{z,1}},\,m_{I_{z,1}}}}\mathrm{e}^{-\beta\left[g\mu_{\mathrm{B}}J(j_1h_{z,1}+j_2h_{z,2})-2J_{\mathrm{ex}}J^2j_1j_2+A_JJ\left(j_1m_{I_{z,1}}+j_2m_{I_{z,2}}\right)\right]} \tag{4.38}$$

where $j_i=-1,+1$, for $J_{z,i}=-J,+J$ respectively and m_I goes from $-I$ to $+I$. Using Eqs. (4.29), (4.30) and (4.31), M, χ and c can be analytically computed in the low temperature limit.

To calculate magnetization and susceptibility, Hamiltonian can be simplified even more due to the fact that hyperfine interaction does not depend on magnetic field and it disappears with the derivatives. We can then write

$$\mathcal{H}_{\mathrm{mag}}=-g\mu_{\mathrm{B}}J\left(h_{z,1}\sigma_{z,1}+h_{z,2}\sigma_{z,2}\right)-2J_{\mathrm{ex}}J^2\sigma_{z,1}\sigma_{z,2} \tag{4.39}$$

This Hamiltonian is analogue to a Hamiltonian of two $1/2$ spins whose axis are misaligned. Energy levels can be written in the basis $\{|\pm J,\pm J\rangle\}$ as

$$\begin{aligned}
E_{|1,1\rangle}&=-g\mu_{\mathrm{B}}JH\left(\cos\theta\left(1+\cos\delta\right)+\sin\theta\sin\phi\sin\delta\right)-2J_{\mathrm{ex}}J^2\\
E_{|1,-1\rangle}&=-g\mu_{\mathrm{B}}JH\left(\cos\theta\left(1-\cos\delta\right)-\sin\theta\sin\phi\sin\delta\right)+2J_{\mathrm{ex}}J^2\\
E_{|-1,1\rangle}&=-g\mu_{\mathrm{B}}JH\left(\cos\theta\left(-1+\cos\delta\right)+\sin\theta\sin\phi\sin\delta\right)+2J_{\mathrm{ex}}J^2\\
E_{|-1,-1\rangle}&=-g\mu_{\mathrm{B}}JH\left(\cos\theta\left(-1-\cos\delta\right)-\sin\theta\sin\phi\sin\delta\right)-2J_{\mathrm{ex}}J^2
\end{aligned} \tag{4.40}$$

Calculating Eqs. (4.29) and (4.30) with $\mathcal{H}_{\mathrm{mag}}$ and averaging according to Eq. (4.32) enables finding an analytical expression for $\overline{\chi}$:

$$\overline{\chi}=\frac{2}{3}\frac{g^2\mu_{\mathrm{B}}^2J^2}{k_{\mathrm{B}}T}\left(1+\cos\delta\tanh\left(2\beta J_{\mathrm{ex}}J^2\right)\right) \tag{4.41}$$

Using J_{ex} from specific heat at zero field and the above analytical formula it is possible to fit the susceptibility curves and obtain the angle δ.

Concerning specific heat at zero field, $\mathcal{H}_{\mathrm{Ze}}=0$, and if $\left|\widetilde{C}\right|>A_J$, the system presents two coupled energy levels, a ferromagnetic $|\pm m_J,\pm m_J\rangle$ and an antiferromagnetic $|\pm m_J,\mp m_J\rangle$ state. For a two-level system, magnetic specific heat c_{m}, which is dominant, shows a Schottky-type anomaly [4.31],

$$c_{\mathrm{m}}=\Delta E^2\beta^2\frac{\mathrm{e}^{-\beta\Delta E}}{\left(1+\mathrm{e}^{-\beta\Delta E/2}\right)^2} \tag{4.42}$$

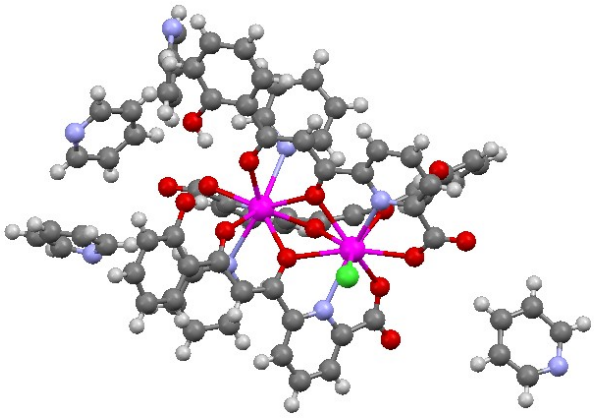

Figure 4.8: Tb_2 dimer. White atoms are hydrogen, grey atoms are carbon, lilac atoms are nitrogen, red atoms are oxygen, green atom is chlorine and magenta atoms are the two Tb ions.

where $\Delta E \cong \left|\widetilde{C}\right| J^2$ is the energy difference between both levels. The maximum fulfills the condition $k_{\mathrm{B}}T = 0.42\Delta E$.

In this temperature regime, the lattice contribution to the specific heat is negligible and can in any case be obtained from non-magnetic dimers. On the other hand, the hyperfine contribution may slightly change the shape of the Schottky anomaly. For this reason, although Eq. (4.42) can be used at first sight to obtain ΔE, to properly fit experimental data, numerical computing is used to calculate c_{m}.

4.6 Experimental study of molecular qugates with asymmetrical environment. Non-Kramers case: Tb_2

4.6.1 Main characteristics of a Tb_2 dimer

The first molecule to be studied is a "homonuclear" dimer with two identical Tb^{3+} ions, whose molecular structure is shown in Fig. 4.8. It is formed from H_3L ligands and a $TbCl_3$ salt.

Among the different "homonuclear" dimers, we have chosen Tb_2 because of the large angular momentum $J = 6$ that Tb^{3+} ions possess. Thanks to

this, the effect of the magnetic asymmetry can be easier to determine. Tb^{3+} is a non-Kramers ion, which means that we can use the diagonal Hamiltonian, described in section 4.5.3. Due to the unequivalent coordinations of both ions, we will consider in the following subsections that their anisotropy axes are not aligned, as shown in Fig. 4.7. Any misalignment can change the way the magnetic field is coupled to each ion and, thus, ions can be distinguishable.

Other properties of Tb^{3+} ions, which are relevant for this section are tabulated in table 4.1.

Magnitude	Nomenclature	Tb^{3+}
Total angular momentum	J	6
Nuclear spin	I	3/2
Gyromagnetic ratio	g_J	3/2
Hyperfine constant	A_J/k_B	0.025 K

Table 4.1: Main properties of Tb^{3+}.

4.6.2 Magnetic susceptibility and specific heat measurements

As we have seen above, susceptibility and specific heat measurements allow us to find the three unknown parameters of $\mathcal{H}$: the anisotropy constant D, the exchange interaction J_{ex} and the misalignment δ between the anisotropy axes $\widehat{z}_1$ and $\widehat{z}_2$.

Figure 4.9 shows the in-phase susceptibility measurement, which gives the equilibrium paramagnetic response. We can observe two different drops, a small one at high temperatures and a large one for low temperatures. Here we can define μ_{eff} from χT equations as

$$\chi T = \frac{N_A}{3k_B}\mu_{eff}^2 \tag{4.43}$$

where μ_{eff} depends on the spin coupling.

Above $T \approx= 100$ K, $\mu_{eff} \approx \sqrt{3k_B\chi T/N_A} \approx 13.7(1)\mu_B$. This agrees with the effective moment of two uncoupled free ions,

$$\mu_{eff} = g_J\mu_B\sqrt{2J(J+1)} = 13.74\mu_B \tag{4.44}$$

At lower temperatures, $10 \leq T \leq 100$ K, a drop is observed. This can be assigned to the thermal depopulation of excited magnetic energy levels. Between 3 K and 10 K, $\mu_{eff} \approx 12.5(1)\mu_B$, close to the effective moment of

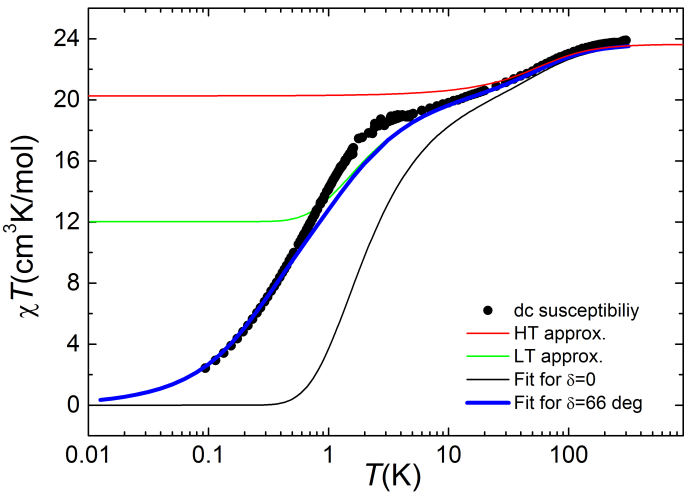

Figure 4.9: In-phase susceptibility of Tb_2. Red line is the fit for high temperature (Eq. (4.35)) and $D/k_B = 17$ K, whereas the green line represents the low temperature approximation, given by Eq. (4.41), with $J_{ex}/k_B = -0.015$ K. Black line is the result of computed calculations with the whole Hamiltonian for $\delta = 0^o$ whereas blue line has been computed with $\delta = 66^o$.

two uncoupled ions whose angular momenta point up or down along their anisotropy axes ($J_z = \pm 6$),

$$\mu_{\text{eff}} = g\mu_B\sqrt{2J^2} = 12.72\mu_B \tag{4.45}$$

Between 3 K and room temperature, the susceptibility can be fitted using the high temperature approximation for non-Kramers ions, as shown in Fig. 4.9 (red line). Fitting Eq. (4.35) to the experimental data gives $D/k_B = 17$ K. This means that the first exited levels are separated from the ground level by $\Omega/k_B = (2J-1)D \approx 187$ K.

Below 3 K a new drop is observed, It can be associated to an antiferromagnetic coupling of both spins, giving a negative sign for J_{ex}.

Specific heat measurements, shown in Fig. 4.10, indicate the existence of a Schottky anomaly, probably broadened, due to the hyperfine contribution. Even so, it is centered at $T_{max} \cong 0.9$ K and we can estimate J_{ex} using the condition $k_B T_{max} = 0.42\Delta E$, where $\Delta E = 4J_{ex}J^2$ is the splitting between levels corresponding to the ferromagnetic and antiferromagnetic coupling of the two Tb^{3+} spins. Hence, $\Delta E/k_B = 2.14(2)$ K and $J_{ex}/k_B \approx -0.014(8)$ K. The sign of J_{ex} is determined from susceptibility data.

The last parameter to be fit is the misalignment δ between the two anisotropy axes of Tb^{3+} ions. Figure 4.9 shows that the theoretical χT obtained using

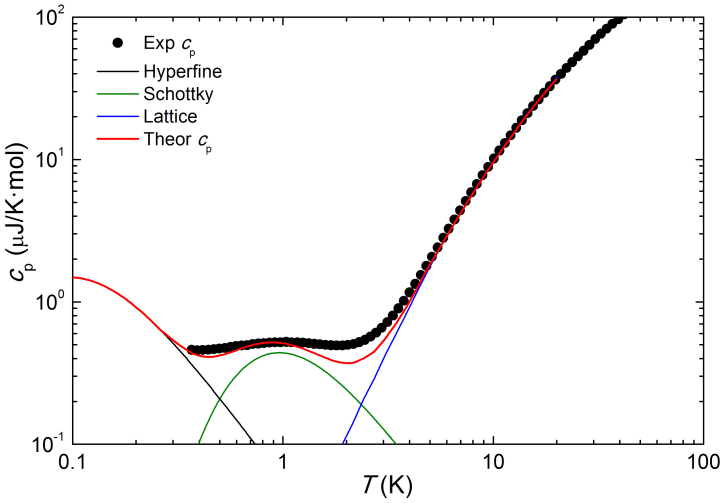

Figure 4.10: Zero-field specific heat of Tb_2. Three contributions can be observed: the hyperfine interaction (black line), Schottky anomaly (green line) and lattice contribution (blue line), last one obtained from the non-magnetic YLa dimer in section 4.4.2. Red line is the total fit of specific heat.

Eq. (4.41) for $\delta = 0^o$ does not match at all with the experimental data. This means that even the antiferromagnetic states ($|+6,-6\rangle = |\Uparrow_1, \Downarrow_2\rangle$ and $|-6,+6\rangle = |\Downarrow_1, \Uparrow_2\rangle$) preserve a net magnetic moment and the two ions couple differently to an external magnetic field. This situation can be taken into account by considering two different effective gyromagnetic ratios. As an example, if the magnetic field H is applied along the anisotropy axis of the first ion, then $g_1 = g_J = 3/2$ and $g_2 = g_1 \cos\delta$ making the two ions nonequivalent. Fig.4.9 also shows the best theoretical fit of χT, with $\delta = 66^o$.

Figure 4.11 shows the lowest energy levels structure at zero-field. The ground state is a doublet where the two ions are coupled antiferromagnetically (lowest energy). This allows a good definition for "qubits". These levels are separated between them by $\Delta E = 2.14$ K. The first excited level is really far from the ground state, at $\Omega = 187$ K.

4.6.3 Further measurements

With the purpose of confirming the fits obtained in the section above ($D/k_B = 17$ K, $J_{ex}/k_B - 0.014(8)$ K and $\delta = 66^o$) some other measurements have been performed. We have measured specific heat data for $H \neq 0$, shown in Fig. 4.12. This quantity depends on the magnetic field dependence of the energy levels, which strongly depend on the misalignment δ. The results agree with calculations made for $\delta = 66^o$ and the rest of fitted parameters.

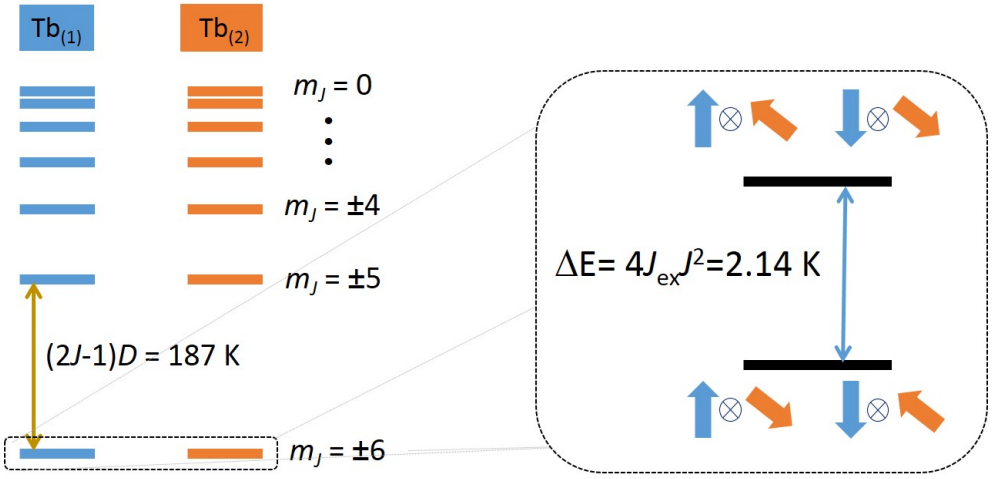

Figure 4.11: Zero-field energy level structure of Tb_2. The ground state is a doublet which is separated more than 180 K from the first excited state. The doublet, separated by a energy of 2.14 K, stablishes a good definition of coupled "qubits" whose levels will split when applying an external magnetic field. As the spins are not aligned, the anitferromagnetic state will also split with the magnetic field, giving a four-level system, needed for performing qugates.

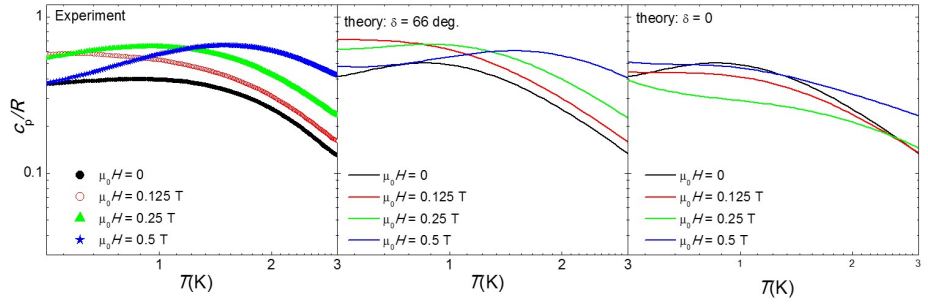

Figure 4.12: Left. Magnetic heat capacity for a powdered sample of Tb_2. Comparing simulations for $\delta = 0^o$ (right) and $\delta = 66^o$ (center), it is clear that specific heat depends strongly on δ. Results are in quantitative and qualitative agreement with calculations made for $\delta = 66^o$ and the rest of the fitted parameters.

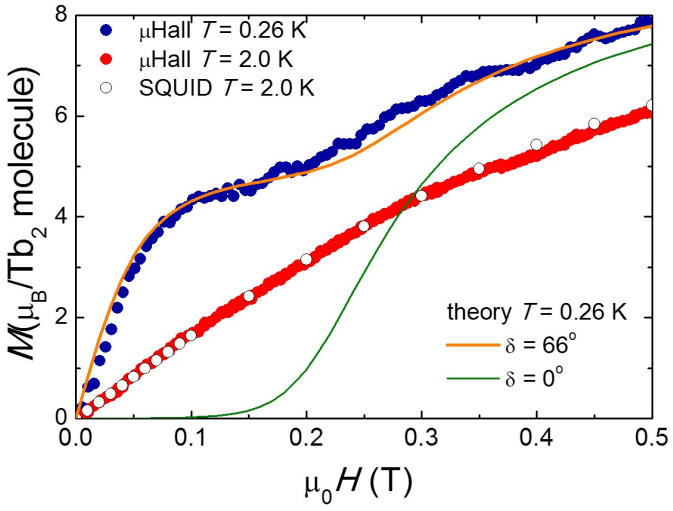

Figure 4.13: Magnetization isotherms of Tb_2. Lines represent calculations, made at $T = 0.26$ K, for aligned ($\delta = 0$) and misaligned ($\delta = 66^o$) anisotropy axes.

We have also measured magnetization isotherms at $T = 0.26$ K and $T = 2$ K, using a micro-Hall magnetometer. The results are shown in Fig. 4.13. Magnetization has a paramagnetic response, starting already from $H = 0$, which shows that there is a net magnetic moment in the ground state. Because of this non-perfect cancellation of the spins, the magnetization has a strong dependence on δ, as shown in Fig. 4.13, where calculation with and without δ dependence are plotted. These results confirm in an independent way, that the set of parameters, given above, properly describe the magnetic properties of this molecular system.

4.6.4 EPR experiments: CNOT and SWAP transitions

The experiments just described shows that Tb_2 can be effectively described by Eq. (4.37). I next discuss the use of Tb_2 as a two-qubit quantum gate. Figure 4.14 shows the energy level spectrum calculated for $\delta = 66^o$ and $m_{I_{z,1}} = m_{I_{z,2}} = -3/2$ (for simplicity).

The combination of spin-spin coupling and a magnetic asymmetry gives rise, at any magnetic field value, to an energy level scheme with non-degenerate energy splittings. For instance, at $\mu_0 H = 0.07$ T, only transitions between states $|\Uparrow_1\Downarrow_2\rangle$ and $|\Downarrow_1\Uparrow_2\rangle$ will be resonant with the energy of $\nu = 9.8$ GHz photons (coincident with X-band EPR). This transition the provides a realization of a SWAP operation, flipping $|\Uparrow_1\Downarrow_2\rangle$ into $|\Downarrow_1\Uparrow_2\rangle$ and leaving any other state

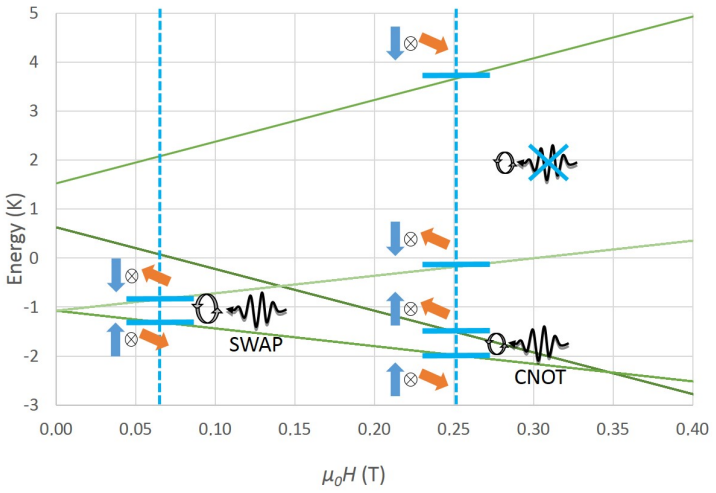

Figure 4.14: Field-dependent magnetic energy levels of Tb_2 for $\delta = 66^o$, $J_{ex} = -0.015$ K and $m_{I_{z,1}} = m_{I_{z,2}} = -3/2$. $\mu_0 H$ represents the magnetic field applied along the z axis.

unperturbed. If the two qubits were indistinguishable, this operation would be impossible a magnetic field can not split the antiferromagnetic levels.

At $\mu_0 H = 0.25$ T, CNOT operation is feasible using the same energy radiation, which becomes then resonant to the transition $|\Uparrow_1 \Downarrow_2\rangle \longrightarrow |\Uparrow_1 \Uparrow_2\rangle$. Note that no other transition is possible with $\nu = 9.8$ GHz photons at this magnetic field. SWAP and CNOT operations can, therefore, be selected by tuning the local magnetic field, which is often easier than changing the radiation energy. Qubits can be easily reset by cooling down to 0.1 K, where the ground state is populated by more than a 99%.

Just one condition remains: checking that all these transitions are allowed. e.g. by the presence of weak exchange or anisotropy terms. In a perfect diagonal Hamiltonian like Eq. (4.22), they would be forbidden. However, terms like ΔJ_x (in Eq. (4.24)) or $-2J_{ex}J_{1x}J_{2x}$, which can be nonzero, allow them. We have checked this by performing continuous-wave EPR measurements on a Tb_2 podwer sample as a function of the magnetic field. Figure 4.15 shows the absorption derivative measured at 6 K. It consists of two broad absorption lines, centered at $\mu_0 H = 0.068$ T and $\mu_0 H = 0.46$ T, respectively, which can be associated with the SWAP and CNOT transitions. The difference between these fields and those predicted above is due to the random orientation of the molecules in the sample and to the nuclear spins.

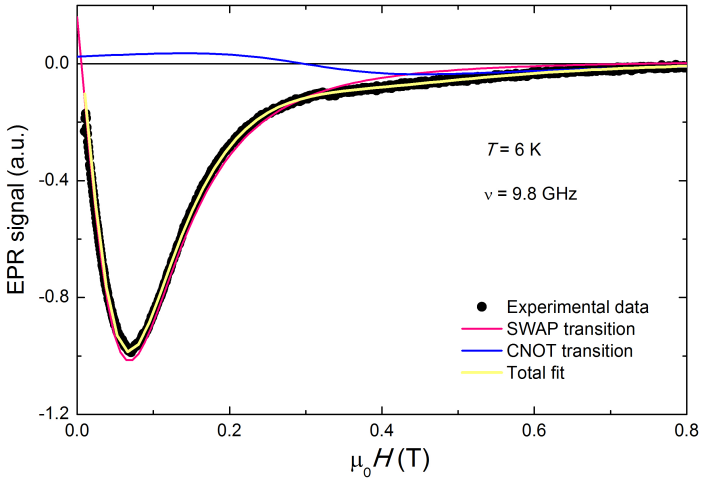

Figure 4.15: EPR absorption spectrum of a powder Tb_2 sample.

4.7 Experimental study of molecular qugates with asymmetrical environment. Kramers case: Dy_2

4.7.1 Main characteristics of a Dy_2 dimer

We consider now a "homonuclear" dimer formed by two Dy^{3+} ions. As shown in Fig. 4.16, this dimer has the same molecular structure than the Tb_2 dimer. It is formed from H_3L ligands and $DyCl_3$.

Dy^{3+} possesses a $J = 15/2$, which means that it is a Kramers ion. This ensures that its ground state is at least double degenerated. On the other hand, unlike Tb_2, only one half of the Dy^{3+} ions carry nuclear moments and the hyperfine coupling is about 3 times smaller, which means that effects of the hyperfine couplings on the measurements will be less important. Besides, different isotopes have also different hyperfine splittings, which can interfere. There is a more detailed analysis about the effects of hyperfine couplings in chapter 6.

As both ions are identical, addressability of qubits in Dy_2 should be given by a misalignment of the main anisotropy axes, the same way as in the case of Tb_2. A summary of the main properties of Dy_2 is listed in table 4.2.

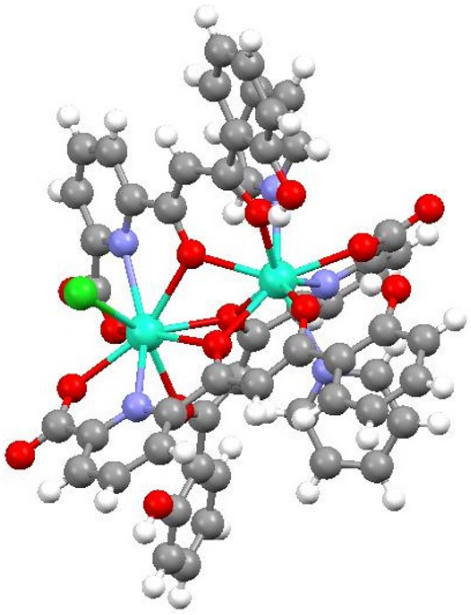

Figure 4.16: Molecular structure of the Dy_2 dimer. White atoms are hydrogen, gray atoms are carbon, lilac atoms are nitrogen, red atoms are oxygen, the green atom is chlorine and cyan atoms are dysprosium.

Magnitude	Nomenclature	Tb^{3+}
Total angular momenta	J	15/2
Nuclear spin (only a 44.4% of the spins)	I	5/2
Gyromagnetic ratio	g	4/3
Hyperfine constant	A_J/k_B	-5.56 mK (^{161}Dy) 7.8 mK (^{163}Dy)

Table 4.2: Main properties of Dy^{3+}.

4.7.2 Magnetic susceptibility and specific heat measurements

Susceptibility data, in Fig. 4.17, show two drops, as we have already seen in the case of Tb_2. At room temperature, susceptibility agrees with the effective moment of two uncoupled free ions,

$$\mu_{\text{eff}} = \sqrt{3k_B\chi T/N_A} = 15.1(5)\mu_B \tag{4.46}$$

$$\mu_{\text{eff}_{theo}} = g\mu_B\sqrt{2J(J+1)} = 14.1(4)\mu_B \tag{4.47}$$

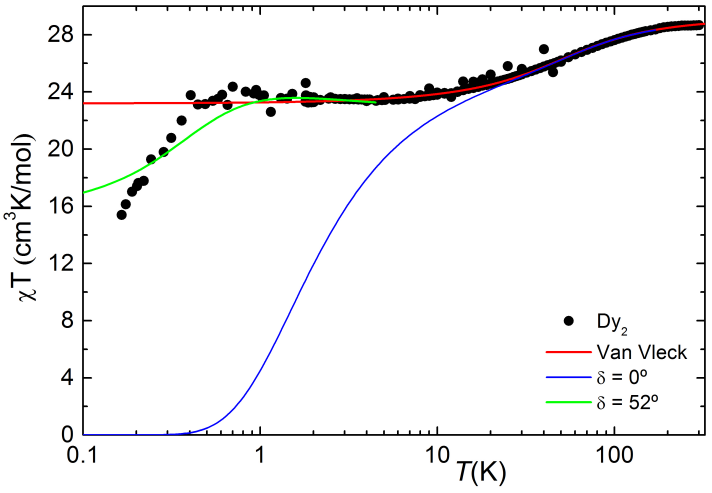

Figure 4.17: In-phase susceptibility of Dy_2. Red line is the Van Vleck approximation for high temperature. Blue line is the computed calculations for $\delta = 0°$ whereas the green line has been computed for $\delta = 52°$.

Below room temperature, magnetic susceptibility drops. This drop correspond to a thermal depopulation of the highest energy levels. In general for Kramers ions, $g_x \neq 0$ and $g_y \neq 0$, which means that the lowest energy state could be any z projection or even a superposition of some of them. The plateau between 0.4 K and 10 K can give us any clue about the ground state doublet. In this range, the effective moment is $\mu_{\text{eff}} = 13.6(2)\mu_{\text{B}}$. For this value and using Eq. (4.36) we get,

$$\sqrt{\langle g^2 \rangle} S = 9.6(3) \tag{4.48}$$

To estimate the z projection at which corresponds this value we can consider the equivalence $\langle g^2 \rangle S^2 \equiv g_J m_J$, where $S = 1/2$ is the effective spin and $g_J = 4/3$ is the gyromagnetic ratio of Dy^{3+}. Hence, we obtain that

$$m_J = \pm 7.2(2) \approx \pm 15/2 \tag{4.49}$$

which means that the ground state doublet is the maximal projection over the z axis, and therefore, $g_x, g_y \ll g_z$. It can be probable that there also exist some little superposition of other doublets explaining why m_J is closer to 7, that to 15/2. Van Vleck susceptibility fitting (Eq. (4.34))can be used to determine the

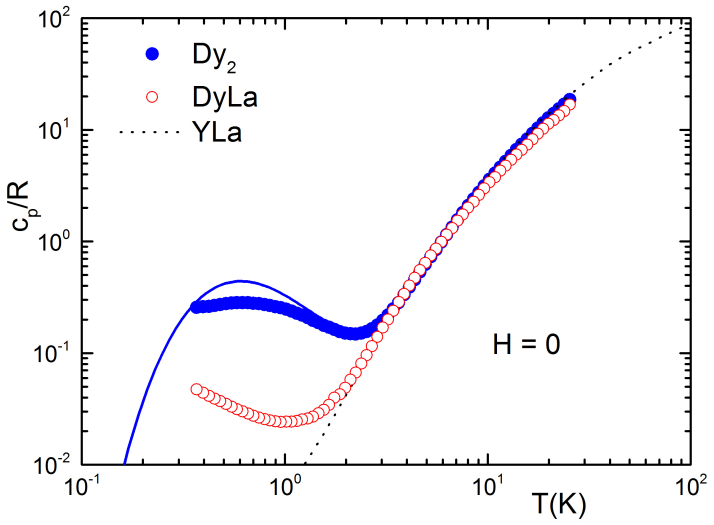

Figure 4.18: Specific heat measurements of Dy_2 and DyLa. Dy_2 shows a Schottky anomaly at about 0.61 K, thus indicating the presence of spin coupling.

energy gap between the ground state doublet and the excited ones, Ω. From the fit,

$$\begin{aligned} \Omega &= 100 \text{ K} \\ C_0 &= -0.14 \\ C_1 &= 0.15 \\ C_2 &= 1.24 \end{aligned} \tag{4.50}$$

Among the different measurements performed, the one that shows clearly the coupling between the Dy^3 ions at low temperatures is the specific heat, shown in Fig. 4.18. This time we have compared the specific heat of the dimer with that of a monomer, with just one Dy^{3+} ion. Data show that, at low temperatures, Schottky anomaly appears for the dimer, whereas the monomer signal remains almost ten times smaller. This indicates that there exist a coupling between both ions. The peak looks broader than the simulation probably due to the contribution of the hyperfine coupling. It is centered at $T_{\max} \approx 0.61$ K, thus indicating an energy difference of $\Delta E/k_{\mathrm{B}} = T/0.42 = 1.45$ K, which separates the two coupled states.

The drop in susceptibility data below 0.4 K agree with an antiferromagnetic coupling, which means that the ground entangled state (our quantum "0") is therefore $|\uparrow\downarrow\rangle + |\downarrow\uparrow\rangle$, whereas the first excited is $|\uparrow\uparrow\rangle + |\downarrow\downarrow\rangle$.

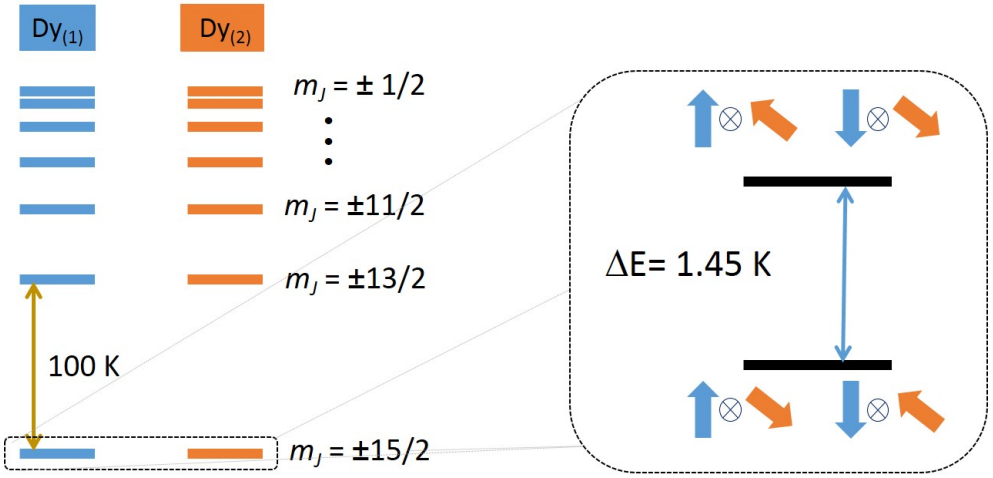

Figure 4.19: Zero-field energy level structure of Dy_2. The ground state is a doublet which is separated by 100 K from the first excited state. The doublet is separated by an energy of 1.45 K.

As well as in the case of Tb_2, theoretical susceptibility for aligned z axes does not fit at all with the experimental data. Best fit has been found for $\delta = 52°$ considering. It does not fit as well as in the case of Tb_2, which is probably due to the so strict approximation $g_x, g_y = 0$.

Figure 4.19 shows the zero-field level structure that sums up the characteristics obtained for this system. The ground state doublet is the maximum projection over the z axis for each Dy^{3+} ion, $m_J = \pm 15/2$. Each doublet is well separated from the excited doublets by an energy gap $\Omega = 100$ K. Both doublet are entangled so that the antiferromagnetic state is the state with lowest energy and the ferromagnetic one is the state with higher energy. Both states are separated by an energy $\Delta E = 1.45$ K. Anisotropy axes are rotated $\delta = 52°$ so that, even at zero temperature, the system keeps a magnetic moment. This fact, provoked by local asymmetry, allows to distinguish one spin from the other.

Finally, Fig. 4.20 shows the magnetic-field dependence of the energy levels used to perform quantum gates. Axes misalignment allows the antiferromagnetic levels to split, giving a four-level system, unequally split. For instance, at 69 mT, an excitation of frequency 7.5 GHz, could perform a SWAP operation. CNOT operation could be carried out, for example, at 200 mT, by exciting with an energy frequency of 4.17 GHz.

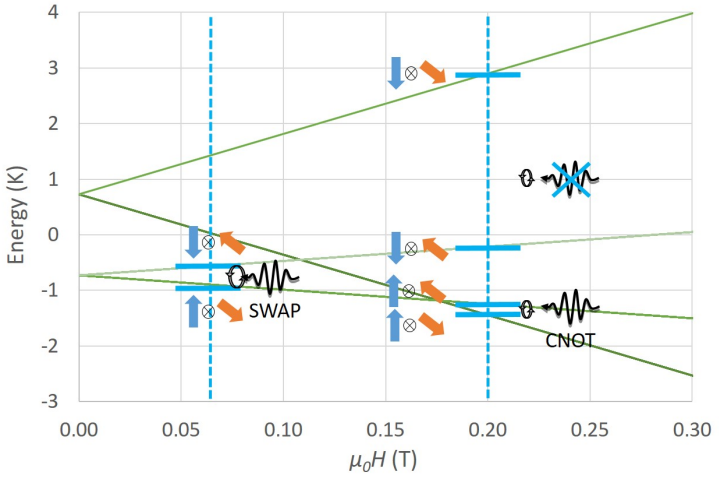

Figure 4.20: Field-dependent magnetic energy levels of Dy_2 for $\delta = 52°$ and $\Delta E = 1.45$ K.

4.8 Experimental study of molecular qugates with different components: ErCe

4.8.1 Main characteristics of ErCe dimer

The ErCe dimer is a "heteronuclear" dimer because it is formed by two different ions: Ce^{3+} and Er^{3+}, both Kramers ions. Its molecular structure is shown in Fig. 4.21. This molecule has been synthesized from H_3L ligands and nitrate salts: $Ce(NO_3)_3$ and $Er(NO_3)_3$ [4.32].

The interest for these ions comes from their big differences in their magnetic characteristics. Er^{3+} ion has a net angular momentum $J_{Er} = 15/2$ and a gyromagnetic ratio $g_{Er} = 6/5$, whereas Ce^{3+} has $J_{Ce} = 5/2$ and $g_{Ce} = 6/7$. This fact and the asymmetrical environment assure us the proper identification of both qubits.

On the other hand, stable Ce^{3+} ions do not have any nuclear magnetic moment and therefore they do not have hyperfine interaction. In the case of Er^{3+}, only 22.9% of stable isotopes carry a nuclear spin (corresponding to the ^{167}Er isotope) and we will not take it into account. This allows us to eliminate the hyperfine interaction from the Hamiltonian and contributes to reduce decoherence [4.33].

In contrast to Tb^{3+} and Dy^{3+}, Ce^{3+} and Er^{3+} do not have, in their respective coordinations, a fully uniaxial anisotropy. Therefore, their interaction with the crystal field does not assure us that the ground states could be $|J_z\rangle = |\pm J\rangle$.

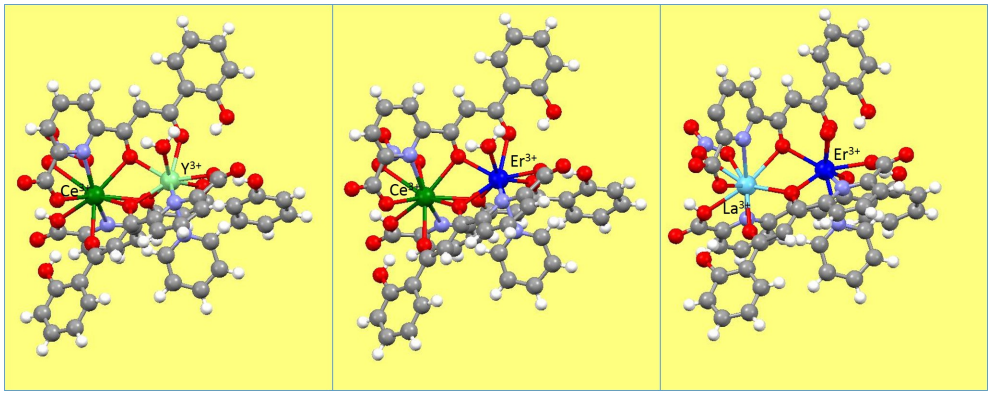

Figure 4.21: YCe (left), ErCe (center) and ErLa (right) dimers. White atoms are hydrogen, grey atoms are carbon, lilac atoms are nitrogen and red atoms are oxygen. Ce^{3+} ions, in dark green, occupy the biggest place into the cluster, whereas Er^{3+} ions, in dark blue, are in the smallest one. Monomers are completed with non-magnetic ions Y^{3+}, in light green, and La^{3+}, in light blue.

They are, nevertheless, Kramers ions, which means that the crystal field leads to a doubly degenerate ground state, although not necessarily the maximum projection along the z axes.

To determine the ground single doublet of each ion we have also performed measurements on monomers, i.e. dimers where one of the ions is non-magnetic. Thus, we have also studied the YCe dimer, where Y^{3+} has $J = 0$, and ErLa dimer, with La^{3+} also having $J = 0$. Ce^{3+} and Er^{3+} occupy the same place in monomers as they do in dimer and, therefore, they are subjeted to approximately the same crystal field.

4.8.2 Measurements on YCe and ErLa monomers

As we have seen in section 4.5, studying separately each ion provides a unique opportunity to obtain the parameters of the zeroth-order approximation Hamiltonian, i.e. the g-tensor from Eq.(4.17) . We are also interested on knowing what J_z projection corresponds to the lowest energy doublet. Susceptibility measurements are shown in Fig. 4.22. The plateau observed at low temperature corresponds to the magnetic behaviour of the ground state doublet, described in Eq. (4.41). The low limit of χT is

$$\begin{aligned} \chi T_{\mathrm{Er}} &= 3.70 \text{ cm}^3\text{K/mol} \\ \chi T_{\mathrm{Ce}} &= 0.35 \text{ cm}^3\text{K/mol} \end{aligned} \tag{4.51}$$

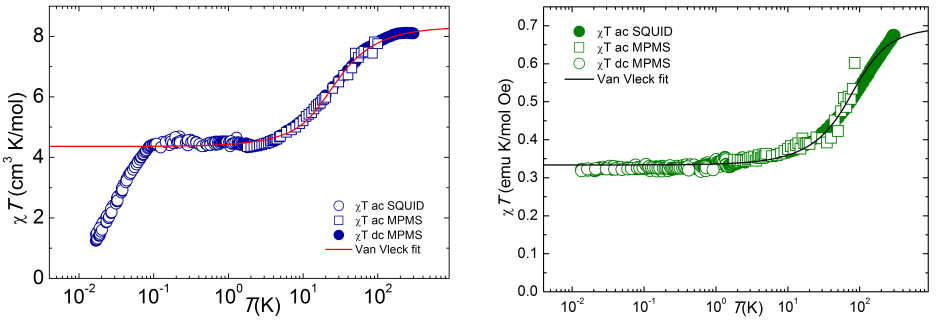

(a) (b)

Figure 4.22: Temperature dependence on the equilibrium magnetic suseptibility of ErLa (a) and YCe (b) dimers. Fits have been done using Eq. (4.34).

which agrees with the following projections of J_z:

$$\begin{aligned} J_{z,\mathrm{Er}} &= \pm 9/2 \\ J_{z,\mathrm{Ce}} &= \pm 3/2 \end{aligned} \tag{4.52}$$

This value does not correspond to the maximum projection and, therefore, $g_x \neq 0$ and $g_y \neq 0$.

At higher temperatures, χT increases, as a result of the gradual population of excited Kramers doublets. Fitting the data to Van Vleck's equation (Eq. (4.34)) we obtain the energy gap Ω between the ground and first excited doublets: $\Omega_{\mathrm{Er}}/k_{\mathrm{B}} = 43$ K and $\Omega_{\mathrm{Ce}}/k_{\mathrm{B}} = 230$ K. Below 0.1 K, χT of ErLa exhibits a drop that can be associated to magnetic order, probably induced by dipolar interactions between spins in different molecules. In YCe we do not see this drop because of the smaller magnetic moment of Ce^{3+}.

The existence of non negligible g_x and g_y, makes the model a bit more complicated to fit. EPR measurements can provide us information about the principal values of g's. Fig. 4.23 shows EPR data on powder samples of ErLa and YCe. The spectra have been obtained at a frequency $\nu = 9.8$ GHz (X-band). Fitting the spectra to accord with our theoretical model, we have obtained the values for g-tensors listed in Table 4.3.

Using these data we can check the projection of J_z that plays the role of ground state effective spin. With the equivalence $g_J \vec{J} = \widetilde{g}\vec{S}$ described above, we can approximate,

$$\begin{aligned} g_{\mathrm{Er}}\,|J_{z,\mathrm{Er}}| \approx |g_z|\,S \Longrightarrow J_{z,\mathrm{Er}} \approx \pm 4.20 \Longrightarrow J_{z,\mathrm{Ce}} = \pm 9/2 \\ g_{\mathrm{Ce}}\,|J_{z,\mathrm{Ce}}| \approx |g_z|\,S \Longrightarrow J_{z,\mathrm{Ce}} \approx \pm 1.56 \Longrightarrow J_{z,\mathrm{Ce}} = \pm 3/2 \end{aligned} \tag{4.53}$$

which agrees with the susceptibility data. However, the states are mixed with other spins projections on account of the non-zero transverse $\widetilde{g}$ factors.

	Er^{3+}	Ce^{3+}
$\|g_x\|$	1.80	1.00
$\|g_y\|$	3.70	1.75
$\|g_z\|$	10.0	2.67

Table 4.3: Absolute value for principal values of g-tensor for Er^{3+} and Ce^{3+} ions obtained from EPR spectrum.

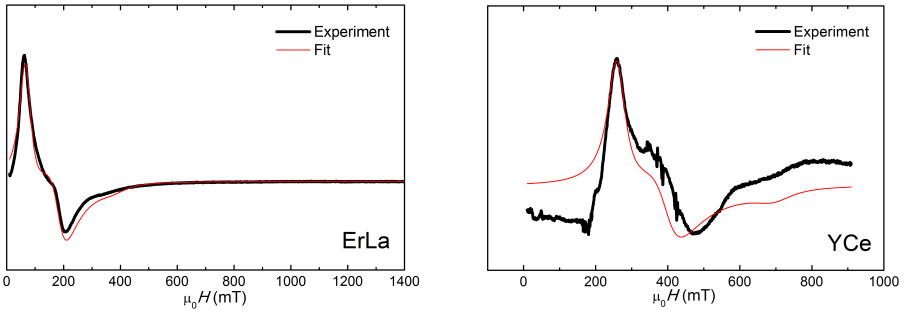

(a) (b)

Figure 4.23: X-band continuous wave EPR spectra of ErLa and YCe. Fits are based on the $S = 1/2$ Hamiltonian which describes the magnetic properties of the ground state doublet.

The big difference between Ω_{Er} and Ω_{Ce} and between the $\widetilde{g}$ values confirm that both ions behave completely different and can be used as addressable qubits. It is also interesting to point up that g_x and g_y are on the same order than g_z. This is very uncommon in lanthanide qubits, where g_x/g_z and g_y/g_z use to be typically on the order of 10^{-3} or even less. This fact would probably come from the very low symmetry of the compound.

Fig. 4.27 shows the energy level scheme of each ion at zero field. The ground state level doublet is in both cases well separated from the excited levels. The energy gap differs, due to their different magnetic moments and their different interaction with the crystal field. That provides a proper definition of two different qubits. The existence of different $\widetilde{g}$s makes them magnetically nonequivalent and therefore separately addressable. Last step consists of measuring the coupling interaction between both ions.

4.8.3 Measurements on ErCe dimer

Measurements on the ErCe dimer can confirm the existence of a coupling between Er^{3+} and Ce^{3+} magnetic moments by simply comparing their data

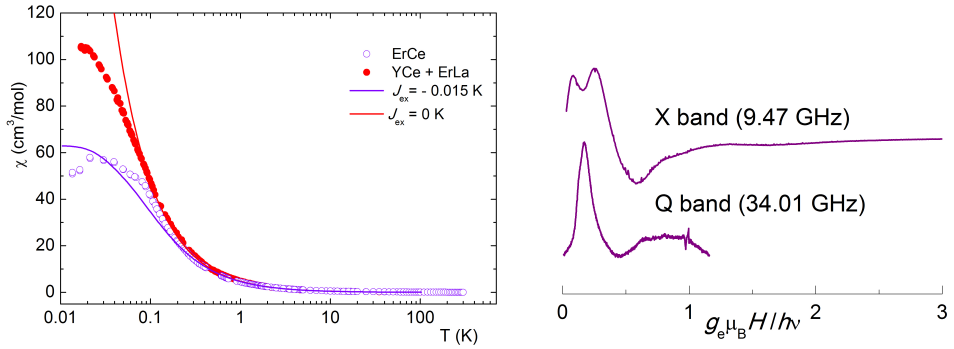

(a) (b)

Figure 4.24: a). Temperature dependence of the equilibrium magnetic susceptibility of ErCe, compared to the sum of susceptibilities of YCe and ErLa. Lines shows the fit of Eq. (4.22) for a non coupled system and a coupled one. Results accord to a misalignment of 70°. b). EPR spectra of ErCe measured at 5 K and two different frequencies. Both spectra do not scale properly, which means that there is a coupling between Ce^{3+} and Er^{3+} ions.

with measurements performed on the monomers. In first place, Fig. 4.24(a) shows the magnetic susceptibility of ErCe dimer, compared with the sum of data obtained for the monomers, ErLa and YCe. Above approximately 0.2 K, χ coincides, due to the weakness of the exchange interaction. However, coupling effects become visible below this temperature, where χ_{ErCe} is clearly smaller than the corresponding value for both non-coupled ions. This fact suggests that the coupling is antiferromagnetic and, therefore, J_{ex} will be, as in the cases of Tb_2 and Dy_2, negative.

EPR measurements on X-band (in Fig. 4.26) also confirm that the magnetic energy level spectrumof ErCe is not just the sum of the ErLa and YCe spectra. Furthermore, measurements performed on X-band (at $\nu = 9.8$ GHz) and on Q-band (at $\nu = 34$ GHz) do not scale (see. Fig. 4.24(b)), which means that resonant fields are not just proportional to ν and therefore provides further evidence for the coupling between the spins of both lanthanides.

Finally, the same conclusions can be extracted from specific heat data (Fig. 4.25). Specific heat for ErCe at zero-field does not coincide with the one for non-interacting ions below 1 K; it is larger. The extra contribution reflects the splitting in energy of different ferro- and antiferromagnetic configurations of the two spin qubits. This contribution tends to vanish as the magnetic field increases, i.e. when Zeeman interaction becomes stronger than exchange interaction, which shows the existence of a $J_{\mathrm{ex}} \neq 0$ and, therefore, a coupling between Er^{3+} and Ce^{3+}.

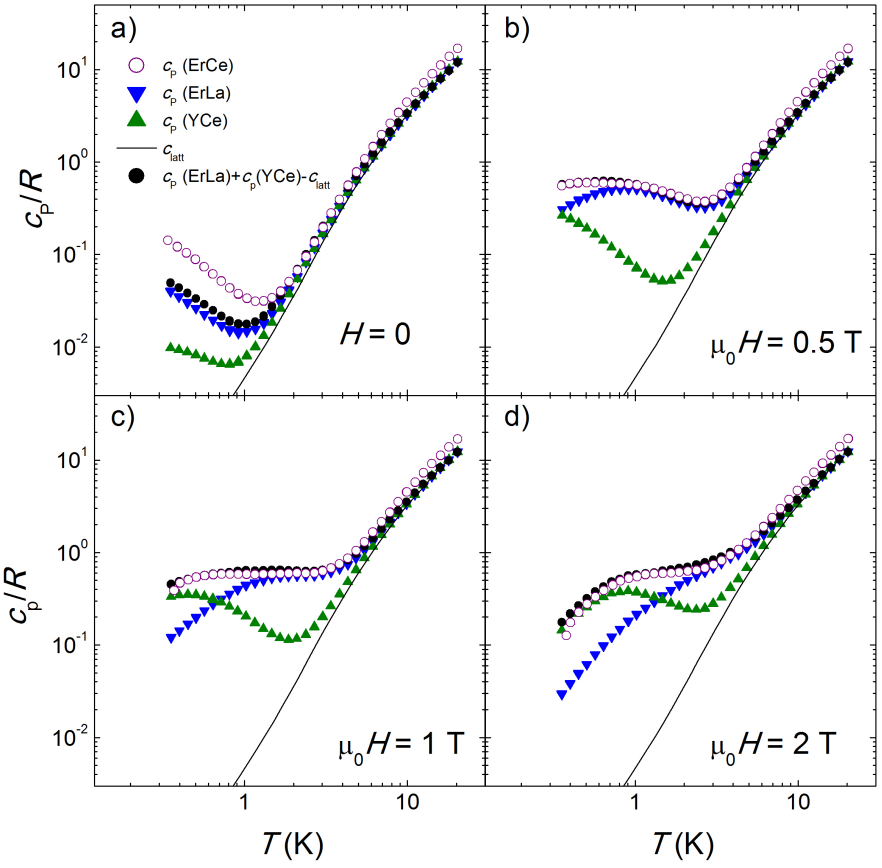

Figure 4.25: Specific heat for the three clusters at different magnetic fields. In zero-field graph, it is possible to notice that, at sufficiently low temperatures, the sum of the YCe and ErLa contributions is less that ErCe specific heat, which means that there exists an extra coupling contribution in the dimer.

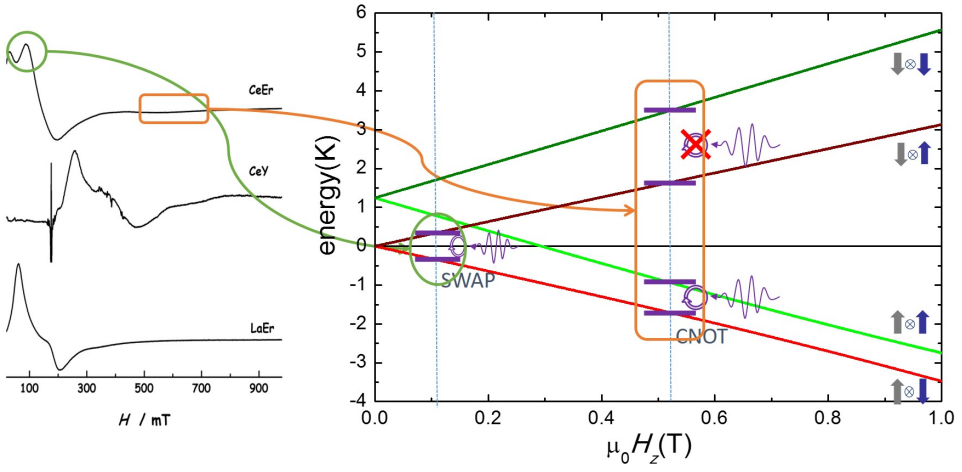

Figure 4.26: EPR spectra of the monomers and the dimer. It is clear that ErCe spectrum does not match with YCe and ErLa. It also has two aditional peaks that can be associated to a SWAP and CNOT transitions. Right. Full energy level scheme for ErCe and its dependence on the magnetic field.

In order to determine $J_{\rm ex}$, the spin Hamiltonian described in Eq. (4.22) has been used to numerically compute χ and $c_{\rm p}$. As in the case of Tb_2 the possibility of misalignment, δ, has also been taken into account, finding a good agreement between theoretical calculations and experimental data for $J_{\rm ex} = -0.015$ K and $\delta = 70^{\rm o}$. Hence, the energy gap at zero field between the antiferro- and the ferromagnetic levels is $\Delta E = 2J_{\rm ex}J_{z,1}J_{z,2} = 0.20$ K. The presence of non-zero $J_{{\rm ex},x}$ and $J_{{\rm ex},y}$ components gives rise to a splitting of the levels into 4 singlets.

Figure 4.27 shows schematically the energy levels of ErCe at zero field. Each ion has separately a single doublet as ground state which is well separated from the excited states ($\Omega_{\rm Er} = 43$ K and $\Omega_{\rm Ce} = 230$ K). At sufficiently low temperatures both doublets are coupled into four levels, two antiferromagnetic and another two ferromagnetic, which are separated by $\Delta E = 0.20$ K.

4.8.4 Study of coherence time

Finally, as we have already described in section 4.2, a crucial step for evaluating the suitability of a given candidate for quantum information processing is to measure coherence times associated with CNOT and SWAP operations. Time domain EPR spectroscopy can be a good method for obtaining these data. The sample used was a solution of ErCe dimers in ethanol/methanol in order to reduce the dipole-dipole interactions between different dimers. Radiofrequency

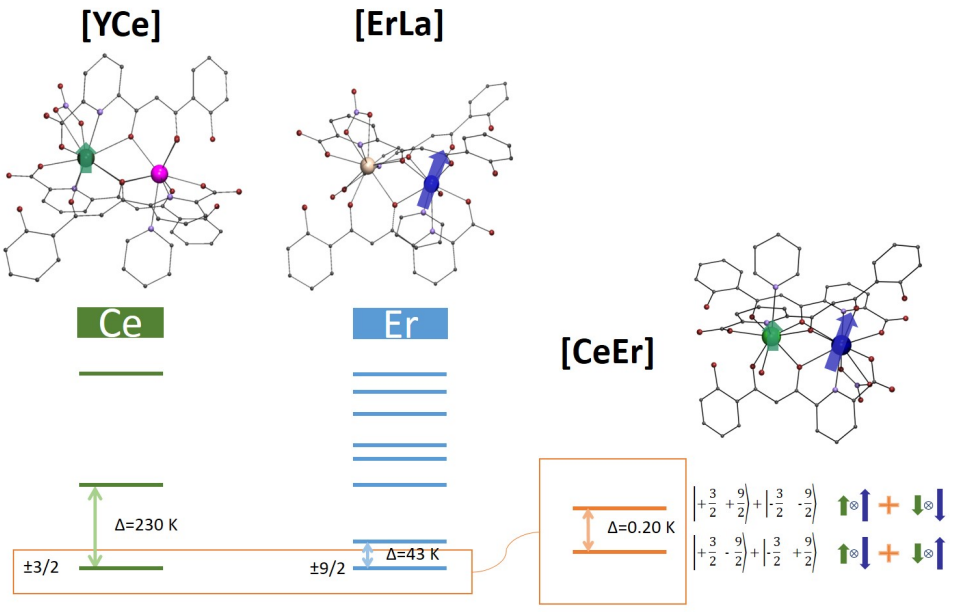

Figure 4.27: Level spectra of YCe and ErLa. The ground state doublet in both cases is separated enough from the excited levels. The energy gap differs, due to their different magnetic momenta and their different interaction with the crystal field. That makes them completely addressable. In the ErCe dimer, the ground state doublets are coupled, being the antiferromagnetic levels those with less energy.

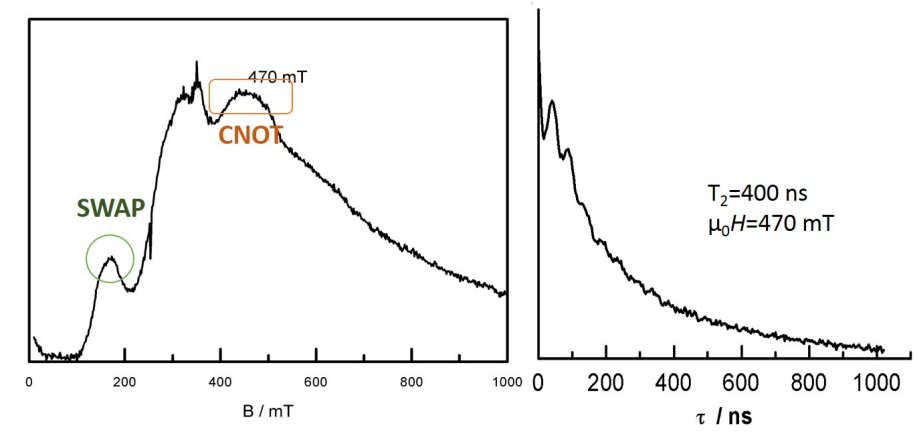

(a)

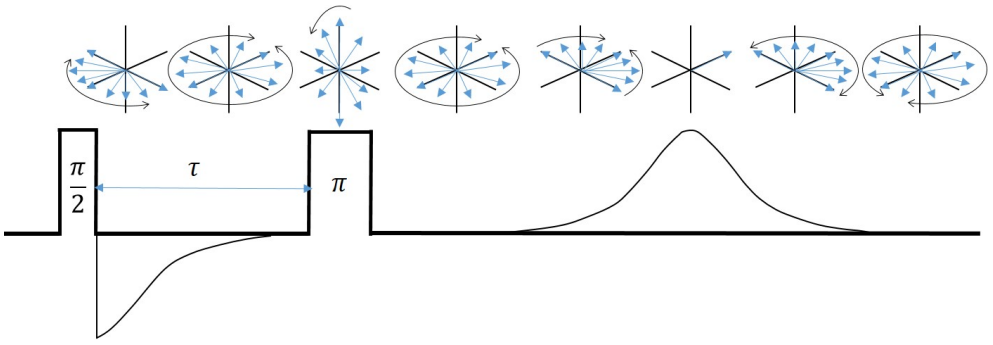

(b)

Figure 4.28: a). Left. Echo-detected EPR spectrum of a solution of ErCe in ethanol/methanol, measured at a fixed separation between the $\pi/2$ and π pulses of $\tau = 140$ ns. Right. Decay with τ of the spin-echo measured at 470 mT, which corresponds to a CNOT operation. An exponential fit gives a decoherence time $T_2 = 410$ ns. b). Scheme of Hanh-echo sequence used in the experiment. It consists of an application of a $\pi/2$ pulse, followed by a π pulse that refocuses the angular momenta. Arrows describe the behaviour of the angular momenta when pulses are applied.

pulses of a given length wave, vary the magnetic field. Fig. 4.28(a) shows the echo intensity obtained, as a function of the magnetic field, $\mu_0 H$.

At around $\mu_0 H = 470$ mT an echo signal has been detected, which approximately agrees with the field region where the CNOT transition $|10\rangle \longrightarrow |11\rangle$ is expected to be induced. The decay of the echo signal is also shown in Fig. 4.28(a). The estimated decoherence time T_2 for the CNOT transition, is about 410 ns. This value is still far away from that of other molecular candidates (of the order of μs [4.33]). Further experiments, using more diluted samples in order to reduce dipole-dipole interactions between molecules, and deuterated ligands, to reduce hyperfine couplings, could improve coherence.

4.9 Conclusions

Among the already long list of experimental candidates to realize the quantum hardware, we have studied the suitability of Single Molecule Magnets for this purpose. In particular, we have focused on a certain family of molecular clusters that can contain almost whatever two lanthanide ions, which can act as single or coupled qubits. This flexibility enables a vast choice of quantum gate designs.

Among the possibilities, we have chosen three particular clusters in order to study, on the one hand, the effects of asymmetric environment as a way to address qubits inside the cluster (Tb_2 and Dy_2) and, on the other hand, the behaviour of two different lanthanides as uncoupled (YCe and ErLa) and coupled qubits (ErCe). In every case we have concluded that they meet the ingredients required to implement SWAP and CNOT quantum gates, i.e. the existence of well defined, addressable qubit states, the coupling between them and the posibility to induce the relevant transitions coherently.

In the case of Tb_2 and Dy_2 clusters, the definition of control and target qubits (addessability) is based on the magnetic inequivalence of the two ions, achieved by chemically engineering dissimilar coordination spheres, that produces a misalignment between their spin anisotropy axes of 66^o for Tb_2 and 52^o for Dy_2. In the case of Tb^{3+}, the lowest energy levels closely correspond to $\pm J$ angular momentum projections. The ground level doublet is separated from the first excited states by more than 187 K, giving a good definition of each qubit (two level system). They are coupled by an exchange interaction that splits them into an antiferro- and ferromagnetic levels, separated by an energy of 2.14 K at zero-field. Specific heat, magnetic susceptibility and EPR measurements confirm the theoretical model designed for this system.

In the case of Dy_2, we have obtained that, despite having transverse anisotropy, g_x and g_y are small enough to consider each ion as an effective $S = 1/2$ with dominant uniaxial anisotropy, in the same way as Tb_2. The ground state doublet is formed by the states $m_J \approx \pm 15/2$. The ground level doublet is separated from the first excited doublet by 100 K. The antiferromagnetic states is also the lowest energy state of the two coupled qubits, separated from the ferromagnetic states by an energy gap of 1.45 K.

Concerning the ErCe cluster, control and target qubits can be defined by the intrinsic differences between Er^{3+} and Ce^{3+} ions, which exhibit very dissimilar angular momenta and gyromagnetic ratio, although an additional misalignment of 70^o between the spin anisotropy axes has also been found. Measurements on monomers YCe and ErLa have shown that their lowest energy states do not coincide with any projection of $\vec{J}$. The ground level doublets of each ion are also well separated from the excited ones (230 K in the case of Ce^{3+} and 43 K in the case of Er^{3+}). Antiferromagnetic coupling has been shown by direct comparison between data measured on the monomers and the dimer. Fits to the theoretical model conclude that there exists a splitting of $\Delta E \approx 0.20$ K at zero field, between antiferro- and ferromagnetic levels.

We have also performed time-domain EPR experiments to determine the coherence time of CNOT operations in the ErCe cluster. We have obtained an echo at 470 mT with a coherence time of about 410 ns. This fact shows that it is possible to perform quantum operations with the spins of these molecules.

These molecular clusters have, besides, the advantage of being stable in solution, which opens the possibility of depositing them onto devices able to manipulate its quantum spin state. Hence, to be able to process many atoms at a time, it is necessary to design an architecture that allows to tune each molecular cluster in or out resonance. This possibility will be explored in chapter 7.

Bibliography

[4.1] D. P. DiVincenzo, "Quantum computation," *Science*, vol. 270, p. 255, 1995.

[4.2] J. A. Jones and M. Mosca, "Implementation of a quantum algorithm on a nuclear magnetic resonance quantum computer," *Journal of Chemical Physics*, vol. 105, no. 5, p. 1648, 1998.

[4.3] Wikipedia.
`http://en.wikipedia.org/wiki/Cytosine` (last view 06/06/2015).

[4.4] A. Stute, B. Casabone, P. Schindler, T. Monz, P. O. Schmidt, B. Brandst'atter, T. E. Northup, and R. Blatt, "Tunable ion-photon entanglement in an optical cavity," *Nature*, vol. 485, p. 482, 2012.

[4.5] J. Clarke and F. K. Wilhelm, "Superconducting quantum bits," *Nature*, vol. 453, p. 1031, 2008.

[4.6] B. L. Lynn Yarris.
`http://newscenter.lbl.gov/2013/06/05/hyperpolarized-nuclei-in-diamond/` (last view 07/06/2015).

[4.7] F. de Martini, V. Buzek, F. Sciarrino, and C. Sias, "Experimental realization of the quantum universal NOT gate," *Nature*, vol. 419, p. 815, 2002.

[4.8] D. Porras and J. I. Cirac, "Effective quantum spin systems with trapped ions," *Physical Review Letters*, vol. 92, no. 20, p. 207901, 2004.

[4.9] D. Leibfried, E. Knill, S. Seidelin, J. Britton, R. B. Blakestad, J. Chiaverini, D. B. Hume, W. M. Itano, J. D. Jost, C. Langer, R. Ozeri, R. Reichle, and D. J. Wineland, "Creations of a six-atom "Schrödinger cat" state," *Nature*, vol. 438, 2005.

[4.10] A. Friedenauer, H. Schmitz, J. Glueckert, D. Porras, and T. Schaetz, "Simulating a quantum magnet with trapped ions," *Nature Physics*, vol. 4, p. 757, 2008.

[4.11] A. O. Niskamen, K. Harrabi, F. Yoshirara, Y. Nakamura, S. Lloyd, and J. S. Tsai, "Quantum coherent tunable coupling of superconducting qubits," *Science*, vol. 316, p. 723, 2007.

[4.12] J. H. Plantenberg, P. C. de Groot, C. J. P. M. Harmans, and J. E. Mooij, "Demonstration of controlled-NOT quantum gates on a pair of superconducting quantum bits," *Nature*, vol. 447, p. 836, 2007.

[4.13] A. Wallraff, D. I. Schuster, A. Blais, L. Frunzio, R. S. Huang, J. Majer, S. Kumar, S. M. Girvin, and R. J. Schoelkopf, "Strong coupling of a single photon to a superconducting qubit using circuit quantum electrodynamics," *Nature*, vol. 431, p. 162, 2004.

[4.14] G. Burkard, D. Loss, and D. P. DiVincenzo, "Coupled quantum dots as quantum gates," *Phys. Rev. B*, vol. 59, no. 3, p. 2070, 1999.

[4.15] R. Hanson and D. D. Awschalom, "Coherent manipulation of single spins in semiconductors," *Nature*, vol. 453, p. 1043, 2008.

[4.16] J. R. Weber, W. F. Koehl, J. B. Varley, A. Janotti, B. B. Buckley, C. G. V. de Walle, and D. D. Awschalom, "Quantum computing with defects," *Proc. Natl. Acad. Sci. U. S. A.*, vol. 107, no. 19, p. 8513, 2010.

[4.17] R. Sessoli and D. Gatteschi, "Single-molecule magnets," *Angewandte Chemie*, vol. 42, no. 3, p. 268, 2003.

[4.18] J. R. Friedman, M. P. Sarachik, J. Tejada, and R. Ziolo, "Macroscopic measurement of resonant magnetization tunneling in high-spin molecules," *Phys. Rev. Lett.*, vol. 76, p. 3830, 1996.

[4.19] J. M. Hernández, X. X. Zhang, F. Luis, J. Bartolomé, J. Tejada, and R. Ziolo, "Field tuning of thermally activated magnetic quantum tunnelling in Mn_{12} - ac molecules," *Europhys. Lett.*, vol. 35, no. 4, p. 301, 1996.

[4.20] L. Thomas, F. Lionti, R. Ballou, D. Gatteschi, R. Sessoli, and B. Barbara, "Macroscopic quantum tunneling of magnetization in a single crystal of nanomagnets," *Nature*, vol. 383, p. 145, 1996.

[4.21] G. Christou, D. Gatteschi, D. N. Hendrickson, and R. Sessoli, "Single-molecule magnets," *MRS Bulletin*, vol. 25, p. 66, 2000.

[4.22] D. Aguilà, L. A. Barrios, F. Luis, A. Repollés, O. Roubeau, J. Teat, and G. Aromí, "Synthesis and Properties of a Family of Unsymmetric Dinuclear Complexes of Ln^{III} (Ln = Eu, Gd, Tb)," *Inorganic Chemistry*, vol. 49, p. 6784, 2010.

[4.23] K. W. H. Stevens, "Matrix elements and operator equivalents connected with the magnetic properties of rare earth ions," *Proc. Phys. Soc.*, vol. 65, p. 209, 1952.

[4.24] P. J. Alonso and J. I. Martínez, "Magnetic properties of a Kramers doublet. an univocal bridge between experimental results and theoretical predictions," *J. Magn. Reson.*, vol. 255, p. 1, 2015.

[4.25] C. P. J. Poole and H. Farach, *Theory of Magnetic Resonance*. New York: Wiley Interscience, 1972.

[4.26] A. Abragam and B. Bleaney, *Electron Paramagnetic Resonance of Transitions Ions*. Oxford, UK: Oxford University Press, 1970.

[4.27] J. S. Griffith, "Spin hamiltonian for even-electron systems having even multiplicity," *Physical Review*, vol. 132, no. 1, p. 316, 1963.

[4.28] J. L. García-Palacios, J. B. Gong, and F. Luis, "Equilibrium susceptibilities of superparamagnets: longitudinal and transverse, quantum and classical," *J. Phys.: Condens. Matter*, vol. 21, no. 45, p. 456006, 2009.

[4.29] R. L. Carlin, *Magnetochemistry*. Berlin: Springer, 1986.

[4.30] J. H. van Vleck, *The theory of electric and magnetic susceptibilities*. Oxford at the Clarendon Press, 1932.

[4.31] H. B. Callen, *Thermodynamics and an Introduction to Thermostatistics*. John Wiley & Sons, þ2 ed., 1985.

[4.32] D. A. Aguilà, L. A. Barrios, V. Velasco, O. Roubeau, A. Repollés, P. J. Alonso, J. Sesé, S. J. Teat, F. Luis, and G. Aromí, "Heterodimetallic [LnLn'] lanthanide complexes: toward a chemical design of two-qubit molecular spin quantum gates," *J. Am. Chem. Soc.*, vol. 136, p. 14215, 2014.

[4.33] C. J. Wedge, G. A. Timco, E. T. Spielberg, R. E. George, F. Tuna, S. Rigby, E. J. L. McInnes, R. E. P. Winpenny, S. J. Blundell, and A. Ardavan, "Chemical engineering of molecular qubits," *Phys. Rev. Lett.*, vol. 108, p. 107204, Mar 2012.

Chapter 5

Molecular prototypes for 3-qubit gates

5.1 Introduction

The next step in scaling up quantum computing inside a molecular magnet is to explore the possibility of realizing a 3-qubit gate. As we pointed up in chapter 4, some other candidates such as ionic traps [5.1] or superconducting qubits [5.2] have achieved this goal, performing operations over 3 qubits and beyond.

In this chapter a new cluster formed by a magnetic core of three ions is studied. This core contains two Cu^{2+} ions ($S = 1/2$) as qubits 1 and 3 and a lanthanide ion as qubit 2. Moving from spin dimers to spin trimers represents a great synthetic challenge in itself specially on account of the need of making all three qubits different from each other. For this reason, it has been not possible to achieve the chemical flexibility we had in the case of dimers, where we could choose the ions without changing the structure. In particular, we have chosen to study a CuErCu trimer, with three magnetic cores, and a CuLaCu trimer, with just two magnetic cores (to study the behaviour of copper). Synthetizing a molecular trimer with just the lanthanide as magnetic core (eg. a ZnErZn trimer) has proved to be unfeasible.

The inclusion of a third qubit opens up the possibility to study two different dimensions in quantum computing. On the one hand it allows us to study 3 qubit gates, such as the universal reversible CCNOT (Toffoli) and the CSWAP gate (Fredkin). On the other hand, we can explore the mechanisms for correcting quantum errors, which are highly related to decoherence and are based on performing identical operations over different identical qubits. 3-

qubit gates are interesting for this goal due to their appearance in some error correction schemes. Next two sections give a wider description for these two subject, related to the ideal and the real quantum computing. Section 5.4 and the following ones are devoted to the experimental study of spin trimers.

5.2 Universal 3-qubit gates: Toffoli and Fredkin

The same way that in classical computing universal gates (NAND and NOR) have three bits (two inputs and one output), universal gates for reversible quantum computing have also three qubits. Two well-known examples are Fredkin and Toffoli quantum gates, that we describe below.

The Toffoli gate, also known as CCNOT gate, consists of a reversible gate that flips the third qubit if and only if the first two qubits are both in state "1". Then, the state $|110\rangle$ turns into $|111\rangle$, whereas $|010\rangle$ remains unaffected. This can be expressed as the quantum operator:

$$TOFFOLI = \begin{pmatrix} 1 & 0 & 0 & 0 & 0 & 0 & 0 & 0 & 0 \\ 0 & 1 & 0 & 0 & 0 & 0 & 0 & 0 & 0 \\ 0 & 0 & 1 & 0 & 0 & 0 & 0 & 0 & 0 \\ 0 & 0 & 0 & 1 & 0 & 0 & 0 & 0 & 0 \\ 0 & 0 & 0 & 0 & 1 & 0 & 0 & 0 & 0 \\ 0 & 0 & 0 & 0 & 0 & 1 & 0 & 0 & 0 \\ 0 & 0 & 0 & 0 & 0 & 0 & 1 & 0 & 0 \\ 0 & 0 & 0 & 0 & 0 & 0 & 0 & 0 & 1 \\ 0 & 0 & 0 & 0 & 0 & 0 & 0 & 1 & 0 \end{pmatrix}$$

Figure 5.1(a) shows the icon for this gate. This gate is universal [5.3] and can serve alone for reversible computing. However it is quite common. in order to simplify the constructions, to use the ensemble of NOT-CNOT-TOFFOLI qugates as the universal reversible basis which means that any logical operation can be performed by only using these three gates. For instance, we can perform an AND operation with a Toffoli gate, an OR operation with Toffoli and NOT gates, and a FAN-OUT operation with a CNOT gate, as shown in Fig. 5.2.

The Fredkin gate, also known as CSWAP gate, consists of a reversible gate that performs a SWAP gate (defined in chapter 4) if and only if the first qubit is in state "1". For instance, the state $|110\rangle$ will turn into $|101\rangle$, whereas the state $|010\rangle$ will remain unchanged. This gate is represented by the quantum operator:

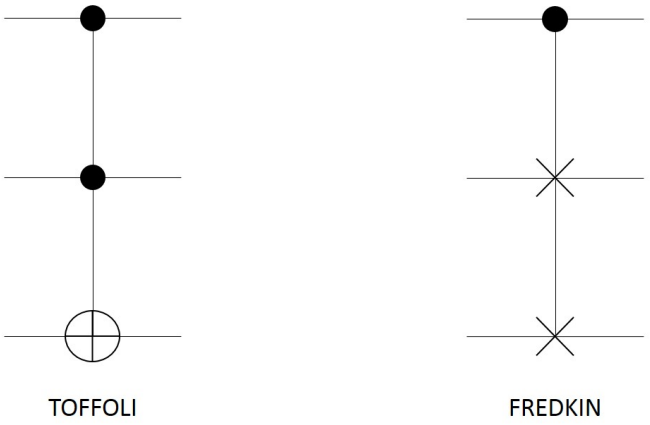

(a) (b)

Figure 5.1: a). Icon for Toffoli gate. b). Icon for Fredkin gate.

$$FREDKIN = \begin{pmatrix} 1 & 0 & 0 & 0 & 0 & 0 & 0 & 0 & 0 \\ 0 & 1 & 0 & 0 & 0 & 0 & 0 & 0 & 0 \\ 0 & 0 & 1 & 0 & 0 & 0 & 0 & 0 & 0 \\ 0 & 0 & 0 & 1 & 0 & 0 & 0 & 0 & 0 \\ 0 & 0 & 0 & 0 & 1 & 0 & 0 & 0 & 0 \\ 0 & 0 & 0 & 0 & 0 & 0 & 0 & 0 & 1 \\ 0 & 0 & 0 & 0 & 0 & 0 & 1 & 0 & 0 \\ 0 & 0 & 0 & 0 & 0 & 0 & 0 & 1 & 0 \\ 0 & 0 & 0 & 0 & 0 & 1 & 0 & 0 & 0 \end{pmatrix}$$

Figure 5.1(b) shows the icon for this gate. It plays an important role in quantum error correction as we explain in next section.

5.3 Quantum error correction

We have already talked about the necessity to have coherence in order to successfully perform quantum operations. However, in any realistic scenario, errors occur and ways to correct for them need to be implemented. In an ideal situation, qubits are supposed to evolve unitarily followingh Schrödinger's equation. But even in the case of a really high coherent system, there are uncontrolable factors, such as incoming stray particles or momentary coupling with the thermal bath, that can affect the computation.

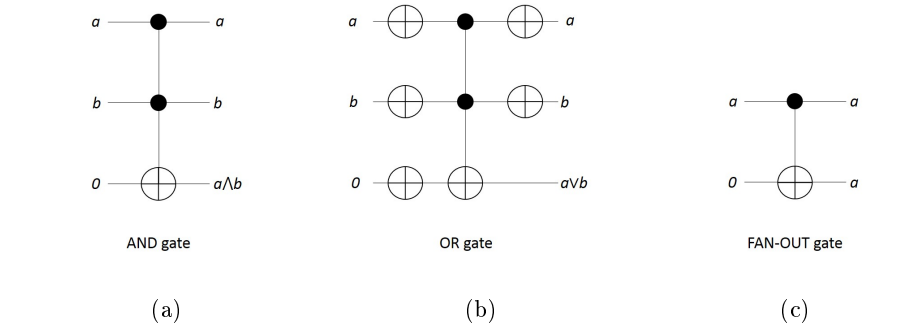

(a) (b) (c)

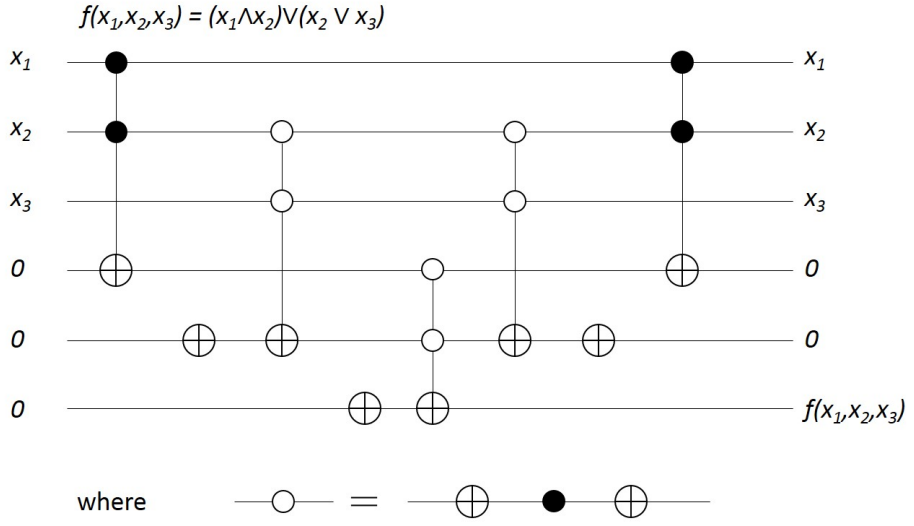

(d)

Figure 5.2: a). Icon for AND operation, made of a single Toffoli gate. b). Icon for OR operation, made of a single Toffoli gate and five NOT gates. c) Icon for FAN-OUT operation, made of a single CNOT gate. d). Example of computing via reversible substitution. Except for the operation in the middle, which writes the final result, the rest can be undone reversibly, saving the energy.

Errors are usually classified into two types: dissipation and decoherence. In a dissipation process, qubits interchange energy between them and flip in a spontaneous way. It is called bit flip error and can be described as

$$a\,|0\rangle + b\,|1\rangle \overset{\text{Bit Flip}}{\longrightarrow} b\,|0\rangle + a\,|1\rangle \tag{5.1}$$

Decoherence consists basically on the entanglement of the qubit state with that of the environment, provoking that a pure state becomes progressively a mixed state. It alters the relative phases of the computational basis, causing an error called phase shift error. This error evolves with time. For the state $a\,|0\rangle + b\,|1\rangle$, the density matrix evolves with time as

$$\rho(t) = \begin{pmatrix} |a|^2 & \mathrm{e}^{-t/\tau} ab^* \\ \mathrm{e}^{-t/\tau} a^* b & |b|^2 \end{pmatrix}$$

where τ is the decoherence time. It depends on many factors. The more important are the nature of the quantum system, the number of coupled qubits, the temperature and the rate of interactions with environmental degrees of freedom. Some of the intrinsic decoherence properties of various materials have been collected by David DiVincenzo in [5.4].

Unlike classical computing, where only bit flip errors can occur, in a qubit $a\,|0\rangle + b\,|1\rangle$, a and b span a continuum of values and errors become more subtle and insidious to detect. It can even happen that amplitudes $|a|$ and $|b|$ remain the same. Any error in a single qubit can be described as a linear combination of both errors. Nevertheless, phase shift errors become dominant in most cases, because the decoherence uses to be much shorter than the time needed for bit flip errors to appear, and therefore,

$$a\,|0\rangle + b\,|1\rangle \longrightarrow a\,|0\rangle + b\mathrm{e}^{\imath\phi}\,|1\rangle \tag{5.2}$$

A related difficulty is that it is not possible to read the state of a qubit while is being computed without necessarily and irreversibly perturbing the future curse of computations. Detecting and reducing errors seems therefore quite obscure. The most successful method for it comes from a variation of a classical method, based on replicated computations. This method establishes that if the individual chances of any one computing obtaining the "correct" answer is greater than 50%, then, if we replicate the same computation on many different computers, the probability of the majority vote being correct increases over 50%. The more replicas, the more probability [5.3].

This method can not be directly applied to quantum computing because it would destroy the computation. Instead of that two new ingredients are used:

entanglement and symmetrization [5.5]. If we have R replicas of the same quantum computation $|\phi(t)\rangle$, the joint state of all R computations would be the tensor product of all of them. Ideally, if there are no errors, all $|\phi(t)\rangle$ will be exactly the same. However, each quantum computation might experience some error which is in principle random and uncorrelated to those which affect the other computations. Then we have:

$$|\Psi(t)\rangle_{correct} = |\phi(t)\rangle \otimes |\phi(t)\rangle \otimes ... \otimes |\phi(t)\rangle \tag{5.3}$$

$$|\Psi(t)\rangle_{buggy} = |\phi(t)_1\rangle \otimes |\phi(t)_2\rangle \otimes ... \otimes |\phi(t)_R\rangle \tag{5.4}$$

If the joint state is projected into the symmetric subspace SYM, the correct part of the quantum computation is always guaranteed to lie within SYM,

$$\langle \Psi_{correct}| \, U_{SYM} \, |\Psi_{buggy}\rangle \tag{5.5}$$

As an example, we specified the case for one qubit, replicated three times. We need to place three additional ancillae (originally in state $|0\rangle$) in an equally weighted superposition. We use for that the following gates:

$$U_1 = \begin{pmatrix} \frac{1}{\sqrt{2}} & -\frac{1}{\sqrt{2}} \\ \frac{1}{\sqrt{2}} & \frac{1}{\sqrt{2}} \end{pmatrix}$$

$$U_2 = \begin{pmatrix} \frac{1}{\sqrt{3}} & 0 & -\sqrt{\frac{2}{3}} & 0 \\ \frac{1}{\sqrt{3}} & \frac{1}{\sqrt{6}} & \frac{1}{\sqrt{6}} & -\frac{1}{\sqrt{3}} \\ \frac{1}{\sqrt{3}} & -\frac{1}{\sqrt{6}} & \frac{1}{\sqrt{6}} & \frac{1}{\sqrt{3}} \\ 0 & \sqrt{\frac{2}{3}} & 0 & \frac{1}{\sqrt{3}} \end{pmatrix}$$

Then we apply permutations between the R individual quantum computers, conditioned on the weighted superposition of the ancillae, using Fredkin gates, described in previous section. After that, we undo the operations over the ancillae and measure them. If they come to the original state $|0\rangle$, then $|\Psi\rangle$ has been correctly projected into SYM and their errors have been corrected without needing to measured and disturbed it. Fig. 5.3 shows the circuit for correction errors.

Although Toffoli gate has been presented as the universal quantum gate in ideal quantum computing, we can observe here that the realization of a Fredkin gate is also crucial for real quantum computing due to its importance in quantum error correction.

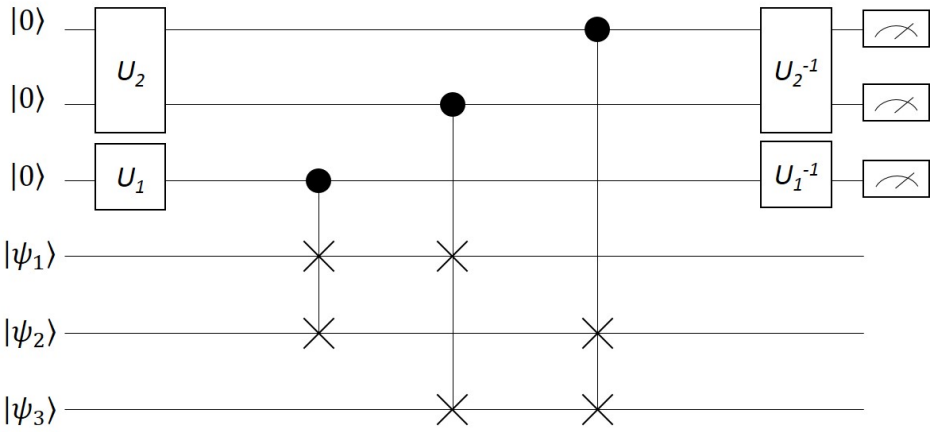

Figure 5.3: Quantum circuit for error correction via symmetrization for three replicas of 1 qubit. The full error symmetrization operator can be constructed as $U_{SYM_3} = (U_2^{-1} \otimes U_1^{-1} \otimes \mathbb{I}_8) \cdot \text{FREDKIN}_{1,5,6} \cdot \text{FREDKIN}_{2,4,6} \cdot \text{FREDKIN}_{3,4,5} \cdot (U_2 \otimes U_1 \otimes \mathbb{I}_8)$ where $\text{FREDKIN}_{i,j,k}$ means a Fredkin gate with control qubit i, and the SWAP between qubits j and k.

5.4 Experimental requirements for quantum gates

Requirements for building 3- qubit gates are quite similar to those described in section 4.2 for 2-qubit gates. The experimental candidate should have a sufficiently long coherence to perform many computations before the states decay and each qubit should be addressable. This point looks a bit more complicated than in the case of two qubits because three different qubits are needed. In the case of a Toffoli qugate, there are two control qubits and a target qubit, whereas in the case of Fredkin gate, there is just one control qubit and two target qubits.

Finally, there must exist an interaction between each two qubits, i.e., three different interaction terms instead of just one. Building entanglement between the three qubit means that these interaction terms must exist.

5.5 Synthesis and main characteristics of spin trimers

Spin trimers consist of a magnetic core of three ions, shielded by organic and non-magnetic molecules, as shown in Fig. 5.4. This molecular ligand

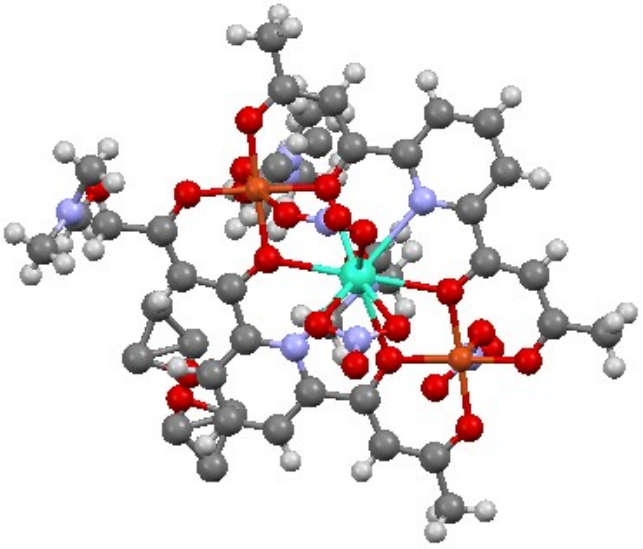

Figure 5.4: Molecular structure of trimers. White atoms are hydrogen, grey atoms are carbon, lilac atoms are nitrogen, red atoms are oxygen, orange atoms are copper and the turquoise atom is the lanthanide (lanthanum or erbium depending on the case).

shield determines the distances between ions and isolates the core from other molecules. To our work we have chosen a spin trimer whose core is formed by two Cu^{2+} ions and a lanthanide in the middle. This trimer synthesized for the first time in 2004 by T. Shiga and coworkers [5.6, 5.7]. The ligand 2,6 di(acetoacetyl)pyridine, commonly named L^{2-} is designed to have three metal-binding sites: two small terminal sites, designed to allocate two Cu^{2+} ions, and one large central site, designed to allocate a Ln^{3+} ion. The three ions are bridged by oxygen atoms.

Trimers are synthesized using L^{2-} ligands, $Cu(NO_3)_2$ and $Ln(NO_3)_3$. Thus, two L^{2-} ligands sandwich two Cu^{2+} ions and one Ln^{3+} ion, forming a nearly planar $\{Cu_2Ln(L)_2\}$ molecule with linear nuclei. Ln^{3+} ion has coordination 10, whereas Cu^{2+} have coordination 5 each (see Fig. 5.5).

Cu^{2+} ions have an angular momentum $J = S = 1/2$ and a gyromagnetic factor $g_S = 2.2$ [5.8]. It represents a natural two level system and can therefore act as a qubit. As central qubit, we have chosen the Er^{3+} ion, whose angular momentum is $J = 15/2$, with a gyromagnetic factor $g_J = 6/5$. As a Kramers ion, it has a ground state doublet that can also define the qubit basis states.

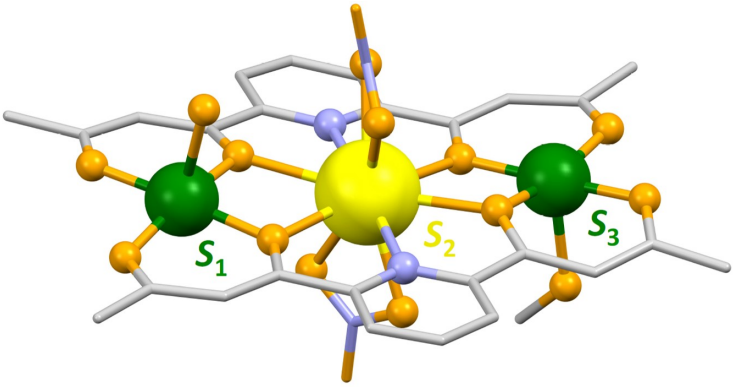

Figure 5.5: Detail of the molecular trimer. Cu^{2+} ions, in green, have coordination 5. Ln^{3+}, in yellow, has coordination 10. The three ions are aligned. Three spin-spin interaction terms are expected: a weak coupling between both Cu^{2+}, J_{13} and two weak couplings between Ln^{3+} and both Cu^{2+}, J_{12} and J_{23}.

In order to study separately the properties of Cu^{2+} ions, we have also studied a trimer formed by them and an ion of La^{3+} which does not have magnetic interaction due to its null angular momenta $J = 0$.

5.6 Spin Hamiltonian

As in the case of dimers, the Hamiltonian for each ion has two terms, the crystal field interaction term and the Zeeman term. There is also a third term that accounts for the interaction between the three spins. As shown in Fig. 5.5, we next label Cu^{2+} ions as 1 and 3, and Ln^{3+} as 2.

5.6.1 Single ion Hamiltonian

Crystal field interaction

Due to its spin S=1/2, Cu^{2+} does not have anisotropy because there is only one doublet that is split only by a magnetic field or by the interaction with other spins. As it was already discussed in chapter 4, La^{3+} ions are non magnetic. Therefore:

$$\mathcal{H}_{Cu_{cf}} = 0 \tag{5.6}$$

$$\mathcal{H}_{La_{cf}} = 0 \tag{5.7}$$

In the case of Er^{3+}, its anisotropy term coincides to that described in Eq. (4.10)

$$\mathcal{H}_{Er_{cf}} = \sum_{p} \sum_{q=-p}^{p} B_p^q(r) O_p^q(\vec{J}) \tag{5.8}$$

Zeeman interaction

La^{3+} is diamagnetic, thus

$$\mathcal{H}_{La_{Ze}} = 0 \tag{5.9}$$

while Cu^{2+} has a simple Zeeman term corresponding to a spin $S = 1/2$,

$$\mathcal{H}_{Cu_{Ze}} = -g_S \mu_B \vec{H} \vec{S} \tag{5.10}$$

where $\vec{H}$ is the magnetic field and $g_S \approx 2.2$ [5.8]. In the case of Er^{3+},

$$\mathcal{H}_{Er_{Ze}} = -g_J \mu_B \vec{H} \vec{J} \tag{5.11}$$

with $g_J = 6/5$.

The total Hamiltonian for each single ion is then,

$$\mathcal{H}_{La} = 0 \tag{5.12}$$

$$\mathcal{H}_{Cu} = -g_S \mu_B \vec{H} \vec{S} \tag{5.13}$$

$$\mathcal{H}_{Er} = \sum_{p} \sum_{q=-p}^{p} B_p^q(r) O_p^q(\vec{J}) - g_J \mu_B \vec{H} \vec{J} \tag{5.14}$$

As it was mentioned in section 4.5.2, if we only consider the ground state doublet, of Er^{3+}, its Hamiltonian can be written in terms of an effective spin 1/2 and hence [5.9],

$$\mathcal{H}_{Er_{eff}} = \mu_B \vec{H} \widetilde{g} \vec{S} \tag{5.15}$$

where $\widetilde{g}$ is an effective gyromagnetic tensor with principal axes x, y and z, and $S = 1/2$.

5.6.2 Spin-spin interaction terms

While the terms mentioned above are exactly the same as in the case of a molecular dimer, exchange interactions must be described with three different terms: one accounting for the interaction between the Cu^{2+} ions and two accounting for the coupling between Cu^{2+} and Er^{3+}, which are not necessarily equal to each other. In general, exchange Hamiltonian between two Kramers ions i and j can be written as [5.10],

$$\mathcal{H}_{ex} = -\vec{J}_i \widetilde{J}_{ij} \vec{J}_j \tag{5.16}$$

where $\widetilde{J_{ij}}$ is a tensor.

5.6.3 Spin Hamiltonian for CuLaCu

Because of the non-magnetic character of La^{3+}, the Hamiltonian reduces to the simply form,

$$\mathcal{H}_{CuLaCu} = \underbrace{-\widetilde{g}_1 \mu_B \vec{S_1} \vec{H}}_{ZeemanCu_1} \underbrace{-\widetilde{g}_3 \mu_B \vec{S_3} \vec{H}}_{ZeemanCu_3} \underbrace{-J_{13} \vec{S_1} \vec{S_3}}_{Ex\ term} \tag{5.17}$$

where g_i and J_{ij} have been taken as scalar coefficients. In the case of spin alignment, $g_1 = g_3$ and the Hamiltonian has an analytic solution. In terms of $|S_T\ S_z\rangle$,

$$\begin{aligned} E_{|0,0\rangle} &= 0 \\ E_{|1,-1\rangle} &= -J_{13} + g\mu_B H_z \\ E_{|1,0\rangle} &= -J_{13} \\ E_{|1,1\rangle} &= -J_{13} - g\mu_B H_z \end{aligned} \tag{5.18}$$

For $\vec{H} = 0$ the system presents two unique states which are separated by an energy $J_{1,3}$ that can be determined by measuring specific heat in a similar way it was determined in the case of dimers. Nevertheless, and although both magnetic Cu^{2+} ions are equal, their local principal axes could be misaligned. As we already saw in the case of Tb_2 this fact can be accounted for introducing different gyromagnetic factors for each ion. g_1 and g_3 can also be determined from susceptibility and specific heat data measured under different magnetic fields.

5.6.4 Spin Hamiltonian for CuErCu

The Hamiltonian of CuErCu must include the Hamiltonian for the single ion Er^{3+} and two additional interaction terms with its two Cu^{2+} neighbors:

$$\mathcal{H}_{CuErCu} \approx \mathcal{H}_{CuLaCu} + \mathcal{H}_{Er_{eff}} + \mathcal{H}_{ex_{12}} + \mathcal{H}_{ex_{23}} \tag{5.19}$$

where Er^{3+} is labelled as qubit 2. In Eq. (5.19) we have made the simplifying assumption that $\widetilde{g}_1$,$\widetilde{g}_2$ and J_{13} remain approximately the same as in the case of CuLaCu.

Considering only interactions between the ground state doublet of Er^{3+} and Cu^{2+} levels, $\mathcal{H}_{ex}$ can also be expressed in terms of two effective spins 1/2 as shown in section 4.5.2:

$$\begin{aligned} \mathcal{H}_{ex_{12}} &= -\frac{1}{g_{S_1} g_{J_2}} \vec{S}_1 \widetilde{g}_1 \widetilde{J}_{12} \widetilde{g}_2 \vec{S}_2 \\ \mathcal{H}_{ex_{23}} &= -\frac{1}{g_{J_2} g_{S_3}} \vec{S}_2 \widetilde{g}_2 \widetilde{J}_{23} \widetilde{g}_3 \vec{S}_3 \end{aligned} \tag{5.20}$$

5.7 Experimental study of molecular 3-qubit gates

The goal is to determine all parameters that define the magnetic response of CuErCu. We first address the simpler case of CuLaCu, which gives us access to the properties of each Cu^{2+} ion and their mutual coupling and, then, we proceed with the properties of CuErCu.

5.7.1 CuLaCu

Due to the diamagnetism of La^{3+}, CuLaCu is a system with only two spins, acting as qubits. In this aspect it is quite similar of dimers studied in chapter 4 and it could be also used for performing CNOT and SWAP operations over it. The goal therefore is to determine the gyromagnetic factors of both copper ions, g_1 and g_3 (~ 2.2 in the literature [5.8]) and the interaction constant $J_{1,3}$, from the Hamiltonian for this system, described by Eq. (5.17).

Figure 5.6(a) shows specific heat measurements obtained at zero field. The data show a peak at around 0.45 K, similar to a Schottky-like anomaly [5.11], which indicates the existence of a coupling between the two Cu^{3+} ions, separated by an energy $\Delta E = 4\,|J_{13}|\,S^2 \approx 1.1$ K. The anomaly reflects the energy splitting between states with overal $S = 0, 1$, thus a singlet and a triplet. Simulation for both signs of J_{13} shows that it is negative and coupling is, therefore,

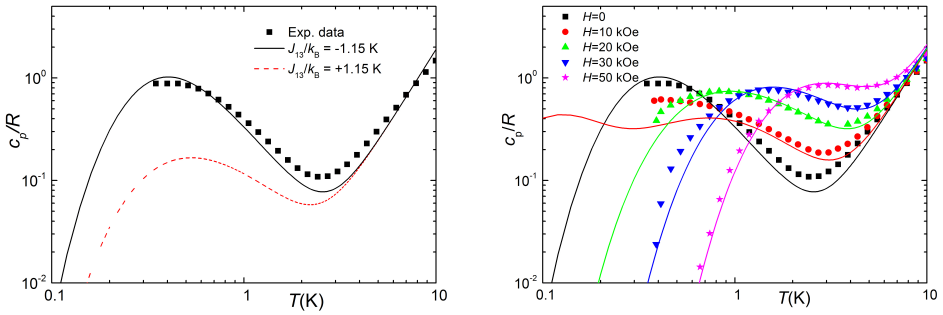

(a) (b)

Figure 5.6: a) Specific heat at zero magnetic field. Lines represent the simulations for $J_{1,3} = \pm 1.15 k_{\mathrm{B}}$. The black line accords to the experimental data, showing that the coupling is antiferromagnetic. b) Specific heat at different magnetic fields. Lines represent the simulations for $J_{1,3} = -1.15 k_{\mathrm{B}}$ and an average $g = 2.16$.

antiferromagnetic. Specific heat data (Fig. 5.6(b)) measured at different magnetic fields allows us to properly fit $J_{13}/k_{\mathrm{B}} = -1.15$ K and an average value for $\bar{g} = 2.16$, in very good agreement with the literature [5.8]. All specific heat curves agree well with these values except for $H = 1$ kOe, where the proximity of the crossing between states $|\uparrow\uparrow\rangle$ and $|\uparrow\downarrow\rangle - |\downarrow\uparrow\rangle$ probably brings to the fore the effects of additional interactions, such as dipolar coupling between molecules or hyperfine interactions.

The drop observed in susceptibility measurements, shown in Fig. 5.7(a), also confirms the antiferromagnetic coupling. In the high temperature limit, $\chi T \approx 0.875$ cm^{3}K/mol tends to the paramagnetic limit

$$\chi T = \frac{N_{\mathrm{A}} \mu_{\mathrm{B}}^2 S^2 (\bar{g}^2 + \bar{g}^2)}{k_{\mathrm{B}}} \tag{5.21}$$

with $\bar{g} = 2.16$. In the very low temperature regime, χ vs T representation, in Fig. 5.7(b), shows that susceptibiliy does not go to zero, which would correspond to a perfect antiferromagnetic coupling. This means that Cu^{2+} are nonequivalent. As well as in the case of Tb_2 and Dy_2, this can be implement by considering two proportional gyromagnetic factors that agree with the paramagnetic limit,

$$\begin{aligned} g_1 &= k g_3 \\ g_1^2 + g_3^2 &= \bar{g}^2 + \bar{g}^2 \end{aligned} \tag{5.22}$$

Figure 5.7(b) shows the best fit for $k = 0.7$ and, therefore, $g_1 = 1.63$ and $g_3 = 2.34$. Considering that $k = \cos\delta$, z axes of Cu^{2+} ions could be misaligned

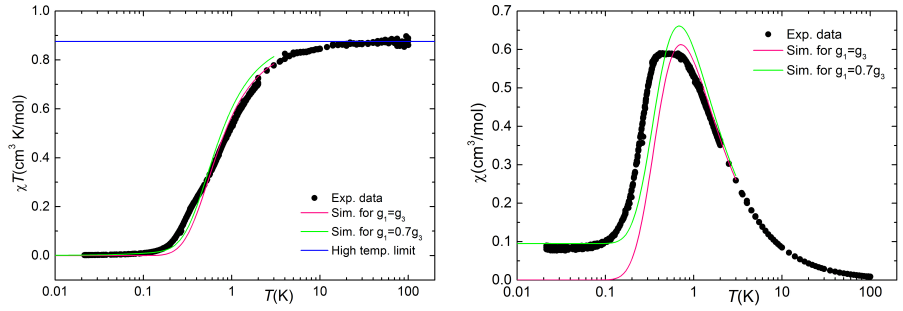

(a) (b)

Figure 5.7: a) χT experimental data from 20 mK to 100 K. Blue line indicates the high temperature limit for $g = 2.16$. Pink and green lines show the fitting for $g_1 = g_3$ and $g_1 = 0.7g_3$ respectively. b) χ vs. T representation of the experimental data. It shows clearly that, at very low temperatures the magnetic moment does not vanish, which means that copper spins antiferromagnetic coupling is not complete and, therefore, they are not equivalent.

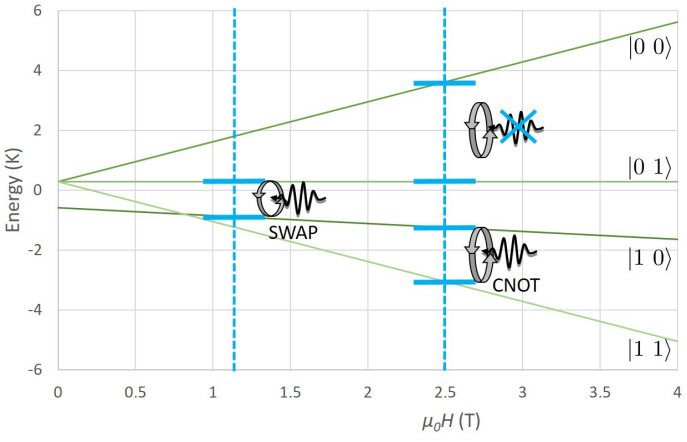

Figure 5.8: Full energy level scheme for CuLaCu, assuming that $J_{1,3}/k_{\mathrm{B}} = -1.15$ K, $g_1 = 1.63$ and $g_3 = 2.34$.

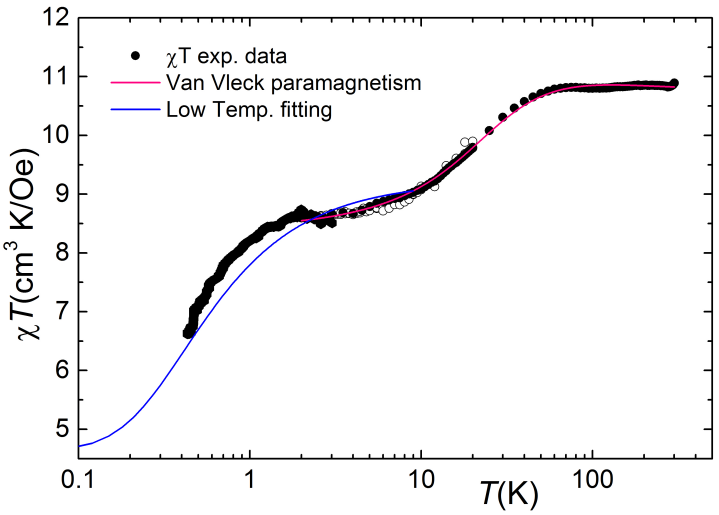

Figure 5.9: χT experimental data for CuErCu trimer. It shows a first drop, associated to the depopulation of excited energy levels and a second one, associated to the coupling between Cu^{2+} ions.

by $\delta \approx 45.6^{o}$. The fact that both ions are distinguishable allows us to well define a qubit basis for performing CNOT and SWAP operations, as shown in Fig. 5.8.

5.7.2 CuErCu

Once we have obtained information about the role of the Cu^{2+} ions, next step is introducing the Er^{3+} effects. The CuErCu trimer has the same structural characteristics as CuLaCu and it is possible to start considering right the parameters from the previous section: $J_{13}/k_{\mathrm{B}} = -1.15$ K, $g_1 = 1.63$ and $g_3 = 2.34$. Therefore only J_{12}, J_{23} and $\widetilde{g}_2$ from the Hamiltonian described in Eq. (5.19) remain unknown.

Figure 5.9 shows the magnetic susceptibility of the CuErCu dimer. In the high temperature regime, susceptibility is much larger than that of CuLaCu, shown in Fig. 5.7(a). This reveals the presence of Er^{3+}, whose angular momentum is much higher. The Van Vleck formula of the high-T susceptibility (see Eq. (4.34)) allows us to obtain the energy difference Ω between the ground

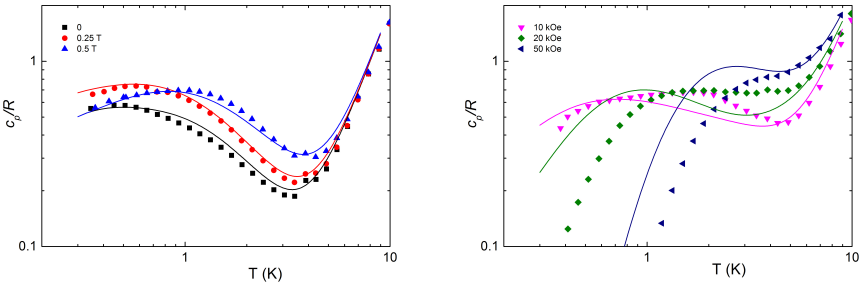

Figure 5.10: a) Specific heat data for $H < 0.5$ T. Lines are theoretical fits for $J_{12} = -0.28$ K, $J_{13}/k_B = -1.15$ K, $g_1 = 1.63$ and $g_3 = 2.34$. b) Specific heat data for $H > 0.5$ T. Lines are theoretical values for these parameters.

state doublet and the first excited state. The total fit has been done considering both contributions, from Cu^{2+} and Er^{3+},

$$\begin{aligned} \Omega/k_B &= 82.60 \text{ K} \\ C_0 &= 12.81 \\ C_1 &= 5.83 \\ C_2 &= 1.27 \end{aligned} \tag{5.23}$$

Due to the very different molecular geometry, $\Omega/k_B = 82.60$ K has nothing to do with that determined for ErLa dimer. Ground state does not coincide either. In the range between 2 K and 8 K, only the ground state doublet of Er^{3+} is populated, whereas Cu^{2+} are still in the paramagnetic regime. For this case we have $\mu_{eff} = 8.35\mu_B$. Comparing with theoretical

$$\mu_{eff} = \mu_B \sqrt{g_1^2 S(S+1) + g_3^2 S(S+1) + g_2^2 J^2} \tag{5.24}$$

and considering $g_2 = g_{Er} = 6/5$ we get $\langle J_z \rangle = \pm 6.6 \approx \pm 13/2$.

Below 2 K, a new drop appears. This drop coincides in temperature with the coupling between the two Cu^{2+} ions we have seen in section 5.7.1, an can therefore be associated to the same phenomenon. Coupling between Cu^{2+} and Er^{3+} is not reflected on the experimental data, which means that J_{12} and J_{23} must be very weak and it should appear at lower temperatures.

Specific heat data does not provide either much information about J_{12} and J_{23}. For small magnetic fields ($H < 0.5$ T) fits agree reasonably well with $J_{12} = J_{23} = -0.28$ K, as it is shown in Fig. 5.10(a), but fails for higher magnetic fields. Figure 5.10(b) shows some examples of this. Some qualitative

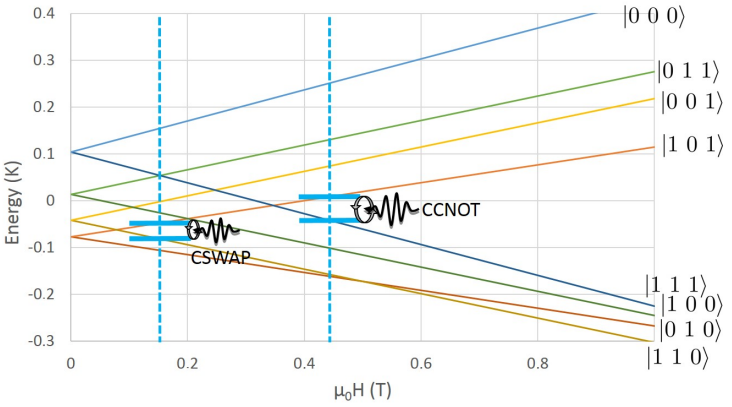

Figure 5.11: Full energy level scheme for CuErCu, assuming that $J_{12} = -0.28$ K, $J_{13}/k_B = -1.15$ K, $g_1 = 1.63$ and $g_3 = 2.34$, which is valid for $H < 0.5$ T.

description of the data can be obtained, but it does not fit properly. The sign of J_{12}, J_{23} reveals a weak antiferromagnetic coupling between Cu^{2+} and Er^{3+} ions, in disagreement with [5.7]. This suggests that J_{12} and J_{23} are very weak and that specific heat data are probably reflecting other unknown interactions such as hyperfine or intermolecular coupling at very low T or the influence of excited states at very high fields. On the other hand it could also occur that J_{13}, g_1 and g_2 also changes due to the presence of Er^{3+} and, then, more experimental measurements are necessary. Further measurements, such as low temperature ac susceptibility and EPR will provide a better values for all these parameters.

Figure 5.11 shows the energy levels splitting for low magnetic fields. The existence of three different qubits allows to perform a CCNOT gate, by using the copper qubits as control qubits and the erbium qubit as the control one. CSWAP is also possible by using copper-1 as a control qubit and exchanging states of erbium and copper-3.

5.8 Conclusions

In this chapter we have studied the properties of molecular trimers CuLaCu and CuErCu, to determine whether they can be used as molecular quantum gates. Their low temperature energy level diagrams have been determine on basis of the modelization of magnetic susceptibility and heat capacity.

The Cu^{2+} ions in CuLaCu are weakly antiferromagnetically coupled, with an exchange interaction parameter $J_{13}/k_B = -1.15$ K, and have significantly different gyromagnetic factors ($g_1 = 1.63$ and $g_3 = 2.34$), which make them

valid for performing 2-qubit gates such as CNOT or SWAP gates, at high fields and frequencies.

In CuErCu we have found that ground state doublet $m_J = \pm 13/2$ differs from that found in ErLa monomer, probably due to the totally different molecular geometry. The large separation between the ground state doublet and the excited ones (more than 82 K) allows Er^{3+} to act as an effective spin 1/2, very weakly coupled to the Cu^{2+} ions. This antiferromagnetic coupling has not been properly stimated due to its weakness, although it is valid at low magnetic fields and frequencies, making possible the realization of 3-qubit gates, such as CCNOT and CSWAP gates.

Further work on this topic involves a better definition of the coupling parameters, J_{12}, J_{23} and J_{13}, as well as a study of the coupling of these molecules to superconducting resonators.

Bibliography

[5.1] D. Leibfried, E. Knill, S. Seidelin, J. Britton, R. B. Blakestad, J. Chiaverini, D. B. Hume, W. M. Itano, J. D. Jost, C. Langer, R. Ozeri, R. Reichle, and D. J. Wineland, "Creations of a six-atom "Schrödinger cat" state," *Nature*, vol. 438, 2005.

[5.2] A. O. Niskamen, K. Harrabi, F. Yoshirara, Y. Nakamura, S. Lloyd, and J. S. Tsai, "Quantum coherent tunable coupling of superconducting qubits," *Science*, vol. 316, p. 723, 2007.

[5.3] C. P. Williams, *Explorations in quantum computing.* London: Springer, þ2 ed., 2011.

[5.4] D. P. DiVincenzo, "Quantum computation," *Science*, vol. 270, p. 255, 1995.

[5.5] A. Barenco, A. Berthiaume, D. Deutsch, A. Ekert, R. Jozsa, and C. Macchiavello, "Stabilisation of quantum computations vy symmetrisation," *SIAM Journal on computing*, vol. 26, no. 5, p. 1541, 1997.

[5.6] T. Shiga, M. Ohba, and H. Okawa, "A series of trinuclear $Cu^{II}Ln^{III}Cu^{II}$ complexes derived from 2,6-Di(acetoacetyl)pyridine: Synthesis, Structure, and Magnetism," *Inorg. Chem.*, vol. 43, no. 14, p. 4435, 2004.

[5.7] T. Shimada, A. Okazawa, N. Kojima, S. Yoshii, H. Nojiri, and T. Ishida, "Ferromagnetic exchange cocoupling showing a chemical trend in Cu-Ln-Cu complexes (Ln = Gd, Tb, Dy, Ho, Er)," *Inorg. Chem.*, vol. 50, p. 10555, 2011.

[5.8] A. Abragam and B. Bleaney, *Electron Paramagnetic Resonance of Transitions Ions*. Oxford, UK: Oxford University Press, 1970.

[5.9] P. J. Alonso and J. I. Martínez, "Magnetic properties of a Kramers doublet. an univocal bridge between experimental results and theoretical predictions," *J. Magn. Reson.*, vol. 255, p. 1, 2015.

[5.10] D. A. Aguilà, L. A. Barrios, V. Velasco, O. Roubeau, A. Repollés, P. J. Alonso, J. Sesé, S. J. Teat, F. Luis, and G. Aromí, "Heterodimetallic [LnLn'] lanthanide complexes: toward a chemical design of two-qubit molecular spin quantum gates," *J. Am. Chem. Soc.*, vol. 136, p. 14215, 2014.

[5.11] H. B. Callen, *Thermodynamics and an Introduction to Thermostatistics*. John Wiley & Sons, þ2 ed., 1985.

Chapter 6

Quantum spin relaxation in molecular dimers

6.1 Introduction

Quantum coherence is one of the basic ingredients for quantum computing. We can describe coherence as the ability of a quantum state to maintain its pure quantum evolution for a certain time [6.1, 6.2]. The larger this time, the more robust the system is against external perturbations. A "pure" coherent state, would occur only in a completely isolated system, which is not physically possible [6.3]. An extremely isolated real system can have, nevertheless, very long coherence times. Concerning quantum computing, quantum coherence times must be orders of magnitude longer than the time required to perform an individual quantum operation [6.4]. Some experimental candidates such as superconducting qubits [6.5], ion traps [6.6] or semiconductor quantum dots [6.7], already show long enough coherent times to perform certain quantum operations.

Single Molecule Magnets are magnetic moments shielded by organic, non-magnetic structures that keep them away from external interactions. This lattice, however, vibrates with temperature and produces phonons that might interact with the magnetic moments [6.8].

The group of processes whereby a quantum state loses its coherence are called as relaxation processes [6.9, 6.10]. There exists mainly two types of relaxation processes: those in which the spins energy does not vary, which are called Spin-Spin Relaxation (SSR) and those which require an exchange of energy, which are called Spin-Lattice Relaxation (SLR).

In this chapter we offer a brief description of these processes, emphasizing those related to SLR processes, which are the most relevant in our research and which represent the ultimate limit to quantum coherence, once the influence of SSR processes has been minimized. In particular we are interested in exploring the influence on the characteristic relaxation time τ of hyperfine and spin-spin couplings. We also explore pure quantum tunneling processes whose role on SLR is not well understood yet. To carry out this study, we analyze different samples, beginning with monomers of lanthanide ions with different nuclear spin concentrations and continuing with dimers. In this manner, the influence of different interactions can be studied separately in detail.

6.2 Relaxation processes

Relaxation processes are classified into two types. Spin-Spin relaxation (SSR) and Spin-Lattice relaxation (SLR).

Spin-spin relaxation or spin flip-flop processes is similar to the bit flip process we described in section 5.3. Two spins flip their states so that,

$$|\uparrow\downarrow\rangle \longrightarrow |\downarrow\uparrow\rangle \tag{6.1}$$

This process does not change the energy of the global system, nor the populations. This flip however induces small fluctuations on the local dipolar field, and can therefore slightly modify the phase, of a third spin placed in the neighbourhood, thus changing its quantum state. The characteristic relaxation time for this process is usually referred to as T_2 and it remains active down to very low temperatures [6.11, 6.12].

In a Spin-Lattice relaxation process [6.13], the populations of the spin system energy levels evolve towards a thermal equilibrium in which they obey Boltzmann's law [6.14]. Then, the spin temperature $T_S = \epsilon_{ab}/k_B \ln(n_a/n_b)$, which is related to the populations of two different energy levels n_a, n_b and to the difference of energies ϵ_{ab} between them, approaches the temperature of the lattice that is supposed to be in good thermal equilibrium with a thermal bath (e.g. our cryostat or the mixing chamber of a dilution refrigerator).

Spin-lattice relaxation is mostly produced by the interaction between the spin system and its environment. The local coordination of each spin creates a crystalline field. Lattice vibrations (or phonons) modulate deformations of this coordination that couple to the spin via the spin-orbit interaction. This modulations introduce dynamic terms in the spin Hamiltonian that are forbidden for the static lattice [6.15]. This dynamic lattice can then induce transitions between different spin states. The characteristic relaxation time for this process is often referred to as T_1 and can be directly measured from ac magnetic

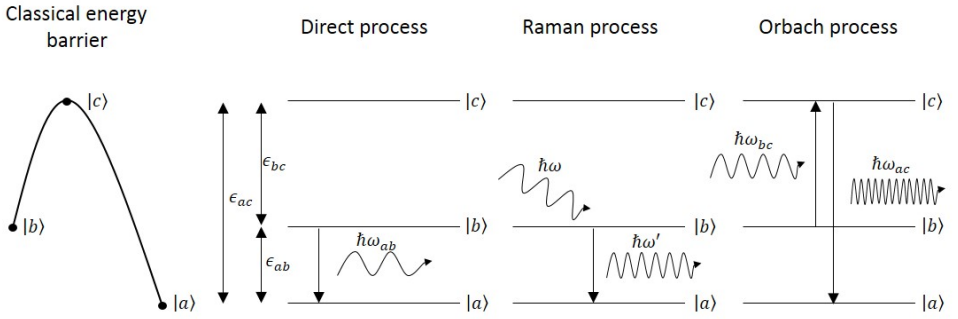

Figure 6.1: Schematic representation of the three relaxation processes, assuming a three-level system: direct, Orbach and Raman. The first image shows the classical model for a potential barrier.

measurements. In the following we describe the main spin-lattice relaxation processes that are usually relevant in the case of lanthanide ions.

6.2.1 Spin-Lattice relaxation mechanisms

SLR is dominated by transitions linking the two lowest-lying magnetic states. There exist three well-known ways for phonons to interact with the quantum spin states. Which of these is dominant depends on temperature and magnetic field [6.13]. To describe them, let's assume first a spin system with only three energy levels, $|a\rangle$, $|b\rangle$ and $|c\rangle$ as shown in Fig. 6.1.

Direct process

A direct process consists of the absorption or emission of a single phonon to pass from one state (say $|a\rangle$) to another (say $|b\rangle$) [6.16]. The phonon energy must match the energy difference between both levels,

$$\epsilon_b = \epsilon_a + \hbar\omega_{ab} \Longrightarrow \epsilon_{ab} = \hbar\omega_{ab} \tag{6.2}$$

The direct process involves only two spin states and just one phonon. For a two-level system [6.17]

$$\mathrm{T}_{1\mathrm{D}}^{-1} \propto \epsilon_{\mathrm{ab}}^{\gamma} \coth\left(\frac{\epsilon_{\mathrm{ab}}}{\mathrm{k_B T}}\right) \tag{6.3}$$

where T is the temperature and the exponent $\gamma = 5$ for Kramers ions and $\gamma = 3$ for non-Kramers ions. This equation is valid for sufficiently low T, such that

the population of excited levels above $|b\rangle$ (e.g. $|c\rangle$) can be safely neglected. In the region $\epsilon_{ab} \ll k_{\mathrm{B}}T \ll \epsilon_{bc}$, $\mathrm{T}_{1\mathrm{D}}^{-1}$ depends linearly on temperature. For $k_{\mathrm{B}}T \ll \epsilon_{ab}$ it tends to a constant value as shown in Fig. 6.2.

Direct processes also depend strongly on the applied magnetic field H. For Kramers ions $\mathrm{T}_{1\mathrm{D}}$ vanishes at $H = 0$ because the ground level is degenerated. For $H \neq 0$, it depends on the fourth power of the applied field [6.13]:

$$\mathrm{T}_{1\mathrm{D}}^{-1} \propto \mathrm{H}_0^4 \tag{6.4}$$

For non-Kramers ions, however, the dependence occurs on the second power of H.

Raman process

This process involves the inelastic scattering of an incoming phonon. It consists of the absorption of a phonon of energy $\hbar\omega$ that causes a level transition to a virtual state, followed by the emission of another phonon with a higher energy $\hbar\omega'$ [6.18]. The net energy released from the transition matches ϵ_{ab}:

$$\hbar\omega + \epsilon_{ab} = \hbar\omega' \tag{6.5}$$

This process involves two phonons instead of one. It strongly depends on T because its probability is determined by the density of phonons populated at each temperature. According to theory, it depends very weakly on magnetic field. For a Kramers ion,

$$\mathrm{T}_{1\mathrm{R}}^{-1} \propto \mathrm{T}^9 \frac{1 + \mathrm{p}\alpha\mathrm{H}^2}{1 + \alpha\mathrm{H}^2} \tag{6.6}$$

where α is a parameter which includes the Curie constant and the magnetic specific heat at zero field. For non-Kramers ions, $\mathrm{T}_{1\mathrm{R}}^{-1}$ depends on the seventh power of T.

Orbach process

The Orbach process is also a two-phonon process. It involves a real transition to an excited state $|c\rangle$ whose energy is a quantity ϵ_{bc} above the ground doublet defined by states $|a\rangle$ and $|b\rangle$ [6.19]. In the easiest case, with only three levels involved, state $|b\rangle$ absorbs a phonon of energy $\epsilon_{bc} = \hbar\omega_{bc}$ and evolves to an

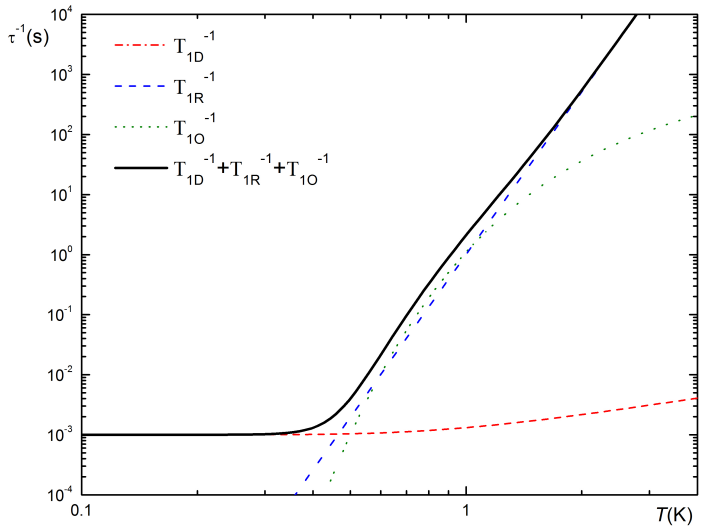

Figure 6.2: Relaxation rate calculated with Eq. (6.11) for the arbitrarily chosen values $\epsilon_{ab}/k\mathrm{B} = 1$ K, $\epsilon_{bc}//k\mathrm{B} = 7$ K, $\alpha_D = 0.001$, $\alpha_O = 3.5$ and $\alpha_R = 1$. Orbach and Raman processes compete at high temperatures.

excited state $|c\rangle$. Then, it emits a phonon and relaxes to the ground state $|a\rangle$. Conservation of energy gives

$$\epsilon_b + \hbar\omega_{bc} = \epsilon_c = \epsilon_a + \hbar\omega_{ac} \tag{6.7}$$

This process is thermally activated and competes with the Raman process at high temperatures. Its probability depends exponentially on the ratio between the energy gap ϵ_{bc} and $k_\mathrm{B}T$:

$$\mathrm{T}_{1\mathrm{O}}^{-1} \propto \epsilon_{\mathrm{bc}}^{3} \mathrm{e}^{\frac{-\epsilon_{\mathrm{bc}}}{\mathrm{k_B T}}} \tag{6.8}$$

This expression coincides with an Arrhenius law,

$$\tau(T)^{-1} = \tau_0^{-1} \mathrm{e}^{\frac{-U}{k_\mathrm{B} T}} \tag{6.9}$$

commonly used in other physical and chemical processes that depend on temperature, such as the variation of diffusion coefficients, population of crystal vacancies or chemical reaction rates. In our case the prefactor τ_0 is the relaxation time limit for infinite temperature and U is the activation energy.

The overall relaxation rate τ^{-1}, which can be measured on a particular sample, can be written in principle as a sum of these three contributions,

$$\tau^{-1} = \mathrm{T}_{1\mathrm{D}}^{-1} + \mathrm{T}_{1\mathrm{R}}^{-1} + \mathrm{T}_{1\mathrm{O}}^{-1} \tag{6.10}$$

For Kramers ions the three processes give:

$$\tau^{-1} = \alpha_D \epsilon_{ab}^5 \coth\left(\frac{\epsilon_{ab}}{k_\mathrm{B}T}\right) + \alpha_O \epsilon_{bc}^3 \exp\left(-\frac{\epsilon_{bc}}{k_\mathrm{B}T}\right) + \alpha_R T^9 \tag{6.11}$$

where α_D, α_O and α_R are parameters independent on T for direct, Orbach and Raman processes respectively. Figure 6.2 shows that direct processes dominate at low temperatures whereas Raman and Orbach compete at high temperatures.

Reality is, however, not so simple because our samples have more than three levels and relaxation processes, specially direct and Orbach processes, can occur for phonons of different energies depending on the target level. That implies a more complex treatment, which was deeply considered in [6.20,6.21], and does not take part of this work.

Pure quantum spin tunneling

There are also some other SLR processes, probably induced by off-diagonal terms of the spin Hamiltonian, which have not been totally explained yet. Raman and Orbach processes, described above, are expected to die rapidly out for $T \leq 1$ K. On the other hand, direct processes have a very low probability for $H \to 0$, when also ϵ_{ab} vanishes. Research with Single Molecule Magnets [6.14, 6.22] reveals, however, that below $T = 1$ K some relaxation processes, which are independent of temperature, remain active. These processes have been associated to a phenomenon of pure quantum tunneling through the anisotropy energy barrier [6.22]. The existence of these quantum tunneling processes are usually associated with hyperfine couplings and dipolar spin-spin interactions.

For a Kramers ion, at zero field, the ground state doublet is degenerated, thus the tunneling splitting vanishes and tunneling is forbidden. However, dipolar interactions with electronic spins in the neighborhood and hyperfine couplings with nuclear spins, split the doublet by the amount

$$\Delta\epsilon = \left(\Delta^2 + \xi_{\mathrm{dip}}^2\right)^{1/2} \tag{6.12}$$

where $\Delta \leq 1$ mK is the quantum tunnel splitting associated with transverse dipolar and hyperfine couplings and ξ_{dip} is the dipolar bias. Prokof'ev and Stamp proposed that flip-flop transitions between nuclear spins can generate a dynamic component for the dipolar bias that carry electronic spins to resonance conditions, allowing spin tunneling [6.11]. Tunneling relaxation rates $\mathrm{T_T}$

depend on the distribution of dipolar energy bias $P(\xi_{\mathrm{dip}})$ and on the quantum tunneling splitting Δ

$$\mathrm{T}_{\mathrm{T}}^{-1} = \frac{\Delta^2}{\hbar}\mathrm{P}(\xi_{\mathrm{dip}}) \tag{6.13}$$

6.2.2 Experimental methods for measuring relaxation processes

Our main interest is to measure Spin-Lattice relaxation times in a broad temperature range. It's important to keep in mind that our dimers contain lanthanides which have many energy levels, not only electronic but also nuclear ones, and relaxation times could be composed by many different relaxation processes.

τ can be obtained from ac susceptibility measurements as a function of temperature and applied frequency. In this chapter we have used three experimental methods, described below, to obtain τ.

Direct measurement from χ vs. T measurements

In measurements at $f = \omega/2\pi = constant$, exchanges of energy between the spins and the lattice are shown as a peak of the imaginary part of susceptibility χ'', corresponding to an absorption of energy by the former. The peak indicates the temperature at which $\omega \approx \tau^{-1}$ and relaxation processes become visible in the measurement. The real part χ' also shows a transition between the equilibrium susceptibility χ_{T} and the adiabatic susceptibility, χ_{S}.

χ vs. f measurements

For a spin system with just one relaxation time, isothermal curves can be treated by the Debye theory for relaxation processes [6.23]. The complex susceptibility then equals

$$\chi^* = \chi' - \mathrm{i}\chi'' = \chi_{\mathrm{S}} + \frac{\chi_{\mathrm{T}} - \chi_{\mathrm{S}}}{1 + (\mathrm{i}\omega\tau)^2} \tag{6.14}$$

We show how this curve looks like in Fig. 3.7, where we first introduce the magnetic susceptometry. The transition vetween isothermal and adiabatic responses takes place at $\omega\tau \simeq 1$. The drop $\Delta\chi = \chi_{\mathrm{T}} - \chi_{\mathrm{S}}$ follows approximately a Curie - Weiss law [6.24]

$$\Delta\chi \approx \frac{C}{T - \theta} \tag{6.15}$$

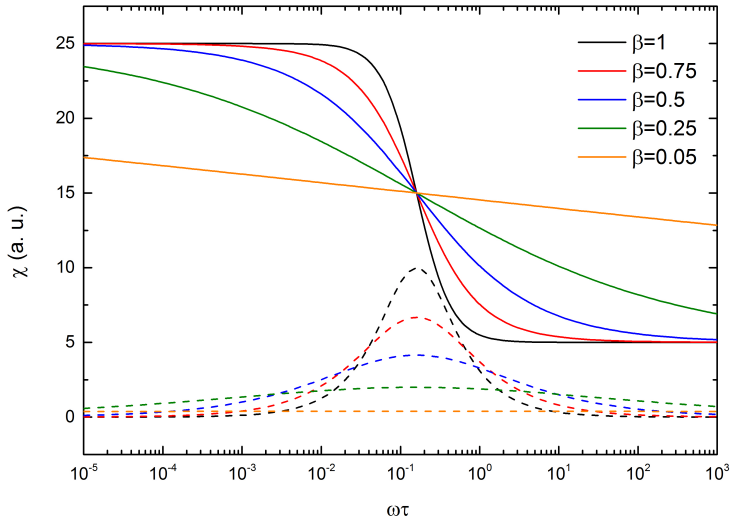

Figure 6.3: Example of Cole-Cole equation for several values of β. We have taken the following arbitrary values for all the simulations: $\chi_S = 5$ a.u., $\chi_T = 25$ a.u.

where C is the Curie constant and θ is the Weiss temperature that is determined by spin-spin interactions.

When several relaxation times contribute, such as it occurs with our samples, Debye theory does not properly fit the dependence of χ on ω. A continuous distribution of relaxation times broadens the peak of the imaginary component and reduces its amplitude [6.25].

To address this situation, Kenneth S. Cole and Robert H. Cole [6.26, 6.27] came up with an empirical law (the Cole-Cole equation) that considers the broadening of the relaxation by just adding a distribution parameter $0 < \beta < 1$ into the Debye equation:

$$\chi^* = \chi_S + \frac{\Delta\chi}{1 + (i\omega\tau)^\beta} \tag{6.16}$$

As $\chi^* = \chi' - i\chi''$, we can split the equation into real and imaginary parts,

$$\chi' = \chi_S + \frac{\Delta\chi\left(1 + (\omega\tau)^\beta \cos\frac{\pi}{2}\beta\right)}{1 + 2(\omega\tau)^\beta \cos\frac{\pi}{2}\beta + (\omega\tau)^{2\beta}} \tag{6.17}$$

$$\chi'' = \frac{\Delta\chi(\omega\tau)^\beta \sin\frac{\pi}{2}\beta}{1 + 2(\omega\tau)^\beta \cos\frac{\pi}{2}\beta + (\omega\tau)^{2\beta}} \tag{6.18}$$

When $\beta = 1$, Cole-Cole equation turns into Debye equation. $\beta = 1$ means a single relaxation process whereas $\beta = 0$ would mean a flat distribution of

relaxation processes over the whole range of frequencies. Figure 6.3 shows how the curve changes when we reduce β.

Indirect measurement for a previously determined β

In the case we can obtain a robust value for χ_S and β, including a possible evolution with temperature $\beta(T)$, $\chi_S(T)$, χ vs. T representation can give us more information on τ even when the maximum of χ'' is not accesible within the temperature and frequency ranges. In this case, by simply solving Cole-Cole equation for τ, in the regime where $\chi'' \neq 0$ and $\chi' - \chi_S \neq 0$, we find

$$\tau \simeq \frac{1}{\omega}\left(\frac{r_1}{\sin\frac{\pi}{2}\beta - r_1\cos\frac{\pi}{2}\beta}\right)^{1/\beta} \tag{6.19}$$

where

$$r_1 = \frac{\chi''}{\chi' - \chi_S} \tag{6.20}$$

6.3 Relaxation processes in a single lanthanide ion

6.3.1 ErLa

We first consider the Spin-Lattice relaxation of a ErLa molecular dimer. Because La^{3+} is non magnetic and Er^{3+} ions carry no nuclear spins (except for the stable isotope $^{167}Er^{3+}$ which exists in a 22.9% and has $I = 7/2$), this corresponds to the simplest situation of a quasi isolated magnetic ion.

As it is described in section 4.8.2, the ground level doublet of ErLa is associated with $J_z = \pm 9/2$ and the next energy levels are separated by at least $\Omega/k_B = 43$ K (see Fig. 6.4(b)).

The large energy difference between the ground doublet and the rest of the levels indicates that we are in a regime where $k_B T \ll \epsilon_{bc}$, which means that higher levels are not populated and will not significantly contribute to SLR because there are hardly any such energetic phonons. The only processes that can survive must therefore involve transitions within the electronic ground doublet, as in an effective two level system. As Er^{3+} is a Kramers ion, the splitting in the ground doublet should be small because, at $H = 0$, the doublet is completely degenerated. According to previous experiments on other SMM which contained Er^{3+}, $\Delta \approx 8 \times 10^{-5}$ K [6.22].

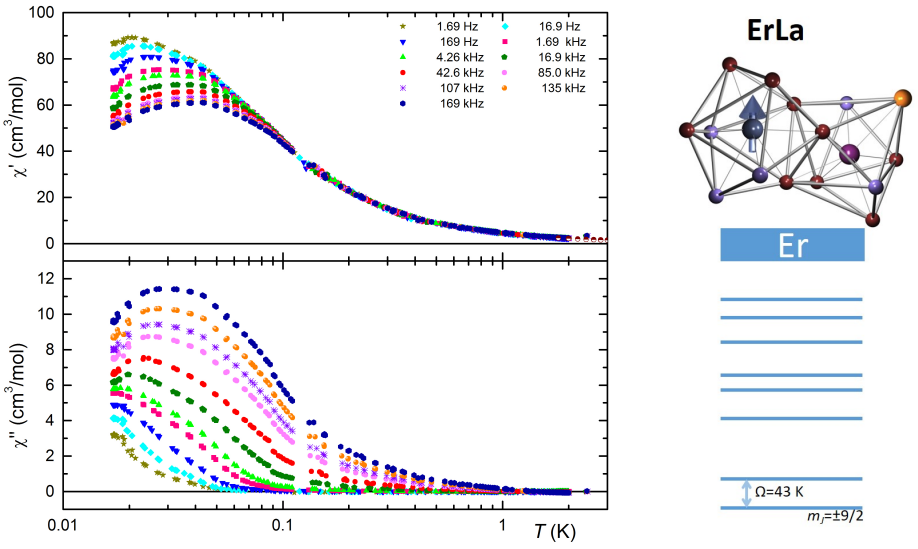

(a) (b)

Figure 6.4: a) χ vs. T measurements of ErLa. The imaginary part shows a maximum on each frequency that indicates the point where transition takes place. b) Energy level structure of ErLa dimer.

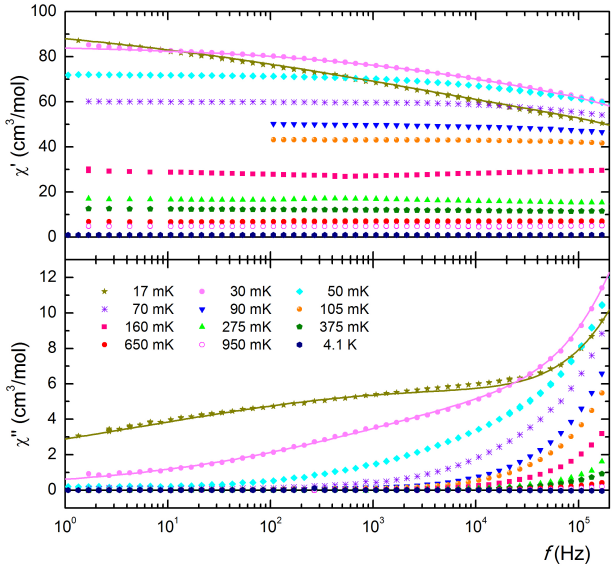

Figure 6.5: χ vs. f measurements of ErLa. Real part is flat, showing a paramagnetic behaviour, whereas imaginary shows a broad peak at about 1 kHz, just for very low temperatures.

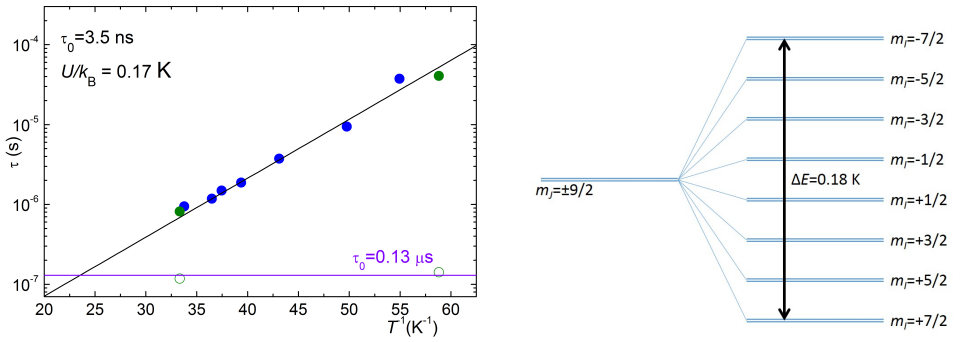

(a) (b)

Figure 6.6: a) Activation law for ErLa monomer. Solid points correspond to the relaxation of Er^{3+} ions which carry nuclear spin whereas open points correspond to relaxation of those which do not carry any nuclear spin. b) Hyperfine energy level structure of Er^{3+} with nuclear spin $I = 7/2$. The activation energy coincides with the energy difference between $m_I = \pm 7/2$ states.

In spite of these considerations, dynamic susceptibility experiments (Fig. 6.4(a)) shows that the spins of ErLa remain in thermal equilibrium down to very low T. Only below 200 mK does χ' deviate from χ_T and a non zero χ'' is observed. This means that spins are able to relax very rapidly, with characteristic times shorter than a μs, down to the close neighborhood of absolute zero.

Further insight into the relaxation mechanisms can be gathered from χ vs. f data, shown in Fig. 6.5. There, high temperature curves confirm the paramagnetic behavior of the sample and no drop is observed within the frequency range. The imaginary part, however, exhibits the outset of a peak beyond 100 kHz, which indicates a relaxation process that may occur at about 1 MHz. On the other hand, low temperature data show a second relaxation process which get faster with increasing temperature. The real part χ' presents a drop that becomes inappreciable above 70 mK, while the imaginary part shows a broad and weak peak, which moves towards higher ω with increasing temperature, until it merges with the high frequency peak. It is remarkable that the amplitude of the broad peak is much smaller than that of the high frequency peak, revealing that a majority of spins relax very rapidly ($\tau^{-1} > 1$ MHz) at any temperature.

The experimental data allow us to obtain different pairs (T,τ). Figure 6.6(a) shows an activation law for the relaxation process, where $\tau_0 = 3.5$ ns and the activation energy $U/k_B = 0.17$ K. This energy does not correspond to the tunnel splitting between the ground state doublet, which is expected to be

much smaller, or with any other electronic energy splitting. The non-zero χ'' observed at high frequencies gives us a second relaxation process with $\tau \approx 0.13$ μs, which is approximately independent of T.

As I argue next, the presence of a fraction of $^{167}Er^{3+}$ ions with nuclear spin $I = 7/2$ can explain the small drop $\Delta\chi'$ and the activation energy. The hyperfine interaction splits the electronic ground state doublet into eight electronuclear spin levels, as shown in Fig. 6.6(b), with energies given by,

$$E_{m_I} = A_J m_J m_I \tag{6.21}$$

where $A_J/k_B = -5.78$ mK is the hyperfine constant for $^{167}Er^{3+}$, $m_J = \pm 9/2$ is the J ground state and m_I is the z projection of I. The energy difference between $m_I = +7/2$ and $m_I = -7/2$ is $\Delta E = 0.18$ K, which agrees well with the activation energy obtained experimentally.

On the other hand, the fact that $\Delta\chi' \ll \chi_T$ is due to the small amount of $^{167}Er^{3+}$ (about 22.9% of all the Er^{3+} ions). Then, whereas in the relaxation process at high frequency all the spins relax by quantum tunneling, only the ions that carry nuclear spin are responsible for a thermally activated relaxation. Relaxation appears therefore diluted and it is not well appreciated.

The relaxation at high frequency is approximately independent of temperature, which indicates that a direct process or pure quantum tunneling is taking place. This means that Δ is larger than it was expected to be. A possible explanation is the low symmetry that this kind of molecules have. Local coordination might introduce non-negligible off-diagonal terms to the Hamiltonian, that change the local crystal field, allowing quantum tunneling between two states whose transition was forbidden. At high temperatures this process becomes predominant over relaxation between hyperfine levels, that only remains visible for very low temperatures.

6.3.2 DyLa

I next consider the SLR of a DyLa molecular dimer. The main difference with respect to ErLa is the fraction of Dy^{3+} isotopes with nonzero nuclear spin. There exist mainly four stable isotopes of Dy, ^{162}Dy (25.5%) and ^{164}Dy (28.2%), which do not carry any nuclear spin, and ^{161}Dy (18.9%) and ^{163}Dy (25.5%), which have a nuclear spin $I = 5/2$. As well as Er^{3+}, Dy^{3+} has $J = 15/2$ although, as we describe in section 4.7, its ground state $m_J = \pm 15/2$ is the maximum projection of J on the z axis.

The energy gap between the ground state electronic doublet and the first excited one is $\Omega/k_B \approx 100$ K. As this energy difference is much larger than

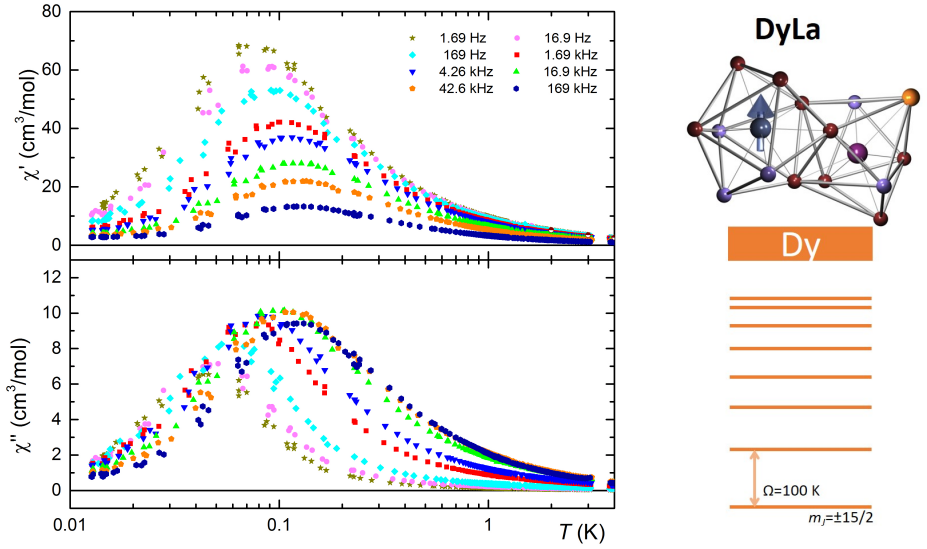

Figure 6.7: a) χ vs. T data of DyLa measurements at different frequencies. Imaginary part shows a peak for each frequency that indicates the point where transition takes place, in this case, at higher temperatures than in the case of ErLa. b) Energy level structure of the DyLa dimer.

$k_{\mathrm{B}}T$, it is therefore possible to discard transitions to the excited levels. As a Kramers ion, its ground state is degenerated for $H = 0$ and therefore, the splitting Δ will be very small and principally caused by dipolar interactions and the transverse hyperfine couplings.

Figure 6.7(a) shows, however, some relaxation processes are already visible at 2-3 K, where curves for different frequencies do not match. This fact is quite different to the case of ErLa, where the system keeps its equilibrium down to 0.1 K. The imaginary part shows clearly a well defined peak for each frequency near 0.1 K, also higher than in the case of ErLa. This indicates the contribution of transitions that remain active well below the temperature region in which transitions between the ground and the first excited electronic states are relevant. Transitions between electronuclear levels could again be the source of this behavior.

χ vs. f data (Fig. 6.8) confirm the existence of broad relaxation processes for all the range of temperatures that we have measured, from 4 K down to 13 mK. The imaginary part shows very broad peaks whose position and width change with temperature. Cole Cole fits do not accurately account for these data because χ'' peaks are broader that what would correspond to the drop observed in χ'. Displacements of the peaks with T suggest the presence

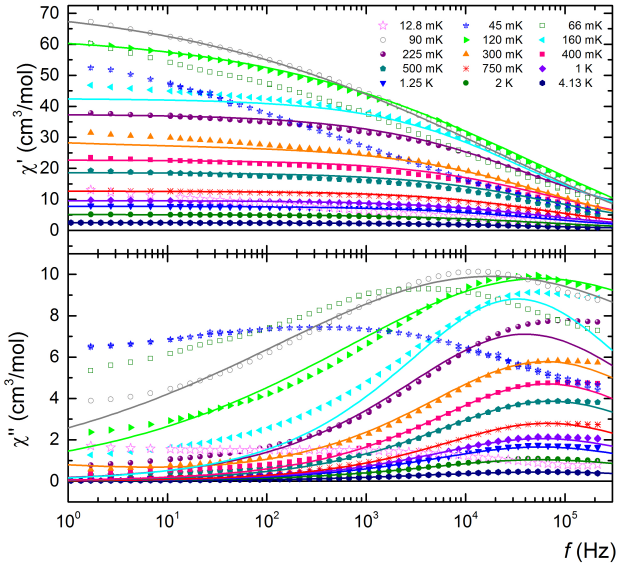

Figure 6.8: χ vs. f measurements of DyLa. Real part shows a larger drop $\Delta\chi$ and the peak of the imaginary part gets broader and broader when temperature goes down.

of various relaxation processes occurring at different rates. Below 90 mK it results totally impossible to fit Cole-Cole functions. $\Delta\chi$ drop is better observed than in the case of ErLa. If we assume the presence of hyperfine transitions, the larger $\Delta\chi$ is probably due to the higher percentage of ions with non-zero nuclear spin.

Taking the $f = 169$ Hz curve and $\beta = 0.465$ from χ vs. f, as Cole-Cole fittings suggest, we have completed the $\tau(T)$ curve for this dimer (Fig. 6.9). It shows at least two different processes with two relaxation rates which are very close; a thermally activated relaxation, with $U/k_B = 0.27$ K and $\tau_0 = 1.67$ μs, and a thermally independent relaxation at $\tau_0 \approx 2.7$ μs. At very low temperatures $\tau(T)$ ($T \leq 50$ mK) tends to a constant value $\tau_0 \approx 0.19$ ms.

The value of U agrees well with an average value of the hyperfine splitting of both isotopes, calculated with eq. (6.21):

$$\begin{aligned} \Delta E_{^{161}Dy}(18.9\%) &= 0.21 \text{ K} \\ \Delta E_{^{163}Dy}(25.5\%) &= 0.29 \text{ K} \\ \Delta E_{av} &= 0.26 \text{ K} \end{aligned} \tag{6.22}$$

where $A_J(^{161}Dy) = -5.56$ mK and $A_J(^{163}Dy) = 7.8$ mK, and $m_J = \pm 15/2$. There are two noticeable conclusions for these values.

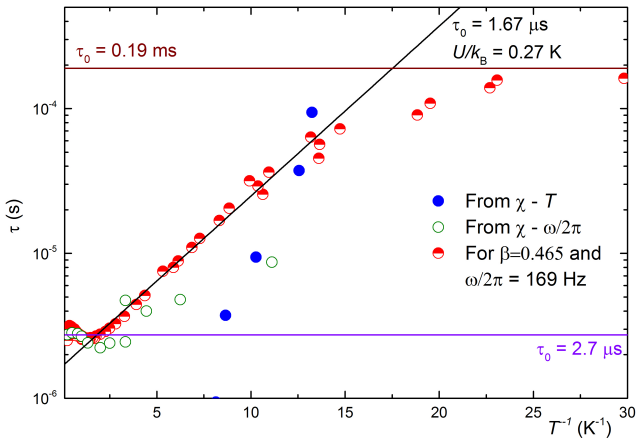

Figure 6.9: SLR relaxation time of a DyLa monomer.

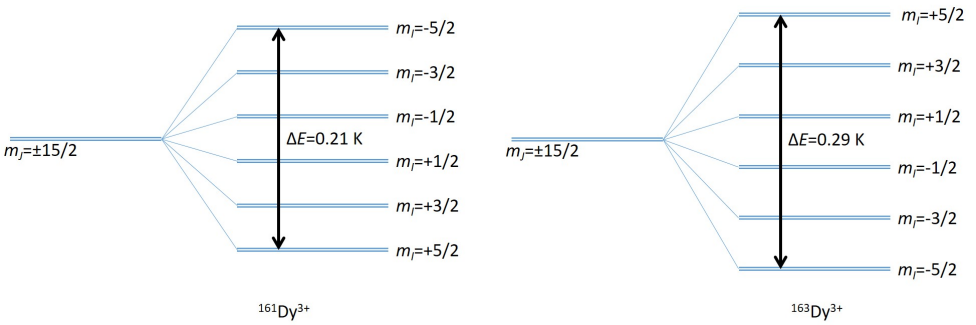

Figure 6.10: Hyperfine energy level structure for Dy^{3+} with nuclear spin. The opposite sign of the hyperfine constant for both isotopes changes the level structure.

On the one hand, there exists effectively two different hyperfine level systems which are responsible for the broadening of the relaxation distribution of times. The broad distribution (even broader that in the case of ErLa, whose nuclear momentum is higher) is then compatible the fact that $^{161}Dy^{3+}$ and $^{163}Dy^{3+}$ have different hyperfine constants and therefore, they split in different energy levels, giving two different systems with six hyperfine doublets, as shown in Fig. 6.10, each one relaxing at different times. This explains why Cole Cole fits do not match because this approximation is only valid for just one spin system instead of two. On the other hand, the sign of $A_J(^{161}Dy)$ and $A_J(^{163}Dy)$ does not coincide, which means that their nuclear spin states split in the opposite order, as shown in Fig. 6.10. This will gain special relevance in the case of the Dy_2 dimer, which is studied in the next section, due to the high number of possibilities to couple levels.

Thermally independent relaxation might come from a possible increasing of the tunneling splitting of the ground doublet, in the same way as it happened with ErLa, due to the low symmetry of the system that introduces additional off-diagonal terms in the Hamiltonian.

6.4 Relaxation processes in molecular dimers

In this section we study relaxation processes when we put two magnetic ions in the same molecular dimer. The presence of two weakly coupled ions multiplies the number of available levels within the ground state doublets. The site of La^{3+}, which does not have any magnetic momentum, is now occupied by a magnetic ion. As this site has a different local coordination, thus a different crystal field, differences between the magnetic anisotropies of both are also expected to play a role.

We next describe the studies performed on Er_2 and Dy_2 dimers and compare then to their corresponding monomers ErLa and DyLa.

6.4.1 Er_2

For the case of the Er_2 dimer and according to the theory developed for dimers, described in chapter 4 the energy level spectrum of ErLa monomer is also approximately valid for each Er^{3+} ion, as a first order approximation. Both ions have then a ground state doublet well isolated from the higher levels to consider them as the only populated levels. These states are coupled with those of the other lanthanide so that there is an additional level splitting Δ=1.5 K between the ferromagnetic levels $\{|\uparrow\uparrow\rangle, |\downarrow\downarrow\rangle\}$ and the antiferromagnetic ones

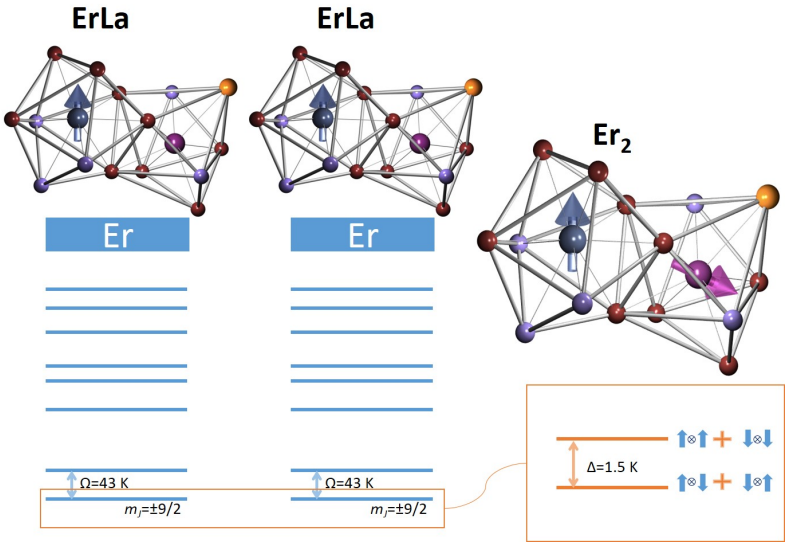

Figure 6.11: Schematic representation of the electronic energy level structure of Er_2. The electronic spin system can be considered as two independent Er^{3+} ions (right) whose ground levels are coupled.

$\{|\uparrow\downarrow\rangle, |\downarrow\uparrow\rangle\}$. This fact modifies the level spectrum and there will be four accessible levels (neglecting, by the moment, hyperfine splitting of the 23% of the Er^{3+} ions). Figure 6.11 shows the electronic energy level structure of Er_2.

Ac susceptibility data measured as a function of T are shown in Fig. 6.12. Relaxation starts to be observable at higher temperatures than it does in the case of the monomer. The real part of the susceptibility shows changes below 0.3 K that depend on frequency. The peak is lower than in the case of the two monomers, thus indicating an antiferromagnetic coupling of the two Er^{3+} ions. A non-zero χ'' is observed already below 3 K, showing peaks below 100 mK.

χ vs. f data (Fig. 6.13) show effectively a weak broad relaxation ($\beta \approx 0.3$) at around 100 Hz, for very low temperatures and a larger contribution for $\omega/2\pi \geq 200$ kHz. The low ω peak in the imaginary part changes its position with T. The real part shows a bigger drop $\Delta\chi$ than in the case of ErLa, which means that the fraction of spins relaxing at this slow rate is also larger. The position of the high-frequency χ'' peak seems to depend very little on T. Although it can not be correctly fitted, it seems to be slower than that of the monomer, $\tau \approx 0.5$ μs.

Using $\beta = 0.3$ and $\chi_S = 0$ we have obtained some more pairs (T,τ). Figure 6.14 shows that Er_2 sample has two well-defined relaxation times. At high temperatures ($T \geq 50$ mK), transitions are thermally activated with $U/k_B = 1.44$ and $\tau_0 = 19$ fs. The activation energy $U/k_B = 1.44$ K is larger

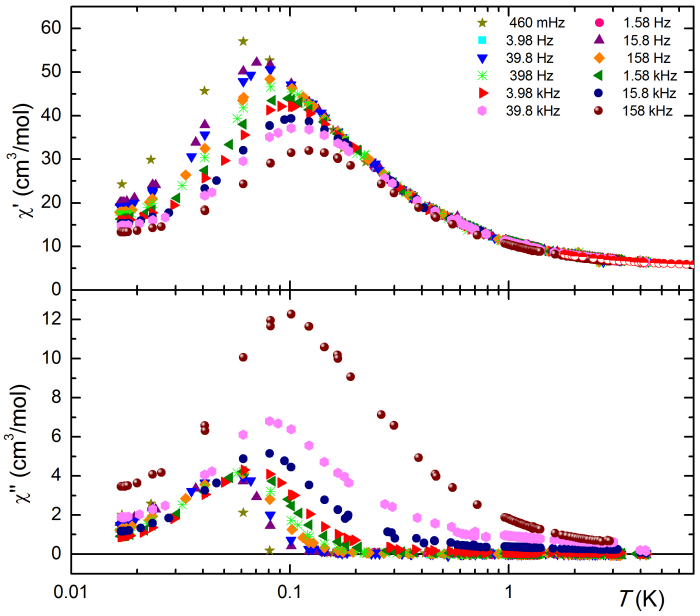

Figure 6.12: χ vs. T measurements of Er_2 at different temperatures.

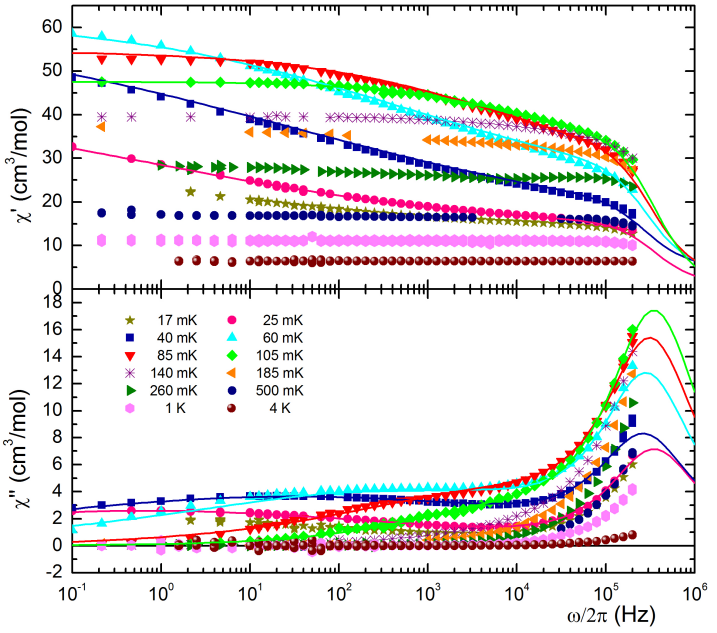

Figure 6.13: χ vs. f measurements of Er_2. Lines are the Cole-Cole fits for two relaxation parts, a broad one around $\tau = 5$ ms and the other one below $\tau = 0.5$ μs.

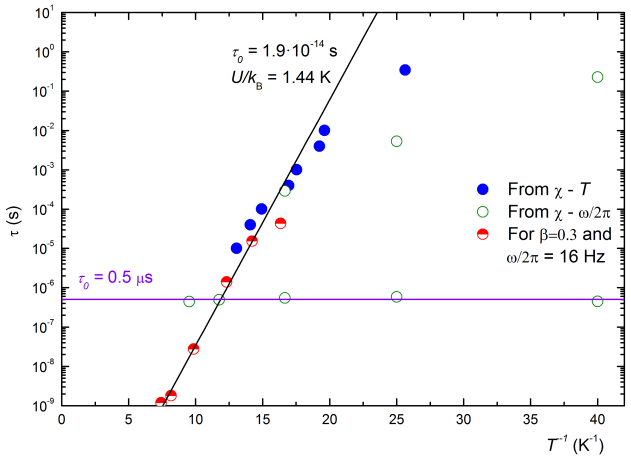

Figure 6.14: Activation law for Er_2 dimer. It shows clearly a thermally activated process and a thermally saturation at $\tau = 125$ μs.

than the hyperfine splitting. It actually agrees better with the energy gap between the levels split by the intramolecular exchange interaction.

Below 80 mK, an temperature independent relaxation process, quite similar to that observed for the ErLa, shows up. It might be also associated to tunneling splitting between the not fully compensated antiferromagnetic states.

6.4.2 Dy_2

The intricate energy level structure of Dy^{3+}, having two isotopes with different hyperfine splitting, constitutes a perfect example to determine how relaxation changes when more energy levels are involved. A powder sample can have different isotopes inside each molecule, existing therefore up to nine different hyperfine energy level structures corresponding to different combinations between ions with no nuclear spins, $^{161}Dy^{3+}$ ions and $^{163}Dy^{3+}$ ions. This fact increases considerably the number of possible mechanims involved. Like in the case of Er_2, Dy_2 has two electronic ground doublets $m_J = \pm 15/2$ which are coupled and well separated from the excited levels. As deduced in section 4.7, antiferromagnetic and ferromagnetic states are split by an energy $\Delta \approx 1.3$ K (see Fig. 6.15).

Unlike the case of Er_2, in which hyperfine splitting is ten times smaller than the splitting between the entangled states, hyperfine splitting in Dy_2 (up to 0.29 K) is comparable to the exchange splitting.

Ac susceptibility data are shown in Fig. 6.16. They show broad χ'' maxima, centered at about 0.2 K. Susceptibility has approximately the same height as in

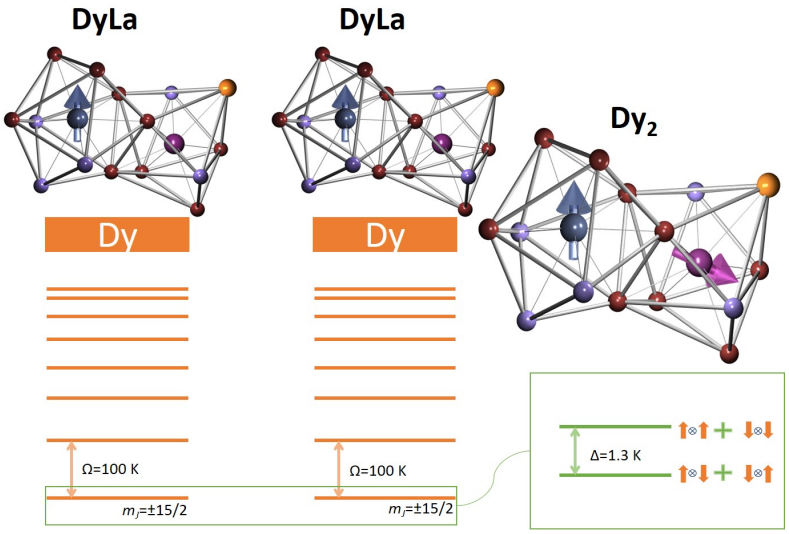

Figure 6.15: Energy level structure of Dy_2 dimer. The spin system is considered as two independent Dy^{3+} ions whose ground levels are coupled.

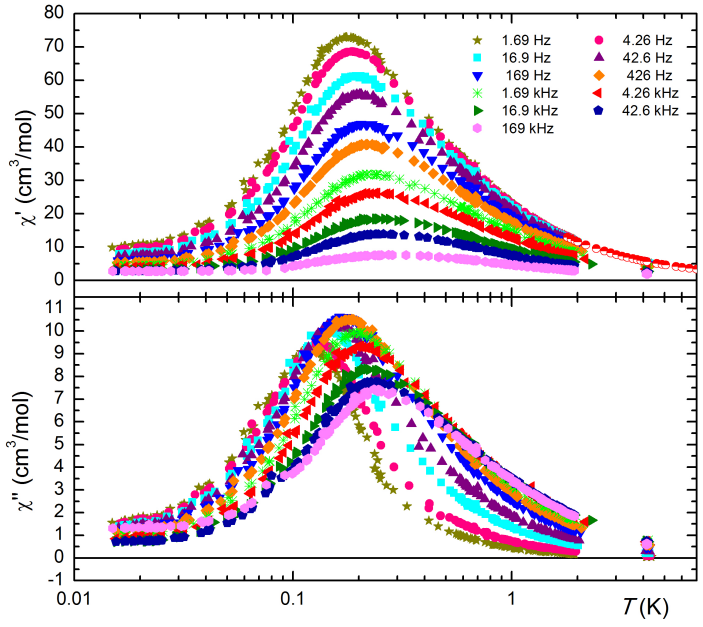

Figure 6.16: χ vs. T representation of measurements on Dy_2. Transitions are concentrated between 0.1 K and 1 K.

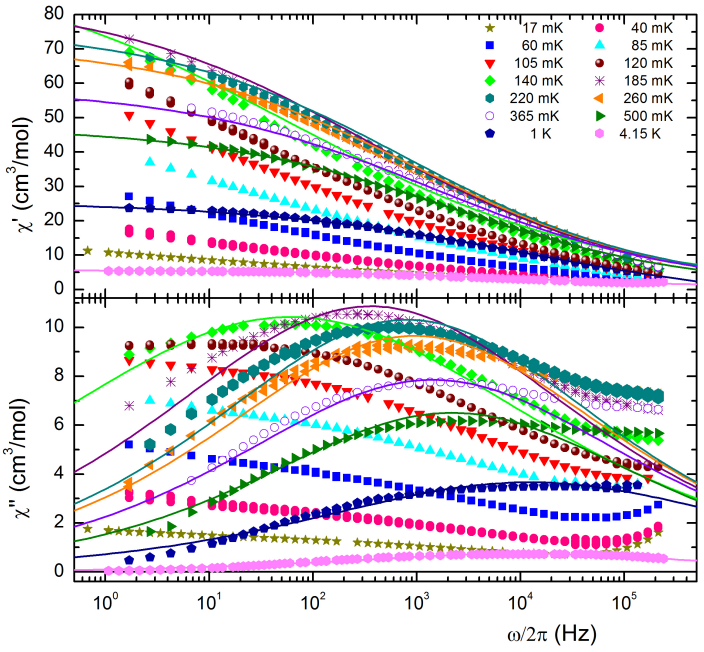

Figure 6.17: χ vs. f measurements of Dy_2. Relaxation shows a wide distribution of times, related to many transitions. Lines are the Cole-Cole fits.

the case of DyLa, which suggests that relaxation is of the same nature. On the other hand, the ground state of Dy^{3+} coincides with the maximum projection over z. This means that, unlike the case of Er_2, g_x and g_y are negligible and do not modulate the crystal field. This also allows susceptibility to grow more than in the case of Er_2. The imaginary part shows peaks which change less with frequency than in the case of the monomer.

χ vs. f data (Fig. 6.17) exhibit some differences with respect to the monomer (Fig. 6.8). The real part shows a larger drop than in the case of the monomer and peaks of the imaginary part are centered within the frequency range. Cole-Cole fits reveal a lower β, which is of the order of 0.25, approximately one half of the case of the parameter found for DyLa. At high frequencies and very low temperatures the imaginary part shows a tiny increase that might indicate the existence of faster relaxation processes, which become then visible.

We have obtained additional pairs (T,τ) by taking $\beta = 0.27$ and $f = 16.9$ Hz. The Arrhenius plot (Fig. 6.18) shows a more complex behaviour with, at least, three different contributions. At high temperatures, above 500 mK a thermally activated relaxation process with $\tau_0 = 2.2$ μs and $U/k_B = 1.84$ K dominates. Between 140 mK and 500 mK, there is a similar relaxation with

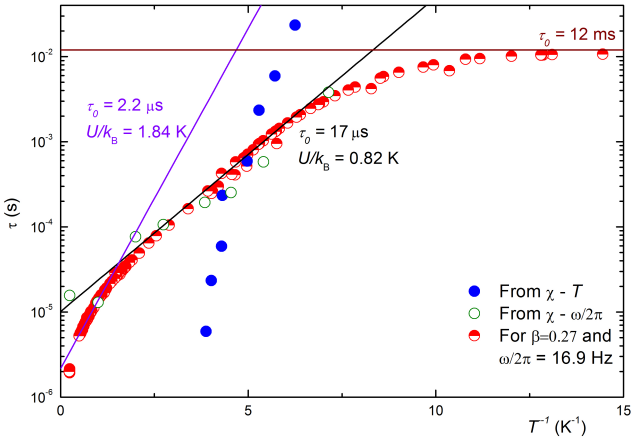

Figure 6.18: Activation law for Dy_2 dimer.

$\tau_0 = 17$ μs and $U/k_B = 0.82$ K. The activation energies of both processes agree better with the exchange splitting than with the hyperfine splitting. They are slower than in the case of DyLa. Each visible transition might be the result of several processes, including different electronuclear states, which are comparable in magnitude. The existence of two different isotopes with different hyperfine splittings may explain the presence of two different activation laws.

At low temperatures relaxation tends to a thermally independent process at $\tau_0 = 12$ ms, probably induced by pure quantum tunneling between two of the multiple accessible levels.

6.5 Summary and conclusions

In a quantum computer, quantum states must be stable to perform coherent operations on them. However, in a real architecture, qubits can not be completely isolated due to the necessity to modify and control their quantum state. As a consequence, each state has lifetime limits. The longest coherence time that is achievable, provided other sources of decoherence can be minimized, is a physical mechanism called spin-lattice relaxation. Energy exchanges between quantum states and lattice phonons can provoke transitions between energy levels that could even be forbidden under isolated circumstances.

In this chapter we have studied experimentally SLR times of four simple molecular clusters, having either one isolated magnetic ion or two coupled ones. Table 6.1 shows a summary of the relaxation rates obtained for different dimers.

Sample	τ_0	U/k_B (K)
ErLa	3.5 ns	0.17
	0.13 μs	0
DyLa	1.67 μs	0.25
	2.7 μs	0
	0.19 ms	0
Er_2	19 fs ms	1.44
	0.5 μs	0
Dy_2	2.2 μs	1.84
	17 μs	0.82
	12 ms	0

Table 6.1: Summary of activation laws for ErLa, DyLa, Er_2 and Dy_2.

For single qubits with no nuclear spin, relaxation times τ are well defined due to the existence of one unique decay, from the first excited energy level to the ground state. In the case of ErLa monomer, however, we have obtained a single relaxation time of $\tau_0 = 3.5$ ns with an activation energy $U/k_B = 0.17$ K much higher than the splitting of the electronic levels. This can be associated to hyperfine transitions in the almost 23% of Er^{3+} that possess nuclear spin.

For DyLa, whose hyperfine structure is much more complicated, the decay behavior is similar but slower $\tau_0 = 1.67$ μs, with an activation energy $U/k_B = 0.27$ K that can also be associated with the hyperfine splitting. Both monomers show, besides, a thermally independent process at high temperatures at 0.13 μs and 2.7 μs respectively, which can be associated to direct quantum tunneling of the electronic spins of $I = 0$ isotopes. Tunneling rate are faster than those found previously for other Er and Dy single-ion magnets, probably on account of the lower coordination symmetry of our molecules.

In the case of dimers, candidates for quantum gates, there are at least four electronic accessible levels, thus increasing the possibilities for relaxation. The two studied dimers Er_2 and Dy_2 react however in different ways. For Er_2, relaxation between the coupled states gives rise to an activation law with $\tau_0 = 19$ fs and of the order of the splitting between antiferromagnetic and ferromagnetic levels ($U/k_B = 1.44$ K).

For Dy_2, hyperfine splitting is of the same order than the entangled splitting and, moreover, there are two different isotopes with different hyperfine splitting. We observe two clear thermally activated processes. Their respective activation energies, 1.84 K and 0.82 K, agree with the exchange splittings, showing that these relaxation processes are a mixture of transition between both hyperfine and coupled levels.

Bibliography

[6.1] P. C. E. Stamp and I. S. Tupitsyn, "Coherence window in the dynamics of quantum nanomagnets," *Phys. Rev. B*, vol. 69, no. 1, p. 014401, 2004.

[6.2] D. A. Wollman, D. J. Vanharlingen, W. C. Lee, D. M. Ginsberg, and A. J. Leggett, "Experimental determination of the superconducting pairing state in YBCO from the phase coherence of YBCO-Pb dc SQUIDs," *Phys. Rev. Lett.*, vol. 71, no. 13, p. 2134, 1993.

[6.3] J. F. Fernández, "Dipolar ordering of molecular magnets," *Phys. Rev. B*, 2002.

[6.4] K. Bader, D. Dengler, S. Lenz, B. Endeward, S. D. Jiang, P. Neugebauer, and J. van Slageren, "Room temperature quantum coherence in a potential molecular qubit," *Nature Communications*, vol. 5, p. 5304, 2014.

[6.5] J. Clarke and F. K. Wilhelm, "Superconducting quantum bits," *Nature*, vol. 453, p. 1031, 2008.

[6.6] A. Friedenauer, H. Schmitz, J. Glueckert, D. Porras, and T. Schaetz, "Simulating a quantum magnet with trapped ions," *Nature Physics*, vol. 4, p. 757, 2008.

[6.7] R. Hanson and D. D. Awschalom, "Coherent manipulation of single spins in semiconductors," *Nature*, vol. 453, p. 1043, 2008.

[6.8] N. V. Prokof'ev and P. C. E. Stamp, "Spin environments & the suppression of quantum coherence," *Quantum Tunneling of Magnetization - QTM '94*, vol. 301, p. 347, 1995.

[6.9] P. C. E. Stamp, "Dissipation and decoherencia in quantum magnetic systems," *Physica B*, vol. 197, p. 133, 1994.

[6.10] I. Zapata, F. Sols, and A. J. Leggett, "Phase dymanics after connection of two separate Bose-Einstein condensates," *Phys. Rev. A*, vol. 67, no. 2, p. 021603, 2003.

[6.11] N. V. Prokof'ev and P. C. E. Stamp, "Low-temperature quantum relaxation in a system of magnetic nanomolecules," *Phys. Rev. Lett.*, vol. 80, no. 26, p. 5794, 1998.

[6.12] J. F. Fernández and J. J. Alonso, "Magnetization process of single molecule magnets at low temperatures," *Phys. Rew. Lett.*, 2003.

[6.13] R. Orbach, "Spin-Lattice Relaxation in Rare-Earth Salts," *Proc. Roy. Soc. London Series A Mathematical and Physical Sciences*, vol. 264, no. 1319, p. 458, 1961.

[6.14] A. Repollés, A. Cornia, and F. Luis, "Spin-lattice relaxation via quantum tunneling in diluted crystals of Fe_4 single-molecule magnets," *Phys. Rev. B*, vol. 89, no. 5, p. 054429, 2014.

[6.15] M. Affronte, M. L. Baker, S. J. Blundell, L. Bogani, L. F. Chibotaru, R. Clérac, A. Cornia, C. Coulon, N. D. y M. Evangelisti, S. Gao, A. Ghirri, S. Hill, S. D. Jiang, F. Luis, M. Mannini, C. J. Milios, V. Pianet, F. Troiani, M. Urdampilleta, R. E. P. Winpenny, and B. W. Wang, *Molecular Nanomagnets and Related Phenomena*. Springer, 2014.

[6.16] W. Heitler and E. Teller, "Time effects in the magnetic cooling method," *Proc. Roy. Soc. London. Series A, Mathematical and Physical Sciences*, vol. 155, no. 886, p. 629, 1936.

[6.17] S. Greulich-Weber and A. Zrenner, "Physik kohärenter quantensysteme." Lecture Notes, 2007. Universität Paderborn.

[6.18] J. H. van Vleck, "Paramagnetic relaxation times for Titanium and Chrome Alum," *Phys. Rev.*, vol. 52, p. 426, 1940.

[6.19] C. B. P. Finn, R. Orbach, and W. P. Wolf, "Spin-Lattice Relaxation in Cerium Magnesium Nitrate at Liquid Helium Temperature: A New Process," *Proc. Phys. Soc.*, vol. 77, p. 261, 1960.

[6.20] E. Burzurí, *Dipolar order and quantum phase transitions in magnetic materials*. PhD thesis, Universidad de Zaragoza, 2011.

[6.21] F. Luis, J. Bartolomé, and J. F. Fernández, "Resonant magnetic quantum tunneling through thermally activated states," *Phys. Rev. B*, vol. 57, no. 1, p. 505, 1998.

[6.22] F. Luis, M. J. Martínez-Pérez, O. Montero, E. Coronado, S. Cardona-Serra, C. Martí-Gastaldo, J. M. Clemente-Juan, J. Sesé, D. Drung, and T. Schurig, "Spin-lattice relaxation via quantum tunneling in an er^{3+}-polyoxometalate molecular magnet," *Phys. Rev. B*, vol. 82, p. 060403, 2010.

[6.23] P. Debye, "Part 1. dielectric constant. energy absorption in dielectrics with polar molecules," *Trans. Faraday Soc.*, vol. 30, p. 679, 1934.

[6.24] P. Curie, "Sur les propiétés magnétiques de l'oxygène à diverses températures," *C. R. Acad. Sci.*, vol. 115, p. 1292, 1892.

[6.25] Y. P. Kalmykov, W. T. Coffey, D. S. F. Crothers, and S. V. Titov, "Microscopic models for dielectric relaxation in disordered systems," *Phys. Rev. E*, vol. 70, p. 041103, 2004.

[6.26] K. S. Cole and R. H. Cole, "Dispersion and Absorption in Dielectric - I Alternating Current Characteristics," *J. Chem. Phys.*, vol. 9, p. 341, 1941.

[6.27] K. S. Cole and R. H. Cole, "Dispersion and Absorption in Dielectrics - II Direct Current Characteristics," *J. Chem. Phys.*, vol. 10, p. 98, 1942.

Chapter 7

Experimental study of molecular qubits on surfaces

7.1 Introduction

In previous chapters of this thesis, we have studied properties of SMM in their natural environment. In bulk samples, molecular are "protected" by their own crystalline structure. Thanks to the certainty that all the SMM inside a sample are identical, magnetic properties of one single molecule can be determined by magnetic measurements on the bulk sample. The question arises when we intend to use SMM as single quantum bits or quantum gates, what occurs if we extract just one molecule from its surrounding and put it into a "quantum circuit".

On the one hand, Single Molecule Magnets owe their behaviour as magnetic memory to the rigid molecular structure that keeps couplings between magnetic momenta. They are relatively complex molecules and some strains coming from external factors might partially deform their shape. Whether this deformation affects to SMM behaviour or not, will depend on its robustness and will determine if it can be used in combination to other elements of a quantum computer, such as resonant superconducting circuits [7.1].

On the other hand, SMM must be able to magnetically coupled to these elements. Circuits based on cavity quantum electrodynamics (circuits QED) are considered as suitable circuits, able to tune each spin qubit separately. Thus, spin qubits would be placed along a superconducting coplanar waveguide resonator at positions where there is a magnetic field maximum. Each spin is tuned into or out of resonance using a wire or microcoil to apply a local

magnetic field [7.2]. Here we use the last of these issues. More specifically, our susceptometer devices.

Our goal is to check whether the relevant magnetic properties of single molecule magnets are sufficiently robust when they are deposited on a surface. Measuring properties of samples consisting of a few molecular layers is, in itself, an experimental challenge. For this, we make use of the μSQUID susceptometers developed as part of this thesis work, which are described in chapter 3. We have performed measurements on the "famous" SMM Mn_{12} [7.3–7.6] and on a Dy_2 dimer, whose bulk magnetic behaviour has been studied in chapters 4 and 6. Besides information on basic parameters, susceptibility allows us to estimate also the minimum number of molecules that can be successfully coupled to a superconducting circuit fulfilling two of the conditions that we have pointed out above.

We first offer a brief description of Dip Pen Nanolithography technique that is able to deposit molecular materials in a controlled manner and which has been used for placing minute amounts of Mn_{12} and Dy_2 directly on the pick up coils of the microsusceptometers. Then some theoretical calculations concerning coupling between superconducting coil and SMM are presented. The last sections are devoted to discuss the experimental results obteined for different arrays of Mn_{12} and Dy_2 molecules.

7.2 Molecular deposition: DPN technique

Dip-Pen Nanolithography (DPN) is a direct-write scanning-probe-based lithography in which an atomic force microscope (AFM) tip is used to deliver chemical agents directly to nanoscopic regions of a target substrate [7.7]. The AFM tip acts itself as a pen whose ink is formed by a solution that contains the molecules to be deposited. The substrate is seen as a "paper" where the AFM tip "writes". Figure 7.1(a) shows an illustrative picture of the writing process.

This technique was introduced for the first time in 1999 [7.8] as a positive printing mode of nanolithography in which the substrate does not suffer from harsh solvents or chemical etching agents. Molecules are delivered from the AFM tip via capillary transport and can be deposited in either ambient or inert environment without exposing them to ionizing UV or electronic beam radiation.

DPN offers a really high resolution, in the range of nm, and it can be used for a wide variety of "ink-substrate" combinations. Inks can be composed of nanoparticles, small organic molecules, biological polymers or metal ion complexes. The substrate can be either metallic or insulating. This method opens

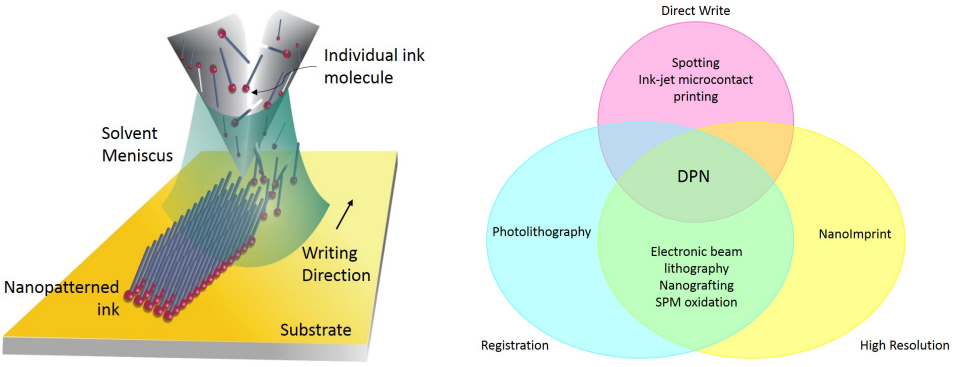

(a) (b)

Figure 7.1: a) Dip-Pen nanolithography. b) Comparison of the capabilities of DPN with various other lithographic tools.

new possibilities in fields ranging from molecular electronics to biomedicine. Highest resolutions are achieved for molecular inks with a specific affinity for the substrate. On the other hand, the ink can also be formed by a solution of a solid sample, diluted in inert solvents and transferred to the substrate. This technique has less resolution, in the range of μm [7.9], due to the dispersion of the molecules inside the solution, but allows the deposition of more complex molecules, such as bio-molecules and some inorganic molecules.

Among typical lithography techniques, DPN is one of the techniques that better combines direct writing capability with high resolution. Figure 7.1(b) shows a comparison between the capabilities of Dip-Pen nanolithography and other known lithography techniques [7.7].

For the realization of this work single molecule magnets have been deposited using two different DPN equipments. Samples of Mn_{12} were deposited by a Nscriptor DPN System in collaboration with E. Bellido, P. González-Monje and D. Ruiz-Molina, from the *Institut Català de Nanociència i Nanotecnologia* (ICN2). Samples of Dy_2 were deposited by a Nanoink DPN 5000 System in collaboration with M. C. Pallarés and A. Gracia Lostao, from the *Instituto de Nanociencia de Aragón* (INA).

7.3 Theoretical coupling of Single Molecule Magnets to superconducting circuits

In order to obtain the magnetic flux that an ensemble of SMM (in particular Mn_{12}) couples with a μSQUID pick-up coil, calculations have been performed

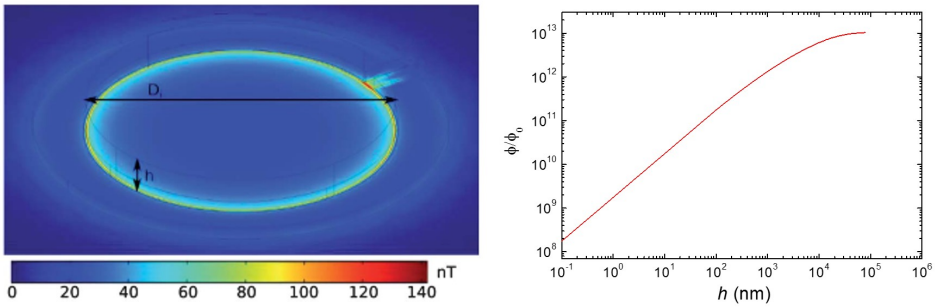

Figure 7.2: Left. Theoretical plot of the magnetic field intensity generated by a homogeneously magnetized disk, located inside one of the μSQUID pickup coil. Right. Dependence of the coupled flux as a function of height h of the disk deposited on one of the pickup coils, for Mn_{12}.

by M. Jenkins [7.9] using the commercial simulation software COMSOL [7.10]. Fig. 7.2 shows the results for the simulation considering the sample as an homogeneus disk, with density equal to that of Mn_{12} and magnetic axis randomly oriented. As shown in section 3.7, the magnetic field coupling is more intense next to the coil than in the center.

The relation between the coupled flux and the number of spins N in the array has also been calculated. The flux increases linearly with N until it saturates. The saturation occurs when the disk grows in height and there is a point where spins are so far to the coil that do not couple significantly to the coil.

7.4 Mn_{12} measurements on 30 μm loop SQUIDs

7.4.1 Mn_{12}bz molecules

As introduced in section 3.7.6, Mn_{12} is one of the most studied SMM. Its molecular structure, shown in Fig. 7.3(a), contains four Mn^{4+} ions in a central tetrahedron surrounded by eight Mn^{3+} ions, antiferromagnetically coupled to the former. The molecule possesses therefore a high-spin ground state $S = 10$ [7.11, 7.12].

Mn_{12} shows also two well defined relaxation processes, one slow and another one fast that coexist [7.13]. Some molecules shows slow relaxation ($\tau \sim$s at 4.2 K), but a fraction of them show a faster relaxation ($\tau \sim$ ms at 4.2 K). In most Mn_{12} derivatives slow relaxation (SR) is dominant and therefore, studies on fast relaxation (FR) are more limited than studies in SR. In 1998, K. Takeda and coworkers reported a Mn_{12} species that showed two relaxation processes

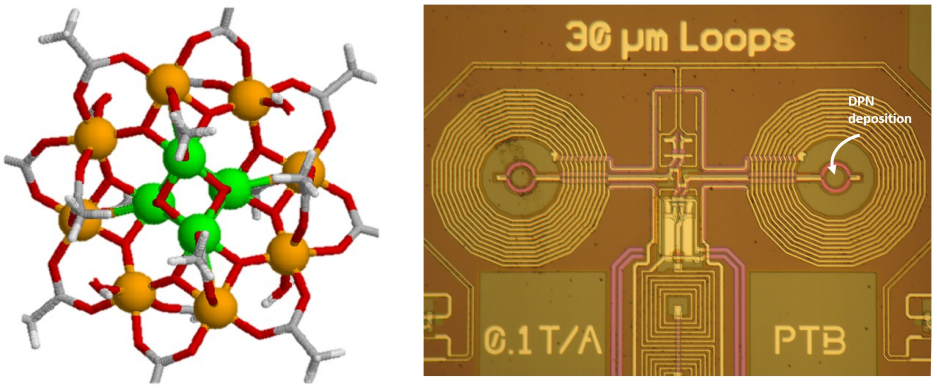

(a) (b)

Figure 7.3: a) Structure of a Mn_{12} molecular cluster [7.3]. Green atoms are Mn^{4+} ($S = 3/2$) and golden atoms are Mn^{3+} ($S = 2$). b) 30 μm SQUID loop susceptometer. The samples were deposited by DPN on one of the pickup coils.

whose intensities were of the same order [7.14] and only four years later they were able to synthesize Mn_{12} species with very different SR:FR ratios [7.6].

For our measurements we have chosen one of these Mn_{12} species showing both relaxation processes, with FR dominant over SR to study whether the effect of the substrate depends on the molecular structure. Mn_{12} clusters are attached to crystal-solvent molecules formed by bezoic acids that help them to crystallize. Hereafter we will call this Mn_{12} species as Mn_{12}bz.

7.4.2 Fabrication of Mn_{12}bz arrays by DPN lithography

To determined whether Mn_{12}bz keeps its properties as SMM when it is subdued to strain effects coming from the SQUID surface, we have carried out a series of measurements with different arrays. In section 3.7.6 we have already shown some effects caused by the reduction of the sample size in a similar Mn_{12} crystal. In that case, measurements showed small changes of the relaxation times although SMM behaviour was retained.

DPN deposition, however, leads to a more aggressive modification of the molecular environment. Whereas in the case of the experiments carried out with the nanoloop, the crystalline structure of Mn_{12} was preserved, in the case of DPN, Mn_{12} must be diluted in a solvent and, then, recrystallize again under the strong influence of the underlying substrate.

We have performed five different measurements to check both the sensitivity of the susceptometer and the behaviour of Mn_{12} for different layer thicknesses:

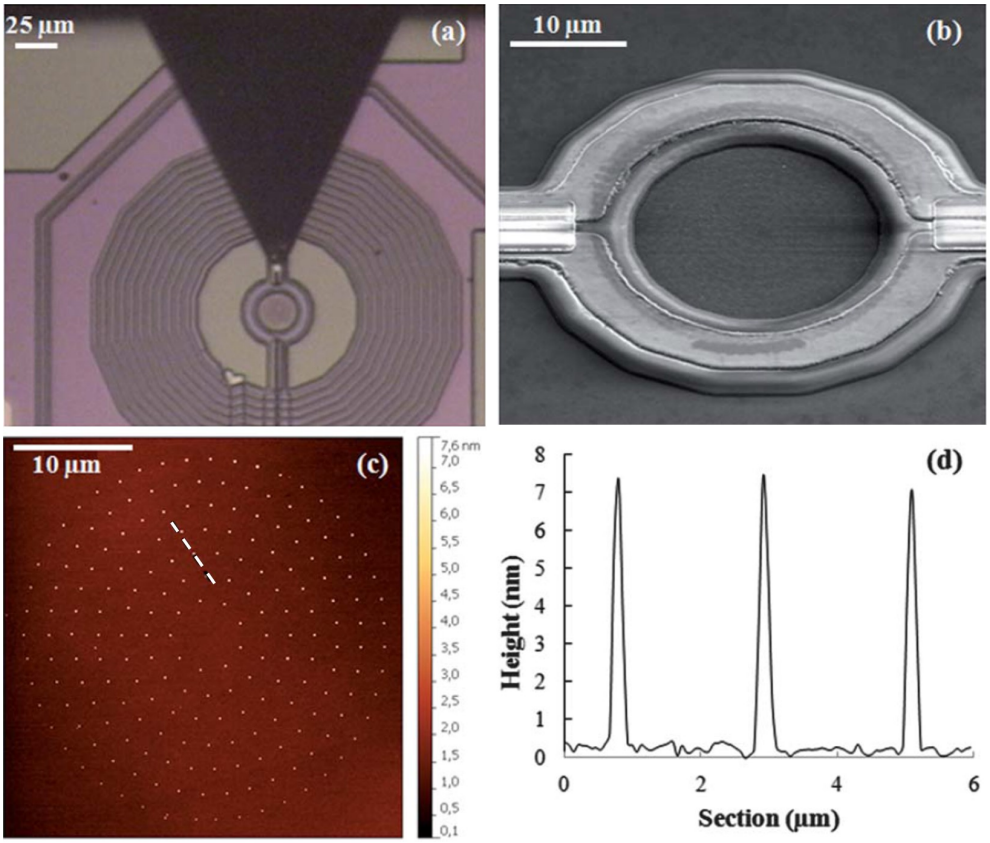

Figure 7.4: Nanostructured deposition of Mn_{12} on the pickup coil. a) Optical image of the μSQUID susceptometer right after the deposition process. b) FE-SEM image taken on the pickup coil with the deposited sample. c) AFM topography image of a similar array fabricated by using the same experimental conditions. d) Height profile measured by scanning the tip along the white dashed line in image (c).

one bulk measurement with the original sample, three DPN depositions with increasing amounts of the sample and one last bulk measurement on the same solution used for DPN recrystallized. To dilute Mn_{12} crystal, a solvent composed by 95% N,N-dimethylformamide (DMF)- 5% Glycerol, which has good properties for DPN, has been used.

First deposition

The first DPN sample DPN1 consists of a circular pattern of 1320 identical dots deposited inside the pickup coil. Figure 7.4 shows several images of the deposition process. Pictures at the top of the figure show an optical and a SEM image of the pattern deposited inside the coil. Picture c) shows an

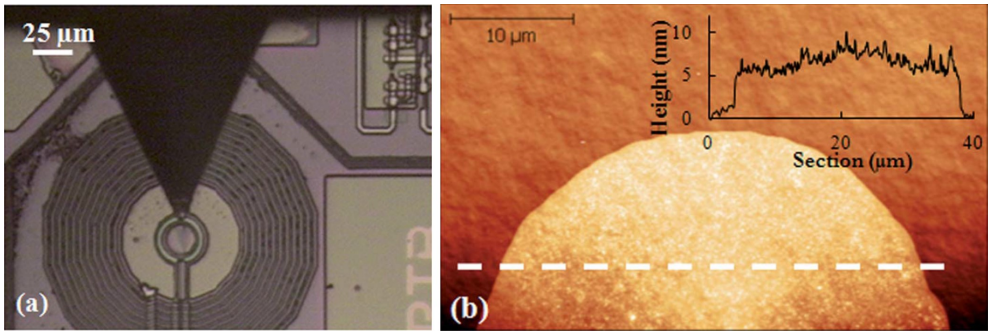

Figure 7.5: a) Optical image of the susceptometer after depositing the second sample. b) AFM topography image of a deposit under identical conditions to those used for the second sample.

AFM topography image of a replica, deposited on a surface with the same composition (Si/SiO_2). The purpose of this is to prevent the sensor from possible electrostatic discharges and to measure the dimensions of the dots. Picture d) shows the height profile measured on the replica. It reveals the formation of highly uniform in size dots, with an average diameter of about 249 nm and a height of $\sim$7 nm ($\sim$ 4 molecular layers).

Second deposition

The second DPN sample DPN2 consists of a circular pattern, similar to the one in the first deposition, but with larger dots. In this case, the larger volume of the dots makes them merge together on the substrate, forming a continuous thin film that covers the entire coil. Figure 7.5 shows an optical image of the susceptometer after depositing the sample and the AFM topography of a replica. The height profile of the replica indicates a similar height to the first deposition, $\sim$7 nm ($\sim$ 4 molecular layers).

Third deposition

Finally, the last deposition DPN3 has been made of a large droplet directly deposited onto the center of the coil. Figure 7.6 shows an optical image taken after depositing the droplet. On this occasion, the drop is easily visible inside the coil. AFM also shows an homogeneus deposition all over the surface. The topographic profile shows an average height of $\sim$15-20 nm.

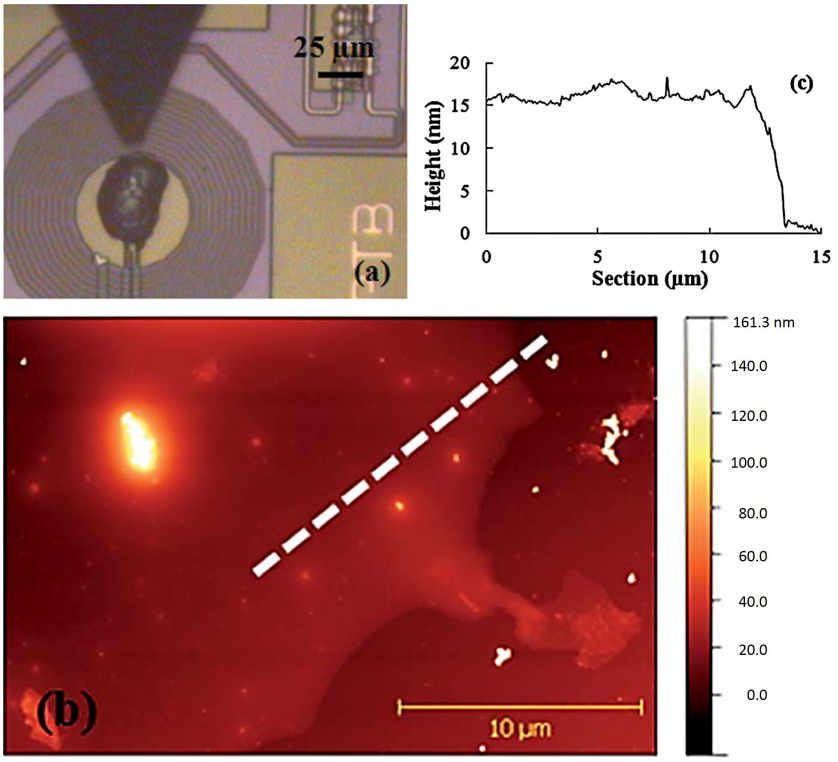

Figure 7.6: a) Optical image of the susceptometer after depositing a big drop on the pickup coil. b) AFM topography image of the replica sample fabricated under the same conditions. c) Height profile measured along the white dashed line.

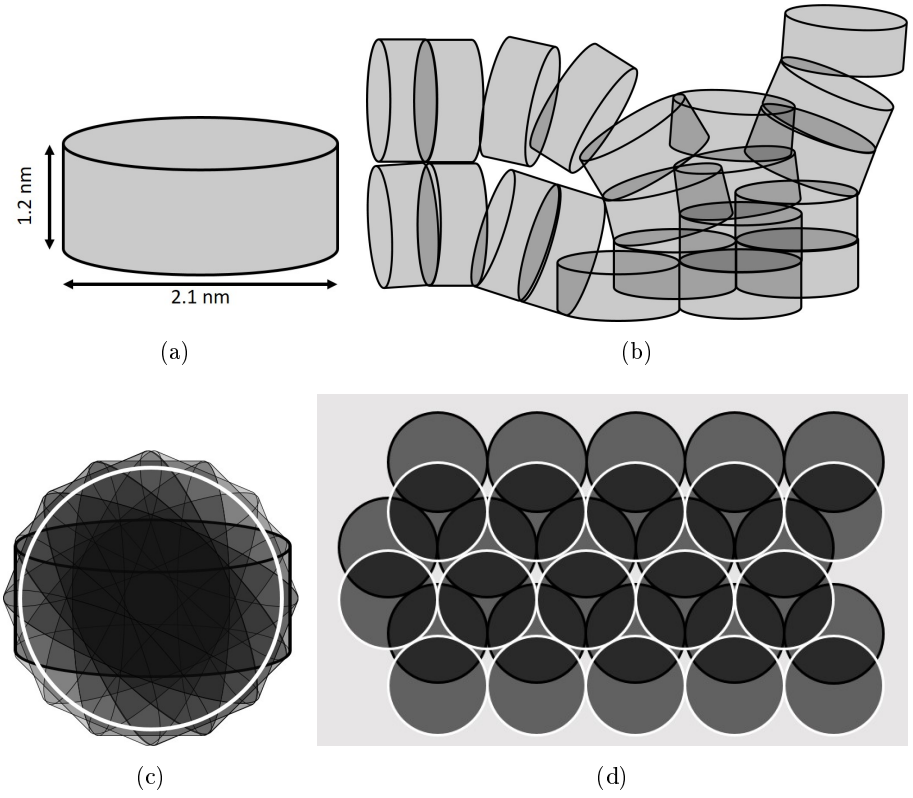

Figure 7.7: a) Disk-like shape of a molecule of Mn_{12}bz. b) Amorphous deposition of Mn_{12}bz molecules. c) Spherical model for the molecule taking into account its free rotation. d) Hexagonal-closed package of spherical particles.

7.4.3 Estimation of the number of Mn_{12}bz molecules deposited with DPN

After depositing the ink on the surface, the solvent is expected to evaporate within a short period of time. Mn_{12}bz then self-organizes on the surface. This molecule has a disk shape of approximately $2r = 2.1$ nm diameter and $h = 1.2$ nm height (see Fig. 7.7(a)). This gives a density of

$$\rho = \kappa \frac{1}{\pi r^2 h} = 0.24\kappa \text{ molec/nm}^3 \tag{7.1}$$

where κ is the packaging density to be determined.

While the solvent is evaporating, Mn_{12}bz molecules are deposited on the surface in an amorphous manner, similar to that shown in Fig. 7.7(b), where there exists a sort of local order, but no real crystalline lattice. To estimate the the total number of molecules on dots formed under these conditions, we can model the multiple rotations as a spherical particle with the same density, i.e. a sphere with $2r = 1.99$ diameter (see Fig. 7.7(c)). Considering the densest packaging of identical spheres, which is the hexagonal-closed-package (see Fig. 7.7(d)), we obtain $\kappa = 0.74048$, and then,

$$\rho = 0.18 \text{ molec/nm}^3 \tag{7.2}$$

For the first deposition we have 1320 identical dots of 249 nm in diameter and 7 nm in height, which give a total volume of 4.5×10^8 nm^3 and therefore $\sim 8.1 \times 10^7$ molecules (about 4 monolayers).

The second deposition is a circular film with a 27 μm diameter and 7 nm height. Its total volume is 4.0×10^9 nm^3 and the total number of molecules $\sim 7.2 \times 10^8$, also with 4 monolayers.

The last deposition has the same surface as the second one, but an average height of 17.5 nm. The total volume is therefore 1.0×10^{10} nm^3 which then gives 1.8×10^9 molecules.

7.4.4 ac susceptibility measurements

Figure 7.8 shows the ac susceptibility, measured at 4.2 K, of the different samples, including bulk and samples deposited. Although deposited samples does not have the same relaxation times that bulk sample, signal outputs differ, thus indicating that the SQUID is able to detect them. We can convert the voltage output to coupled flux, by using Eq. (3.14). As shown in Fig. 7.9,

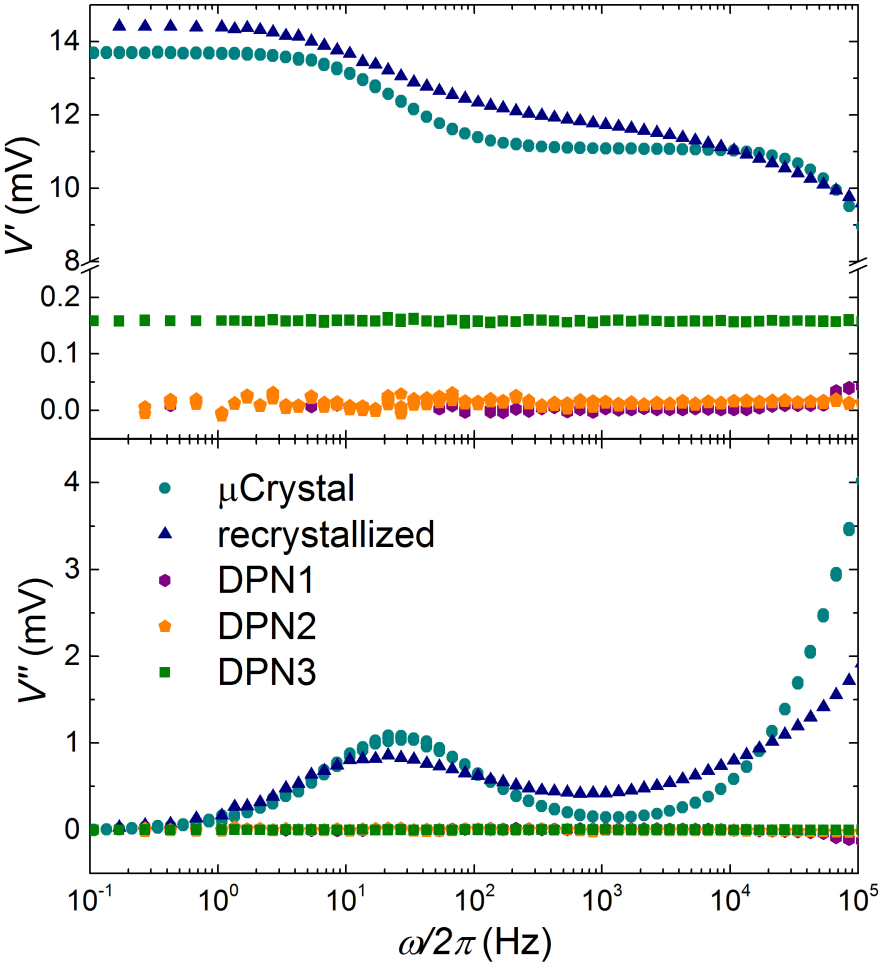

Figure 7.8: Output signals measured for different depositions of Mn_{12}bz.

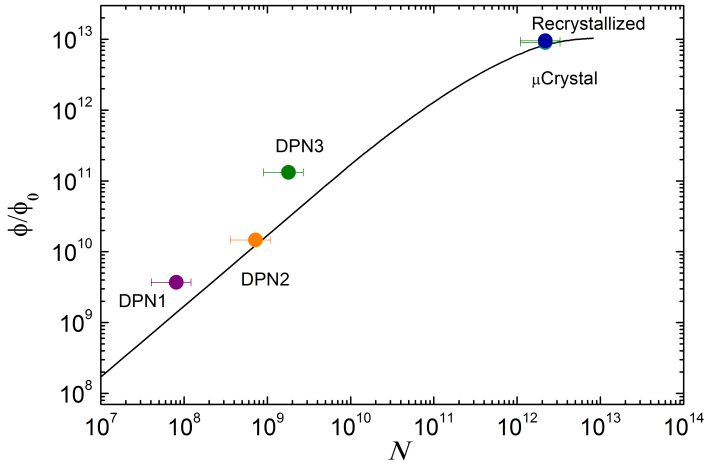

Figure 7.9: Dependence of ϕ as a function of the number of Mn_{12}bz molecules. Solid line is the theoretical simulation.

data agree reasonably well with theoretical simulation, taking into account the difficulty of estimating the number of molecules.

The Mn_{12}bz μcrystal shows clearly two relaxation processes: a slow one at about 30 Hz and a fast one beyond 10 kHz, which is dominant as can be deduced from the height of the imaginary peaks. The recrystallized sample also shows two magnetic relaxation processes. These experiments show that Mn_{12}bz preserves its magnetic memory, and its spin, even after the chemical process associated with the solution and fast recrystallization. However, we find that the imaginary susceptibility peaks and the steps in the real susceptibility are broader than those found in the μcrystal, thus suggesting the presence of larger dispersions of relaxation times. This fact is easily understandable: recrystallization in a quasi amorphous way increases the number of lattice defects and this fact leads into a broader distribution of molecular environments [7.15].

The output measured for the three depositions, DPN1, DPN2 and DPN3 reveals that the dependence of V' and V'' on frequency changes drastically with respect to that found for the bulk samples. The real part remains constant whereas the imaginary part vanishes at any frequency. This behavior agrees with the fact that Mn_{12}bz molecular magnets, deposited on silicon substrates, remain in equilibrium up to very high frequencies and therefore show that their spins relax much faster than in the case of the bulk.

7.4.5 Discussion

Modification of relaxation mechanism may come from changes in the medium stiffness and density with respect to the sample, due to the amorphous crystallization. Similar studies however show that long-range crystalline disorder affects little the anisotropy, magnetic relaxation and magnetic quantum tunneling of this material [7.13, 7.15]. Previous studies in frozen solutions [7.16, 7.17] already showed a lowering on the magnetic relaxation, but not a complete disappearance of the SMM behavior.

Another possible explanation can be related to surface effects on the magnetization relaxation of Mn_{12}bz upon surface deposition. This can be our case due to the strong interaction of the first molecular layer with the surface and molecular strains appearing at the utmost solid-air interphase. Such interactions can modulate the molecular mechanical properties and "deform" the molecule. Deformation can strongly affect the anisotropy parameters and modify the magnetization relaxation properties of the molecule [7.18, 7.19]. While these effects do not become dominant in crystals or thick films (such as the sample measured on the nanoloop in section 3.7.6), in the case of deposition of a few layers, they turn out to be crucial.

7.5 Dy_2 measurements on 30 μm loop SQUIDs

7.5.1 Dy_2 molecules

The magnetic core of Dy_2 molecules contains only two magnetic spins instead of the twelve magnetic spins of Mn_{12} molecules. Interactions with the surface are the main responsible for mechanical deformations in the spin structure and, therefore, in the total spin, as we have shown in the previous section. Dy_2 is a more compact molecule than Mn_{12}, which means that interactions are much weaker and it has less possibilities to be deformed due to the fact that it has less degrees of freedom. On the other hand, the lower symmetry of the coordination sphere of the two Dy^{3+} protected it from strict crystalline conditions. This makes it, in principle, more robust against external strengths.

The main properties of the bulk sample have been already studied on chapters 4 and 6. Each Dy^{3+} has a ground state doublet associated with J_z components $m_J = \pm 15/2$, separated from the first excited by an energy gap of about 100 K. Both spins are coupled and the energy gap between the antiferromagnetic (AFM) and the ferromagnetic (FM) couplings is approximately 1.3 K. Anisotropy axes are rotated an angle $\delta \approx 52^\circ$ with respect to each other. The

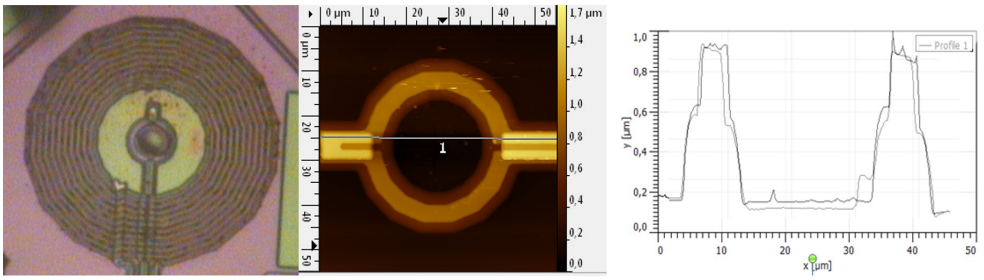

Figure 7.10: Left. Optical image of the susceptometer after depositing a big droplet on the pickup coil. Center. AFM topography image of the first deposition inside the SQUID. Right. Height profile measured along the white line before and after the deposition. Profile also measures the coil height (about 0.9 μm high).

dynamic susceptibility shows a relaxation process below about 0.2 K with an activation energy that matches the AFM-FM gap.

7.5.2 DPN lithography of Dy_2

As in the previous case, we have performed a series of measurements on samples of variable thickness in order to determine whether the magnetic properties change when Dy_2 is subject to surface strain effects. Apart from bulk measurements, already analyzed in chapters 4 and 6, we have performed measurements on two samples, deposited on the pickup coil by DPN. The solvent was also composed of DMF and glycerol.

The first DPN deposition consists of a large droplet, directly deposited on the center of the coil. Figure 7.10 shows an optical image of the device taken after the droplet was deposited. AFM measurements have also been done to obtain the height profile of this sample. In this case, it has been measured directly on the original deposition and not in a replica, as we had done for Mn_{12} samples. The drop has approximately 40 nm high, which corresponds to about 20 molecular layers.

AFM measurements of the second deposition are shown in Fig. 7.11. The deposition was done by using a circular pattern of dots as can be appreciated from the AFM pictures. The first one shows an image of the sample, directly deposited onto the SQUID, whereas the second one is an overhead shot of a replica, deposited on a Si/SiO_2 substrate, equivalent to that of the coil. The height profile in the replica shows a height of about 10 nm, which corresponds to approximately 5 monolayers.

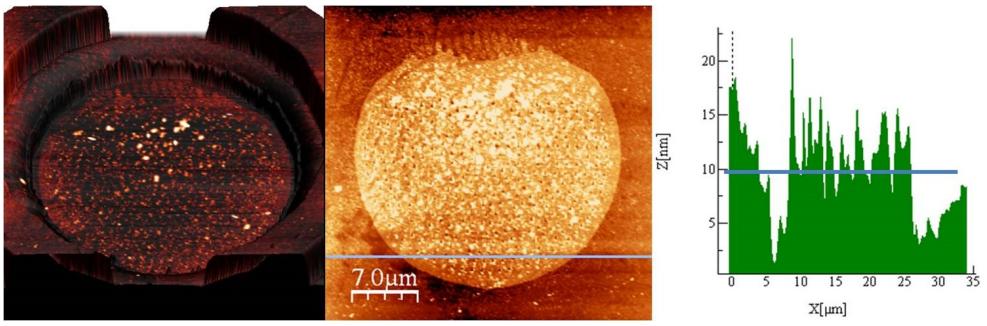

Figure 7.11: AFM topography images of the second deposition. Left. AFM topography of the pattern inside the SQUID. Center. Overhead shot of a replica. Right. Height profile measured along the blue line in the replica.

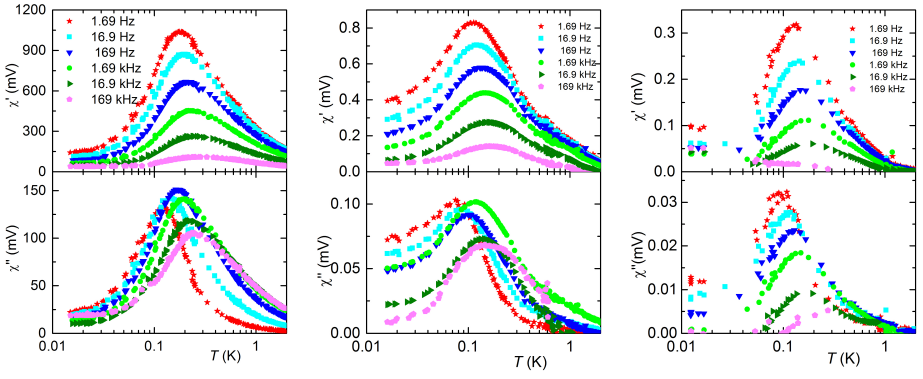

(a) (b) (c)

Figure 7.12: Output signal of ac susceptibility measurements for different depositions of Dy_2. a) Bulk sample. b) First deposition, with 20 monolayers. c) Second deposition, with 5 monolayers.

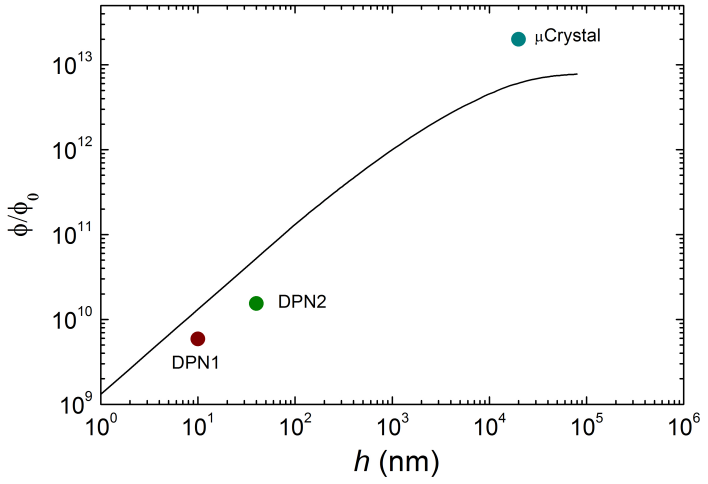

Figure 7.13: Dependence of ϕ as a function of the height of the Dy_2 droplet. Solid line is the theoretical simulation.

7.5.3 ac susceptibility measurements

As we said in previous chapters, relaxation processes in Dy_2 are not visible for ac susceptibility measurements at 4.2 K, and therefore, this single measurement can not give us much information about the surface strain effects on its SMM behavior. For this reason we have carried out ac susceptibility measurements at lower temperatures.

Figure 7.12(a) shows the signal output of the SQUID as a function of T for the case of the bulk sample, already studied in section 6.4.2. The real part has its characteristic peak at about 0.2 K that decreases with increasing frequency. These maxima are associated with a thermally activated process involving transitions between the electronuclear levels, split by the combination of hyperfine and exchange interactions.

Figures 7.12(b) and 7.12(c) correspond to the first and second arrays, respectively, for the same frequencies. In both cases, the same relaxation peak is observed at a similar temperature. Small differences nevertheless are observed, mainly from temperatures below 20 mK. These changes are more noticeable for the imaginary part.

The output signal, approximately proportional to the number of molecules (as observed in Fig. 7.13), is much smaller than in the case of the bulk sample, in relatively well agreement with theoretical simulation. Thus, data from the second deposition are also a bit more noisy, due to its proximity to the SQUID sensitivity.

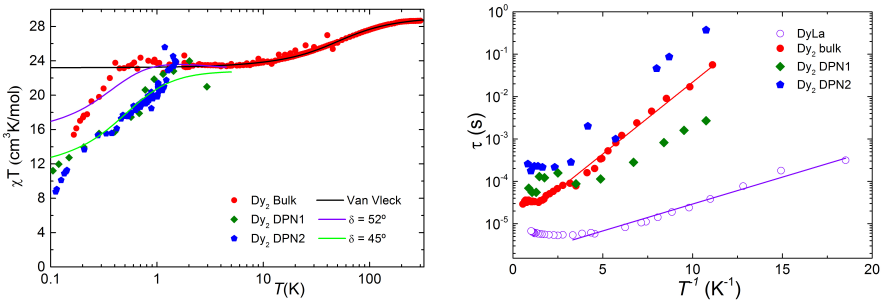

(a) (b)

Figure 7.14: a) χT vs. T representation. Solid lines are simulations for Van Vleck limit and susceptibility considering a rotation of 52° and 45°. b) Activation laws for the DyLa dimer in bulk and for the three measurements of Dy_2.

χT vs. T curve (in Fig. 7.14(a)) agrees with an antiferromagnetic coupling of the Dy^{3+} ions showing, however, a larger drop in susceptibility. This drop can be related to changes on the relative angle δ between both anisotropy axis. Simulations agree with a reduction of δ from 52° (in the bulk sample) to 45° (in the DPN samples).

Spin dynamics, plotted in Fig. 7.14(b), shows that relaxation follows nearly the same activation law for each three measurements of Dy_2. DyLa data are also plotted so that we can compare them with Dy_2 data, and check that deposited samples do not behave as monomer but Dy^{3+} are coupled.

7.5.4 Discussion

As we pointed up at the beginning of this section, Dy_2 offers more guaranties to keep its robustness when it is subdue to surface strains. Dy^{3+} ions do effectively keep coupling antiferromagnetically and coincides with simulations for a ground state $m_J = \pm 15/2$ just as in the case of the crystal bulk sample. This fact offers a promising route towards the integration of single molecules into superconducting devices. The only structural difference to be taken into account is a decrease of the relative angle between both anisotropy axis, which do not seem to be a hindrance for performing quantum computing.

The results also show that spin dynamics remains almost equal, which means that surface deposition does not affect relaxation times or coherence. There are only differences at very low temperatures, when relaxation on deposited samples seems to be slower.

7.6 Conclusions

In this chapter we have studied how surface strains can affect the structure of a small amount of SMM deposited on a Si/SiO_2 surface, considering that these strains may affect the magnetic behavior of the molecules. As strain can provoke mechanical deformations, the more complex the molecular structure is, the more probabilities to be affected by strain it has.

Another goal pursued in this chapter has been studying whether these small amounts of molecules can be successfully coupled to superconducting circuits. Theoretical simulations performed by COMSOL agree with this hypothesis for single molecule magnets with high spin or whose Hamiltonian contain non-negligible off-diagonal terms.

Experimental depositions have been made using Dip-Pen Nanolithography, a technique that have been emerged as an useful tool to deposit high resolute nanostructural patterns made of dilutions of SMM, on substrates of Si/SiO_2. In particular we have studied two different samples, Mn_{12}bz and Dy_2, achieving the following conclusions:

In the case of Mn_{12}bz, dilution and amorphous recrystallization shows already some changes in the molecular spin dynamics. Although it shows two relaxation processes at the same frequencies that the crystal bulk sample, keeping therefore its SMM behavior, they are broader, probably caused by the absence of crystal field. In deposited samples, however, relaxation processes get faster than the limits we are able to measure and Mn_{12}bz looses, therefore, its magnetic memory due to dominance of molecules affected by surface strains. On the other hand, coupling with the superconducting pickup coil of the SQUID seems to agree with the previous simulations, showing that the high spin of Mn_{12}bz (S=10), is enough to assure the coupling even for 4 molecular monolayers.

Dy_2 measurements has shown that, in this case, the dimer keeps its spin dynamics, and therefore its coherent time, when a minute amount of material is deposited on the surface of the SQUID, even for just 5 molecular monolayers. ac susceptibility remains qualitatively equal and shows a larger drop for low temperatures, which means that the angle between the anisotropy main axis of both Dy^{3+} ions is smaller and therefore, the antiferromagnetic energy level is lower. This small change does not affect the behavior of Dy_2 as quantum gate and therefore it is possible to consider Dy_2 dimer (and other dimers with the same structure) valid enough to be integrated on superconducting structures.

In general, Dy_2 has shown a robuster behavior than that of Mn_{12}bz due mainly to the simpler magnetic structure, that allows less possibilities for de-

formation. Both have shown that recrystallization affects little to the spin dynamics. Real changes come from mechanical deformations of the molecule due to the strong interaction of the first molecular layer with the surfaces and molecular strengths appearing at the solid-air interphase.

Bibliography

[7.1] M. Jenkins, U. Naether, M. Ciria, J. Sesé, J. Atkinson, C. Sánchez-Azqueta, E. del Barco, J. Majer, D. Zueco, and F. Luis, "Nanoscale constrictions on superconducting coplanar wavegwave resonators," *Applied Physics Letters*, vol. 105, p. 162601, 2014.

[7.2] M. Jenkins, T. Hümmer, M. J. Martínez-Pérez, J. J. García-Ripoll, D. Zueco, and F. Luis, "Coupling single-molecule magnets to quantum circuits," *New Journal of Physics*, vol. 15, p. 095007, 2013.

[7.3] J. R. Friedman, M. P. Sarachik, J. Tejada, and R. Ziolo, "Macroscopic measurement of resonant magnetization tunneling in high-spin molecules," *Phys. Rev. Lett.*, vol. 76, p. 3830, 1996.

[7.4] J. M. Hernández, X. X. Zhang, F. Luis, J. Bartolomé, J. Tejada, and R. Ziolo, "Field tuning of thermally activated magnetic quantum tunnelling in Mn_{12} - ac molecules," *Europhys. Lett.*, vol. 35, no. 4, p. 301, 1996.

[7.5] J. M. Hernández, X. X. Zhang, F. Luis, J. Tejada, J. R. Friedman, M. P. Sarachik, and R. Ziolo, "Evidence for resonant tunneling of magnetization in Mn_{12} acetate complex," *Phys. Rev. B*, vol. 55, p. 5858, 1997.

[7.6] K. Takeda, K. Awaga, T. Inabe, A. Yamaguchi, H. Ishimoto, T. Tomita, H. Mitamura, T. Goto, N. Mori, and H. Nojiri, "Magnetic anisotropy, tunneling effects, high-frequency epr, and molecular structure of fast-relaxation species of Mn_{12}," *Phys. Rev. B*, vol. 65, p. 094424, 2002.

[7.7] D. S. Ginger, H. Zhang, and C. A. Mirkin, "The evolution of Dip-Pen Nanolithography," *Angewandte Chemie*, vol. 43, p. 30, 2004.

[7.8] R. D. Piner, J. Zhu, F. Xu, S. Hong, and C. A. Mirkin, ""Dip-Pen" nanolithography," *Science*, vol. 283, p. 661, 1999.

[7.9] M. Jenkins, *Coupling Quantum Circuits to Magnetic Molecular Qubits*. PhD thesis, Universidad de Zaragoza, 2015.

[7.10] E. Bellido, P. Gonzalez-Monje, A. Repolles, M. Jenkins, J. Sese, D. Drung, T. Schurig, K. Awaga, F. Luis, and D. Ruiz-Molina, "Mn_{12} single molecule magnets deposited on μSQUID sensors: the role of interphases and structural modifications," *Nanoscale*, vol. 5, no. 24, p. 12565, 2013.

[7.11] A. Caneschi, D. Gatteschi, R. Sessoli, A. l. Barra, L. C. Brunel, and M. Guillot, "Alternating-current susceptibility, high-field magnetization, and millimeter band EPR evidence for a ground S = 10 state in $[Mn_{12}O_{12}(CH_3COO)_{16}(H_2O)_4]_2{\cdot}CH_3COOH{\cdot}4H_2O$," *J. Am. Chem. Soc.*, vol. 113, no. 15, p. 5873, 1991.

[7.12] R. Sessoli, H. L. Tsai, A. R. Schake, S. Wang, J. B. Vincent, K. Folting, D. Gatteschi, G. Christou, and D. N. Hendrickson, "High-spin molecules: $[Mn_{12}O_{12}(O_2CR)_{16}(H_2O)_4]$," *J. Am. Chem. Soc.*, vol. 115, p. 1804, 1993.

[7.13] H. J. Eppley, H. L. Tsai, N. de Vries, K. Folting, G. Christou, and D. N. Hendrickson, "High-spin molecules: unusual magnetic susceptibility relaxation effects in $[Mn_{12}O_{12}(O_2CEt)_{16}(H_2O)_3]$ ($S = 9$) and the one-electron reduction product (PPh4) $[Mn_{12}O_{12}(O_2CEt)_{16}(H_2O)_4]$ ($S = 19/2$)," *J. Am. Chem. Soc.*, vol. 117, p. 301, 1995.

[7.14] K. Takeda, K. Awaga, and T. Inabe, "Crystal structure and magnetic properties of $[Mn_{12}O_{12}(O_2CPh)_{16}(H_2O)_4]{\cdot}2(PhCO_2H)$: Evidence of domain formation with different blocking temperatures," *Phys. Rev. B*, vol. 57, p. R11062, May 1998.

[7.15] C. Carbonera, F. Luis, J. Campo, J. Sánchez-Marcos, A. Camón, J. Chaboy, D. Ruiz-Molina, I. Imaz, J. van Slageren, S. Dengler, and M. González, "Effect of cryscrystal disorder on quantum tunneling in the single-molecule magnet Mn_{12} benzoate," *Phys. Rev. B*, vol. 81, p. 014427, 2010.

[7.16] A. Caneschi, T. Ohm, C. Paulsen, D. Royal, C. Sangregorio, and R. Sessoli, "Quantum tunneling of the magnetic moment in manganese and iron molecular clusters," *J. Magn. Magn. Mater.*, vol. 117-181, p. 1330, 1998.

[7.17] F. E. Hallak, J. van Slageren, J. Gómez-Segura, D. Ruiz-Molina, and M. Dressel, "High-frequency esr and frequency domain magnetic resonance spectroscopic studies of single molecule magnets in frozen solution," *Phys. Rev. B*, vol. 75, p. 104403, 2007.

[7.18] N. Domingo, F. Luis, M. Nakano, M. Muntó, J. Gómez, J. Chaboy, N. Ventosa, J. Campo, J. Veciana, and D. Ruiz-Molina, "Particle-size

dependence of magnetization relaxation in Mn_{12} crystals," *Phys. Rev. B*, vol. 79, p. 214404, 2009.

[7.19] M. Muntó, J. Gómez-Segura, J. Campo, M. Nakano, N. Ventosa, D. Ruiz-Molina, and J. Veciana, "Controlled crystallization of Mn_{12} single-molecule magnets by compressed CO_2 and its influence on the magnetization relaxation," *J. Mater. Chem*, vol. 16, p. 2612, 2006.

General conclusions

This work we have presented here means a first step in the use of SMM, not only as quantum memories, but also as active elements of quantum computing. We have shown how to perform the two universal quantum gates: CNOT and CCNOT, which, together with the NOT gate, form the basis for universal and reversible quantum computing. We have also dealed with the problem of putting these molecules on surfaces that can interact with them. In parallel we have tested and developed a new generation of μsusceptometer SQUID that allows us to characterize the magnetic response of SMM. The general conclusions that can be extracted from this thesis are the following ones:

We have studied the main characteristics of a new generation of 30 μm-loop SQUID sensors. Noise measurements reveals a dominant contribution of the electronic noise. By including a low-noise amplifier stage, we have successfully obtained the intrinsic μSQUID noise $S^{1/2} = 1.7 \pm 0.2\ \mu\phi_0/\sqrt{\text{Hz}}$.

We also have developed a trustful method to correctly characterize the output signal of the bare susceptometer and substrate it ti the signal of an hypothetical sample on it. This correction consist of direct subtraction and a phase correction. Different ways to reduce the background signal have also been explored, although none of them have reported results satisfactory enough to systematically apply them.

To improve sensitivity of he sensor we have upgraded the 30 μm-loop SQUID susceptometer to measure nanometric samples. To achieve this goal a nanoloop has been fabricated in series to the pickup coil of the SQUID. In this way, the sensitivity in the coil center is improved up to ten times, from $\sim$0.55 T/A to $\sim$6 T/A, with satisfactory results.

On the other hand, we have studied single molecular magnets composed by two or three magnetic ions and we have shown that they are good candidates for performing quantum operations, in particular CNOT and SWAP quantum gates for the dimer and Toffoli and Fredkin gates for the trimers.

In the case of dimers, we have studied "homonuclear" Kramers (Dy_2) and non-Kramers (Tb_2) dimers and the "heteronuclear" Kramers ErCe dimer. These molecules meet the ingredients required to implement SWAP and CNOT quantum gates, i. e., quantum entanglement, addressable qubits and transitions in coherent times. For each case, the ground entangled state corresponds to the antiferromagnetic coupling, separated from the ferromagnetic one in 1-2 K. Specific heat confirms the theoretical model, designed for dimers, and CNOT and SWAP operations have been done on these dimers, by using EPR technique.

A further study of spin dynamics has revealed that nuclear spin affects the relaxation processes of dimers, even when not the 100% of the lanthanide ions possess this hyperfine splitting. ac susceptibility measurements have shown that monomers ErLa and DyLa have at least two relaxation processes, on the order of μs, one associated to qubits without nuclear spin, and the other one, also on the same order but slower, related to relaxation of qubits with nuclear spins, that compete with the first one. Dimers, Er_2 and Dy_2, also show these double relaxation, apart from an additional one, associated to the AFM-FM splitting.

The low temperature energy levels diagram if linear CuLaCu and CuErCu trimers have also been determined. We have found that Cu^{2+} ions of CuLaCu are weakly antiferromagnetically coupled and have significantly different gyromagnetic factors, thus introducing the necessary asymmetry that produces the conditions for a potential 2-qubit processor, just as in the case of dimers. As for CuErCu, Er^{3+} ion has been demonstrated to act as an effective spin-1/2, very weakly coupled to the Cu^{2+} ions. Estimations for this coupling are only valid for low magnetic fields and frequencies, allowing to perform Fredkin and Toffoli gate computations, only for these conditions. Further measurements will be necessary to defined a model that agrees with magnetic behaviour at high magnetic fields and frequencies.

Finally, we have studied the strain effects on the dimers when they are deposited on surfaces of Si/SiO_x, using DPN technique, and their coupling to superconducting circuits. Dimers, in particular Dy_2, have shown to be robust enough to keep their magnetic behaviour even for minute amount of sample (down to 5 monolayers) in contrast to other more complex SMM, as the Mn_{12}bz, whose relaxation becomes fast enough to loose its magnetic memory.

In general, we have demonstrated that lanthanide dimers are capable to act as quantum gates and are robust enough to be integrated into superconducting circuits. Coupling to these circuits has been also checked. Next step would be to design appropriate superconducting circuits, able to properly tune the studied SMM and interact individually with them.

Conclusiones generales

El trabajo aquí presentado constituye un primer paso hacia la utilización de imanes moleculares, no sólo como memorias de almacenamiento cuántico, sino como elementos activos de un ordenador cuántico. Hemos demostrado cómo realizar las puertas CNOT y CCNOT, dos de las puertas cuánticas universales que, junto con la puerta NOT, constituyen la base de la computación cuántica universal y reversible. También hemos considerado el problema que surge al colocar estas moléculas sobre superficies que puedan interaccionar con ellas. Por otro lado, y simultáneamente, hemos testado y mejorado una nueva generación de μsusceptómetros SQUID que nos han permitido una mejor caracterización de la respuesta magnética de los imanes moleculares. Las conclusiones generales que pueden obtenerse de esta tesis doctoral son las siguientes:

Hemos estudiado las principales características de una nueva generación de sensores SQUID con diámetro de 30 μm. Medidas sobre el ruido del sensor ponen de manifiesto que el ruido provocado por la electrónica es dominante. Añadiendo una etapa amplificadora de bajo ruido, hemos podido medir con éxito el ruido intrínseco del SQUID, $S^{1/2} = 1.7 \pm 0.2\ \mu\phi_0/\sqrt{\text{Hz}}$.

También hemos desarrollado un método fiable con el que caracterizar correctamente la señal de salida del susceptómetro vacío, con el fin de poder sustraerla apropiadamente de la señal de salida del susceptómetro, cuando está midiendo una hipotética muestra. La corrección consiste, fundamentalmente, en la sustracción de la señal de fondo más una corrección en la fase. También se han probado diferentes formas de reducir la señal de fondo, aunque ninguna de ellas nos ha reportado resultados lo suficientemente satisfactorios como para aplicarlas sistemáticamente.

Con el fin de mejorar la sensibilidad del sensor, hemos llevado a cabo una mejora del susceptómetro SQUID de 30 μm, para, así, poder medir muestras de tamaño nanométrico. Para ello, se ha fabricado mediante la técnica FIB una nanoespira es serie con la bobina del propio SQUID. De esta manera, la sensibilidad en el centro de la espira aumenta hasta diez veces, de $\sim$0.55 T/A hasta $\sim$6 T/A, con resultados satisfactorios.

Por otro lado, hemos estudiado imanes moleculares compuestos por dos o tres iones magnéticos, demostrando que son buenos candidatos para llevar a cabo operaciones cuánticas tales como las puertas CNOT y SWAP, para imanes con dos átomos magnéticos (dímeros), y las puertas Toffoli y Fredkin, para imanes con tres átomos magnéticos (trímeros).

En el caso de los dímeros, hemos estudiado tanto sistemas "homonucleares", Kramers (Dy_2) y no Kramers (Tb_2), como un sistema Kramers "heteronuclear", el dímero de ErCe. Estas moléculas reúnen los ingredientes necesarios para implementar las puertas cuánticas SWAP y CNOT y que son los siguientes: entrelazamiento cuántico, qubits distinguibles y capacidad de realizar transiciones en un tiempo coherente cuánticamente. En los tres casos, el estado entrelazado de menor energía ha resultado ser el estado antiferromagnético, separado del estado ferromagnético por 1-2 K. Las medidas de calor específico confirman el modelo teórico, diseñado para estos dímeros, y las operaciones CNOT y SWAP han podido ser realizadas mediante técnicas de EPR.

Un estudio más en profundidad sobre la dinámica de espín ha revelado que la presencia de espín nuclear afecta en los procesos de relajación de los dímeros, incluso cuando no todos los iones poseen este desdoblamiento hiperfino. Según las medidas de susceptibilidad ac, realizadas para los monómeros ErLa y DyLa, aparecen al menos dos procesos de relajación del orden de los μs, uno asociado a la relajación de qubits sin espín nuclear y otro, un poco más lento, relacionado con la relajación de qubits con espín nuclear. Los dímeros Er_2 y Dy_2 también muestran esta doble relajación, además de una relajación adicional, asociada al desdoblamiento entre niveles AFM y FM.

También se han determinado por otro lado los niveles de energía de los trímeros lineales CuLaCu y CuErCu. Hemos descubierto que los iones de cobre(II) en el trímero de CuLaCu están débilmente acoplados antiferromagnéticamente y que sus factores giromagnéticos son significativamente diferentes. Esto produce la asimetría necesaria para poder usarlos como un potencial procesador de 2 qubits, del mismo modo que en el caso de los dímeros. En cuanto al trímero de CuErCu, se ha demostrado que el ion erbio actúa como un espín efectivo 1/2, muy débilmente acoplado a los iones cobre(II). Los ajustes teóricos para este acoplo sólo son válidos, desafortunadamente, cuando se aplican campos magnéticos bajos y excitaciones de baja frecuencia, permitiendo la realización de puertas Toffoli y Fredkin sólo bajo estas circunstancias. Será necesario por tanto realiza más medidas para poder definir un modelo que permita explicar el comportamiento magnético del sistema para altos campos y frecuencias.

Por último, hemos estudiado los efectos de tensión en superficie sobre los dímeros, al depositarlos en pequeñas cantidades sobre superficies de Si/SiO_x, y

también su capacidad de acoplarse a circuitos superconductores. Los dímeros, en particular el de Dy_2, han demostrado ser lo suficientemente robustos como para preservar su comportamiento magnético incluso para la deposición de una minúscula cantidad de material, hasta las 5 monocapas, en claro constaste con otros imanes moleculares más complejos, como el Mn_{12}bz, cuya relajación se vuelve tan rápida que acaba perdiendo su propiedad de memoria magnética.

En general, hemos demostrado que los dímeros de Ln son capaces de funcionar como puertas lógicas cuánticas y, además, son lo suficientemente robustos como para poder integrarse en circuitos superconductores. El acoplo entre ambos sistemas también lo hemos demostrado. El próximo paso sería diseñar un circuito superconductor apropiado que fuera capaz de sintonizar con los imanes moleculares e interactuar individualmente con ellos.

List of publications

1. Christian Cervetti, Angelo Rettori, Maria Gloria Pini, Andrea Cornia, Ana Repollés, Fernando Luis, Martin Dressel, Stephan Rauschenbach, Klaus Kern, Marko Burghard, and Lapo Bogami. "The classical and quantum dynamics of molecular spins on graphene", *Nature Materials*, Accepted.

2. David Aguilà, Leoni A. Barrios, Verónica Velasco, Olivier Roubeau, Ana Repollés, Pablo J. Alonso, Javier Sesé, Simon J. Teat, Fernando Luis, and Guillem Aromí. "Heterodimetallic [LnLn'] Lanthanide Complexes: Toward a Chemical Design of Two-Qubit Molecular Spin Quantum Gates", *Journal of the American Chemical Society*, vol. 136, no. 40, p. 14215, 2014.

3. Dietmar Drung, Jan-Hendrik Storm, Frank Ruede, Alexander Kirste, Marcel Regin, Thomas Schurig, Ana Repollés, Javier Sesé, and Fernando Luis. "Thin-Film Microsusceptometer With Integrated Nanoloop", *IEEE Transactions on applied superconductivity*, vol. 24, no. 4, p. 1600206, 2014.

4. Ana Repollés, Andrea Cornia, and Fernando Luis. "Spin-lattice relaxation via quantum tunneling in diluted crystals of Fe-4 single-molecule magnets", *Physical Review B*, vol. 89, no. 5, p. 054429, 2014.

5. Miguel Clemente-León, Eugenio Coronado, Carlos J. Gómez-García, Maurici López-Jordá, Agustín Camón, Ana Repollés, and Fernando Luis. "Insertion of a Single-Molecule Magnet inside a Ferromagnetic Lattice Based on a 3D Bimetallic Oxalate Network: Towards Molecular Analogues of Permanent Magnets", *Chemistry A European Journal*, vol. 20, no. 6, p. 1669, 2014.

6. Elena Bellido, Pablo González-Monje, Ana Repollés, Mark Jenkins, Javier Sesé, Dietmar Drung, Thomas Schurig, Kunio Awaga, Fernando Luis, and Daniel Ruiz-Molina. "Mn-12 single molecule magnets deposited on

mu-SQUID sensors: the role of interphases and structural modifications", *Nanoscale*, vol. 5, no. 24, p. 12565, 2013.

7. Dietmar Drung, Jan-Hendrik Storm, Frank Ruede, Alexander Kirste, Marcel Regin, Thomas Schurig, Ana Repollés, Javier Sesé, and Fernando Luis. "Thin-Film Microsusceptometer With Integrated Nanoloop", *2013 IEEE 14th International Superconductive Electronics Conference (ISEC)*, 2013.

8. Juan Bartolomé, Fernando Bartolomé, Laura Martínez García, Adriana I. Figueroa, Ana Repollés, María José Martínez-Pérez, Fernando Luis, César Magén, Sonja Selenska-Pobell, Frank Pobell, Thomas Reitz, Rico Schoenemann, Thomas Herrmannsdoerfer, Mohamed L. Merroun, Andreas Geissler, Frank Wilhem, and Andrey Rogalev. "Strong Paramagnetism of Gold Nanoparticles Deposited on a Sulfolobus acidocaldarius S Layer", *Physical Review Letters*, vol. 109, no. 24, p. 247203, 2012.

9. Fernando Luis, Ana Repollés, María José Martínez-Pérez, David Aguilà, Olivier Roubeau, David Zueco, Pablo J. Alonso, Marco Evangelisti, Agustín Camón, Javier Sesé, Leoní A. Barrios, and Guillem Aromí. "Molecular Prototypes for Spin-Based CNOT and SWAP Quantum Gates", *Physical Review Letters*, vol. 107, no. 11, p. 117203, 2011.

10. David Aguilà, Leoní A. Barrios, Fernando Luis, Ana Repollés, Olivier Roubeau, Simon J. Teat, and Guillem Aromí. "Synthesis and Properties of a Familiy of Unsymmetric Dinuclear Complexes of Ln(III) (Ln=Eu, Gd, Tb)", *Inorganic chemistry*, vol. 49, no. 15, p. 6784, 2010.